AD-A179 575 COLLISIONAL DYNAMICS OF THE B 3PI(O+) STATE OF BROMINE MONOCHLORIDE(U) AIR FORCE INST OF TECH WRIGHT-PATTERSON AFB OH SCHOOL OF ENGINEERING G P PERRAM AUG 86 1/4

UNCLASSIFIED AFIT/DS/PH/86-1 F/G 7/2 NL

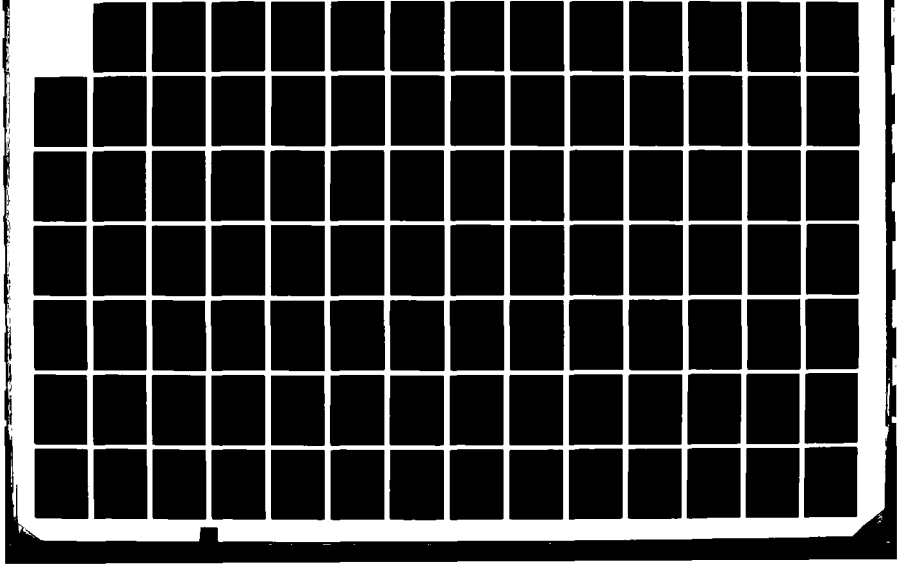

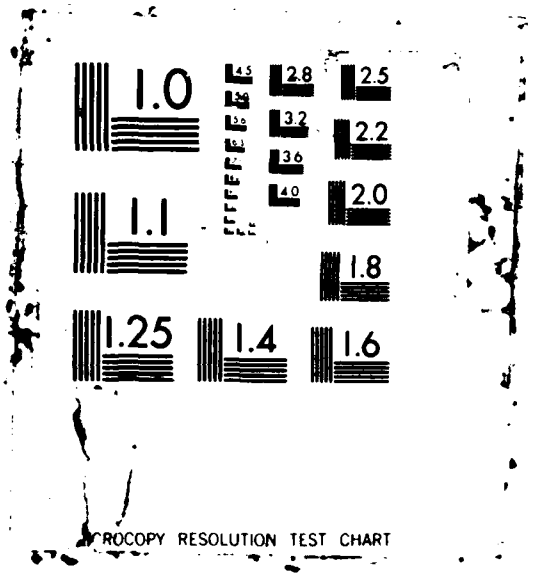
1.0
1.1
1.25
1.4
1.6
2.8
3.2
3.6
4.0
2.5
2.2
2.0
1.8
ROCOPY RESOLUTION TEST CHART

COLLISIONAL DYNAMICS OF THE B $^3\Pi(0^+)$ STATE OF BROMINE MONOCHLORIDE

DISSERTATION

AFIT/DS/PH/86-1

Glen P. Perram
Captain USAF

DEPARTMENT OF THE AIR FORCE
AIR UNIVERSITY
AIR FORCE INSTITUTE OF TECHNOLOGY

Wright-Patterson Air Force Base, Ohio

COLLISIONAL DYNAMICS OF THE B $^3\Pi(0^+)$ STATE OF BROMINE MONOCHLORIDE

DISSERTATION

AFIT/DS/PH/86-1

Glen P. Perram
Captain USAF

AFIT/DS/PH/86-1

COLLISIONAL DYNAMICS OF THE B $^3\Pi(0^+)$ STATE OF BROMINE MONOCHLORIDE

DISSERTATION

Presented to the Faculty of the School of Engineering

of the Air Force Institute of Technology

Air University

in Partial Fulfillment of the

Requirements for the Degree of

Doctor of Philosophy

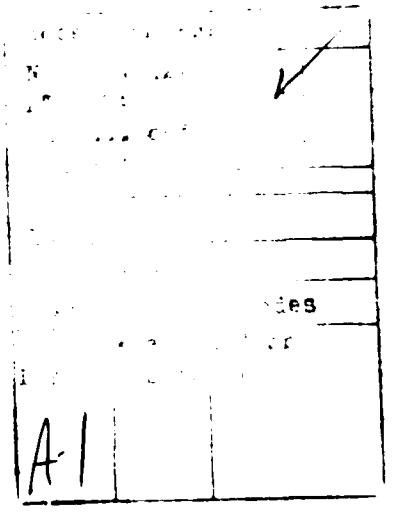

by

Glen P. Perram, B.S., M.S.

Captain USAF

AFIT/DS/PH/86-1

COLLISIONAL DYNAMICS OF THE B $^3\Pi(0^+)$ STATE OF BROMINE MONOCHLORIDE

by

Glen P. Perram, B.S., M.S.

Captain USAF

Approved:

Ernest L. Duke Chairman	4 AUG 1986
James E. Hitchcock	4 Aug 1986
James A. Jupe	4 Aug 1986
Steven J. Davis	4 Aug 1986
William P. Lacky	4 Aug 1986

Accepted:

J. P. Rosenieniecki Dean, School of Engineering	5 Aug. 1986

Acknowledgments

The sponsorship and interest of the Air Force Weapons Laboratory and the financial assistance of the Air Force Office of Scientific Research in support of this research effort and the author's PhD dissertation work with the Air Force Institute of Technology is gratefully acknowledged. The cooperation of these three US Air Force agencies has established a unique research opportunity.

Profound gratitude is expressed to Dr. Steven J. Davis, thesis advisor, for his direction in selecting this investigation topic, for his encouragement, advice, instruction, and guidance in the conduct of the study, and for his interest and support of the author's professional development. Dr. Davis has been a true, trusted, and highly respected counselor throughout this investigation.

The instruction, guidance, support, and discussions provided by Dr. Ernest A. Dorko, committee chairman, is particularly appreciated. Dr. Dorko's instruction in theoretical and experimental approaches to chemical physics, spectroscopy and kinetics in particular, furnished the author with an outstanding background for the conduct of this research.

The author also expresses an important note of gratitude to Mr. Leonard Hanko for his expert technical assistance, to Dr. Robert Shea for computational assistance and occasional discussions, to Lt. Silvia Richert for her assistance in pulsed data aquisition, to SrA. Ulysses Finley and Mr. Sam Herrara for timely assistance with the CW data reduction, to Capt. Paul Wolf for many useful discussions on energy transfer studies and continual friendship, to Lt. Brian McFeeters for execution of an RKR program, and to AFWL glassblowing, metal shop, and metrology support personnel.

Finally, the author has depended on his wife, Michelle, for support in every aspect of this research. Without her love, understanding, patience, listening ear, and much needed advice, this project would not have succeeded.

Glen P Perram

Contents

Page

Acknowledgments iii

List of Figures viii

List of Tables xii

Notation xiv

Abstract xix

I. Introduction

A. Historical Perspective 1
B. Visible Chemical Lasers 2
C. The Halogens and Interhalogens 6
D. The Study of Molecular Energy Transfer 9
E. Problem Statement 11

II. Background Theory

A. Spectroscopy 13
B. Laser Induced Fluorescence Techniques 20
C. Kinetic Analysis 25
1. Introduction 25
2. Master Rate Equation 25
3. Steady-State Solutions 33
a. Electronic Quenching 34
b. Vibrational Transfer 37
c. Rotational Transfer 40
4. Time-Resolved Solutions 43
a. Electronic Quenching 44
b. Radioactive Decay Analogy 46
c. The Eigenvalue Problem 48
d. Pressure Scaling 51
e. The Inverse Problem 51
f. The Montroll-Shuler Model 54
g. Numerical Integration Methods 56

III. Experimental Section

A. Steady-State Experiment 57
B. Pulsed Experiment 63

Contents

Page

IV. Results and Discussion

A. Introduction 70
B. Preliminary Steady-State Results 71
1. Quenching Studies 71
2. Spectrally-Resolved Data 79
3. Rotational Spectra 85
4. Summary of Preliminary Conclusions 91
C. Lifetime Studies 92
1. Excitation Spectra 92
2. Electronic Quenching 93
3. Pressure Dependent Quenching 101
4. Total Removal Rates and Radiative Lifetimes . 106
5. Scaling of Total Removal Rates 109
6. Summary of Pulsed Lifetime Studies 111
D. Temporally-Resolved, Spectrally-Resolved Studies 113
1. Time evolution of BrCl(B;v′) 113
2. Pressure Scaling 114
3. The Montroll-Shuler Solution 116
4. Interpretations of Clyne and McDermid 122
5. Numerical Methods and Vibrational Transfer .. 127
6. Non-Uniqueness of the Numerical Method 131
7. Selection of a Unique Rate Matrix 137
8. The BrCl(B) Quenching Mechanism 144
9. Energy Transfer with Rare Gases 145
10. Summary of Temporally-Resolved Studies..... 154
E. Steady-State Spectrally-Resolved Studies 157
1. Introduction 157
2. Self Vibrational Transfer 158
3. Vibrational Transfer with Helium 168
4. Rotational Transfer 171
5. Summary of the Steady-State Studies 175

V. Conclusions

A. Summary of BrCl(B) Energy Transfer 171
B. Laser Induced Fluorescence and Energy Transfer . 180
C. Proposed Future Investigations 185

Bibliography 187

Organization of Appendices..... 197

Appendix A: Dye Laser Pumped Br_2(B-X) Laser 198

Appendix B: Spectroscopy of BrCl B and X States 226

Appendix C: Experimental Calibrations 240

Appendix D: Basic Energy Transfer Theories 250

Contents

	Page
Appendix E: Eigenvalue Problem	259
Appendix F: Predissociated State Quenching	265
Appendix G: Synthetic CW LIF Spectra	269
Appendix H: Error Analysis	273
Appednix I: Spectral Areas and CW Number Densities	280
Appendix J: Steady-State Removal Rates	284
Vita	286

List of Figures

Figure		Page
1	General Features of a Visible Chemical Laser...	4
2	Correlation Diagram for the Lowest Electronic States of the Halogens.....	14
3	Typical Interhalogen Potential Energy Curves...	14
4	Perturbed BrCl(B) State and Interactions.....	17
5	BrCl Potential Energy Curves.....	19
6	Basic Laser Induced Fluorescence Technique.....	21
7	Time-Resolved Laser Induced Fluorescence.....	24
8	CW Spectrally-Resolved LIF Experiment.....	58
9	CW Excitation Spectrum.....	62
10	Temporally-Resolved LIF Experiment.....	64
11	Single-Shot BrCl(B) Temporally-Resolved Emission Spectra.....	65
12-14	CW Electronic Quenching of BrCl(B) by the Mix..	72
15	CW Pressure Dependent Quenching.....	74
16	CW Total Quenching of BrCl(B,v′=6) by the Mix..	76
17-18	CW Total Quenching of BrCl by Helium.....	78
19-20	CW LIF Emission spectra of BrCl(B;v′).....	80
21	Typical High Resolution CW LIF Emission Spectrum.....	83
22	Low Pressure CW LIF Emission Spectrum.....	83
23	Rotationally-Resolved LIF Emission Spectrum....	86
24	Rotational Temperature of v′=0 at 15 Torr.....	86
25	Simulated CW LIF Transfer Spectrum.....	89
26	Stabilization of Predissociated Distribution...	90
27	Pulsed Excitation Spectrum.....	93

List of Figures

Figure		Page
28	Typical Total Fluorescence Decay Curve.....	94
29-30	Stern-Volmer Plot for Self Electronic Quenching	96
31	Thermalized CW Vibrational Populations.....	98
32	Stern-Volmer for Rare Gas Electronic Quenching.	102
33	Self Quenching Stern-Volmer Plots.....	104
34-35	Total Self Quenching Stern-Volmer Plot.....	107
36-37	Vibrational Scaling of Total Removal Rates.....	110
38	Typical Temporally-Resolved, Spectrally-Resolved LIF Spectra.....	114
39	Pressure Scaling of Pulsed Data.....	115
40	Montroll-Shuler Model Fit to Pulsed Data.....	118
41	Montroll-Shuler Results in a Stern-Volmer Plot.	118
42	Failure of the Montroll-Shuler Model at High v'	119
43a	Montroll-Shuler Fit to the Simulated Spectra...	121
43b	Montroll-Shuler Model Applied to Predissociated Vibrational Manifold.....	121
44-46	Fits to the Pulsed Data With Numerical Solution	134
47	Numerical Solution Logical Flow Chart.....	139
48	High Pressure CW Populations in v'=0.....	142
49	Chlorine Potential Energy Curves.....	146
50	BrCl(B) - Cl_2 Energy Resonances.....	147
51	Pulsed Solutions for Helium Transfer.....	150
52	High Pressure CW Populations for Helium Buffer.	151
53	Scaling of Vibrational Transfer for Rare Gases.	154
54	Relative CW Population Distributions.....	159
55	Scaling of Vibrational Transfer Rates with v'..	163

List of Figures

Figure		Page
56	Comparison of Detailed Balance Rates.....	164
57	CW Vibrational Distribution for He Collisions..	170
58-59	Relative CW Rotational Populations.....	172
60	Scaling of Rotational Rates.....	174
61	Rotational Removal Rates in Various v″ States..	176
A1	Molecular Bromine Potential Energy Curves.....	199
A2	Br_2 Optically-Pumped Laser Experiment.....	201
A3-A4	Br_2 Stimulated Emission Excitation Spectrum....	205
A5-A6	High resolution Br_2 Laser Excitation Spectrum..	208
A7	Comparison of Measured and Calculated Second Differences.....	209
A8	Spectrally-Resolved Br_2 Laser Output.....	209
A9	Br_2 Laser Saturation Test.....	211
A10	Br_2 Laser Output as a Function of Br_2 Pressure.	213
A11	Energy States of Br_2 Laser Model.....	214
A12	Br_2 Laser Pulse Shape.....	221
A13	Br_2 Rotationally-Resolved LIF Emission Spectrum	223
B1-B3	Psuedo CW Spectra.....	233
B4-B6	Pulsed Excitation Spectra.....	236
C1	BrCl(B) Saturation Test.....	241
C2	CW Spectral Response Calibration.....	243
C3-C4	Monochromator Calibration.....	244
C5	Transient Recorder Time Base Calibration.....	246
C6	Pulsed Spectral Response Calibration.....	248
E1	Vibrational Scaling of Rate Matrix Eigenvalues.	264

List of Figures

Figure		Page
F1	Energy States for R-T Model.....	265
G1	BrCl LIF Synthetic Spectra.....	271
I1	Spectral Band Area Deconvolution.....	282

List of Tables

Table	Description	Page
I	Spectroscopic Constants for BrCl X and B Sates	17
II	Steady-State Electronic Quenching Rates.....	73
III	Buffer Gas Electronic Quenching Rates.....	101
IV	BrCl(B) Radiative Lifetimes.....	108
V	BrCl(B) Total Quenching Rates.....	108
VI	Helium Quenching Rates.....	111
VII	Clyne's Second Model Rate Constants.....	124
VIII	Clyne's Third Model Rate Constants.....	125
IX	Numerical Solution Number One.....	132
X	Numerical Solution Number Two.....	133
XI	Comparison of Predicted and Observed Quenching Rates.....	140
XII	Final Pulsed Solution.....	142
XIII	Comparison of Quenching Rates.....	144
XIV	Pulsed Helium Solution Number One.....	148
XV	Pulsed Helium Solution Number Two.....	149
XVI	Rare Gas Fundamental Vibrational Rate Constants	152
XVII	Self Transfer CW Rate Matrix.....	162
XVIII	CW Helium V-T Rate Constants.....	169
XIX	Helium V-T Detail Balance Ratios.....	171
XX	Total Rotational Removal Rates.....	174
XXI	Summary of Quenching, V-T, and R-T Rates.....	181
BI	BrCl Ground State Rotational Constants.....	226
BII	BrCl(B) Rotational Term Values.....	227
BIII	BrCl B-X Transition Wavelengths.....	228

List of Tables

Table	Description	Page
BIV	BrCl B-X Franck-Condon Factors.....	228
BV	Vibrational Energy Spacing in BrCl(B).....	230
BVI	BrCl Absorption Bands.....	231
BVII	Pulsed Emission Band Observation Wavelengths...	237
BVIII	Pulsed Emission Band Overlap Percentages.....	239
CI	CW Relative Spectral Response.....	242
CII	Transient Recorder Time Base Calibration.....	247
CIII	Detectable Emission for BrCl(B;v).....	249
DI	Gas Kinetic Collision Parameters.....	251
JI	Rotational Removal Rate Constant Ratios.....	285

Notation

Symbol	Description	Units
Fundamental constants and variables:		
c	speed of light	m/s
h	Planck's constant	J-s
k_B	Boltzmann constant	J/molec-K
C	arbitrary proportionality constant	*****
$\delta_{i,j}$	Kronecker delta function	*****
P	pressure	torr
T	temperature	K
T_R	rotational temperature	K
v	velocity	m/s
A	area	m^2
V	volume	m^3
V_m	laser mode volume	m^3
L	gain medium length	m
t	time	s
t'	transformed time variable	*****
t_p	pump laser pulse duration	s
Spectroscopic Symbols:		
T_e	total energy of electronic state	cm^{-1}
T_e^o	electronic energy	cm^{-1}
T_p	total energy at crossing point of two potential energy curves	cm^{-1}
$V(r)$	potential energy at internuclear separation r	cm^{-1}
r	internuclear separation	nm

Notation

Symbol	Description	Units
r_e	equilibrium internuclear separation	nm
$G_{v'', v'}$	vibrational energy of state v'	cm^{-1}
$\Delta\varepsilon_{pq}$	energy difference between state p,q	cm^{-1}
ω_e	fundamental vibrational frequency	cm^{-1}
$\omega_e \chi_e$	first anharmonic vibrational term	cm^{-1}
$\omega_e y_e$	second anharmonic vibrational term	cm^{-1}
$B_v, D_v, H_v, B_e, \gamma_e, \beta_e, D_e, H_e$	rotational constants	cm^{-1}
q_{vw}	Franck-Condon factor for states v,w	*****
R_e	electric dipole moment	D
S_J	rotational line strength factor	*****
f_I	intensity factor	*****
λ	wavelength	nm
λ_{pq}	wavelength of emission from state p to state q	nm
λ_p	pump wavelength	nm
ν	frequency	Hz
ν_{pq}	frequency of transition between states p and q	Hz
ν_o	fundamental vibrational frequency	Hz
v	vibrational quantum number	*****
J	rotational quantum number	*****
'	excited electronic state ($B\ ^3\Pi$)	*****
"	ground electronic state ($X\ ^1\Sigma$)	*****
v_o	pumped vibrational state	*****
J_o	pumped rotational state	*****

Notation

Symbol	Description	Units
p	observed ro-vibrational state (v,J)	*****
p_o	pumped ro-vibrational state (v_o,J_o)	*****
q	indexed ro-vibrational state	*****
α	absorption coefficient	cm^{-1}
γ	gain coefficient	cm^{-1}
A_{pq}	Einstein coefficient for spontaneous emission from state p to state q	s^{-1}
B_{pq}	Einstein coefficient for stimulated emission from state p to state q	$m^3/J\text{-}s$
$\Delta\nu_p$	pump laser linewidth	cm^{-1}
$\Delta\nu_a$	absorption transition linewidth	cm^{-1}
$a(\nu)$	absorption lineshape	s
$g_p(\nu)$	pump laser lineshape	s
$g(\nu)$	lasing transition lineshape	s
g_p	degeneracy of state p	*****
I	spectral intensity	$W/cm^2\text{-}Hz$
I_{pq}^{em}	emission intensity from state p to q	$W/cm^2\text{-}Hz$
$D(\nu)$	detection efficiency at frequency ν	*****
θ	relative vibrational energy, $h\nu_o/k_BT$	*****
ρ_m	laser mode density	

Kinetic Symbols:

Γ	decay rate	s^{-1}
Γ_o	collisionless decay rate	s^{-1}
Γ_r	radiative decay rate	s^{-1}
Γ_{pd}	predissociative decay rate	s^{-1}

Notation

Symbol	Description	Units
τ	lifetime	s
τ_o	collisionless lifetime	s
τ_r	radiative lifetime	s
$\tau_v(Y)$	collisional lifetime of state v at buffer concentration Y	s
Y	concentration of arbitrary collision partner	molec/cm^3
M	concentration of the BrCl mix	molec/cm^3
$k^Y(p)$	bimolecular rate constant for a specified reaction of the p excited state of BrCl(B) with collision partner Y	cm^3/molec-s
k_{eq}	electronic quenching rate constant	cm^3/molec-s
k_{ee}	resonant electronic exchange rate constant	cm^3/molec-s
$k_{pd}(v)$	predissociation rate constant, state v	s^{-1}
k_q	total electronic quenching rate constant	cm^3/molec-s
k_Q	total quenching rate constant	cm^3/molec-s
$k_{VT}(p-q)$	V-T transfer from state p to state q	cm^3/molec-s
$k_{VV}(p-q)$	V-V transfer from state p to state q	cm^3/molec-s
$k_V(p-q)$	V-T plus V-V transfer	cm^3/molec-s
$K_V(p)$	total vibrational removal rate constant	cm^3/molec-s
$K_J(p)$	total rotational removal rate constant	cm^3/molec-s
$K_R(p)$	rate constant for total removal from p	cm^3/molec-s
w_{pq}	vibrational transfer probability for transfer from state p to state q	1/s
R_{pq}	energy transfer rate matrix	1/s

Notation

Symbol	Description	Units
S	pump source term	molec/cm3-s
k_p	pump rate constant	1/s
N_p	concentration of excited state p	molec/cm^3
N_T	total excited state concentration	molec/cm^3
N(B;v,J)	concentration of BrCl(B;v,J)	molec/cm^3
N(X;v,J)	concentration of BrCl(X;v,J)	molec/cm^3
x_p	normalized concentration of state p	*****
z_p	transformed concentration of state p	*****
n	photon number	*****
d_i	radioactive decay rate	1/s
y_i	radioactive specie concentration	molec/cm^3
D_{ij}	radioactive decay rate matrix	1/s
l_i	i-th eigenvalue	*****
v_j^i	j-th element of i-th eigenvector	*****
c_i	i-th initial condition constant	*****
K_{eq}	equilibrium constant	*****
f	multi-quantum transfer fraction	*****
η	vibrational power law parameter	*****
σ	cross-section	cm^2
σ_g	gas kinetic collisional cross-section	cm^2
k_g	gas kinetic rate constant	cm^3/molec-s
σ_a	optical absorption cross-section	cm^2
μ	reduced mass of the collision pair	g

Abstract

The radiative and collisional dynamics in the B $^3\Pi(0^+)$ state of bromine monochloride have been studied using time-resolved and steady-state, spectrally-resolved laser induced fluorescence techniques. Radiative lifetimes and rate constants for electronic quenching, state-to-state vibrational transfer, and total rotational removal were obtained from observed BrCl(B-X) emission in the presence of Cl_2, He, Ne, Ar, Kr, Xe, N_2, and O_2 buffer gases. Vibrational states $v'=0-7$ were probed and emission observed from states $v'=0-6$. Energy transfer processes in BrCl(B) are strongly coupled due to similar energies for vibrational spacing and average translation.

The BrCl(B) radiative lifetime is 38.7 +/- 1.7 μs, independent of vibrational state for $v'<6$. The electronic quenching of a thermalized BrCl(B;v′) distribution is inefficient with rate constants ranging from 7.8×10^{-14} cm^3/molec-s for Neon to 4.3×10^{-13} cm^3/molec-s for Cl_2. The electronic quenching due to O_2 collsions is anomolously fast with a rate constant of 6.5×10^{-12} cm^3/molec-s. The quenching of nonthermal vibrational distributions is considerably more rapid and due to both ro-vibrational ladder climbing to predissociated states and resonant electronic transfer to excited electronic

states of Cl_2. The Cl_2 quenching rate constants vary from 4.3×10^{-13} cm^3/molec-s for $v'=0$ to 1.4×10^{-10} cm^3/molec-s for $v'=6$.

Vibrational transfer in BrCl(B) is rapid, as expected from the small vibrational energy spacing. The fundamental rate constant for vibrational transfer from $v'=1$ to $v'=0$ with chlorine as the collision partner is 1.3×10^{-11} cm^3/molec-s. Scaling of the vibrational rate constant with vibrational quantum number obeys a power law with an exponent of 0.63. Vibrational transfer with the noble gases is less efficient with fundamental rate constants ranging from 4×10^{-12} cm^3/molec-s for helium to 2.0×10^{-12} cm^3/molec-s for krypton.

Rotational transfer in BrCl(B) is very efficient with total removal rates ranging from 1.6×10^{-10} cm^3/molec-s for chlorine to 2.43×10^{-10} cm^3/molec-s for argon. Rotational transfer rates scale linearly with the square root of the reduced mass of the collision pair, as predicted by classical angular momentum considerations.

A dye laser pumped Br_2 $B\ ^3\Pi(0_u^+) - X\ ^1\Sigma_g^+$ laser has been demonstrated. Spectroscopic assignments have shown that lasing occurs from $10 \leqslant J' \leqslant 63$ in $12 \leqslant v' \leqslant 17$ using Rhodamine 590 dye. The output appeared limited to the 79-81 isotope of Br_2. By utilizing stimulated emission as a monitor for laser excitation spectra, dramatic increases in the resolution were

obtained that exceed the normal resolution of the dye laser. The Br_2 laser operated at Br_2 pressures of up to 60 torr, despite severe natural predissociation and self quenching. A simple model to explain the characteristics of the Br_2 laser is decsribed.

I. INTRODUCTION

A. Historical Perspective

The earliest chemical lasers[1-5] were based on the establishment of an inversion between vibrational states as proposed by Polanyi[6] in 1965. Exothermic reactions, liberating their energy into the stretching of newly formed chemical bonds can provide both complete and partial vibrational population inversions. These early chemical lasers were pulsed, low power devices used primarily to study chemical kinetics. Only after Cool and Stevens[7] demonstrated an HF chemical laser requiring no electrical input, were high power, highly efficient chemical lasers envisioned.[8]

The subsequent development of chemical lasers such as HF,[9-12] DF,[11,13] CO_2,[14-17] and CO[18-20] was rapid and extensive. High power, pulsed and continuous-wave (CW) devices with high mass flow efficiencies and wavelengths ranging from 126.5 μm to 2 μm were developed.[8]

There are many important potential applications for short wavelength high power chemical lasers. Several of these applications depend on higher mass flow efficiencies and shorter wavelengths than the vibrational transition laser can provide, however. Visible chemical lasers have been considered as fusion drivers.[21] Efficiencies greater than

1kW/kg may be possible. CW visible chemical lasers with outputs greater than 1 watt would provide an advance in highly tunable laser radiation for use in laboratory experiments.[21] The many ro-vibrational transitions from excited electronic states would provide excellent tunability and a chemical pumping source may provide powers greater than those currently available from cw dye lasers. Space based lasers are being strongly considered for strategic defense against nuclear ballistic missile attack. There are several advantages of visible chemical lasers for such an application. The higher energy per quanta of electronic transitions would provide higher mass efficiencies. In addition, shorter wavelength radiation propogates with less divergence. Indeed, there is great interest in the development of a visible chemical laser.

B. Visible Chemical Lasers

To achieve lasing in the visible portion of the spectrum, the higher energies of excited electronic states are required. The advantages of a visible chemical laser are clear: high energy storage (1 MJ/kg), high photon energy (1-6 eV) and short wavelengths (200-1000 nm), wavelength tunability from the many ro-vibrational states, lightweight deployment, high gains, and low pump thresholds.

The requirements for the development of an electronic transition chemical laser are rigorous. Of course, a highly exothermic reaction is required to populate the excited

electronic state. Additionally, the radiative lifetimes of the excited states, shapes and relative positions of the excited and ground potential energy curves, rates for vibrational-translational, vibrational-vibrational, and rotational-translational energy redistribution within both electronic states, quenching, deactivation and loss mechanisms, and the relative pumping rates into the excited states are all important parameters. In short, the complete radiative and collisional dynamics of both electronic states must be favorable.

The general features of a visible chemical laser are shown in figure 1. The excitation mechanism may consist of a direct chemical reaction or transfer from a highly energetic metastable specie. Regardless of the excitation mechanism, the energy will be distributed nonthermally within the excited electronic state. For the most efficient laser operation, a rapid thermalization process should pool the energy into the lowest vibrational level, $v'=0$. To prevent bottlenecking, a rapid removal from the lower laser level is required. Loss mechanisms such as electronic quenching and predissociation will reduce the population inversion and system efficiency.

Recently, much research has been conducted to develop electronic transition lasers, including work on I_2,[22-24] Na_2,[25-27] S_2,[28] Li_2,[29-30] Br_2,[31] IF,[32-33] Te,[34] I^*,[35] and NO[36]. Three important aspects of this research are

(1) optically-pumped laser demonstrations, (2) investigations of potential excitation mechanisms, and (3) studies of the radiative and collisional dynamics of potential lasing species.

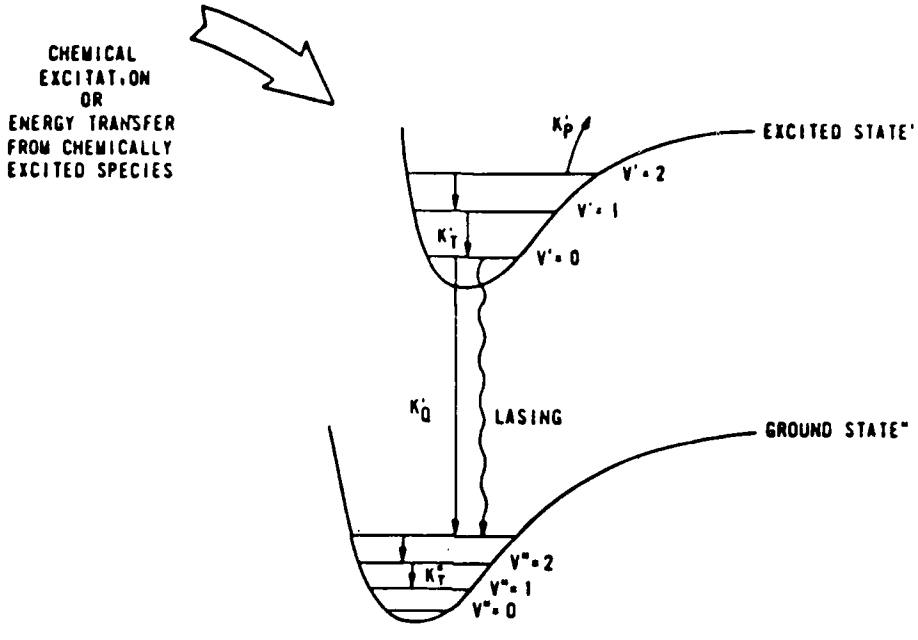

Figure 1. General features of a visible chemical laser.

Optically-pumped laser demonstrations provide a test of laser dynamics. Observations of pressure dependence, output power as a function of time, and saturation and threshold conditions provide a measure of collisional transfer rates affecting the lasing process. Efficiencies and optical gains can be related to theoretical predictions. Estimates of chemical pumping requirements can be established. Several reviews of optically-pumped electronic transition lasers may be found in the literature.[29-30]

Chemical excitation of electronic transition laser species may be accomplished by direct chemical reaction or energy transfer from highly energetic metastable species. Exoergic reactions are likely to populate many electronic states unless some selection rule forces the distribution to a specific state. The total electronic spin quantum number is generally conserved in reactions involving low mass molecules. Thus, selective chemical excitation of an upper laser level may be achieved for molecules with a difference in total electronic spin between the excited and ground electronic states. Such an excited state would be metastable with respect to the ground state, however. Since metastable states are poor laser candidates, the metastable energy must be transfered to a suitable lasing specie. The best example of such a chemical transfer laser is the Chemical Oxygen-Iodine Laser (COIL) where the metastable $O_2(^1\Delta)$ produces excited atomic iodine, I^*. However, the COIL laser operates in the infrared at 1.315 μm and does not classify as a visible chemical laser.

Other metastables including $N_2(A)$, NF(a) and NF(b) have been identified.[38] NO(A-X) and CO(a-X) lasers have been proposed based on transfer from $N_2(A)$.[38] IF(B-X) and BiF(A-X) lasers have been suggested using excited NF as the metastable transfer partner.[38]

A third important area of chemical laser research is the search for good lasing species. The radiative and collisional dynamics of the ground and excited electronic states are of fundamental interest. Many energy transfer studies have been conducted on molecules including I_2,[39-47] Na_2,[48-53] Li_2,[54-56] S_2,[57-58] NO,[59-60] HF,[61-64] OH,[65] BaO,[66] IF,[67-71] and Br_2[72-78].

The search for a visible chemical laser remains an elusive venture. Despite the extensive research to identify good laser candidates, no chemical laser operating at wavelengths less than 1.3 μm has been demonstrated. One particular class of molecules that has a good potential for such a demonstration is the diatomic halogen and interhalogen molecules.

C. The Halogens and Interhalogens

Since the demonstration of an optically-pumped molecular iodine electronic transition laser by Byer et al[22], the halogen and interhalogen diatomic molecules have been studied as potential visible chemical lasers. These studies include spectroscopic and kinetic work via chemiluminescence,[79-88] absorption spectroscopy,[89-102] laser induced fluorescence,[103-124] optical pumping studies[125-128] and laser demonstrations[22-24,31-33,129].

Tne two most studied transitions are the D′-A′ and B-X systems with emission in the ultraviolet and visible,

respectively. Both systems are interesting as potential chemical lasers. All the diatomic halogens and most of the interhalogens have been shown to lase on the D'-A' transition with electrical excitation.[130-133] Optically-pumped I_2,[22-24] Br_2,[31] and IF[32-33] B-X lasers have been demonstrated.

The potential for a chemically pumped B-X transition halogen or interhalogen laser is particularly good for several reasons. First, there exist possible chemical pumping schemes for the B-states of I_2, Br_2, Cl_2 ,IF, BrF, and BrCl.[134] Secondly, the equilibrium internuclear separation of the excited B-state is much larger than that of the ground state. This allows for the establishment of a population inversion between the pumped electronically excited ro-vibrational states and the relatively unpopulated, high-lying ro-vibrational levels of the ground state. Thirdly, the halogen and interhalogen B states have relatively long radiative lifetimes (.2 - 80 μs) and low quenching rates (10^{-14} - 10^{-10} cc/molec-s),[134] both of which are important to maintain a large popoulation inversion. Finally, pulsed and CW optically pumped (B-X) halogen and interhalogen (I_2,Br_2,IF) lasers have been demonstrated.

For these reasons, the Air Force Weapons Laboratory, Kirtland AFB, New Mexico has a great deal of interest in the halogen and interhalogen B-X transition chemical laser. Recent experiments at AFWL have shown that IF holds particular

promise as a visible chemical laser. Optically-pumped IF(B-X) pulsed and CW lasers have been demonstrated and chemically pumped laser demonstrations are being considered.

Bromine monochloride also appears to be a good candidate for an electronic transition chemical laser.[121] BrCl has an advantage over the labile molecule IF. BrCl is stable and may be stored in sealed containers whereas IF is thermodynamically and kinetically unstable and rapidly forms higher fluorides (IF_5). Several hundered torr of BrCl(X) can easily be produced but even a few torr of IF(X) is difficult to generate.

Basic kinetic studies remain to be accomplished for many of the halogens and interhalogens including BrCl. Radiative lifetimes are known, but quenching rates, V-T, V-V, and R-T transfer rates, and the effects of predissociation are not well established, especially on a detailed (v',J') basis. The radiative lifetime of BrCl(B) is 40.2 μs.[122] This lifetime is independent of vibrational level for $v'<7$. At $v'=6$, $J'=42$, the BrCl B state is greatly perturbed due to the intersystem crossing of a repulsive state.[122] The collisionless lifetimes of these predissociated states are less than 1 μs for $v'>6$.[122] The electronic quenching of the BrCl(B) thermalized distribution is slow, 3.9×10^{-13} cc/molec-s.[121] A rapid quenching from high v' is observed and has been attributed to vibrational ladder climbing to predissociated states.[123] As

part of this thesis, it will be shown that such an interpretation is not consistent with detailed balancing, however. No state-selective lifetimes nor time-resolved emission from individual, collisionally-populated vibrational states has been previously observed in BrCl. The only spectrally-resolved LIF work on BrCl(B) has been accomplished in a CW experiment under thermalized conditions.[128] Many important questions remain regarding energy transfer within the B state of BrCl and must be resolved prior to evaluating the potential of BrCl as a chemically pumped laser system.

D. The Study of Molecular Energy Transfer

Since the 1930's, the field of chemical physics has been particularly interested in the problem of inelastic energy transfer among molecules in the gas phase.[135-136] Many studies, both theoretical and experimental, have been conducted to better understand the important elementary processes of energy transfer. Despite the extensive effort, many important questions remain.

The mechanisms for psuedo-first-order gas phase reactions have been studied by observing the pressure dependence of the rates of reaction. The Stern-Volmer technique[137] has been used extensively. Often experimental investigations measure cross sections that are averaged over many parameters such as collision energies and quantum states. Important features of the collision process are obscured by such averages. For

example, logrithmic plots of V-T transfer rates versus pressure over several orders of magnitude of pressure are often inadequate to test even greatly different functional forms that may be predicted for unimolecular reactions.[138] In addition, many-quanta systems in general do not decay as a simple, single exponential and state-averaged lifetimes often yield little or ambiguous information about rates and mechanisms.[139]

There has been much progress in the theoretical development of quantum resolved energy transfer processes,[136,139-152] but the corresponding experimental determination of the state resolved cross sections, $\sigma(q)$, are lacking. The fairly recent advent of narrow-linewidth laser sources has provided the potential for such experiments. Important measurements of these cross sections and their dependence on quantum state, reduced mass, polarizability, temperature, and energy spacing have been and are currently being made.

Detailed cross sections can lead to information such as the determination of intermolecular potentials governing atom-molecule and molecule-molecule collisions. Experimentally determined dependencies on vibrational quantum number and reduced mass of the collison pair are of fundamental and practical importance and can be compared to scaling theories such as the Landau-Teller[153] and SSH theories.[154]

Energy transfer studies have wide application including the fields of atmospheric phenomena, laser physics, sound absorption, and shock wave propogation. Especially in the field of laser physics, energy transfer studies and laser development have grown hand-in-hand.

It is on this basis of practical and scientific need that the following research effort was conducted.

E. Problem Statement

Steady-state (CW) and temporally-resolved (pulsed), spectrally-resolved laser induced fluorescence techniques and optically-pumped laser studies will be used to examine the fundamental physical properties of bromine monochloride (BrCl) and molecular bromine (Br_2) that are relevant to chemical laser development.

Energy transfer studies in the $B^3\Pi(0^+)$ state of BrCl will be the primary focus of this thesis. Specifically, the following energy transfer processes will be investigated:

(1) determination of radiative lifetimes for all the stable vibrational states,

(2) measurement of electronic quenching rates of the thermalized distribution for atomic and molecular buffer gases,

(3) measurement of state-to-state vibrational transfer rates,

(4) measurement of total rotational transfer rates, rotational distributions, and the effects of V,R-T processes,

(5) determination of quenching mechanisms and predissociative losses, and

(6) investigatation of other important energy transfer processes.

Conclusions based on these observations will be made, including:

(1) the suitability of BrCl(B) as the excited state for an electronic transition chemical laser,

(2) the scaling of vibrational and rotational transfer rates with quantum number and reduced mass,

(3) the mechanism for quenching and removal from BrCl(B), and

(4) the applicability of known energy transfer models to BrCl(B), where the vibrational energy spacing is nearly kT.

Questions regarding the importance of spectral response in LIF experiments and the synergy between steady-state and time-resolved experiments will be addressed.

An optically-pumped molecular bromine laser will be demonstrated and used to:

(1) study the instabilities of $Br_2(B)$ due to self quenching and natural predissociation,

(2) obtain laser parameters such as gain and threshold,

(3) test known kinetic rates under lasing conditions, and

(4) compare lasing operation with other halogen and interhalogen lasers.

This important bromine laser work will be presented in appendix A.

II. BACKGROUND THEORY

A. Spectroscopy

The halogen atoms have ground state electronic configurations with outer shells s^2p^5, yielding $^2P_{3/2}$ and $^2P_{1/2}$ atomic states. Molecular orbitals for the diatomic halogens may be established from linear combinations of the atomic states. The lowest energy molecular orbital arises from the configuration $(\sigma_g)^2(\pi_u)^4(\pi_g)^4(\sigma_u)^0$, abbreviated 2440. This configuration provides the $^1\Sigma_g^+$ ground electronic state. Excited electronic states are obtained from the promotion of an electron to the unfilled σ_u orbital. The $^{1,3}\Pi_u$ states are obtained from the 2431 configuration and the $^{1,3}\Pi_g$ states from the 2341 configuration.

A correlation diagram for these states with momentum coupling of Hund's case (a), Λ - Σ coupling, and Hund's case (c), J-J coupling, is given in figure 2. On the left-hand side of the diagram, case (a) coupling is shown. The right-hand side of the diagram provides case (c) coupling and only the electronic angular momentum projected along the internuclaer axis, Ω, is defined. States with the same symmetry are correlated and shown by a solid line connecting the two states. Typical interhalogen potential energy curves for the electronic states given in the correlation diagram are shown in figure 3.

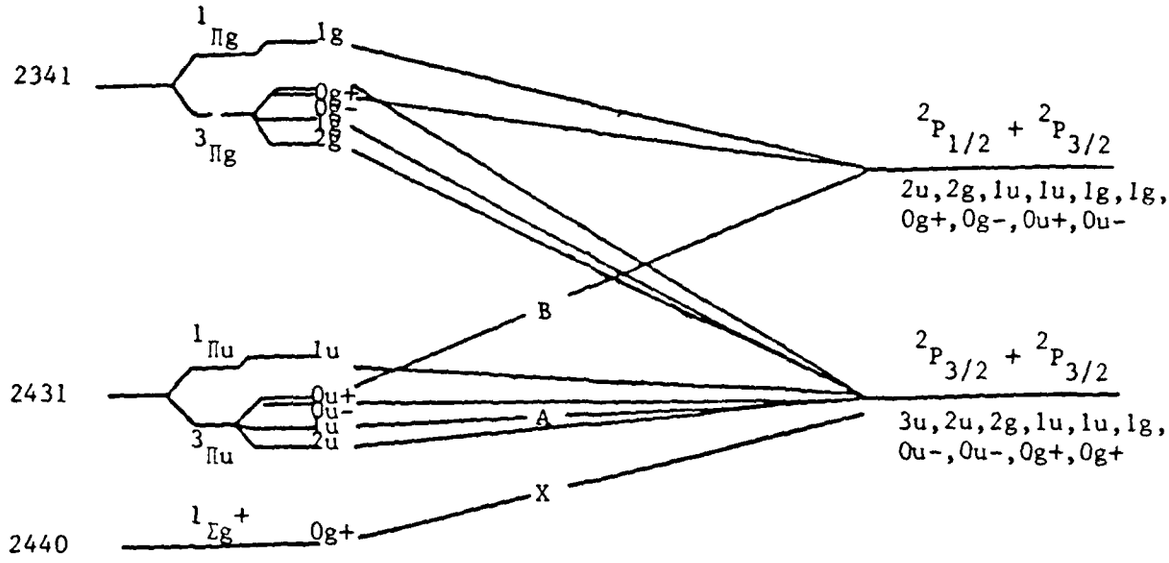

Figure 2. Correlation diagram for the lowest electronic states of the diatomic halogen molecules.

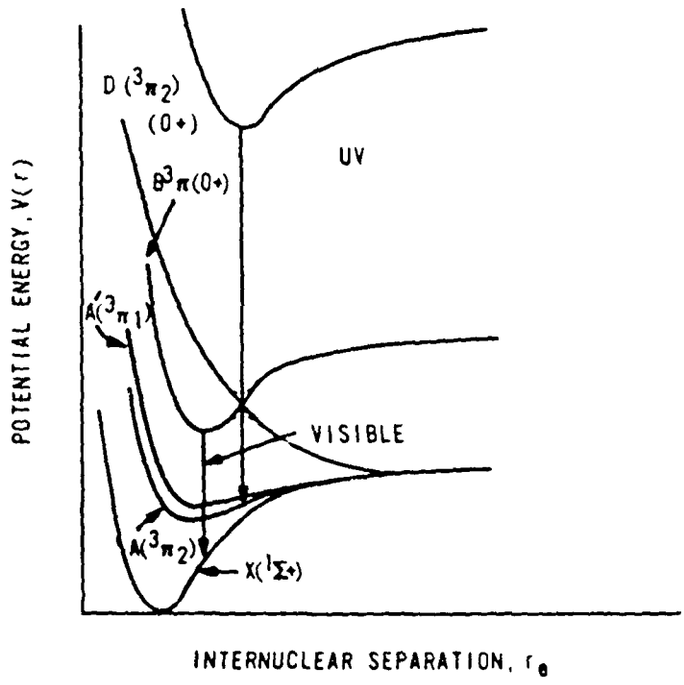

Figure 3. Typical interhalogen potential energy curves.

For the interhalogens, the assignment of $X(^2P_{1/2})$ and $Y(^2P_{3/2})$ is unique and known as $Cl(^2P_{1/2}) + Br(^2P_{3/2})$ for BrCl.[134] No inversion symmetry exists for the interhalogens and the u,g labeling does not apply. Note that the $B^3\Pi(0^+)$ state crosses a repulsive $^3\Pi(0^+)$ state in the correlation diagram. In general, states of the same symmetry and total angular momentum do not cross, but rather are greatly perturbed near their intersection. As a result of this perturbation the interhalogen B state correlates to two $^2P_{3/2}$ separated atom states by way of a potential energy maximum. At moderate vibrational levels, a molecule may predissociate across the unstable maximum, and thus, the collisionless lifetimes of the B state vibrational levels near the potential maximum are shortened. This type of predissociation belongs to Herzberg case I(c)[163] and is typical of the interhalogens.

The spectroscopy of the BrCl B-X system has been studied via chemiluminescence[80,101,164] and absorption[100] experiments. The absorption spectra carefully recorded by JA Coxon[100], provide the best reported spectroscopic constants, RKR potential energy curves and Franck-Condon factors.

The perturbation of the $B^3\Pi$ state by the repulsive 0^+ state is strong in BrCl and a typical least-square fit to a Dunham expansion does not provide a satisfactory representation of Coxon's spectroscopic data. Coxon[100] has

shown that the shift in vibrational energy (Δ_v) due to the perturbation is given by

$$\Delta_v=(W_{bc}^2+(\delta_v/2)^2)^{1/2} - \delta_v/2 \quad (1)$$

where

W_{bc}=matrix element representing the strength of the interaction

δ_v=separation between unperturbed levels

For the interaction $^3\Pi$ and 0^+ states to be equally displaced from the interaction energy, the separation of the unperturbed vibrational states must be

$$\delta_v = T_p - T^o(v') \quad (2)$$

where

T_p=the crossing point energy

$T^o(v')=T_e^o+\omega_e^o(v'+1/2)+\omega_e\chi_e^o(v'+1/2)^2+...$

These states, their interactions, and energies are depicted in figure 4.

By fitting the data to

$$T(v')=T^o(v')-\Delta_v, \quad (3)$$

with parameters W_{bc} and T_p, in addition to the normal vibrational Dunham expansion coefficients for the unperturbed state, the constants of table I were derived.[100]

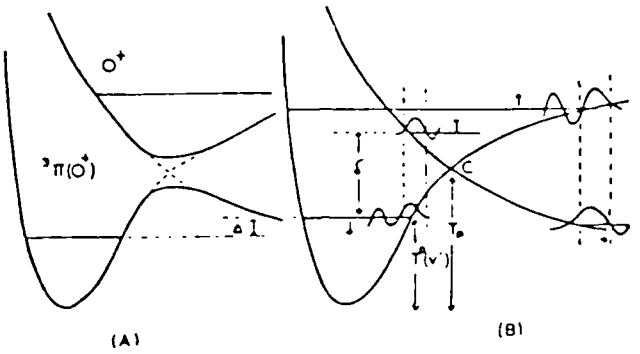

Figure 4. Perturbed BrCl(B) state and interaction energies, from reference 188.

Table I.
Spectroscopic Constants for BrCl X and B states

	$^{79}Br^{35}Cl$		$^{81}Br^{35}Cl$	
	X-state	B-state	X-state	B-state
ω_e	444.28	222.68	442.59	221.87
$\omega_e x_e$	1.843	2.884	1.829	2.848
$\omega_e y_e$	0.0040	-0.0673	0.0039	-0.0653
W_{bo}	------	359.7	------	367.1
T_e	0	16879.91	0	16881.19
T_p	0	18936.36	0	18945.20

No completely adequate fit for rotational constants of the BrCl B state was found by Coxon. Experimental values for the rotational constants B_v, were reported[100] and are listed along with the ground state rotational constants in appendix B.

While the spectroscopic description of the BrCl X and B states by Coxon is the best found in the literature, it is insufficient for the energy transfer studies of this thesis. The study was done in absorption and therefore was limited to $v''<8$. Many of the strongest B-X emission transitions terminate at $7 \leqslant v'' \leqslant 15$. To extend Coxon's work to higher v", transition wavelengths and Franck-Condon factors were calculated from an RKR program using Coxon's X-state constants and B state classical turning points for $0 \leqslant v'' \leqslant 30$ and $0 \leqslant v' \leqslant 8$, see appendix B. This method provided agreement with Coxon's Franck-Condon factors to within 10%. The derived potential energy curves are shown in figure 5 and the resulting transition wavelengths and Franck-Condon factors are listed in appendix B.

The nature of predissociation in BrCl(B) can be further studied by state selective collisionless lifetime measurements as has been done by M. A. Clyne and coworkers.[166] All the BrCl(B) energy levels below $v'=6$, $J'=42$ are stable with respect to predissociation and have radiative lifetimes of about 40 μs.[122] At $v'=6$, $J'=42$ the collisionless lifetime drops immediately to 8.8 μs and continues to fall monotonically to 4.3 μs for $J'=50$.[122] All the rotational levels of $v'=7$ and 8 have lifetimes less than 1 μs.[122] Since predissociation is a nonradiative depletion process, fluorescence intensity from predissociated states is reduced.

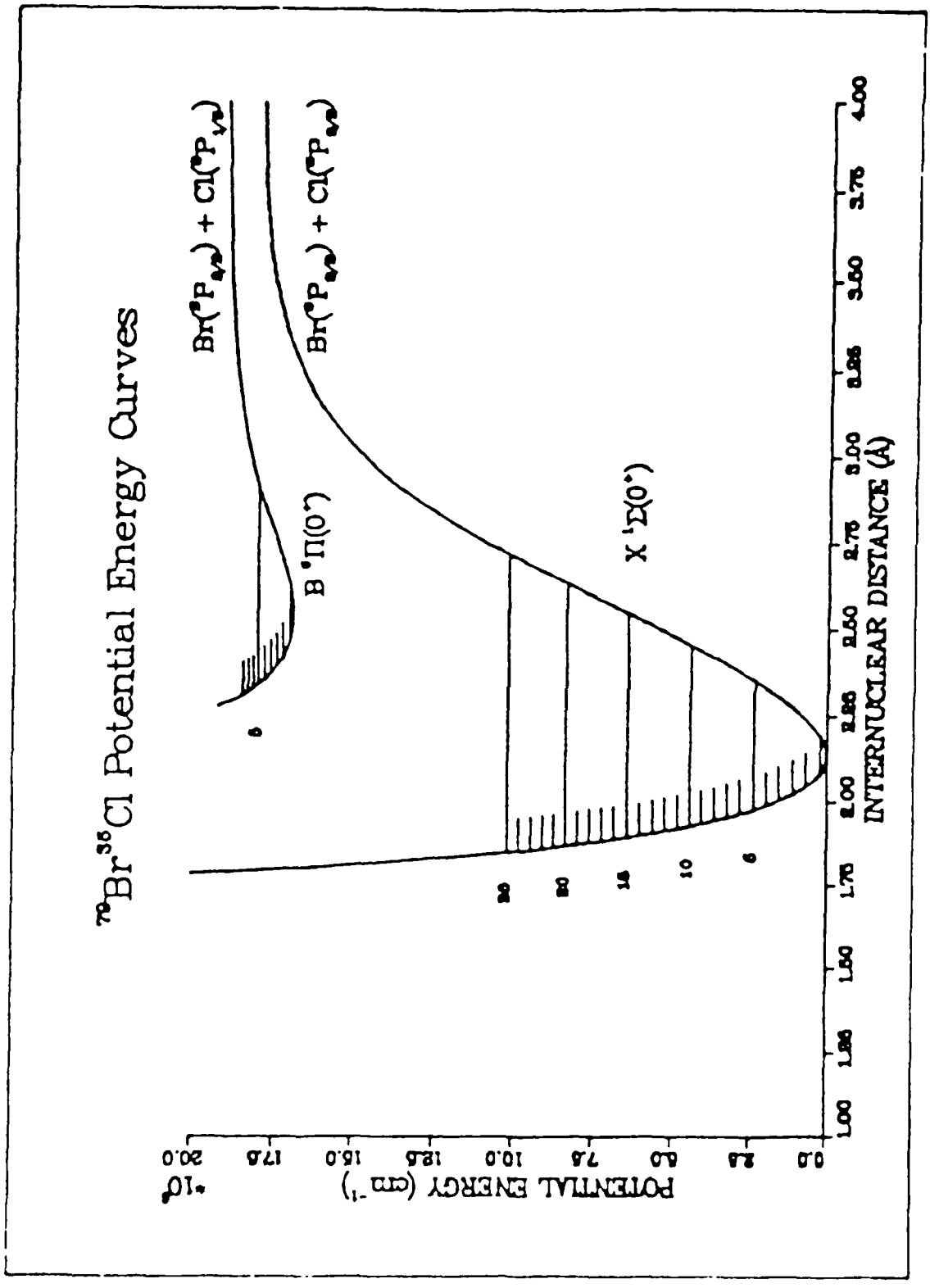

Figure 5. $^{79}Br^{35}Cl$ potential energy curves for the ground $X^1\Sigma(0^+)$ and excited $B^3\Pi(0^+)$ states.

The interaction of the repulsive 0^+ state with the $B^3\Pi$ state in BrCl has important implications for the excited state spectroscopy. Even more interesting are the effects of this predissociation on the kinetics and energy transfer within BrCl(B). The methods of laser induced fluorescence and the kinetic background required to study these processes will be described in the following two sections.

B. Laser Induced Fluorescence Techniques

Laser induced fluorescence (LIF) is an experimental technique based on the population of a specific quantum state, or set of states, by a narrow linewidth laser source and the detection of the subsequent emission from that state or kinetically related states. The range of application for LIF techniques vary from the assignment of molecular spectra to the determination of internal state population distributions of chemical reaction products.[165] The method was first used by Zare et al.[53,173] Since then, LIF has been used by many groups to study energy transfer in such molecules as Na_2,[48-53] Li_2,[54-56] NO[59-60], and S_2[57-58]. MAA Clyne and coworkers have used the methods extensively to study the halogens and the interhalogens.[166]

The basic method is illustrated in figure 6. A laser is used to populate the quantum state N. Collisional energy transfer can then redistribute the population among other

states such as N-1 and N+1. The spectrally-resolved fluorescence intensity from these states yield parent transitions that originate from the initally populated state and satellite transitions that originate from collisionally populated states. The fluorescence intensity of a given transition is proportional to the number density of the excited state (N_v)[163]:

$$I_{vw}^{emm} = (64\pi^4/3) c \nu_{vw}^4 q_{vw} |R_e|^2 (S_J/(2J+1)) N_v \qquad (4)$$

where

I_{vw}^{emm} = emission intensity from state v to state w

ν_{vw} = transition frequency from state v to state w

$q_{vw} = \langle v/w \rangle$ = Franck-Condon factor overlap for states v,w

$|R_e|$ = electric dipole moment

S_J = rotational linestrength factor.

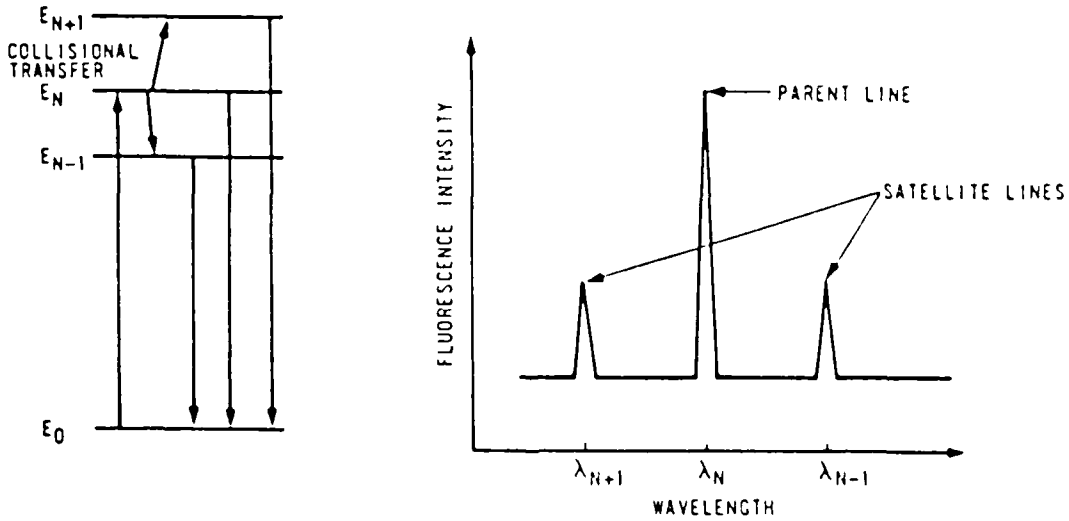

Figure 6. Basic laser induced fluorescence technique.

The portion of the emission intensity actually observed will depend on the experimental detection system. If the detectivity as a function of frequency, $D(\nu)$, is included, the observed emission intensity is

$$I_{vw}^{obs} = I_{vw}^{emm} D(\nu_{vw}) \tag{5}$$

Thus by measuring the relative steady-state intensity of various spectral features the relative steady-state number density of these states can be obtained:

$$N_v/N_u = (I_v^{obs}/I_u^{obs})(\nu_{uw'}/\nu_{vw})^4(q_{uw'}/q_{vw})(D(\nu_{uw'})/D(\nu_{vw})) \tag{6}$$

The relative CW number densities can in turn be related to rate constants as will be shown in section IIC.

Total fluorescence intensity is also proportional to the total excited state density:

$$I_f = \sum_{v,w} I_{vw}^{obs} = \sum_{v,w} (64\pi^4/3) c \nu_{vw}^4 q_{vw} |R_e|^2 D(\nu_{vw}) N_v \tag{7}$$

If the spectral response of the detection system is relatively "flat" so that $D(\nu_{vw})$ is roughly independant of ν for the region of significant emission, then

$$I_f = C\ N_T \tag{8}$$

where

$N_T = \sum_v N_v$

C = a proportionality constant

Often, experimental detection systems are not spectrally flat and the total fluorescence intensity depends on the distribution of population among vibrational levels and the relative detection efficiency for each level. However, if a thermalized distribution N_v exists, the fluorescence intensity will be directly proportional to the total excited state density regardless of detection efficiencies. The problem of detection efficiency is addressed in further detail in section IV and appendix C.

Laser induced fluorescence techniques can be enhanced by adding temporal resolution to the experiment. The general approach is shown in figure 7. A pulsed laser is used to initially populate the excited quantum state. The fluorescence from that state or related states is then monitored as a function of time. By applying an essentially delta-function excitation pulse, the time evolution of a set of coupled quantum states can be observed under various initial conditions. The equations to be derived in section IIC can then be used to extract rate constants for the radiative and collisional processes affecting the excited states.

The pulsed and CW LIF experimental techniques provide similar information about the kinetic processes within the excited electronic state, but are complimentary in nature.

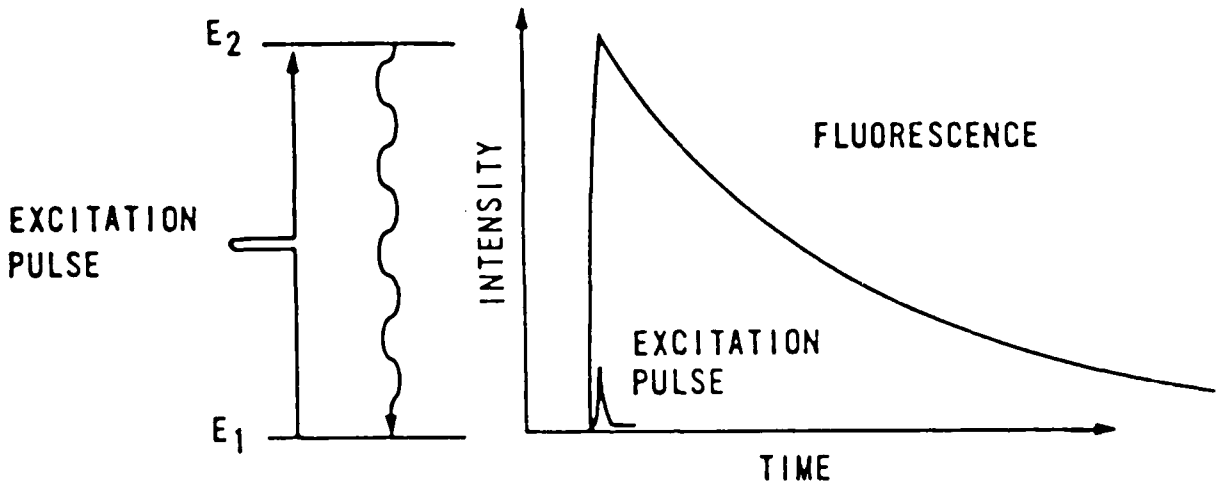

Figure 7. Time-resolved laser induced fluorescence technique.

The steady state experiments are important for measuring relative number densities directly. The CW studies generally have larger average signals and therefore allow for greater spectral resolution and the study of rotational processes. Finally, the CW experiments provide data that is usually easier to interpret than data from pulsed experiments.

The pulsed experiments measure lifetimes directly and provide the only information on the basic time scales for the energy transfer events. The addition of spectral and temporal resolution provides a great deal of information detailing the full time evolution of given quantum states with specific initial conditions.

C. Kinetic Analysis

1. Introduction

The kinetic analysis used to interpret the results of laser induced fluorescence experiments and to determine the mechanisms and rate constants for collision induced energy transfer within the $B^3\Pi 0^+$ state of BrCl are presented in this section. The master rate equation for all the radiative and kinetic processes affecting BrCl(B) will be developed. Solutions to this equation under steady state and time dependent conditions will be examined. The particular problem of extracting state-to-state vibrational transfer rates from pulsed LIF experiments for strongly coupled vibrational states will be discussed. Theories describing the scaling of vibrational transfer cross sections with vibrational quantum number and reduced mass of the collision partner are described in appendix D.

2. Master Rate Equation

Consider a dilute system of non-interacting molecules with many accessible quantum states, BrCl(B;v´,J´), that may interact with a chemically-inert heat bath, Y, consisting of one or more atomic or molecular species. The BrCl(B) concentration must be dilute in the bath gas to insure the kinetic processes are first order with respect to BrCl(B) and to maintain the heat bath at the initial equilibrium

temperature (300 K). Both radiative and collision induced transitions are to be considered. A summary of the terms and symbols used in this analysis may be found in the terminology and notation table on page xiv.

The fundamental energy transfer processes are:

Optical Excitation:

$$BrCl(X;v_o",J_o") + h\nu \xrightarrow{k_D} BrCl(B;v_o',J_o') \qquad (9)$$

Spontaneous Emission:

$$BrCl(B;v',J') \xrightarrow{A} BrCl(X;v",J") + h\nu \qquad (10)$$

Stimulated Emission:

$$BrCl(B;v',J') + h\nu \xrightarrow{B_{10}} BrCl(X;v",J") + 2h\nu \qquad (11)$$

Predissociation:

$$BrCl(B;v',J') \xrightarrow{\Gamma_{pd}} Br(^2P_{3/2}) + Cl(^2P_{3/2}) \qquad (12)$$

Electronic Quenching:

$$BrCl(B;v',J') + Y \xrightarrow{k_{eq}} BrCl^+ + Y \qquad (13)$$

Resonant Electronic Exchange:

$$BrCl(B;v',J') + Y \xrightarrow{k_{ee}} BrCl(X;v_o"J_o") + Y^* \qquad (14)$$

Ro-vibrational Transfer (V,R-T):

$$BrCl(B;v',J') + Y \xrightarrow{k_{VT}} BrCl(B;v'+\Delta v',J+\Delta J') + Y \qquad (15)$$

Vibrational-Vibrational Transfer (V-V):

$$BrCl(B;v',J')+Y_2(w)\xrightarrow{k_{VV}}BrCl(B;v'+\Delta v',J'+\Delta J')+Y_2(w+\Delta w) \quad (16)$$

The specie "Y" is used in equations (13-16) as an arbitrary collision partner.

Process (9), optical excitation, is the means by which the system is perturbed from its equilibrium. Energy is selectively applied to the system via absorption of monochromatic laser radiation. The specific quantum state (v_o',J_o') excited is the initially populated state, or parent state. The pumping rate is proportional to the ground state BrCl number density and the pump rate constant

$$k_p = (B_{01}I_o/c)\int_0^\infty a(\nu)\ g_p(\nu)\ d\nu \quad (17)$$

where

B_{01} = Einstein coefficient for stimulated emission

I_o = incident pump laser intensity

c = speed of light

$g_p(\nu)$ = pump laser linewidth function

$a(\nu)$ = absorption transition linewidth function

To insure selective pumping of a single quantum state, the pump laser linewidth, $\Delta\nu_p$, given by $g_p(\nu)$ must be smaller than the the absorption transiton linewidth, $\Delta\nu_a$, given by $a(\nu)$. Under these conditions the convolution integral in

equation (17) insures k_p will be non-zero for only one absorption transition.

The process of stimulated emission (11) is the inverse of process (9). The two rates may be combined into a single term:

$$S\delta_{v,v_o}\delta_{J,J_o} = (B_{01}I_o/c)[N(X;v_o",J_o")- (g_1/g_o)N(B;v_o',J_o')]\delta_{v,v_o}\delta_{J,J_o} \quad (18)$$

where

g_1, g_2 = the degeneracies of the excited and ground states

$N(X;v_o",J_o")$ = concentration of BrCl ground electronic state, vibrational level $v_o"$, rotational state $J_o"$

$N(B;v_o',J_o')$ = concentration of BrCl excited electronic state, vibrational level v_o', rotational state $J_o"$

δ_{ij} = Kronecker delta function

These rates are labeled S, since they are the net pumping rate or source term. Because the BrCl B-X transition moment is so small, very little population is removed from BrCl(X) to BrCl(B) and $N(X;v_o",J_o") >> N(B;v_o',J_o')$. The source term is then proportional to the total BrCl concentration. Note that the net pump rate would be zero for a saturated transition. If the transition remains saturated (CW condition), the pumping process will dominate all kinetic processes. Any collisional removal from $BrCl(B;v_o',J_o')$ would immediately be offset by an enhanced pumping rate. Thus the $BrCl(B;v_o',J_o')$

population would be held artificially high. Clearly, saturation must be avoided in a CW LIF experiment.

Spontaneous emission, process (10), is simply the radiative decay from the excited state. The rate is proportional to the number in the excited state and the Einstien A coefficient

$$A(v',J' \rightarrow v'',J'') = (64\pi^4/3hc^3)\,|R_e|^2 q_{v'v''}\, S_J/(2J+1) \qquad (19)$$

The radiative lifetime, τ_r, from state v' is

$$1/\tau_r(v') = A(v') = \sum_{v''J''} A(v',J' \rightarrow v'',J'')$$

The final collisionless transfer process is the nonradiative loss via predissociation. As was described in section IIA, BrCl(B;v'>6) may dissociate to two ground state atoms by way of a potential energy maximum. There is no shortening of the radiative lifetime due to predissociation for states below v'=6, J'=42 in BrCl(B). Above this level the lifetime is drastically shortened by rapid predissociation. The collisionless lifetime, Γ_o, for such states is given by

$$1/\tau_o = \Gamma_o = 1/\tau_r + \Gamma_{pd} \qquad (20)$$

These collisionless lifetimes have been measured for various v',J' states by MA Clyne and co-workers.[120-123]

The first collisional processes to be considered are those of electronic quenching (13) and resonant electronic

exchange (14). Electronic quenching refers to the removal of thermalized BrCl(B) to any lower electronic state, $BrCl^+$. Such rates are generally slow and nearly independent of v′ for the interhalogens.[67-69,164] Resonant electronic exchange refers to the direct exchange of the BrCl(B) energy to a nearly resonant excited electronic state of the collision partner, Y^*. Rates for resonant transfer can be nearly gas kinetic and depend strongly on vibrational state. With respect to the rate equation these processes are indistinguishable. Both processes must be considered when interpreting measured rates, however. The total electronic quenching rate is defined as

$$k_q = k_{eq} + k_{ee} \tag{21}$$

A third mechanism is available for the quenching of BrCl(B;v′). Vibrational transfer to predissociated states followed by a rapid dissociation to ground state atoms may be an important process. Such a mechanism would have a unique pressure dependence since it would depend on the full ro-vibrational distribution within the B state. The rate constant k_Q will be defined as the sum of rates due to electronic quenching, resonant electronic exchange, and vibrational ladder climbing to predissociated states.

The thermalization of the B state is controlled by the vibrational and rotational transfer processes of equations (15) and (16). Pure V-T transfer is obtained from

equation (15) when $\Delta J=0$, and pure rotational transfer is obtained when $\Delta v=0$. The rates will depend on the population distribution among the full set of ro-vibrational states. The rate constant will depend on the collision partner, quantum state, and size of the quantum jump. Vibrational-vibrational (V-V) transfer is possible with diatomic buffer gases. The rates for V-T and V-V transfer have the same form and may be combined so that

$$k_V = k_{VT} + k_{VV} \tag{22}$$

The total vibrational transfer out of a specific vibrational state, v, includes the transfer to all other vibrational states (all Δv). The rate constant for total vibrational removal from state v, $K_V^Y(v)$, is defined by equation (23). The total rotational transfer out of the parent rotational state, J, includes the transfer to all satellite rotational states (all ΔJ) within the parent vibrational band. The rate constant for total rotational removal from state J, $K_J^Y(J)$, is defined by equation (24).

$$K_V^Y(v) = \sum_{\Delta v, \Delta J} \sum k_V^Y(v \rightarrow v+\Delta v,\ J \rightarrow J+\Delta J) \tag{23}$$

$$K_J^Y(J) = \sum_{\Delta J} k_V^Y(J \rightarrow J+\Delta J) \tag{24}$$

The total removal from a given vibrational state v, or from a given rotational state (v,J) includes quenching losses as well as the removal as defined in equations (23-24). The rate

constants for these total removal rates are defined in equations (25-26).

$$K_R^Y(v) = K_V^Y(v) + k_q^Y(v) \tag{25}$$

$$K_R^Y(v,J) = K_R^Y(v) + K_J^Y(J) \tag{26}$$

Using these fundamental transfer processes, rates, and definitions, the master rate equation is

$$\begin{aligned} dN(B;v,J)/dt = {} & S\,\delta_{vv_o}\,\delta_{JJ_o} - \Gamma_o(v,J)\,N(B;v,J) \\ & - \sum_Y k_q^Y(v,J)\;Y\;N(B;v,J) \\ & - \sum_Y \sum_{\Delta v} \sum_{\Delta J} k_V^Y(v \to v+\Delta v, J \to J+\Delta J)\;Y\;N(B;v,J) \\ & + \sum_Y \sum_{\Delta v} \sum_{\Delta J} k_V^Y(v+\Delta v \to v, J+\Delta J \to J)\;Y\;N(B;v+\Delta v, J+\Delta J) \end{aligned} \tag{27}$$

The summation over Y indicates the inclusion of all buffer species Y. This master rate equation can be rewritten in a more concise form by making the following definitions:

$p = (v', J')$, label for the observed quantum state (28)

$p_o = (v_o', J_o')$, label for the parent quantum state

$q = (v'+\Delta v', J'+\Delta J')$, label for the indexed quantum state

$w_{pq} = \sum_Y k_V^Y(q \to p)\;Y$, the vibrational transition rate constant from state q to state p

$R_{pq} = w_{pq} - \delta_{pq}\left(\sum_\ell w_{\ell p} + \Gamma_o(p) + \sum_Y k_q^Y(p)\;Y\right)$, the energy transfer rate matrix connecting state q to state p.

δ = Kronecker delta function

Applying the definitions of equation (28) to the terms of the master rate equation (27) provides the relationships of equations (29). Note that the right hand side of these equations are in tensor notation and repeated subscripts imply a summation over all values of that subscript.

$$S\ \delta_{v,v_o} = S\ \delta_{pp_o} \tag{29}$$

$$\sum_Y \sum_{\Delta v} \sum_{\Delta J} k_V^Y(v \to v+\Delta v, J \to J+\Delta J)\ Y\ N(B;v,J) = \sum_1 w_{1p}\ \delta_{pq}\ N_q$$

$$\Gamma_o(v,J)\ N(B;v,J) = \Gamma_o(p)\ \delta_{pq}\ N_q$$

$$\sum_Y k_q^Y(v,J)\ Y\ N(B;v,J) = \sum_Y k_q^Y(p)\ Y\ \delta_{pq}\ N_q$$

$$\sum_Y \sum_{\Delta v} \sum_{\Delta J} k_V^Y(v+\Delta v \to v, J+\Delta J \to J)\ Y\ N(B;v+\Delta v, J+\Delta J) = w_{pq}\ N_q$$

The resulting master rate equation in tensor notation is

$$dN_p/dt = S\ \delta_{pp_o} + R_{pq}\ N_q \tag{30}$$

In order to present the elements of the R_{pq} rate matrix independent of pressure, the following definition is provided:

$$R_{pq} = R'_{pq}\ Y + (\Gamma_o + k_{eq} Y + K_V^Y(p))\ \delta_{pq} \tag{30a}$$

3. Steady-State Solutions

For a CW laser pump source the BrCl system reaches a steady-state condition. The population of any excited state

is independent of time and

$$dN(B;v,J)/dt = 0 \tag{31}$$

This condition will now be applied to the master rate equation with various additional assumptions.

a. Electronic Quenching

The simplest CW experiment is that of measuring total fluorecence at various buffer pressures in order to obtain quenching rates. Fluorescence intensity is proportional to excited state densities as was described in section IIB. Thus, by deriving equations relating relative number density to buffer pressure, a method of experimentally determining kinetic rates will be established.

Summing the master rate equation over all states and applying the steady state condition equation (31) yields

$$0 = S - \sum_p \Gamma_o(p)\ N_p - \sum_Y \sum_p k_q^Y(p)\ Y\ N_p \tag{32}$$
$$- \sum_Y \sum_p \left(\sum_q k_V^Y(p \to q)\ Y\ N_p - \sum_q k_V^Y(q \to p)\ Y\ N_q \right)$$

The thermalization processes do not remove any BrCl molecules from the B state because, for any bath specie Y,

$$\sum_p \sum_q k_V^Y(p \to q)\ Y\ N_p = \sum_p \sum_q k_V^Y(q \to p)\ Y\ N_q \tag{33}$$

Thus the fourth term in equation (32) is zero. If it is assumed that Γ_o and k_q^Y are state independent, then

equation (32) can be solved for the total steady-state excited state density,

$$N_T = \sum_p N_p = S/(\Gamma_o + \sum_Y k_q^Y Y) \qquad (34)$$

If Γ_o and k_q^Y are not state independent, equation (32) does not reduce to a simple result and quenching may exhibit unique pressure effects. This issue will be addressed again in section IV.

Two cases of bath gas composition may be considered. First, the BrCl is produced in a Cl_2:BrCl:Br_2 mixture. The concentration ratios are fixed and this condition may be considered the "self-transfer" case. An overall self-quenching rate for the mix is defined as

$$k_q^M M = k_q^{Cl_2}[Cl_2] + k_q^{BrCl}[BrCl] + k_q^{Br_2}[Br_2] \qquad (35)$$

where

[X] = concentration of specie X

M = total mix concentration

Vibrational and rotational rates for the mix are defined in the same manner. Equation (34) can be rewritten for the self transfer case as,

$$1/N_T = (\Gamma_o/S)(1 + k_q^M M/\Gamma_o) \qquad (36)$$

The second bath gas composition is for a fixed BrCl mix pressure and varying pressure of a second buffer specie, Y. This will be termed the buffer transfer case, and

$$N_T = S / (\Gamma_o + k_q^M M + k_q^Y Y) \quad (37)$$

Ratioing to the zero buffer pressure condition yields,

$$N_T(Y=0)/N_T(Y) = 1 + k_q^Y Y/(\Gamma_o + k_q^M M) \quad (38)$$

The assumption that Γ_o is state independent requires limiting the state sum to stable v' (v'<7) and requiring the radiative lifetime for these state to be independent of vibrational state. This assumption is often required to make the energy transfer equations tractable (see section IIC4e for more details). If there are no resonant electronic exchange reactions, one would also expect k_q to depend only slowly on (v',J') quantum state. Any measured quenching rate will be the vibrational state average of such rates. These assumptions have been applied successfully in the case of IF(B).[67-69] In the case of BrCl(B), the assumptions must be verified by the experimental results.

A second caveat must be made to this analysis. The total fluorescence will be directly proportional to total B state concentration only if all vibrational states are detected with equal efficiency or a thermal vibrational distribution exists (see section IIB). This issue is addressed for the BrCl(B) experiments in chapter III and appendix C.

b. Vibrational Transfer

Spectrally-resolved steady-state LIF data provide information on state-to-state vibrational transfer rates. Again, a relationship betwen the steady-state number densities and total pressure is needed to reduce the data.

The master rate equation, equation (27), under the steady-state conditon, equation (31), can be averaged rotationally by summing over all rotational states. Assuming Γ_o and k_q^Y are independent of rotational state and defining the total population concentration of vibrational state v, N(v), as the sum of the population in all rotational states J,

$$N(v) = \sum_J N(v,J) = \sum_{\Delta J} N(v,J+\Delta J) \tag{39}$$

provides

$$\begin{aligned} 0 = {} & S\,\delta_{vvo} - \Gamma_o(v)\ N(v) - \sum_Y k_q^Y(v)\ Y\ N(v) \\ & - \sum_Y \sum_{\Delta v} \sum_{\Delta J} \sum_J k_V^Y(v \to v+\Delta v, J \to J+\Delta J)\ Y\ N(v,J) \\ & + \sum_Y \sum_{\Delta v} \sum_{\Delta J} \sum_J k_v^Y(v+\Delta v \to v, J+\Delta J \to J)\ Y\ N(v+\Delta v, J+\Delta J) \end{aligned} \tag{40}$$

If it is assumed that the rate for V,R-T transfer is independent of intial rotational state, then

$$\begin{aligned} 0 = {} & S\ \delta_{vvo} - \Gamma_o(v)\ N(v) - \sum_Y k_q^Y(v)\ Y\ N(v) \\ & - \sum_Y K_V^Y(v)\ Y\ N(v) \\ & + \sum_Y \sum_{\Delta v} K_V^Y(v+\Delta v)\ Y\ N(v+\Delta v) \end{aligned} \tag{41}$$

where $K_V^Y(v)$ is defined by equation (23). Solving equation (41) for the number density in a satellite band, v (with $v \neq v_o$), compared to the number density in the parent band, v_o, provides

$$N(v)/N(v_o) = \frac{\sum_Y \sum_{\Delta v} k_V^Y(v+\Delta v \rightarrow v)\ Y\ [N(v+\Delta v)/N(v_o)}{\Gamma_o(v) + \sum_Y (k_q^Y(v) + K_V^Y(v))\ Y} \qquad (42)$$

Equation (42) provides the basis for extracting state-to-state vibrational transfer rate constants, $k_V^Y(v \rightarrow v+\Delta v)$ from data of relative populations, $N(v)/N(v_o)$, as a function of the buffer concentration, Y.

If the buffer pressure is sufficiently low, the sum in the numerator may be limited to $v+\Delta v = v_o$. This is true for single collision conditions because the ratio $N(v+\Delta v)/N(v)$ is significant only for $v+\Delta v = v_o$. To insure single collision conditions, the collisional frequency, ω_c, must be less than the collision free decay rate, Γ_o. For this case,

$$N(v)/N(v_o) = \frac{\sum_Y k_V^Y(v_o \rightarrow v)\ Y}{\Gamma_o(v) + \sum_Y k_q^Y(v)\ Y + \sum_Y K_V^Y(v)\ Y} \qquad (43)$$

It should be noted that the denominator is the reciprocal of the lifetime of the vibrational state v,

$$1/\tau_v = \Gamma_o(v) + \sum_Y k_q^Y(v)\ Y + \sum_Y K_V^Y(v)\ Y \qquad (44)$$

so that

$$N(v)/N(v_o) = \tau_v \sum_Y k_V^Y(v_o \rightarrow v)\ Y \qquad (45)$$

For the self-transfer single collision condition, equation (45) reduces to

$$[N(v)/N(v_o)]_{Y=0} = \tau_v\ k_V^M(v_o \rightarrow v)\ M \qquad (46)$$

The buffer transfer case is simplest when the vibrational transfer due to the base mix pressure is neglected. In this case equation (45) becomes

$$N(v)/N(v_o) = \tau_v\ k_V^Y(v_o \rightarrow v)\ Y \qquad (47)$$

Due to low signal intensities, this condition cannot always be achieved experimentaly. The general case is more difficult since the population in satellite bands that was transferred by self collisions can be reduced by vibrational removal due to the buffer gas.

The general buffer transfer case for a single buffer gas under single collision conditions is best handled by subtracting the relative number $N(v)/N(v_o)$ at zero buffer pressure, equation (46) from equation (45),

$$N(v)/N(v_o) - [N(v)/N(v_o)]_{Y=0} = [\tau_v(Y) - \tau_v(Y=0)]k_V^M(v_o \rightarrow v)M + \tau_v(Y)\ k_V^Y(v_o \rightarrow v)\ Y \qquad (48)$$

The lifetime of state v at a given buffer pressure is given by

equation (44) and therefore the lifetime difference is

$$\tau_v(Y) - \tau_v(Y=0) = -\tau_v(Y)\,\tau_v(Y=0)\,K_R^{Y}(v)\;Y \qquad (49)$$

The definition of equation (25) has been used for $K_R^{Y}(v)$. Substituting this into equation (48) yields

$$N(v)/N(v_o) - [N(v)/N(v_o)]_{Y=0} = -\tau_v(Y)\,\tau_v(Y=0)K_R^{Y}(v)Yk_V^{M}(v_o \rightarrow v)M + \tau_v(Y)k_V^{Y}(v_o \rightarrow v)\;Y \qquad (50)$$

Using equation (46) provides the final result,

$$N(v)/N(v_o) - [N(v)/N(v_o)]_{Y=0} = \tau_v(Y)k_V^{Y}(v_o \rightarrow v)Y\{1-[N(v)/N(v_o)]_{Y=0}[K_R^{Y}(v)/k_V^{Y}(v_o \rightarrow v)]\} \qquad (51)$$

The application of this equation to spectrally-resolved LIF data is not simple. In addition, the assumptions needed for its derivation and application may not be easily fulfilled. Further discussion of these results will be presented in section IV.

c. Rotational Transfer

Rotational transfer within the parent vibrational band will now be considered. The master equation (27) in steady-state, equation (31), for the initially populated state is

$$0 = S - \Gamma(v_o,J_o) - \sum_Y k_q^{Y}(v_o,J_o)\;Y\;N(v_o,J_o) \qquad (52)$$
$$- \sum_Y K_V^{Y}(v_o)\;Y\;N(v_o,J_o) - \sum_Y K_J^{Y}(J_o)\;Y\;N(v_o,J_o)$$
$$+ \sum_Y \sum_{\Delta v} \sum_{\Delta J} K_V^{Y}(v_o+\Delta v \rightarrow v_o, J_o+\Delta J \rightarrow J_o)\;Y\;N(v_o+\Delta v, J_o+\Delta J)$$

The last term of equation (52) represents mutliple collisions that return population to the parent state. Due to the many accessible rotational states, this process is unlikely and may be neglected. This is particularly true when vibrational transfer strongly competes with rotational processes. Neglecting the last term of equation (52), the steady state number density is,

$$N(v_o,J_o)=S/[\Gamma_o(v_o,J_o)+ k_q^Y(v_o,J_o)Y+ K_V^Y(v_o)Y+ K_J^Y(J_o)Y] \quad (53)$$

Identifying the denominator as the reciprocal collisional lifetime of state (v_o,J_o) provides,

$$N(v_o,J_o) = S\ \tau(v_o,J_o) \quad (54)$$

The total number density of the population in v_o' is obtained from equation (41)

$$N(v_o) = \tau_V(v_o)[S+\sum_Y\sum_{\Delta v} K_V^Y(v+\Delta v\rightarrow v)\ Y\ N(v+\Delta v)] \quad (55)$$

The population ratio is then given by

$$[N(v_o,J_o)/N(v_o)][\tau(v_o)/\tau(v_o,J_o)] = 1 - \tau(v_o)\sum_Y\sum_{\Delta v} k_V^Y(v+\Delta v\rightarrow v)\ Y\ [N(v+\Delta v)/N(v_o)] \quad (56)$$

Defining the quantity ξ as

$$\xi = \tau(v_o)\sum_Y\sum_{\Delta v} k_V^Y(v+\Delta v\rightarrow v)\ Y\ [N(v+\Delta v)/N(v_o)] \quad (57)$$

provides

$$[N(v_o)/N(v_o,J_o)](1-\xi) = \tau(v_o)/\tau(v_o,J_o) \quad (58)$$

The lifetime of (v_o,J_o) is

$$1/\tau(v_o,J_o) = 1/\tau(v_o) + \sum_Y K_R^Y(J_o)\ Y \tag{59}$$

And finally,

$$[N(v_o)/N(v_o,J_o)](1-\xi) - 1 = \tau(v_o)\sum_Y K_J^Y(J_o)\ Y \tag{60}$$

Applying equation (60) to the self transfer case,

$$[N(v_o)/N(v_o,J_o)](1-\xi) - 1 = \tau(v_o)\ K_J^M(J_o)\ M \tag{61}$$

The buffer transfer case is again handled by subtracting from equation (61), the same equation evaluated at no buffer pressure:

$$N(v_o)/N(v_o,J_o) - [N(v_o)/N(v_o,J_o)]_{Y=0} = \tag{62}$$

$$\{\xi N(v_o)/N(v_o,J_o) - \xi(Y=0)[N(v_o)/N(v_o,J_o)]_{Y=0}\}$$

$$+ K_J^M(J_o)\ M\ (\tau_v - \tau_v(Y=0)) + K_J^Y(J_o)\ Y\ \tau_v$$

If the effects of back vibrational transfer are neglected ($\xi = 0$) and the definition of equation (63)

$$\Delta_1 = K_J^M(J_o)\ M\ (\tau_v - \tau_v(Y=0)) \tag{63}$$

is applied to the buffer rotational transfer equation (62), the result of equation (64) is obtained.

$$N(v_o)/N(v_o,J_o) - [N(v_o)/N(v_o,J_o)]_{Y=0} - \Delta_1 = \tag{64}$$

$$K_J^Y(J_o)\ Y\ \tau_v$$

Equations (36), (38), (46), (51), (61), and (64) are the basis for the reduction of CW LIF energy transfer data. Once the rate constants have been established, the matrix R_{pq} can be formed and the master rate equation (30) can be solved with the CW condition (31) for the population distributions N_p. This can be accomplished without approximation and the results compared to the experimental data. Such a consistency check is an important test of the assumptions described in this section.

4. Time-Resolved Solutions

For a pulsed laser excitation source with a duration very short compared to the shortest excited state lifetime, the source term in the master equation may be approximated by a delta function with amplitude S, centered at time t=0. An equivalent statement is to let the source term go to zero and apply the initial condition

$$N(v',J')_{t=0} = \delta_{vv_o}\,\delta_{JJ_o}\,N(v_o',J_o')_{t=0} \tag{65}$$

By normalizing the number densities to the number initially pumped up to v_o',J_o' the master rate equation in tensor notation, equation (30), becomes

$$dx_p/dt = R_{pq}\,x_q \qquad x_p(0) = \delta_{pp_o} \tag{66}$$

where

$$x_p = N_p/N_{p_o}(t=0) \tag{67}$$

The well known Stern-Volmer plot is based on equation (71). By observing the characteristic decay of the fluoresecnce intensity, I_f, the lifetime is obtained from

$$\tau = -\Delta t / \Delta \ln(I_f) \tag{72}$$

By plotting $1/\tau$ versus concentration Y, a linear plot with intercept Γ_o and slope k_q^Y is obtained. This method is a well established technique that has been applied successfully to many energy transfer problems.

Often the requirement of a state independent Γ_o and k_q^Y is not fullfilled. The Stern-Volmer analysis may still be applied if single collision conditions prevail. In this case the master equation for state p becomes

$$dx_p/dt = -[\Gamma_o(p) + \sum_Y k_q^Y(p)\ Y + \sum_Y K_V^Y(p)\ Y\ ]\ x_p \tag{73}$$

which again has the solution (71) with lifetime

$$1/\tau(p) = \Gamma_o(p) + \sum_Y [k_q^Y(p) + K_V^Y(p)]\ Y \tag{74}$$

$$= \Gamma_o(p) + \sum_Y K_R^Y(p)\ Y$$

Equation (74) may apply to p=(v,J), a specific ro-vibrational state or to p=(v), a rotationally-averaged state. Thus, by observing spectrally-resolved emission from a parent state under single collision conditions, the collision free lifetime and total removal rate from that state can be obtained.

In order to obtain state-to-state vibrational transfer rates, more sophisticated techniques are required. These methods will be presented in section IIc4e-g. First, some general remarks regarding the vibrational transfer problem will be considered.

b. Radioactive Decay Analogy

The problem of radioactive series decay[167] is similar to that of vibrational energy transfer. Consider the decay series

$$y_1 \xrightarrow{d_1} y_2 \xrightarrow{d_2} y_3 \cdots\cdots y_5 \xrightarrow{d_5} y_6 \tag{75}$$

The system of equations governing such a decay is

$$dy_i/dt = D_{ij}\, y_j \qquad y_i(0) = \delta_{i1}\, y_1(0) \tag{76}$$

where

$$D_{ij} = \begin{cases} -d_i & i=j \\ d_{i-1} & i=j-1 \\ 0 & \text{elsewhere} \end{cases} \tag{77}$$

This reaction mechanism and rate equation is very similar to that of the vibrational transfer problem, equation (66).

The form of the transfer matrices D_{ij} an R_{pq} may be quite different, however. The radioactive series decay matrix, D_{ij}, is bi-diagonal and has no nonzero elements on its upper triangle. This is an artifact of the decay being essentially irreversible. As a result, the eigenvalues for the

system, ℓ_i, are identically equal to the decay rates, d_i. The vibrational transfer matrix, R_{pq}, may have many more nonzero elements. The reverse reactions, or transfer up the vibrational manifold, can be quite probable and will obey detailed balance,

$$R_{pq} = R_{qp} \exp(-\Delta\varepsilon_{qp}/k_B T) \tag{78}$$

where

$\Delta\varepsilon_{qp} = \varepsilon_q - \varepsilon_p$ is the energy difference between states p and q

k_B is the Boltzmann constant

T is the bath gas temperature (300 K)

The matrix R_{pq} is at least tri-diagonal and the eigenvalues are no longer equal to the individual removal rates. That is, the system of differential equations may be strongly coupled. Only if $\Delta\varepsilon_{qp}/kT \gg 1$ will the system be decoupled. In the limit $\Delta\varepsilon_{qp}/kT \to \infty$, the radioactive series decay analogy is exact.

The solution to such a decoupled set of equations is simple. For the case of a two step radioactive decay, the solution is

$$y_2(t) = y_1(0)\,[d_1/(d_2-d_1)][\exp(-d_1 t) - \exp(-d_2 t)] \tag{79}$$

This solution provides the general features of spectrally-resolved, temporally resolved LIF spectra. For a satellite

band, the spectra will exhibit an initial exponential rise followed by an exponential decay. The rise is due to the faster kinetic process, usually the rate of transfer into the observed state. The subsequent decay is characteristic of the slower kinetic process, usually the removal from the observed state.

The radioactive series decay analogy has been used to study energy transfer in HF, where the vibrational spacing is $\Delta\varepsilon_{pq}/kT = 20.$[168] For V-T transfer in IF(B) where $\Delta\varepsilon_{qp}/kT=2$ the analogy was found to be inadequate.[69]

For strongly coupled vibrational manifolds, $\Delta\varepsilon_{qp}/kT<1$, the problem of extracting rate constants for state-to-state vibrational transfer from spectrally-resolved, temporally-resolved data becomes quite difficult. This general problem will be discussed shortly. First some basic properties of the master equation will be presented.

c. The Eigenvalue Problem

The master equation is a coupled set of first order, linear differential equations with constant coefficients. Such a system can be transformed to a system of Volterra Integral Equations of the Second Kind.[169] The solutions are thus unique and depend continuously upon the data. The density distribution $x_p(t)$ may be written as an expansion in

the complete set of orthonormal eigenvectors[170]:

$$x_p(t) = \sum_i C_i \, V_p^{\,i} \exp(\ell_i t) \tag{80}$$

where

$V_p^{\,i}$ is the p-th element of the i-th eigenvector

ℓ_i is the eigenvalue associated with eigenvector V^i

C_i are the initial condition constants

A complete description of the eigenvalue problem may be found in appendix E.

The matrix R_{pq} is real but not symmetric, due to the detailed balance property. Since the matrix is non-Hermitian, complex eignvalues might be expected. But the population densities do not oscillate in time. The matrix R_{pq} does indeed have real, nonpositive eigenvalues as shown in appendix E. It is the detailed balance property that assures exponential decay.

Since the R_{pq} matrix is at least tri-diagonal, the eigenvalues of the system will be a convolution of kinetic rates and no eigenvalue will be equal to the total removal from any state. For a strongly coupled vibrational manifold the convolution will be severe. Equation (74) has already demonstrated that a population in a parent band will decay exponentially with a lifetime given by the total removal rate. This result was derived for single collision conditions.

Under these conditions, the eigenvalues combine in such a way that the decay from the parent band is exactly the rate for total removal. A proof of this statement is given in appendix E.

Due to the strong convolution of kinetic rates to produce eigenvalues for a manifold with $\Delta\varepsilon_{qp}/kT < 1$, the scaling of eigenvalues with vibrational state can be quite different from the scaling of vibrational transfer rates or total removal rates. In fact, the eigenvalues can scale strongly with vibrational state even for the case of no vibrational rate scaling. This occurs when the quenching from one state is much greater than all other states. An example illustrating this point may be found in appendix E.

To summarize; under single collision conditions, the population of a parent band will decay with a lifetime characteristic of the total removal rate from that state. Under multiple collision conditions the decay from a given state reflects the eigenvalue of that state. Such eigenvalues can be a strong convolution of kinetic processes and be completely unrepresentative of the total removal rate from that state. This effect is accentuated for strongly coupled vibrational manifolds.

d. Pressure Scaling

Since the master equation (66) is first order, a simple pressure scaling for distribution x_p might be expected. This is true for the case when the collisionless lifetime, τ_o, is indepedent of quantum state, p. If the following change of variables is applied to the master equation

$$t' = tk_o Y \qquad k' = k/k_o \qquad z(t) = x(t)\ \exp(t/\tau_o) \tag{81}$$

then the master equation becomes

$$dz_p/dt' = -\sum_Y k'_q{}^Y(p)\ z_p - \sum_Y k'_V{}^Y(p)\ z_p + \sum_Y \sum_q k'_V{}^Y(q \to p)\ z_q \tag{82}$$

The solution z_p now depends only on the product

$$t' = t\ k_o\ Y \tag{83}$$

This scaling law can be used as a test of the independence of Γ_o of quantum state p.

e. The Inverse Problem

The previous discussions have centered on what the distribution $x_p(t)$ looks like for a given rate matrix R_{pq}. The problem of experimentally determing V-T transfer probabilities is the inverse of this problem. In this case, we wish to find a transformation that will take observed population distributions $x_p(t)$ into the transition

probabilities of R_{pq}. This inverse problem is much more difficult than the previously described problem.

A mutli-level system has many more transition probabilities than it does have states. The distributuion among n states has as many as n^2-n transition probabilities. For a weakly coupled system, many of these probablities are nearly zero. But as the coupling increases, so does the number of transition probabilities. That is, multi-quantum transfer becomes important.

In order to obtain enough information to determine all n^2-n transition probablities independently, the emission from every state for each initially populated state must be observed.[171] In temporally-resolved spectra it may be possible to substitute a lack of information on certain (v_o', v') emissions with the emission of a given (v_o', v') at widely different times.[171] Note that this problem requires using a large number of noisy spectra all at one time to make a universal fit to the elements of R_{pq}.

T. Carrington has studied the general features of the inverse problem and has found that a much greater degree of precision in the data is required for the inverse problem.[171] Carrington applied his analysis to a typical vibrational manifold with six states and V-T transfer limited to $\Delta v \lesssim 2$. For this example, the accuracy required in observed temporal spectra is approximately ten times greater than the desired

accuracy in the rate constants.[171] P. Wolf experimentally studied the accuracy required in observed temporal spectra for V-T transfer in IF(B). He found a 10% scatter in observed temporal spectra yielded a 50% uncertainty in V-T rate constants.[69] Carrington has also found that the assumption of state-independent collisionless decay rates, Γ_o, is often required to reduce the problem to a tractable form.

The inverse steady-state and pulsed energy transfer experiments are essentially the same problem, with the steady-state experiment being the time-averaged pulsed experiment. The time average is over the complete range of lifetimes for the excited state. This can easily be seen by integrating the pulsed master equation over all time,

$$\int_o^\infty (dx_p/dt)\, dt = \int_o^\infty R_{pq}\, x_q(t)\, dt \qquad (84)$$

The conditions

$$x_p(o) = \delta_{ppo} \qquad x_p(\infty) = 0$$
$$N_p^{ss} = \int_o^\infty x_p(t)\, S\, dt$$

can be used to rewrite equation (72) as

$$R_{pq}\, N_q^{ss} = -S\, \delta_{pp_o} \qquad (85)$$

Equation (85) is identical to the steady-state master equation (29) and thus the steady-state condition is equivalent to a time averaging of the density distributions.

f. The Montroll Shuler Model

Theoretical solutions to the inverse problem have been obtained under assumptions that relate the individual transition probabilities to each other and thus reduce the number of independent transition probablities to be extracted from the spectrally-resolved data. One such solution is the model developed by Montroll and Shuler.[172] Transitions involving $|\Delta v| = 1$ only are included, the scaling of probability with vibrational quantum number is based on the Landau -Teller Model,[153] and detailed balance is used to relate all the vibrational transfer rates to the single fundamental rate constant $k_V^Y(1\text{-}0)$, the rate constant for transfer from $v'=1$ to $v'=0$. The closed form solution for the population in state p, z_p [see equations (81) and (67)], after initially populating state q is

$$z_p(t) = \frac{(1-e^{\theta})\, e^{q\theta}}{(e^{-t'} - e^{\theta})} \left(\frac{e^{-t'} - 1}{e^{-t'} - e^{\theta}}\right)^{p+q} F(-p,-q,1;u^2) \qquad (86)$$

where

$\theta = h\nu_o/kT$

ν_o = the fundamental vibrational frequency

$t' = k_V^Y(1\text{-}0)\ t\ (1-e^{-\theta})$

$u = \sinh(\theta/2)/\sinh(t'/2)$

F = hypergeometric function

The Montroll Shuler Model has the distinct advantage of requiring only one temporal spectrum (the emission from one v'

after initially populating a single v_o') to obtain the rate constant $k_v^Y(1\text{-}0)$, and thus the full rate matrix R_{pq}. A detailed description of this model is given in appendix D.

The Montroll Shuler model has been applied to vibrational transfer in IF(B) and found to be a satisfactory description of the energy transfer processes.[69] The $|\Delta v| = 1$ only assumption is valid since $h\nu_o/kT = 2$ and mutli-quantum transitions are unlikely. The low lying levels of IF(B) are nearly harmonic, $\omega_e\chi_e/\omega_e = 0.007$, and the Landau - Teller scaling should be appropriate. All the vibrational levels in IF(B) for $v'<9$ are stable and radiative lifetimes vary only approximately 20 %.[69] In addition, the electronic quenching rate is roughly independent of v'.[69] The assumption that Γ_o and k_{eq} are independent of quantum state is justified.

The situation in BrCl(B) is not as promising. The vibrational spacing is less ($\Delta\varepsilon_{qp}/kT = 1$), the anharmonicity is larger ($\omega_e\chi_e/\omega_e = 0.013$), and the state independence of Γ_o, and k_q may be completely incorrect.[120-123] Clyne has observed that $k_Q(v)$ varies exponentially with v' for $v'>3$.[123] In addition predissociation sets in at $v'=6$, $J'=42$ and the collisionless lifetime drops from 40.2 μs to 8 μs in one rotational level.[122] Indeed, the Montroll-Shuler model may be a poor description for vibrational transfer within v' levels of BrCl(B).

g. Numerical Integration Methods

No closed form solution to the inverse energy transfer problem for the case of strong vibrational coupling has been found in the literature. This case is difficult theoretically since interactions are strong and the tools of perturbation theory are inappropriate.

The option of guessing a rate matrix R_{pq} and numerically integrating the rate equations (or solving the eigenvalue problem exactly) is always available. By systematically varying the elements of R_{pq}, a best fit to the experimental spectra can be achieved. No assurance for the uniqueness of the solution is provided and computational costs could be excessive for large data samples.

Vibrational energy transfer in BrCl(B) is a complicated process and all the methods for data analysis described in this chapter will be necessary to interpret the experiments. Numerical solutions will be required and based on the eigenvalue solution described in section IIC4c. Further discussion of these numerical methods will be presented in chapter IV as needed.

III. EXPERIMENTAL SECTION

A. Steady-State Experiment

The experimental arrangement for the steady-state experiment is shown in figure 8. The excitation source was a Spectra Physics Model 380A Single Frequency Ring Dye Laser pumped by a Model 171 argon ion laser. The dye laser provided up to 440 mW power with a less than 100 MHz linewidth. Exciton Rhodamine 590 dye was used to cover the wavelength range 570 to 600 nm. This facilitated pumping $v' = 4$, 5 and 6. The output of the dye laser was focused to an approximately 2mm diameter inside the BrCl cell. A Burleigh model WA-20 wavemeter was used to record the dye laser output frequency to an accuracy of approximately 0.01 cm^{-1}.

The BrCl fluorescence cell was a 3 inch diameter by 9.5 inch long pyrex cylinder with 1 inch Brewster windows on both ends. The exterior of the cell was painted black to eliminate stray room light from the fluorescence signal. A 2 inch window was mounted at the center of the cell to view the fluorescence. The pressure in the cell was measured with MKS #310 1 torr and #220 10 torr capacitance manometers. The manometers were calibrated using a Veeco RG75K ionization gauge. Vacuums of 10^{-6} torr were achieved with a Varian HSA 2 inch diffusion pump. The leak plus outgassing rate for the cell was less than 0.01 mtorr/min.

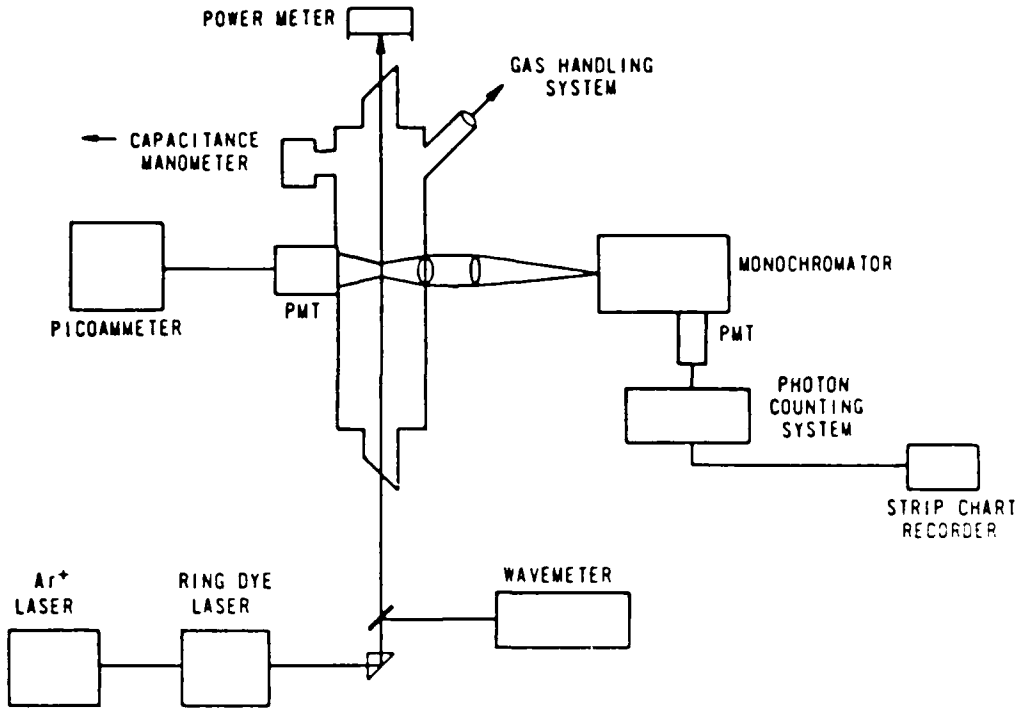

Figure 8. CW spectrally-resolved LIF experiment.

BrCl was produced in a gas handling manifold by mixing Cl_2 and Br_2 gases in a ratio of 15:1. The equilibrium constant for the reaction $Br_2 + Cl_2 \rightleftharpoons 2\ BrCl$ is $K_{eq}=9.6$.[120] The approach to equilibrium is slow and the gases were allowed to react for at least fifteen hours. Once produced, the BrCl mix was stored in a pyrex bomb and was stable for greater than four weeks. Since Br_2 absorbs and emits in the same spectral region as BrCl, excess Cl_2 was used to minimize the equilibrium Br_2 concentration. For the 15:1 initial Cl_2:Br_2 concentration, the resulting equilibrium mix is calculated to be Cl_2:BrCl:Br_2 = 1.0 : 0.14 : 0.002. In such a mixture, the predominant collisional process is BrCl(B) + Cl_2(X).

Control of the cell pressures for the BrCl mix and/or buffer gases was achieved with a Granville-Phillips Variable Leak Valve. Since the fluorescence chamber is a static cell, large back pressures (approximately 50 torr) were used to leak in the buffer gases but prevent the loss of BrCl mix from the cell. In this way, a fixed BrCl mix pressure could be maintained for various buffer gas pressures. Using this procedure, buffer gas pressures as low as 1 mtorr could be added with the leak valve. The cell was sealed off with a teflon valve during emission wavelength scans.

Optical excitation of BrCl(B) is difficult due to the large shift in equilibrium internuclear separation of the excited (B) with respect to the ground (X) electronic states. The absorption coefficient for the BrCl v"=1 to v'=6 transition is[121,100]

$$\alpha = 1.8 \times 10^{-7} \text{ cm}^{-1} \text{mtorr}^{-1}$$

With the cw ring dye laser used in these steady-state experiments, total B-state densities of roughly 10^8 molec/cc were achieved. Fluorescence signals were indeed found to be quite small and required sophisticated signal averaging techniques.

Total fluorescence was observed with a cooled RCA C31034A-02 GaAs photomultiplier tube (PMT) placed normal to the dye laser beam at the back of the fluorescence cell. The

PMT was cooled to -30 C and a 1400 volt photocathode bias was applied. Dark current was about 0.1 nA and typical signal strengths were 0.2 nA to 5 μA. The PMT current was observed on a Keithley model 414S picoammeter and recorded on an HP7100B strip chart recorder.

It was important to monitor the total fluorescence intensity during the spectrally-resolved experiments to correct for mode changes and wavelength drifting of the ring dye laser. Small corrections to pump laser frequency were made by varying the airspace between the mirrors of a Fabry-Perot etalon (FSR=75GHz) within the dye laser cavity. The transmitted power of the dye laser was measured at the output window of the BrCl cell to monitor the dye laser performance.

The spectrally-resolved fluorescence was recorded by dispersing the focused BrCl(B) emission with a McPherson model 218 0.3-meter scanning monchromator with a 1200 grooves/mm grating blazed at 500 nm onto a second RCA C31034A-02 GaAs photomultiplier tube cooled to -30C. The BrCl emission was collimated with a 50 mm focal length aspheric 2 inch diameter lens and focused on the 200 micron slit of the monochromator with a 250 mm lens. The 200 micron slits provided a 0.6 nm instrumental resolution. These monochromator slits were chosen to maximize the observed BrCl(B) emission intensity and still provide sufficient resolution to isolate vibrational emission bands and each

branch of the P-R doublet arising from the parent rotational state.

Due to the very small resolved fluorescence signal intensities, a PARC photon counting system was used to record the emission spectra. The system consisted of a model 1121 amplifier-discriminator and a model 1112 photon counter/processor. Dark current was about 10 cps and typical signals were > 100 cps. The monochromator scan rate was usually 1 nm/min and the photon counts were summed for a one second interval. Spectral resolution was limited by the monochromator, not by the time constant of the averaging process.

The photon counts were recorded on an HP 7100B strip chart recorder as a function of dispersed emission wavelength for a given pump laser wavelength. The relative intensity of these emission bands provided the information necessary for extracting energy transfer rate constants. The emission spectra for initially populated states $v_o' = 4$, 5, and 6 and BrCl mix pressures of 2.0 mtorr to 10 torr were observed. Research grade buffer gases He, Ne, Ar, and Xe at pressures of 5.0 - 200 mtorr were used. Initially populated BrCl rotational states ranged from $J_o' = 15$ to 46.

Steady state excitation spectra were also obtained by scanning the pump laser frequency over 30 GHz intervals and recording the PMT current from the undispersed total

fluorescence. A sample excitation spectrum showing the resolution of the ring laser is given in figure 9. Note that a single ro-vibrational state of a given BrCl isotope may be excited without interference from Br_2 absorptions.

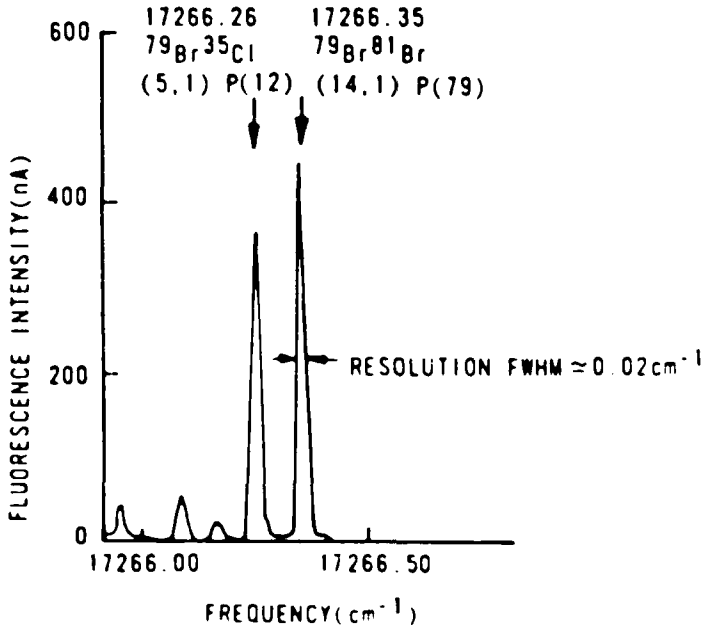

Figure 9. CW excitation spectrum. The 0.02 cm^{-1} resolution is established by the Doppler width. The scan lengths were limited by the ring dye laser etalon. The (5,1) R(10) transition was observed in a different scan region.

Calibrations of the experiment included spectral response, monochromator wavelength and resolution, and linearity of fluorescence intensity as a function of incident dye laser power. Details of these calibrations are presented in appendix C. The spectral response of the system includes the response of all optics, monochromator grating, and

photomultiplier tube. In order to relate intensity to number density via equation (6), relative detection efficiencies must be ccnsidered. These relative detection efficiencies are reported in appendix C.

The pump transition must not be saturated in the CW experiment as was shown in section II. The linearity of fluorescence intensity with incident dye laser power is quite good and displayed in appendix C. As expected, the BrCl B-X transition is not saturated under the conditions of these experiments.

B. Pulsed Experiment

The experimental arrangement for the temporally-resolved experiment is shown in figure 10. The excitation source was a Quanta Ray PDL-1 dye laser pumped by a frequency doubled or tripled Quanta Ray DCR-1 pulsed Nd:YAG laser. The laser output consisted of 8 ns pulses of less than 80 mJ/pulse at a 10 Hz repetition rate. An intracavity etalon was used to narrow the dye laser bandwidth to ~0.03 cm^{-1}. With this etalon output energies were limited to 40 mJ/pulse. Exciton Coumarin 500, Rhodamin 590, Kiton Red 620, and DCM dyes were used to cover wavelengths of 500-550 nm, 550-580 nm, 570-600 nm, and 600-670 nm respectively. This facilitated pumping $v'=0$ through 8. The output of the dye laser was focused to an approximately 2mm diameter inside the BrCl fluorescence cell.

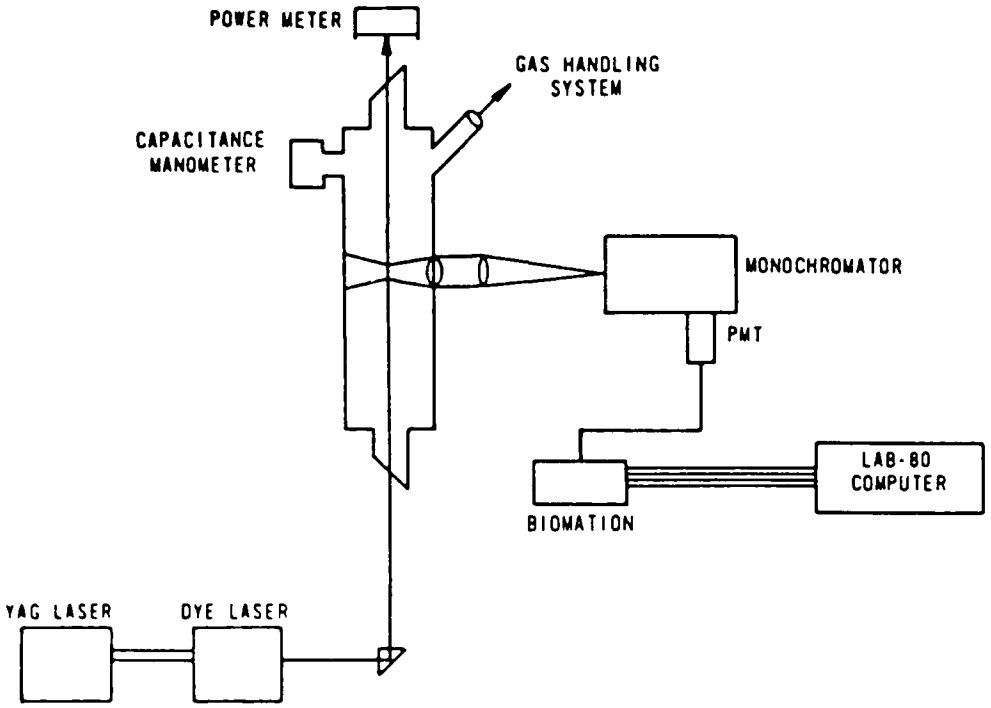

Figure 10. Temporally-resolved, spectrally-resolved LIF experiment.

The fluorescence cell, vacuum system, and gas handling system were essentially identical to those described for the steady state experiment. BrCl was produced in the same manner as for the CW experiment.

Fluorescence intensities in the pulsed experiments were very weak. Figure 11 illustrates a typical result. The photon spikes from a C31034 PMT amplified by an HP461A amplifier are observed on a Model 7884 Tektronix oscilliscope after initially populating $v'=6$ at 560.0 nm and resolving the emission from $v'=0$ at 855.7 nm. Total mix pressures are indicated. In order to obtain usuable, temporally resolved fluorescence spectra, 10^3- 10^4 shots were averaged.

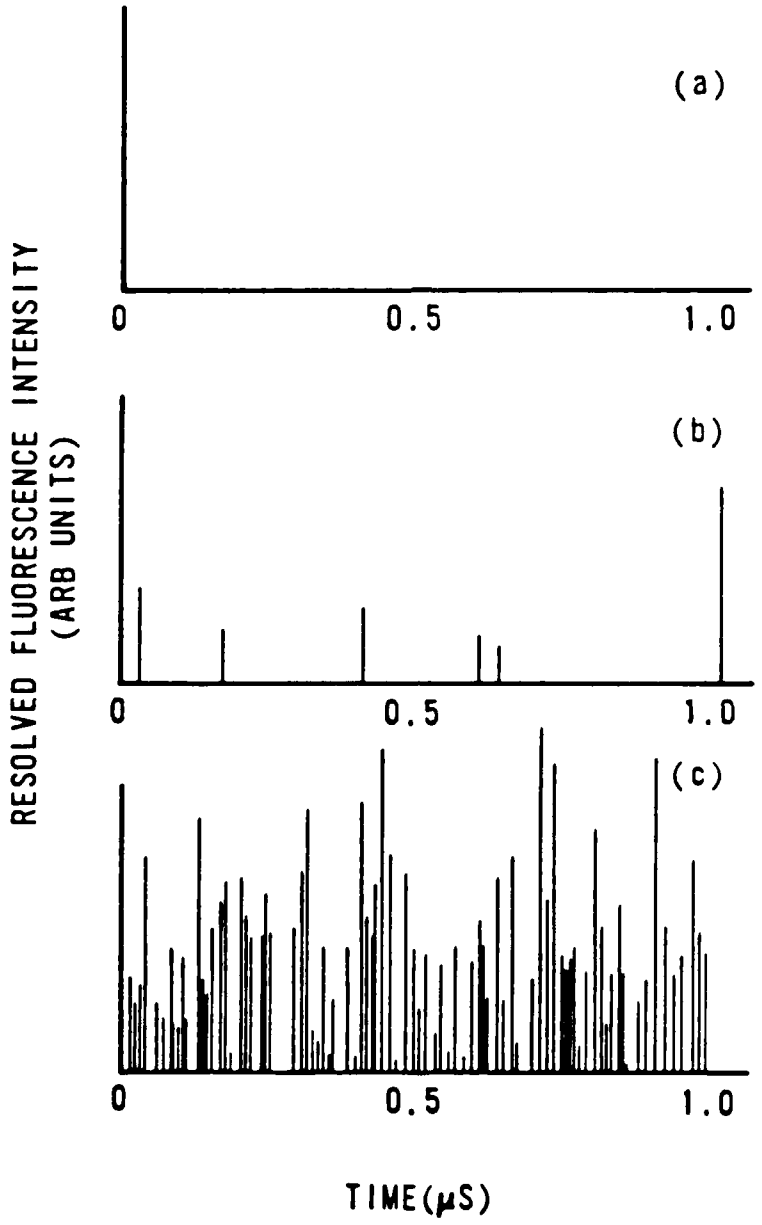

Figure 11. Single-shot BrCl(B) temporally-resolved, spectrally-resolved emission from v'=0 as recorded on an oscilliscope. Total mix pressures are (a) 0.00 torr, (b) 0.27 torr and (c) 1.80 torr.

The averaging was accomplished with a Model 6500 Biomation waveform recorder and Nicolet LAB80 computer.

Since at least some of the BrCl energy transfer processes will have nearly gas kinetic rates, a high degree of time resolution was necessary. The Biomation waveform recorder provided 1024 channels with a resolution as high as 2 ns/channel. Digitized PMT currents were then passed from the waveform recorder to the Nicolet LAB80 computer for signal averaging and data reduction. Shot-averaged data was recorded on floppy disk and eventually transferred to the AFWL CRAY II Computer Common File System for extensive data reduction and manipulation. A copy of the shot-averaged signal was also recorded on an HP 7004B x-y recorder.

The waveform recorder was triggered optically by the doubled-YAG output via a Ge photodiode. The amplified output from the photodiode was used to trigger a pulse generator which in turn provided a sufficient trigger for the Biomation recorder. The diode was used to isolate electrical noise from the DCR-1 flashlamp circuits. The Biomation recorder pre-trigger mode was used to establish baseline signals before the laser pulse. Approximately 100 channels were used to obtain the average baseline and this baseline was subtracted from the entire waveform. The Nicolet LAB80 processor was used to fit single exponential decays to the waveforms, integrate the waveforms, and perform three-point smoothing

averages. The AFWL CRAY II Computer was used for more sophisticated data reduction techniques. The Biomation - LAB80 time scales were calibrated and found to be accurate to within two percent. The details of this calibration are given in appendix C.

Two types of spectra were recorded with the Biomation waveform recorder. First, the decay of total fluorescence was observed by focusing the undispersed emission onto a filtered photomultiplier tube. Two PMT's with different spectral responses were used; an RCA C31034 and an EMI 9558QB S-20. Several long pass optical filters were used to block scattered pump laser radiation and to vary the spectral response of the detection system. These filters included 600 nm and 750 nm Corion interference long pass filters and 630 nm and 670 nm Oriel colored glass long pass filters. The spectral response of the system with either PMT is given in appendix C. Secondly, spectrally-resolved, temporally-resolved spectra were observed by dispersing the BrCl(B) emission with the McPherson model 218 0.3-meter scanning monochromator with a 1200 groove/mm, 500 nm blazed grating. Generally, 800 micron slits were used to provide a 2.5 nm resolution. These monochromator slits were chosen to maximize the observed BrCl(B) emission intensity and minimize vibrational emission spectral overlap. The degree of spectral isolation achieved in this apparatus is demonstrated in appendix B.

The energy transfer processes affecting BrCl(B) were studied by observing both of these types of temporal spectra for various initially populated states (v_o,J_o), for various observed states (v',J') and for various BrCl-Cl_2 and buffer pressures. For the total fluorescence spectra, initially populated states of v_o'=0-7 and pressures 0.2 mtorr to 10 torr were studied. The spectrally-resolved studies included initially populated states of v'= 0-6. Initially populated states were observed for pressures of 5 mtorr to 10 torr. Collisionally populated states were observed for pressures of 50 mtorr to 10 torr. These pressures cover the range from collision-free to thermalized conditions. Emission from all the stable vibrational states (v'=0-6) was observed. Buffer gases included Cl_2, He, Ne, Ar, Kr, Xe, O_2, and N_2 (research grade).

In order to make pump transition assignments, traditional excitation spectra were obtained by scanning the dye laser wavelength and observing the boxcar-averaged total fluorescence signal. For these experiments the Biomation-LAB80 system was replaced with a PARC Model 162 Boxcar Integrator, and the intracavity etalon of the pulsed dye laser was removed to permit extensive scanning (20 nm).

In order to make emission transition assignments and t evaluate the degree of vibrational emission overlap, "psuedo-CW" spectra were obtained by selecting a fixed pump

wavelength and resolving the resultant emission intensity. By selecting the boxcar to integrate over several BrCl(B) lifetimes, an essentially steady-state emission spectrum could be observed under pulsed conditons. Examples of the "psuedo-CW" spectra are given in appendix B.

Diffusion effects can be very important in lifetime measurements, especially when the states are relatively long-lived and the collision frequency is low. The case of $Cl_2(B)$ with a radiative lifetime of 305 μs is a classic example of how diffusion may effect lifetime measurements.[109] Clyne and McDermid have calculated the effect of diffusion on BrCl(B) lifetimes under conditions very similar to our experiments and they conclude it is negligible.[114] No lengthening of measured lifetimes of BrCl(B) for total mix pressure of 0.2 - 2.0 mtorr has been observed in our apparatus when small amounts of He are added to increase the collision frequency and reduce the mean free path, or when the optical system is defocused to observe a larger spatial region.

IV. RESULTS AND DISCUSSION

A. Introduction

The study of energy transfer within the B $^3\Pi 0^+$ state of BrCl was found to be quite difficult. A number of experimental problems (see section III) limit the signal intensities, spectral and temporal resolution, and collision frequency. In addition, the effects of predissociation, small vibrational energy spacing, and significant anharmonicity of the vibrational manifold greatly complicate the transfer processes. Certainly the most difficult issue to handle is the small vibrational spacing, which strongly couples the kinetic processes affecting the B-state vibrational manifold. In order to unravel these processes and obtain values for the rate constants, both the steady-state and pulsed LIF experiments are necessary. The results from one experiment are required to interpret the data of the other experiment. This complementary nature of the experiments will be illustrated throughout this chapter and is a significant finding of this thesis.

The presentation of results will begin with preliminary data and general features of the transfer processes and proceed to the more detailed extraction of state-to-state energy transfer rates. Occassionally, the discussion of one experiment will be interrupted while some results of the other

experiment are presented. This chapter is divided into four sections: (1) preliminary steady-state results (Section B), (2) lifetime studies (Section C), (3) spectrally-resolved, temporally-resolved data (Section D), and (4) steady-state ro-vibrational transfer results (Section E).

B. Preliminary Steady-State Results

1. Quenching Studies

Electronic quenching is best investigated at relatively high pressures where a thermalized ro-vibrational distribution exists. Under these conditions the total fluorescence is directly proportional to the total B state density regardless of the relative detection efficiencies of the various quantum states. In addition, the effects of predissociation are minimized since the distribution lies mostly in low v'.

Figures 12-14 illustrate the electronic quenching of BrCl(B) by the Cl_2 + BrCl mix after initially populating v_o'=4,5, and 6 in the region of 0.5 - 10 torr total mix pressure. The plots are very linear and follow the expression of equation (36). The ratio of the intercept to the slope establishes the ratio of the electronic quenching rate to the radiative rate. Using a radiative lifetime of 38.7 μs (this radiative lifetime will be established in section IVC) provides the electronic quenching rates as listed in Table II. The quoted errors are based on the standard deviation in three

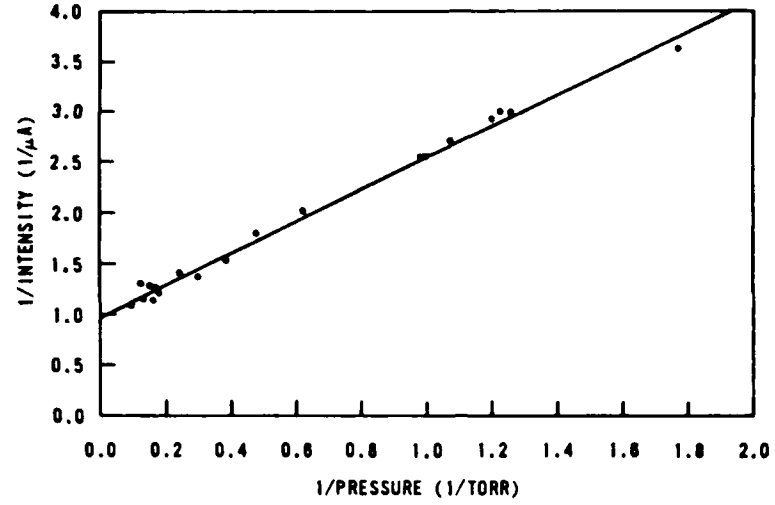

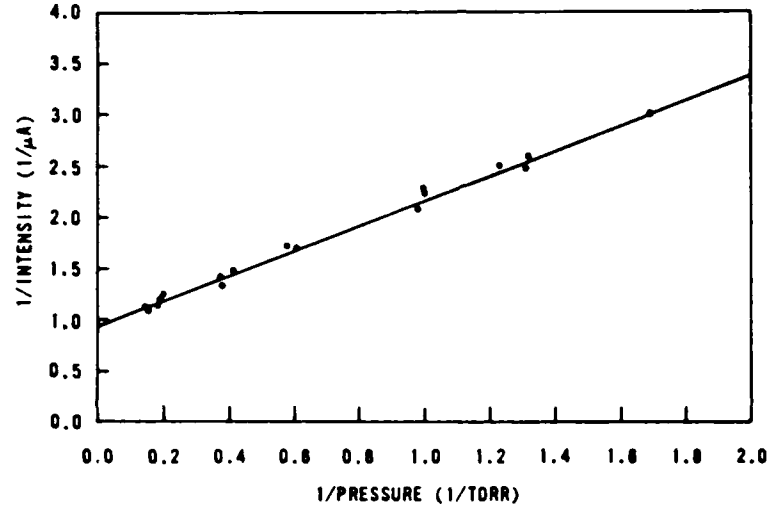

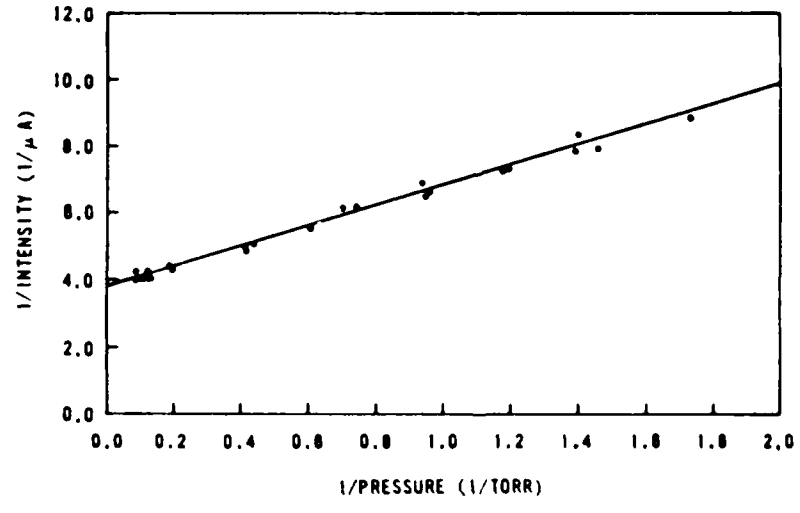

Figures 12-14. CW electronic quenching of BrCl(B) total fluorescence by the mix after initially populating $v_o'=6$ (top), $v_o'=5$ (middle), $v_o'=4$ (bottom). Reported pressures are for the total mix concentration, M.

measurements. The state-averaged value for the electronic quenching of BrCl(B) is k_{eq}^{M}=6.7 +/- 1.1 x 10^{-13} cm^3/molec-s. Clearly, the electronic quenching process is inefficient with respect to gas kinetic collision rates. Due to signal intensity limitations, initially populated states v'<4 were not investigated.

Table II.
Electronic Quenching Rates from CW Experiments

v_o'	k_{eq}^{M} (10^{-13} cm^3/molec-s)
6	5.1 +/- 1.5
5	6.4 +/- 0.7
4	8.4 +/- 1.2

The proof that a thermal distribution exists for the conditions of figures 12-14 requires the analysis of spectrally-resolved data such as shown in figures 19-20. The discussion of section IVC will establish that the BrCl(B) ro-vibrational distribution is nearly thermal for total mix pressures above 1-2 torr. The extraction of electronic quenching rates from pulsed, spectrally unresolved fluorescence lifetime data will also be described in section IVC.

The quenching process is not as simple as the high pressure data indicates. The quenching rate slope of Stern-Volmer plots is strongly dependent on pressure as shown in figure 15. The observed quenching rate rises rapidly as the total pressure is reduced, indicating a secondary removal

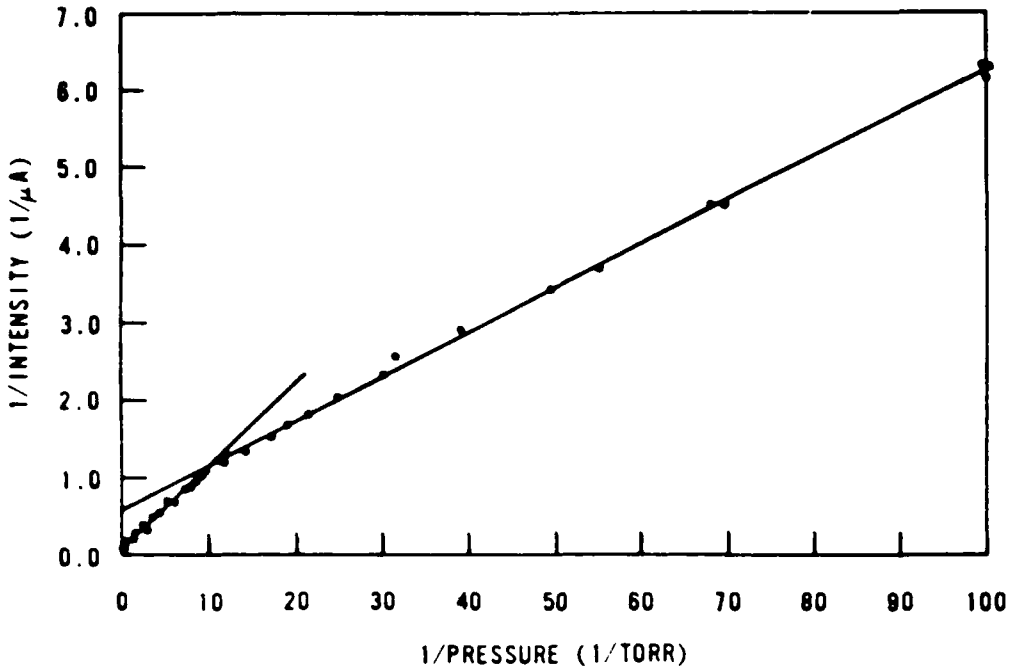

Figure 15. Pressure dependent quenching of BrCl(B) total fluorescence by the mix for initially populated state $v_o' = 5$.

mechanism. The quenching for nonthermal distributions is greater than the electronic quenching of a thermalized distribution. The rates of table II should therefore be considered as upper limits to the electronic quenching rate for a thermalized BrCl(B) distribution. The fact the curves of figures 12-14 are quite linear over an order of magnitude in mix pressures indicates that the quenching rate at these pressures is nearly constant and the approach to a thermal distribution must be nearly complete.

The pressure dependent quenching process is consistent with vibrational ladder climbing to predissociated states as suggested by MA Clyne.[121-123] Predissociation is a non-radiative loss mechanism and population in such states [illegible]

AD-A179 575 COLLISIONAL DYNAMICS OF THE B 3PI(O+) STATE OF BROMINE MONOCHLORIDE(U) AIR FORCE INST OF TECH WRIGHT-PATTERSON AFB OH SCHOOL OF ENGINEERING G P PERRAH AUG 86 2/4

UNCLASSIFIED AFIT/DS/PH/86-1 F/G 7/2 NL

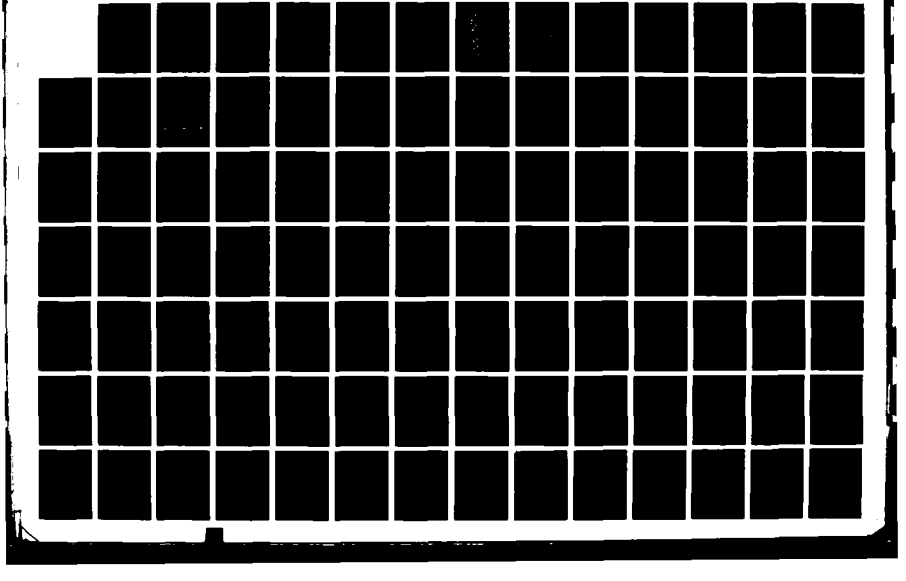

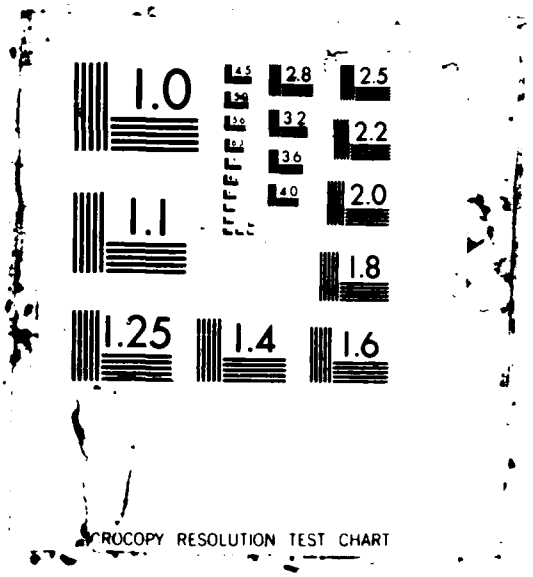
1.0
1.1
1.25
2.8
3.2
3.6
4.0
1.4
2.5
2.2
2.0
1.8
1.6
ROCOPY RESOLUTION TEST CHART

dissociates to two ground state atoms. The rate of transfer to predissociated states depends on the population in high-lying vibrational states and therefore has a unique pressure dependence.

There are other possible explanations for the pressure dependent quenching, but the removal mechanism must certainly be dependent upon the vibrational distribution. Similar pressure dependent effects have been observed for the self-quenching of $Br_2(B)$.[75-77,175] In this case, the collisionless lifetimes are rotational state dependent due to rotational predissociation. The quenching rate for $Br_2(B)$ thus depends on the rotational distribution and has a unique pressure dependence.

The quenching of total fluorescence at very low pressures after initially populating a high-lying vibrational state ($v'=5,6$) provides information regarding the rates for total quenching, k_Q. Single-collision, ro-vibrational transfer to predissociated states is described by the rate constants $k_V^M(p_o-q_{pd})$ where q_{pd} indicates a predissociated state. Since the fluorescence intensity from a predissociated state is greatly reduced, such processes contribute to the quenching of total fluorescence intensity. The rate constant for total fluorescence quenching under single-collision conditions may be written as

$$k_Q^M(p_o) = k_{eq}^M(p_o) + k_{ee}^M(p_o) + \sum_{q_{pd}} k_V^M(p_o \rightarrow q_{pd}) \qquad (87)$$

Figure 16 illustrates the total quenching from $v_o'=6$ at pressures from 0.2 - 10 mtorr and indicates a rate of $k_Q^M(6) = 2.5 \times 10^{-10}$ cm^3/molec-s, a nearly gas kinetic rate. The removal mechanism may be rotational transfer to predissociated rotational states ($J' \geq 42$) within $v'=6$. Resonant electronic exchange reactions (k_{ee}) may also contribute to this rapid rate. The rate for BrCl(B;v') removal varies more than three orders of magnitude for pressures in the range of 1 mtorr to 1 torr. Clearly, it is essential to identify this pressure dependent quenching mechanism. Unraveling the quenching process will depend on the analysis of the pulsed experiments presented in sections IVC-D.

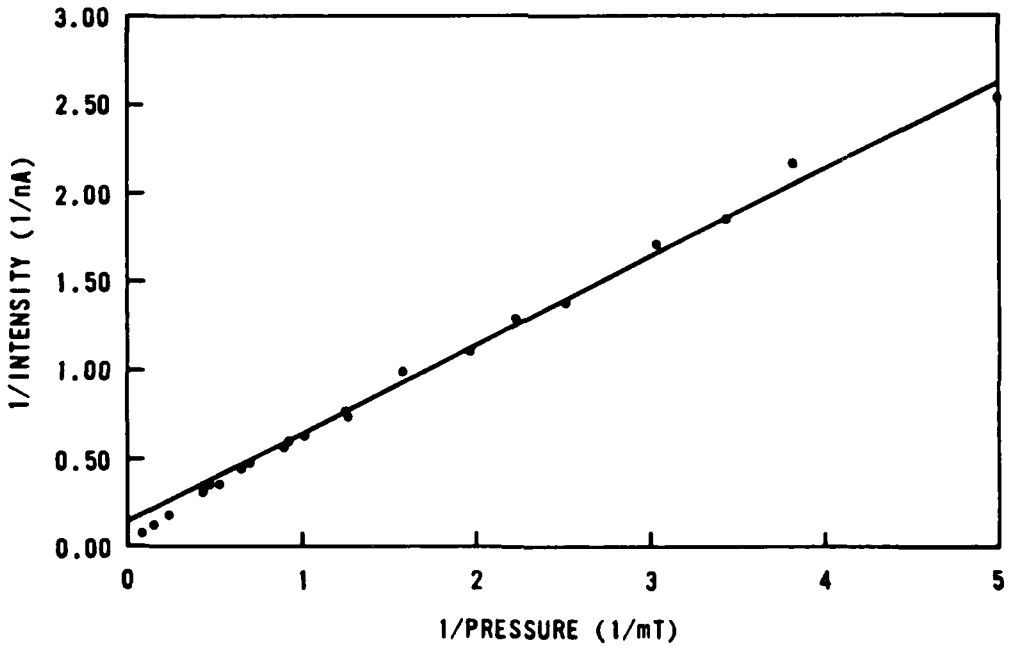

Figure 16. Total quenching of BrCl(B;v'=6) by the mix. Total fluorescence is monitored after pumping $v_o'=6$.

It is difficult to measure the self-transfer total quenching rates under the single-collision conditions of the CW experiments. The rate depends on both the intercept and slope of plots similar to figure 16. The intercepts are very small and sensitive to small errors in pressure and fluorescence intensity measurements. Uncertainties in measured intensities and pressures are magnified since the reciprocals of these quantities are plotted. Pulsed experiments are required to accurately measure these very low pressure total removal rates.

Quenching due to buffer gases can be more accurately obtained. The buffer gas quenching rate is obtained directly from the slope of a plot based on equation (38) and is independent of the plot intercept. Total quenching with helium as the buffer gas for $v_o'=6$ and 5 are shown in figures 17 and 18. The rate constants obtained from equation (38) are $k_Q^{He}(6) = 1.25 \times 10^{-11}$ cm^3/molec-s and $k_Q^{He}(5) = 3.2 \times 10^{-12}$ cm^3/molec-s. The denominator of equation (38) was evaluated from the pulsed lifetime measurements of section IVC. The fast removal from $v_o'=6$ is consistent with rotational transfer to predissociated J levels within $v'=6$. The somewhat slower removal from $v'=5$ is consistent with vibrational ladder climbing to predissociated states. If predissociation is responsible for the removal mechanism, the V,R-T transfer rates must be rapid, approximately 10^{-11} cm^3/molec-s.

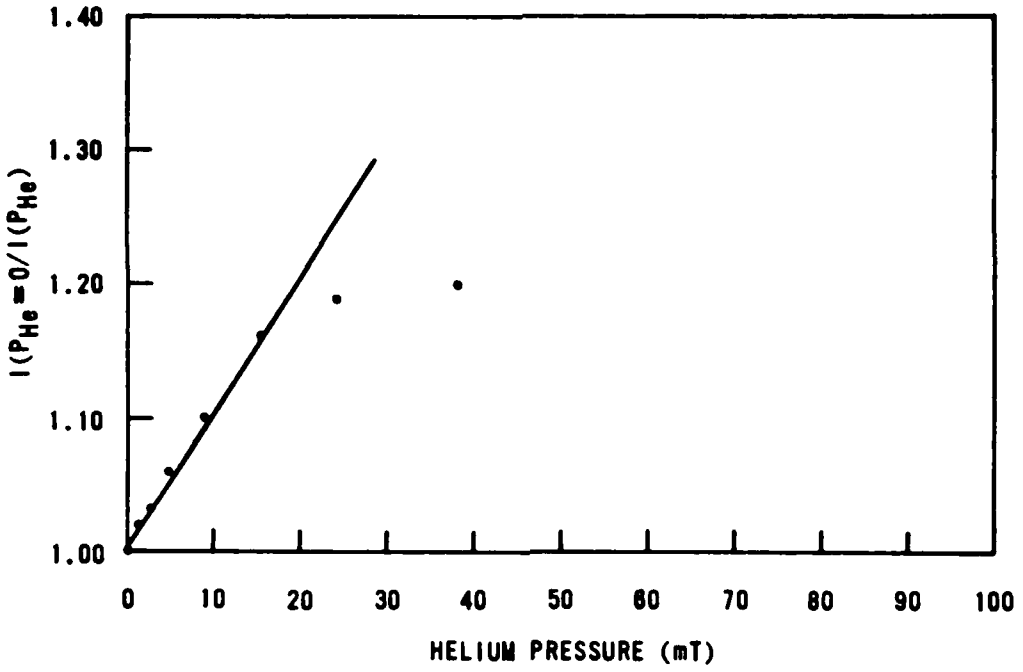

Figure 17. Total CW quenching of BrCl(B;v'=6) by helium.

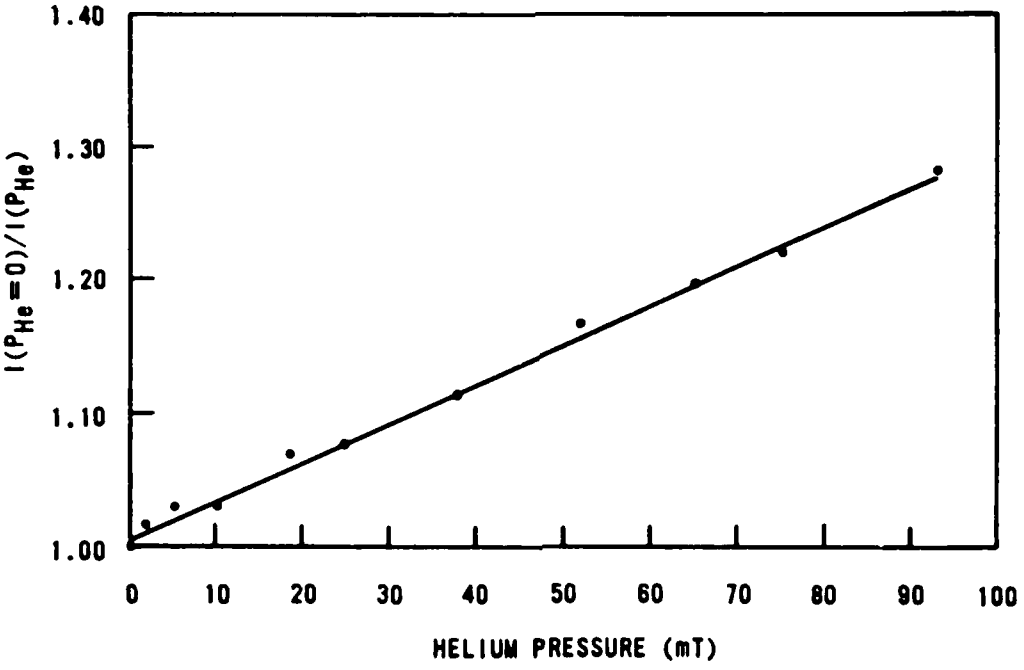

Figure 18. Total CW quenching of BrCl(B;v'=5) by helium.

The determination of the mechanism for quenching requires the data from the pulsed experiments. Before discussing these experiments, the general features of the steady-state spectrally-resolved data will be presented.

2. Spectrally-Resolved Data

A great enhancement in spectral resolution at low pressures over previously observed BrCl(B) CW LIF vibrational transfer spectra[119] has been achieved in the steady-state experimental apparatus described in section IIIA. Full scans of emission wavelenghts (900 nm - 550 nm) after pumping $v_o' = 6$, $J_o' = 37$, for mix pressures of 1 torr and 50 mtorr are shown in figures 19-20. The ring dye laser is operated at a fixed frequency while the emission from the BrCl(B;v') sample is resolved with the scanning monochromator (see Section III).

The strongest transitions in the 1 torr spectrum of figures 19-20 originate from v'=0-2. In addition, the rotational structure appears roughly thermal and well formed vibrational bands are apparent. Clearly, the V,R-T transfer rates must be rapid to obtain these distributions at the relatively low pressure of 1 torr.

The lower pressure scan (50 mtorr) indicates many transitions from all the stable vibrational levels of BrCl(B). Note that no interferrence from Br_2 emission is observed.

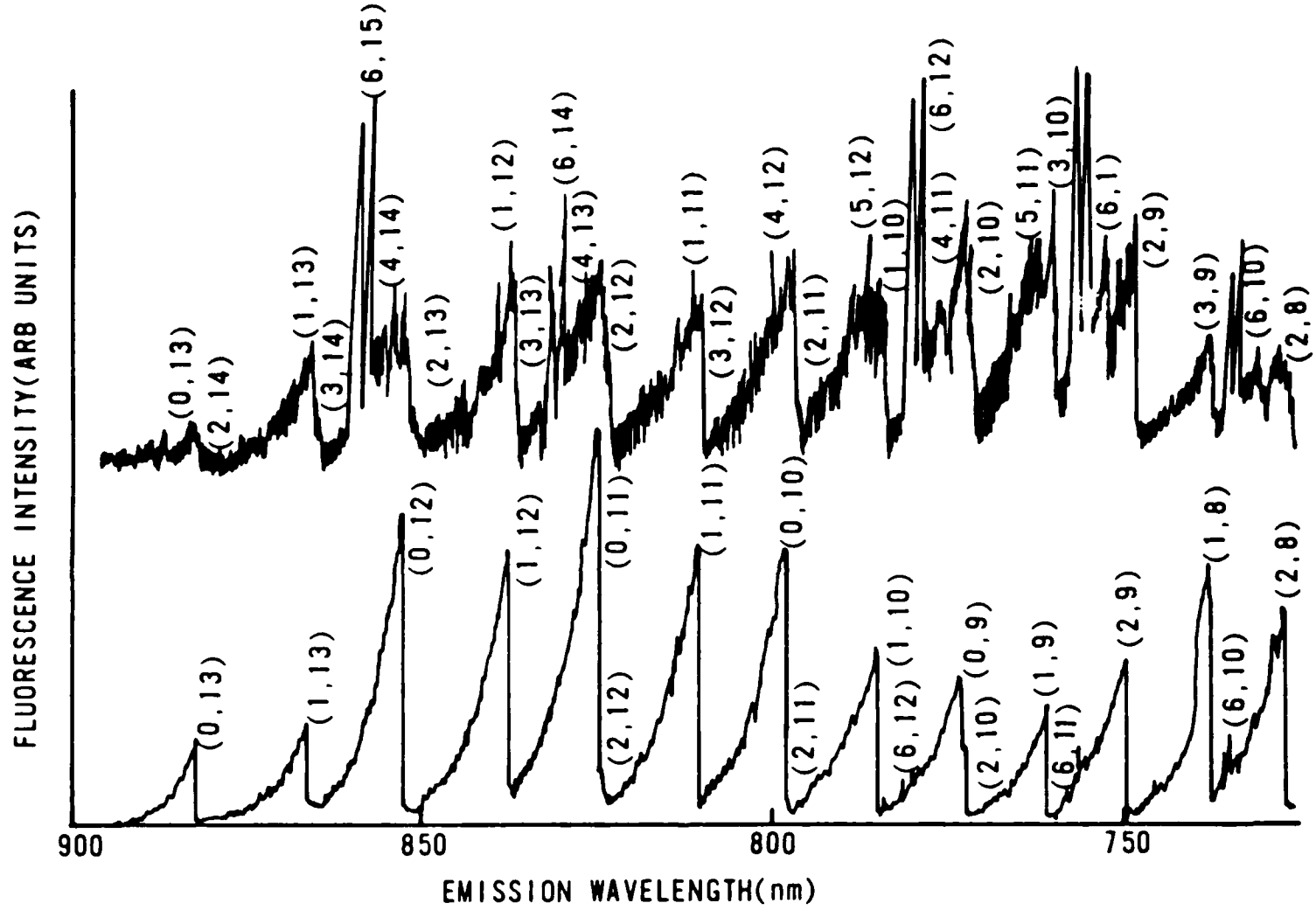

Figure 19. CW LIF emission spectra of BrCl(B;v'). Individual (v',v") vibrational band heads are indicated. The top scan is for a total pressure of 50 mtorr and the bottom scan is for 1 torr. The large spikes particularly evident in the 50 mtorr spectrum are due to the doublet emission from the single, initially populated rotational state. This figure is continued in figure 20.

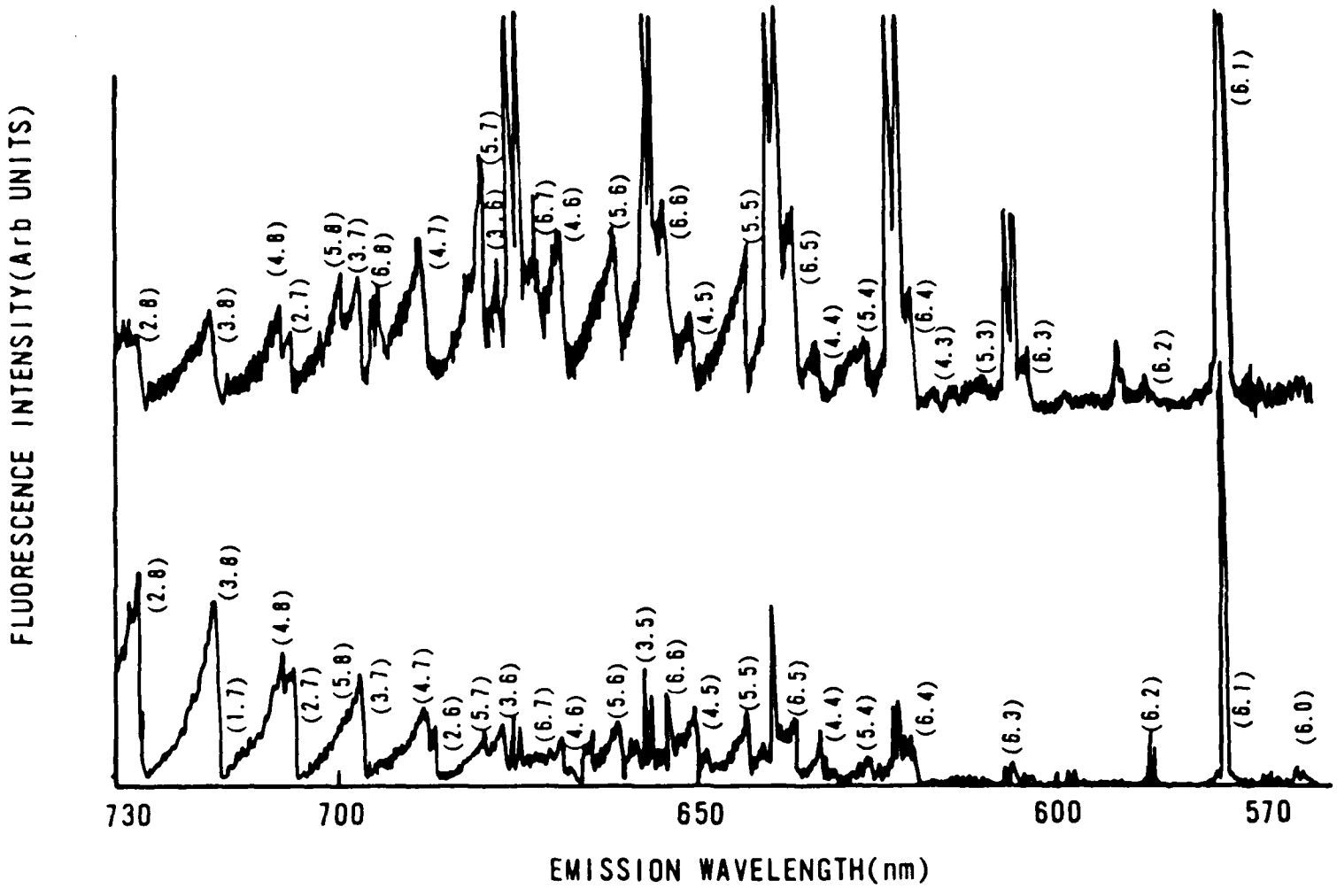

Figure 20. CW LIF emission spectra of BrCl(B;v').
Continued from figure 19.

The rotational structure of $v_o'=6$ is clearly not thermal. Note that the emission from BrCl(B) is widely dispersed with emission from high v' greater at short wavelengths and from low v' greater at long wavelengths. About 60% of the emission is beyond 900 nm and thus is unobservable in the present work.

The higher resolution scans of figures 21-22 provide detailed information on state-to-state vibrational transfer and total rotational removal rates. In figure 21, $v_o'=5$ is initially-populated at a total mix pressure of 73 mtorr. Band heads for emission from v'=3,4,5, and 6 are indicated. The emission from $v_o'=5$ to v"=6 (5,6) is termed the parent band since it arises from the initially populated state. A significant population is observed in the satellite bands (v'=3,4 and 6) indicating rapid vibrational transfer rates.

The double spike in the parent band is the emission from the single, initially populated rotational state, $J_o'= 39$. This doublet is the typical P- and R-branch emission structure for the B-X system of the halogens and interhalogens. The satellite vibrational levels show no obvious memory of the enhanced population in $J_o'= 39$, indicating a high probability for large rotational quantum jumps in V,R-T collisions.

The emission at the very low pressure of 2 mtorr after pumping $v_o'=6$ is shown in figure 22 and indicates very little vibrational or rotational transfer. Almost all the population is in the parent $v_o'=6$, $J_o'= 37$ state. This spectrum almost

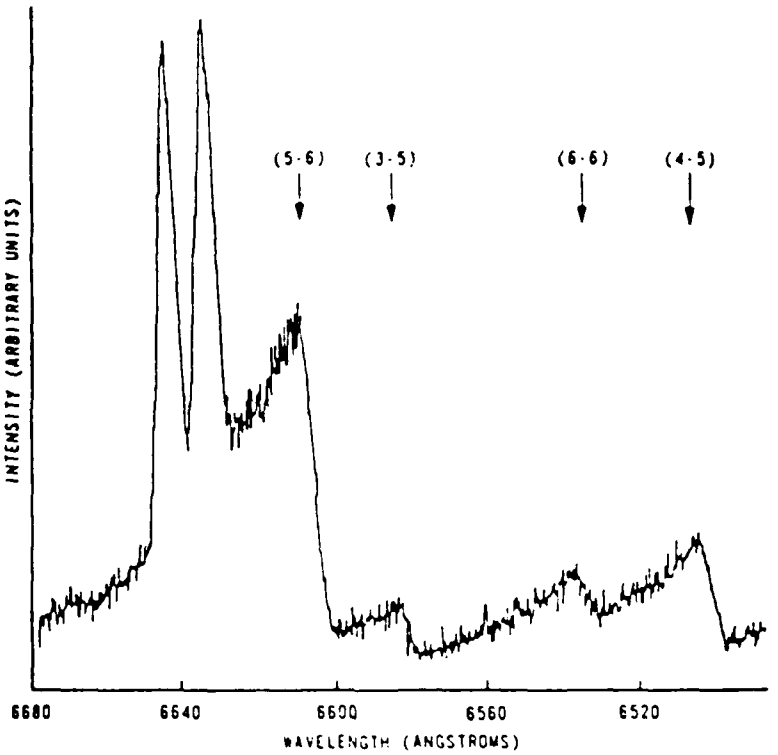

Figure 21. Typical high resolution CW LIF emission spectrum.

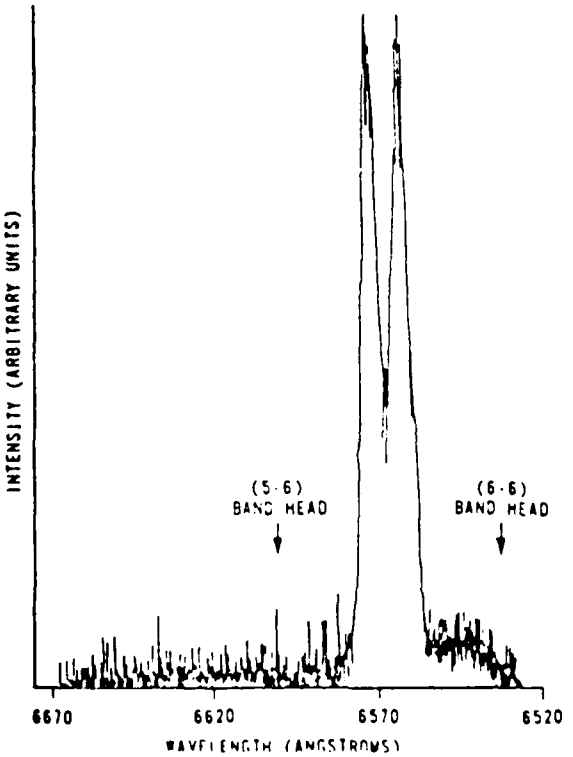

Figure 22. Low pressure CW LIF spectrum.

certainly represents single collision conditions for vibrational transfer. The relative population in the satellite state v′=5 is given by equation (6)

$$[N(5)/N(6)] = [A(5)/A(6)](q_{6,6}/q_{5,6})[D(v=6)/D(v=5)] * (\nu_{6,6}/\nu_{5,6})^4 \quad (6)$$

where

$A(v') =$ the area of the v′ emission band

$q_{v'v''} =$ the Franck-Condon Factor for v′ to v″

$D(v') =$ relative detection efficiency for band v′

$\nu_{v',v''} =$ transition frequency for v′ to v″

Equation (6) establishes the relative number density for the spectra of figure 22 as $[N(5)/N(6)] = 0.099$.

Based on the single collision analysis of equation (46), the state-to-state rate constant for vibrational transfer from v′=6 to v′=5 can be estimated as

$$k_V^M(6-5) = [N(5)/N(6)](1/M)[1/\tau(v=6)]_{2mT} \quad (88)$$

Using the lifetime $\tau(v=6)_{2mT} = 20$ μs from section IVC, the rate constant is estimated as $k_V^M(6-5)=5.6\times10^{-11}$ cm^3/molec-s. This simple example is presented to indicate that the vibrational transfer rates are very rapid. This is consistent with the nearly thermalized distribution at 1 torr in figures 8-9.

The analysis of equation (43) can be used to relate observed relative number densities to the total pressure and extract state-to-state vibrational transfer rates and total rotational removal rates from data similar to that shown in figures 21-22. However, the basic time scale for the energy transfer events, or the denominator of equation (43), cannot be established by the CW analysis. This time scale depends on the quenching mechanism. The extraction of vibrational and rotational rate constants from the CW data will be delayed until section IVE.

3. Rotational Spectra

Figure 23 illustrates the rotationally resolved $v'=0$ to $v''=12$ emission band after initially populating $v_o'=6$ at 15 torr total mix pressure. The resolution appears particularly good due to a near overlap of P(J) and R(J+6) lines.

The Boltzmann distribution for a thermal population among rotational states, J, is given by[163]

$$N(J)/N_T = (hcB_{v'}/k_BT_R)(2J+1)\exp[-B_{v'}J(J+1)hc/k_BT_R] \quad (89)$$

where

$N(J)$ = the population in rotational state J

N_T = the population in all rotational states within v

J = the rotational state quantum number

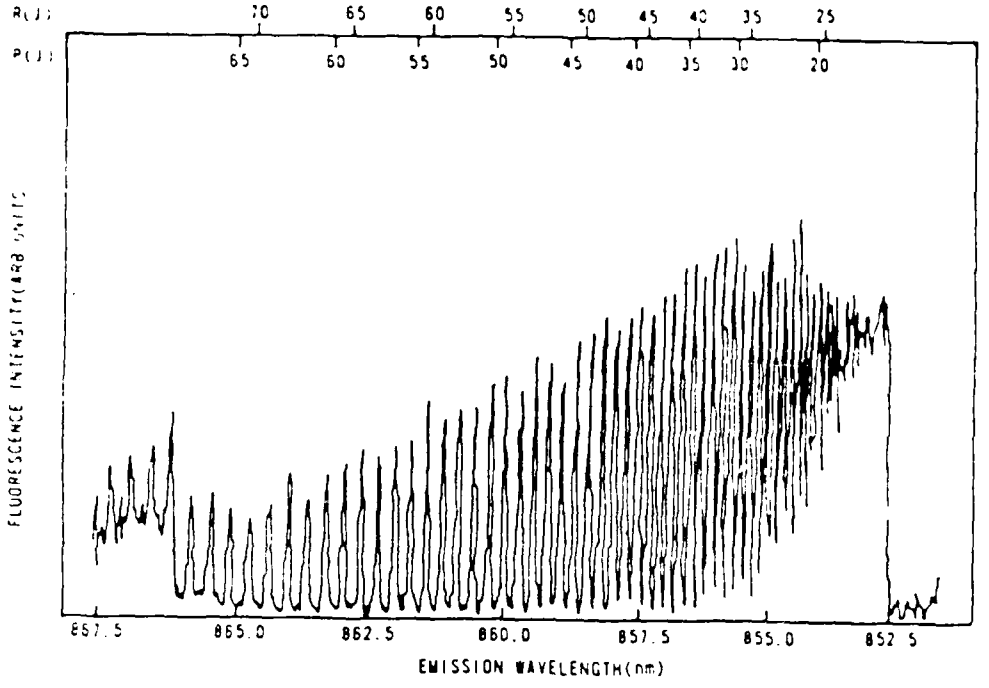

Figure 23. Rotationally-resolved CW LIF emission spectrum.

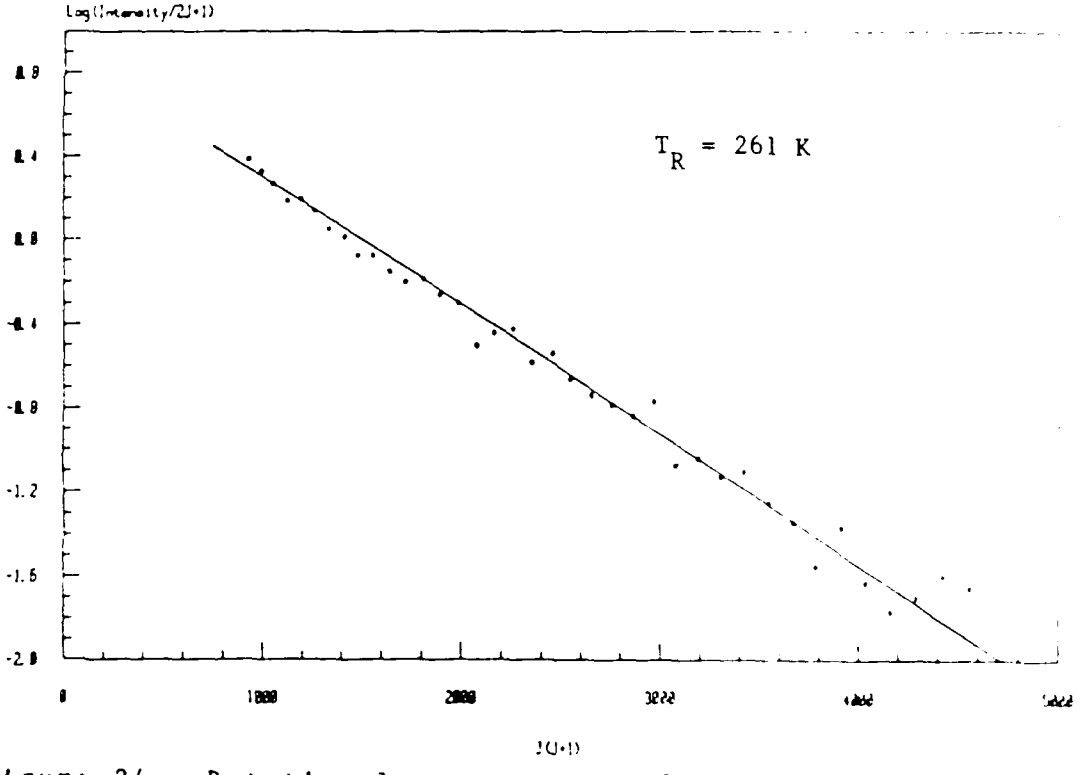

Figure 24. Rotational temperature of $v''=0$ for initially populated state $v_o'=6$ at a total mix pressure of 15 torr.

and

$B_{v'}$ = rotational spectroscopic term value for state v'

h = Planck's constant

c = speed of light

k_B = Boltzmann constant

T_R = rotational temperature

Fluorescence intensity (I_J) is proportional to the number density and thus,

$$\ln (I_J/2J+1) = C - (B_{v'}hc/k_B T_R)\, J(J+1) \qquad (90)$$

where C is an arbitrary constant. The slope of a plot of $\ln (I_J/2J+1)$ versus J(J+1) provides the rotational temperature. Such a plot is given in figure 24 and the resulting rotational temperature is 261 +/- 11 K. Under these conditions, BrCl(B,v'=0) is rotationally in equilibrium with the heat bath.

The plot of figure 24 is limited to J'>30 since the spectral resolution is poor near the band head. Relative fluorescence intensities were obtained from the peak heights of the rotational features in figure 24. The rotational temperature measurement is only approximate since the spectral features are due to the convolved population of J' and J'+4 states.

Signal intensity does not allow for the same degree of spectral resolution at lower pressures. Some information is

available from rotationally convolved spectra, however. A computer model has been developed to predict convolved emission from a set of states observed under finite resolution. This model is presented in detail in appendix G. By comparing the computer predicted and experimentally observed spectra, approximate values for rotational temperature can be extracted. Figure 25 shows a comparison of the observed data and predicted spectra for initially populating $v_o'=6$, $J_o'=37$ at 30.8 mtorr. The continuous, solid line running through the experimental data is the predicted convolved spectra. The agreement is good except on the tale of the $v'=6$ band. The descrepancy is do to a small population in $v'=3$ excluded from the computer model. The stick spectra in the figure 25 indicates the emission spectra under infinite resolution. Note the rotational predissociation that occurs for $J'>41$ in the $v'=6$ band at approximately 657 nm.

The thermal portion of the parent band, $v_o'=6$ ($J \neq J_o$), has a modeled temperature of 1000 K. The modeled temperature of the satellite $v'=5$ band is 500 K. The elevated temperature in the satellite band may be a result of a slight rotational memory of the initially populated rotational state, $J_o'= 37$. The maximum population for a distribution at 300 K is at $J'=32$.

One additional preliminary observation from the CW experiment is important to the interpretation of the pulsed experiments. The quenching of total fluorescence by helium

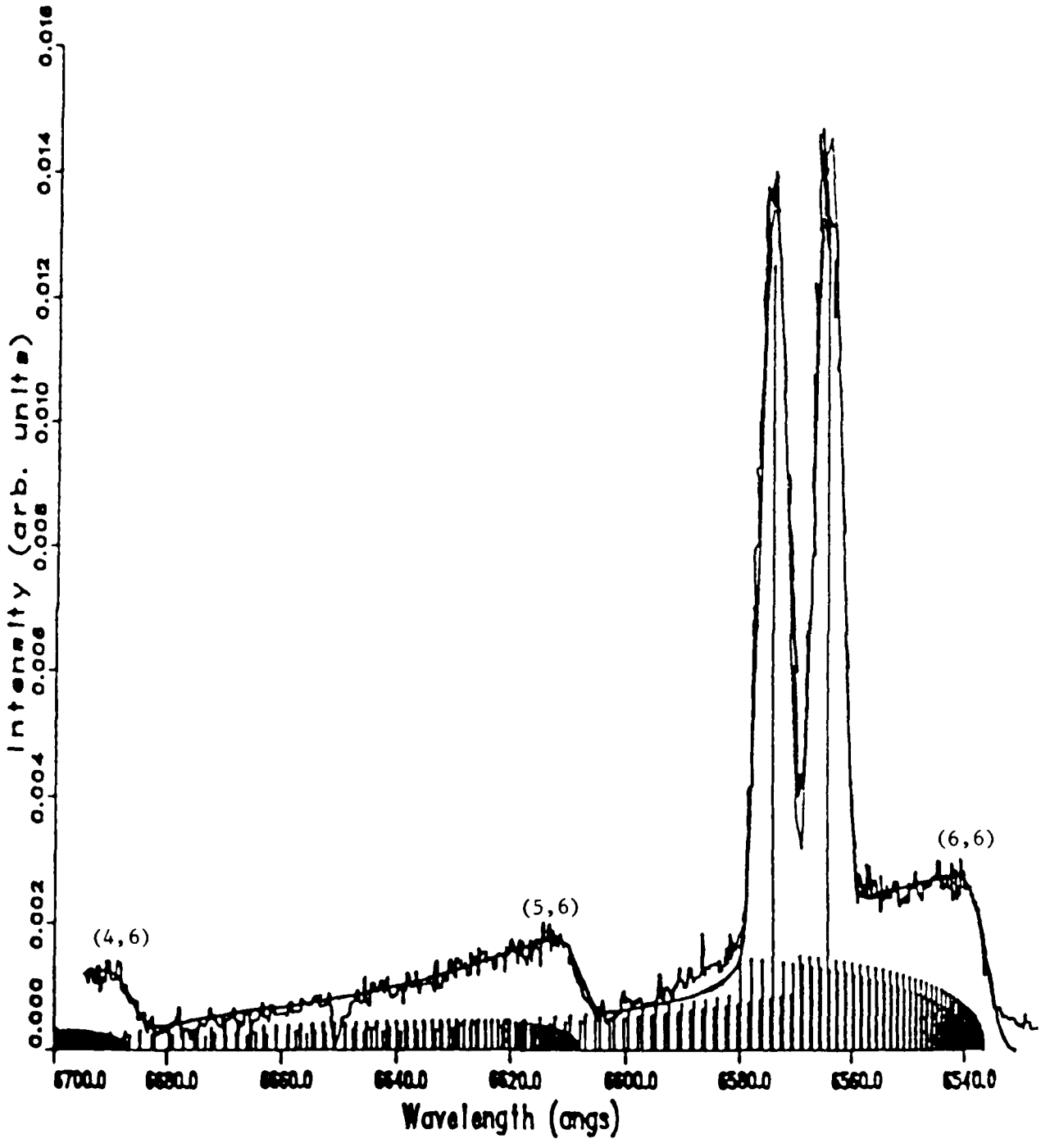

Figure 25. Simulated and observed CW LIF emission spectra.

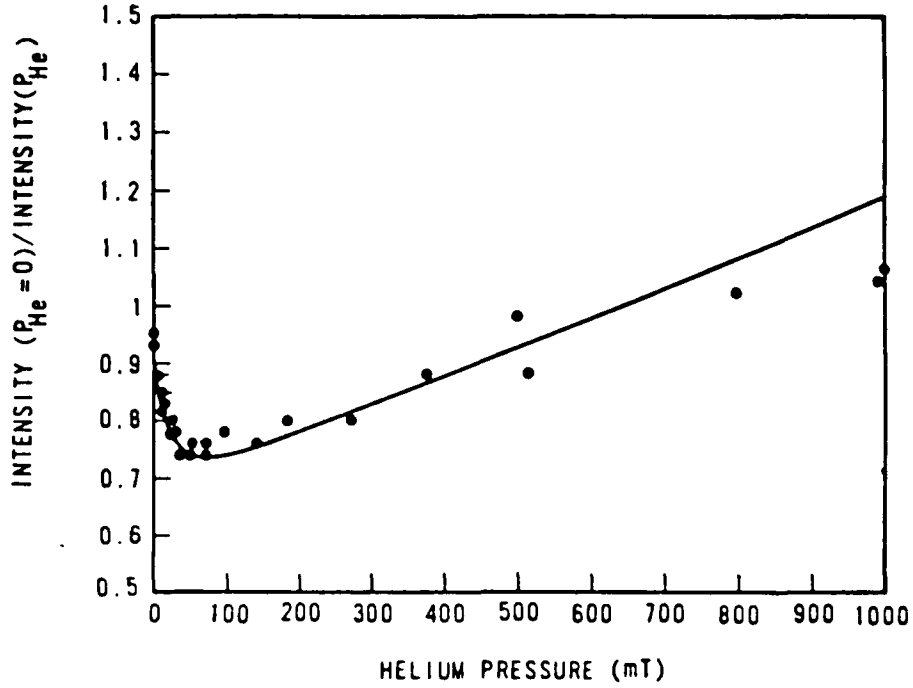

Figure 26. Quenching of BrCl(B) for initially-populating the predissociated state J_o'=44 in v_o'=6, indicating stabilization of the predissociated population. Mix pressure is 6.6 mT.

after initially populating a predissociated rotational state, J_o'= 44 in v_o'=6 is shown in figure 26. For added helium pressures less that 100 mtorr, the fluorescence intensity increases. Rotational transfer to stable states ($J'<42$) and the subsequent fluorescence from these states enhances the emission intensity. The solid curve in figure 26 is the calculated intensity including this stabilization effect and will be discussed further in appendix F. The important conclusion to be drawn from this data is that predissociated states are not completely unstable and V,R-T transfer from predissociated states to stable states plays an important role in BrCl(B) energy transfer processes.

4. Summary of Preliminary Conclusions

Electronic quenching from the thermalized BrCl(B) distribution is slow (approximetely 10^{-13} cm^3/molec-s). There exists a pressure dependent quenching mechanism with rate constants for removal from BrCl(B) ranging from 10^{-13} cm^3/molec-s to 10^{-10} cm^3/molec-s. This unique pressure dependence indicates a ro-vibrational distribution dependence of the quenching mechanism. Pulsed experiments are needed to identify this quenching mechanism. The thermalization process is rapid with vibrational transfer rates of approximately 10^{-11} cm^3/molec-s. Rotational transfer is very efficient and little or no rotational memory is observed in satellite vibrational bands. V,R-T transfer from predissociated states to stable states is an important stabilization process for the BrCl B state.

C. Lifetime Studies

Excitation spectra, electronic quenching rates, and the rates for total quenching and total removal are readily obtained from the pulsed experiments described in section III. Spectral resolution is not required for the total fluorescence lifetime studies described in this section. State-to-state vibrational transfer studies require the full temporally-resolved, spectrally-resolved experiments and will be described in section IVD.

1. Excitation Spectra

Laser excitation spectra are used to make pump transition assignments and observe the relative total fluorescence after initially populating various v′ states. By scanning the output wavelength of the dye laser and observing the boxcar averaged total fluorescence signal, the excitation spectrum of figure 27 was obtained. Additional excitation spectra covering wavelenghts from 570 nm to 675 nm and vibrational states v′=0-7 are presented in appendix B. The resolution is limited by the linewidth of the pump dye laser and is approximately 0.3 cm^{-1}. Band heads for (v′,v") emission are indicated and the pump wavelengths used to populate various v′ states are given in appendix B.

Note the observation of emission after populating v′=7 in the excitation spectrum of figure 27. The v′=7 state is

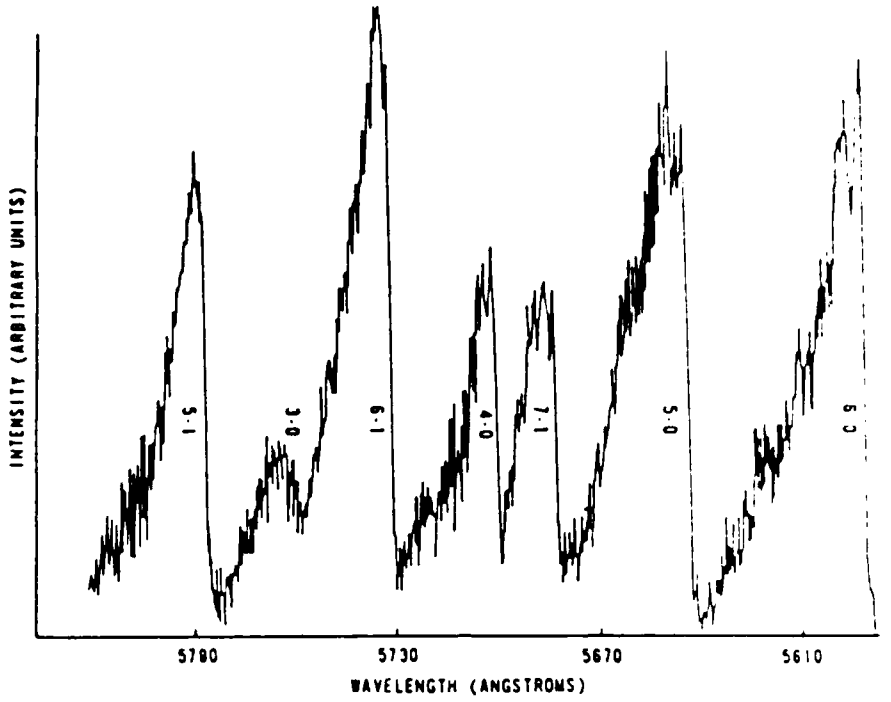

Figure 27. Pulsed excitation spectrum. Total fluorescence is observed as a function of pump laser wavelength at a total mix pressure of 1.5 torr. (v′,v") band heads are indicated for pump transitions. Excitation spectra provide essentially the same information as absorption spectra.

completely predissociated with collisionless lifetimes less than 1 μs. The observed fluorescence intensity does not originate from v′=7, but rather from the stable states of BrCl(B), v′<6. This observation provides further evidence for the collisional stabilization of predissociated distributions.

2. Electronic Quenching

Electronic quenching rates are measured in the pulsed experiment using the Stern-Volmer analysis of section IIC4. The decay of total fluorescence establishes the BrCl(B)

lifetime at a given pressure (see equation (72)). The variation of this lifetime with pressure yields the electronic quenching rate from equation (71). A typical total fluorescence decay curve is shown in figure 28. The upper, linear curve is the logarithm of the lower, fluorescence decay curve and demonstrates that the fluorescence decays as a single exponential. Decay curves were typically observed for time intervals greater than three collisional lifetimes. For experimental conditions where a thermalized distribution is not rapidly attained and the fluorescence is due to the population of many vibrational states, the decay is not a simple single exponential. However, at "long times" the distribution does become thermal and the decay is exponential.

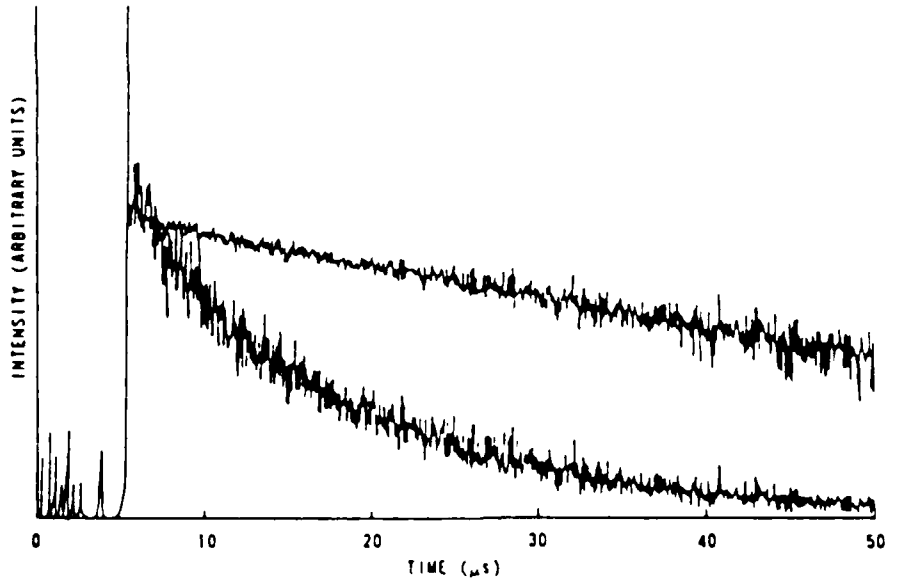

Figure 28. Typical total fluorescence decay curve. Total fluorescence is observed after initially populating $v' = 5$ at 2 torr total mix pressure. In this spectra a C31034 PMT with a 750 nm long pass filter has been used to detect the fluorescence.

These "long time", thermal distribution fluorescence decays were used to obtain the lifetimes for the electronic quenching rates.

Several Stern-Volmer plots for electronic quenching are given in figures 29 and 30. Note that the electronic quenching rates have been observed for a wide range of conditions including many different pumped vibrational states. The average resulting rate constant is $k_{eq}^{M} = 4.3 +/- 0.7 \times 10^{-13}$ cm^3/molec-s. The quoted rate constant and error is based on the average and standard deviation in twelve rate measurements. A complete description of the error analysis may be found in Appendix H. This rate agrees favorably with the rates measured by Wright et. al.[119] (3.4×10^{-13} cm^3/molec-s) and by Clyne and McDermid[121] (3.9×10^{-13} cm^3/molec-s). The different symbols in figure 29 indicate various conditions under which the electronic quenching rate has been measured. In some cases, the decay of spectrally-resolved emission has been used. It is important to note that even $v'=3$ decays at long times as predicted by the electronic quenching rate for pressures as low as several torr. This indicates that $v'=3$ rapidly attains a thermal distribution with $v'=0$ and is consistent with the thermal distributions observed in figures 19-20. In addition, the quenching for $v'<3$ must be roughly independent of vibrational state.

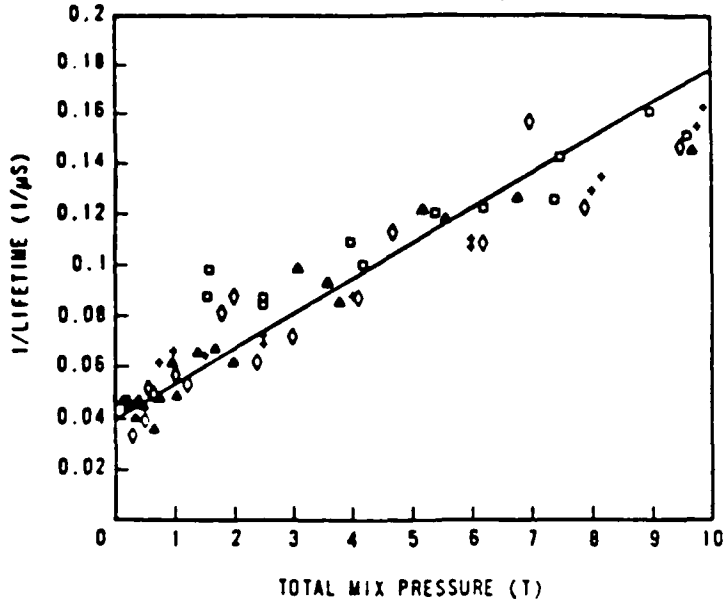

Figure 29a. Stern-Volmer plot for electronic quenching of BrCl(B) by the mix. Initially populated states and observed states are: (□) $v_o'=1$, $v'=1$, (◊) $v_o'=6$, $v'=0$, (+) $v_o'=2$, $v'=2$, (Δ) $v_o'=6$, $v'=1$.

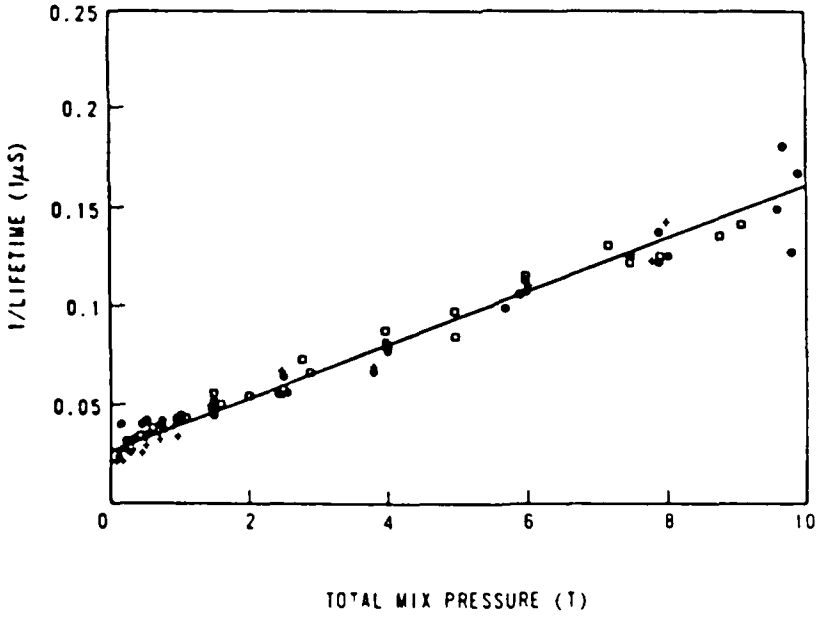

Figure 29b. Stern-Volmer plot for electronic quenching of BrCl(B) by the mix. Total fluorescence is observed with the C31034 PMT and 600 nm long pass filter. Initially populated states are: (+) $v_o'=0$, (□) $v_o'=1$, and (●) $v_o'=2$.

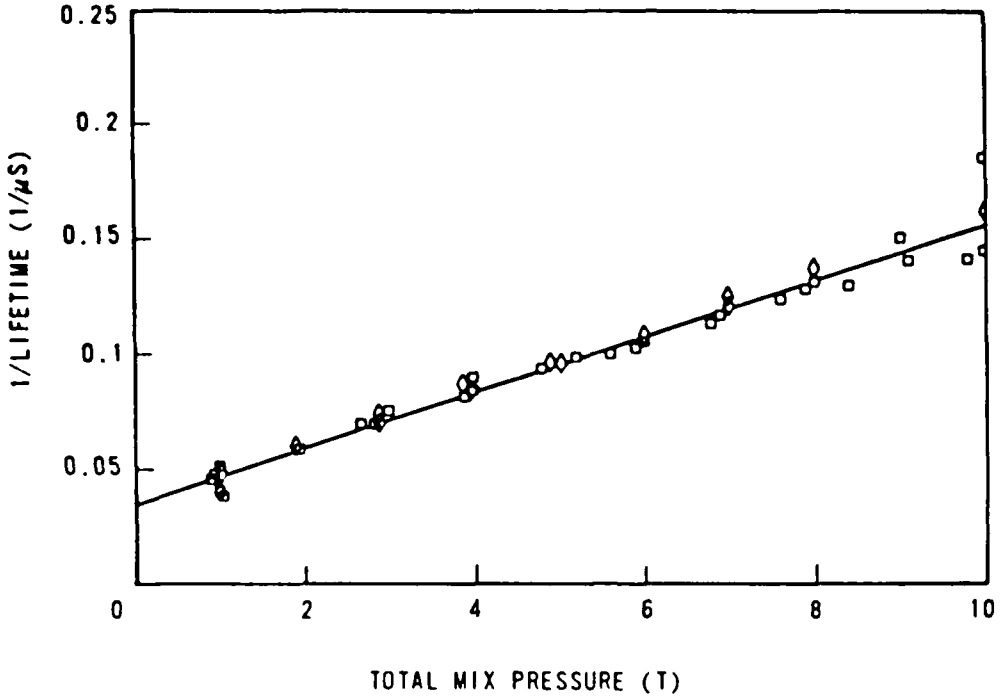

Figure 30a. Stern-Volmer plot for electronic quenching of BrCl(B) by the mix. Total fluoresence is observed with the C31034 PMT and 750 nm band pass filter. Initially pumped states are: (□) $v_o'=6$, (◊) $v_o'=5$.

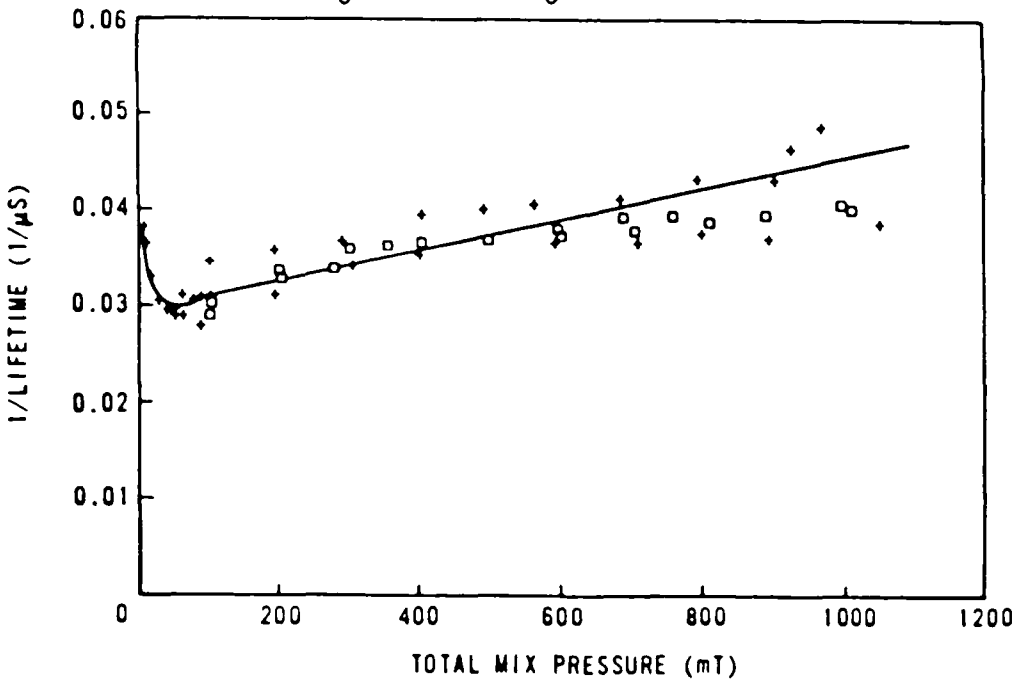

Figure 30b. Stern-Volmer plot for electronic quenching of BrCl(B) by the mix. Total fluorescence was observed with the C31034 PMT and a 750 nm long pass filter. Initially populated states are: (+) $v_o'=6$, (□) $v_o'=5$.

The electronic quenching rate obtained from these pulsed lifetimes applies to the thermalized BrCl(B) distribution, as shown in figure 31. The relative populations $N(v'=1)/N(v'=0)$ are obtained from the data of figures 19-20 and similar data using the equation (6). The intensity of the $v'=0$ to $v''=12$ and $v'=1$ to $v''=11$ transitions is used to establish the relative populations. Figure 31 illustrates the variation of this relative population as a function of total mix pressure. The population ratio for a Maxwell-Boltzmann thermal distribution at 300 K would be $N(1)/N(0)=\exp(-\Delta\varepsilon_{1,0}/k_BT)=0.36$. This thermal distribution is attained for mix pressures greater than approximately 2 torr.

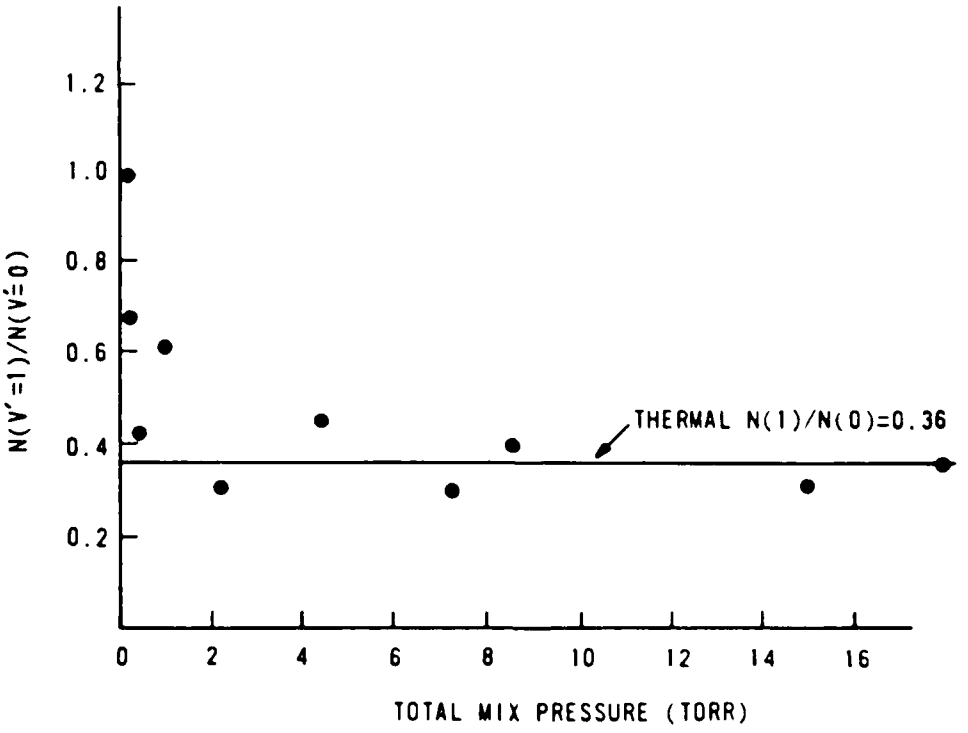

Figure 31. Steady-state vibrational populations indicating a thermal distribution for pressures above about 2 torr.

Of course, there is some transient period before this thermal distribution is attained. The pulsed lifetime data show this transient period as a bend in the logarithm of the total fluorescence decay curves. By establishing the lifetimes at "long times", this transient period is neglected. In this sense, the pulsed lifetime measurements apply only to thermalized distributions.

The Stern-Volmer plots of figure 30 support the thermalized electronic quenching rate just described. The total fluorescence lifetimes of this figure were measured with a 750 nm long pass filter in front of a C31034 PMT. As shown in appendix C, this filter limits the fluorescence primarily to $v'<3$. The electronic quenching rate constant obtained from figure 30 is 3.6 +/- 0.4 x 10^{-13} cm^3/molec-s and is consistent with the above reported rate. The quoted error in this rate constant is based on the standard deviation in three measurements and is described in further detail in Appendix H. Note that the plot of figure 30b is linear to pressures as low as 50 mtorr and the electronic quenching constant remains at 3.6 +/- 0.7 cm^3/molec-s. At these low pressures the distribution is highly nonthermal. Thus, the lowest vibrational states ($v'<3$) decay with the electronic quenching rate regardless of vibrational distribution, indicating the quenching rate for these states is independent of vibrational state.

At mix pressure below 50 mtorr, the lifetimes in figure 30b decrease as the pressure is further reduced. Under these conditions very little population exists in $v'<3$ and the weak fluorescence from $v'>3$ dominates the decay curve. The quenching from these higher lying states is more rapid than the electronic quenching and thus the lifetimes decrease.

The pulsed electronic quenching rate for a thermalized distribution, $k_{eq}^{M} = 4.3 +/- 0.7 \times 10^{-13}$ cm^3/molec-s, is slightly less than the same rate obtained from the CW experiment ($6.7 +/- 1.1 \times 10^{-13}$ cm^3/mole-s). The CW experiment is more susceptible to the effects of a nonthermal distribution and the CW electronic quenching rate is slightly affected by the greater removal from states $v'>3$. Most of the data points in the CW plot of figures 12-14 are for pressures less than 2 torr where a slight deviation from a thermalized distribution exists. In addition, the reciprocal of the pressure is used as the independent variable and the low pressure data points are more favorably weighted than the high pressure data points. Therefore, the electronic quenching rate is best measured in the pulsed experiments, and the rate coefficient obtained from the CW experiments should be considered an upper limit.

Electronic quenching rates for buffer gases, He, Ne, Ar, Kr, N_2, and O_2 have been determined and the results are listed in table III. The rates are obtained by applying the

Stern-Volmer analysis of equation (71). The quoted errors are the expected uncertanties in the slopes and do not reflect systematic errors. Some representative plots are given in figure 32. All the electronic quenching rates are slow ($\sim 10^{-13}$ cm^3/molec-s) except that of oxygen. The fast O_2 quenching rate may be due to a resonant electronic exchange reaction. Possible products of such a quenching reaction would include BrCl(X), BrCl(A) and BrCl(A'). Oxygen quenching of the interhalogen IF(B) is also anamolously fast and has been attributed to the resonant electronic exchange reaction[69]

$$IF(B) + O_2(X) \longrightarrow IF(A') + O_2(^1\Delta_g) \qquad (91)$$

A similar mechanism may be responsible for the rapid oxygen quenching of BrCl(B).

Table III
Buffer Gas Electronic Quenching Rates

Gas	Rate k_{eq}^Y (10^{-13} cm^3/molec-s)
Cl_2	4.3 +/- 0.7
He^2	1.5 +/- 0.2
Ne	0.78 +/- 0.19
Ar	0.81 +/- 0.30
Kr	0.98 +/- 0.14
N_2	1.6 +/- 0.3
O_2^2	65. +/- 5.7

3.Pressure Dependent Quenching

The pressure dependent quenching observed in the CW experiment is confirmed by the lifetime studies of the pulsed experiment. Figure 33 illustrates Stern-Volmer plots for the

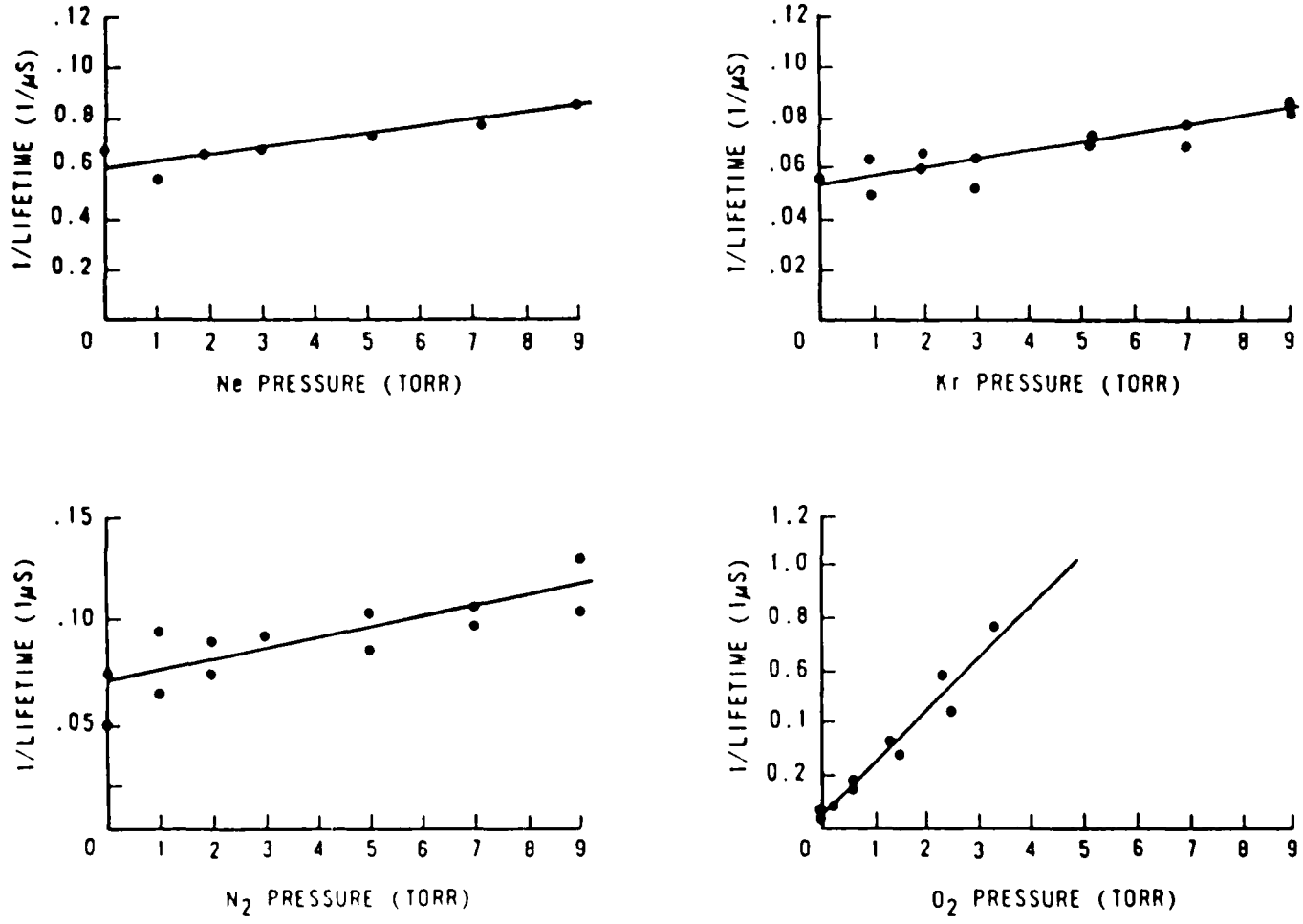

Figure 32. Boffer gas electronic quenching Stern-Volmer plots for (a) He. (b) Kr, (c) N_2 and (d) O_2.

total removal from BrCl(B,v′) after initially populating v_o'=6 for four different spectral response conditions. These Stern-Volmer plots are based on the initial decay of fluorescence at low pressures.

The pressure dependent quenching is most readily observed in the bending of the curve labeled (◊) of figure 33. This pressure dependence is due to a vibrational state dependent removal rate. As the population distribution among vibrational states changes, so does the average removal rate. By observing the removal rate for populations in specific quantum states, the nature of this pressure dependent quenching can be observed.

The curve labeled (○) in figure 33 has a removal rate equal to the mix electronic quenching rate and was obtained from total fluorescence lifetimes using a 750 nm long pass filter. This is the same data as presented in figure 30. The 750 nm filter has the effect of predominately observing states v′<3. Thus, even at very low pressures, the low v′ states decay slowly as defined by the electronic quenching rate. The upper most curve, labeled (□), was obtained by observing the spectrally-resolved emission from v′=6. The total removal from v′=6 is very rapid, $K_R^M(6) = 2.7 \times 10^{-10}$ cm^3/molec-s. This rate includes V,R-T transfer to states v′=6 as well as the total quenching rate. The large magnitude of this rate is

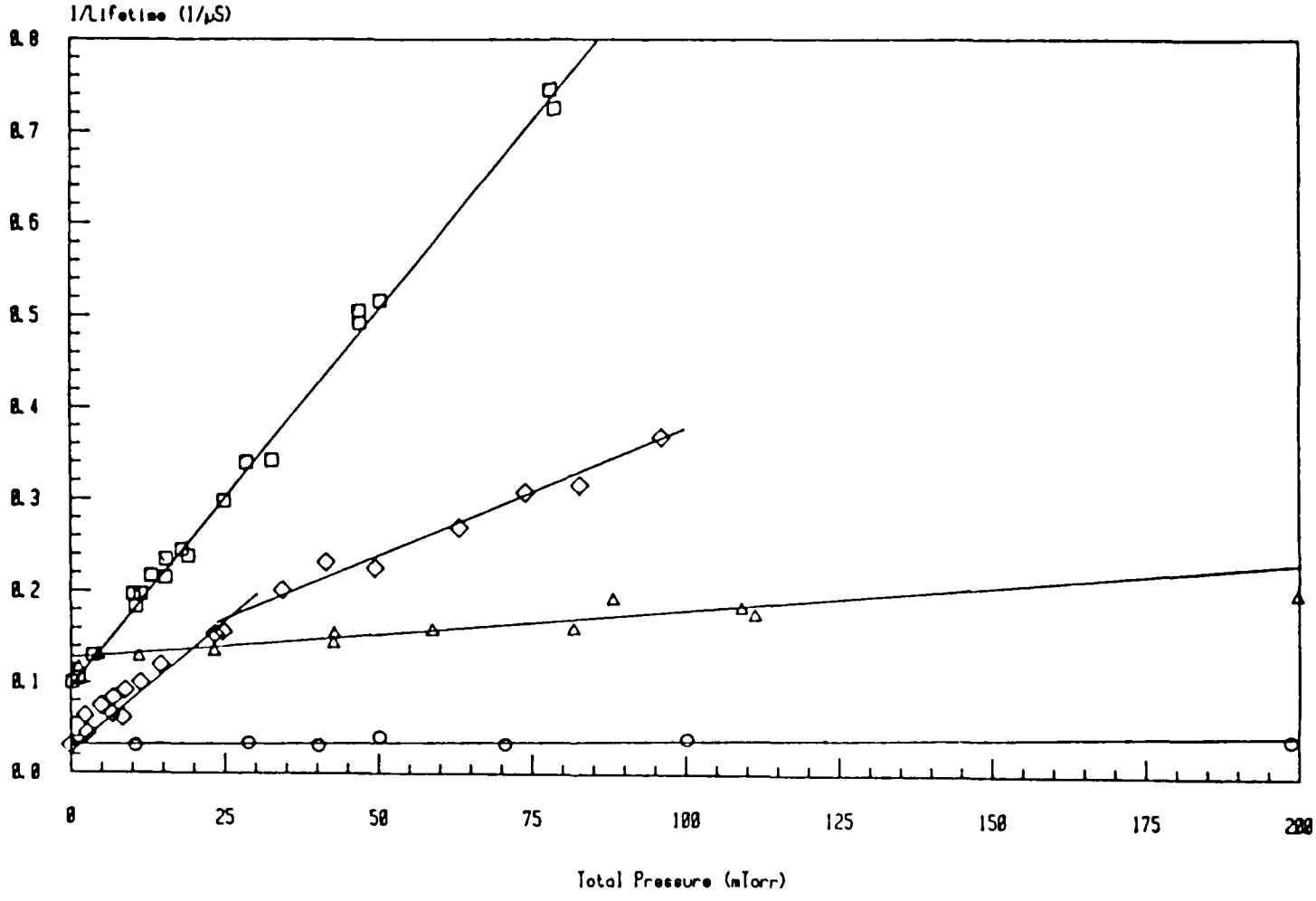

Figure 33. Total quenching Stern-Volmer plots indicating pressure dependent quenching and the importance of spectral response.

due in part to rotational transfer to predissociated rotational levels within $v'=6$.

The two intermediate curves are obtained by observing total fluorescence with a 600 nm long pass filter and an RCA C31034 PMT (Δ) or an EMI 9558QB S-20 PMT ($\diamond$). The total observed fluorescence lifetime depends significantly on the spectral response of the PMT. The relative detection efficiency for each v' state using either PMT is given in appendix C. The C31034 PMT detects $v'<3$ much more efficiently than the S-20 PMT. The two Stern-Volmer plots (Δ,$\diamond$) can then be interpreted as vibrational population distribution weighted convolutions of vibrationally dependent removal rates. The S-20 PMT, detecting high v' most efficiently, more nearly approaches the total removal from $v'=6$ ($\diamond$); whereas the C31034 PMT, with a better detection of low v', more nearly approaches the electronic quenching of $v'<3$ (Δ).

It is clear from these observations that one must be very careful in detailing the spectral response of laser induced fluorescence energy transfer experiments. The interpretation of total fluorescence lifetimes must consider spectral response issues when collisionless lifetimes or total quenching rates depend significantly on quantum state. In such cases, total observed fluorescence is not simply proportional to the total excited state density, but also

depends on the population distribution among ro-vibrational states within the excited electronic state.

4. Total Removal Rates and Radiative Lifetimes

The pressure dependent quenching mechanism is described by distribution dependent total quenching rates. It is therefore important to determine the full vibrational dependence of these quenching rates. In doing so, the radiative lifetimes for the stable vibrational states will also be obtained.

Figures 34-35 illustrate typical total quenching rate Stern-Volmer plots under single-collision and several-collision conditions. The slope of these plots yield the total quenching rate constant from v', $k_Q^M(v')$, and the intercept provides the radiative lifetime of state v', $\tau_R(v')$, as given in equation (74). The gas kinetic collision rate, k_g, for BrCl + Cl_2 collisions is 1.23×10^{-10} cm^3/molec-s and single-collision conditions (defined as one radiative lifetime between collisions) are gauranteed for pressures less than 6.6 mtorr:

$$k_g \, M \, \tau_R = (1.2\times10^{-10})(2.1\times10^{14})(38.7\times10^{-6}) = 1.0 \qquad (92)$$

Thus, plots like that shown in figure 35 meet the single collision requirement for applying equation (74) and obtaining total quenching rates and radiative lifetimes. The resulting rates and radiative lifetimes for are listed in tables IV-V.

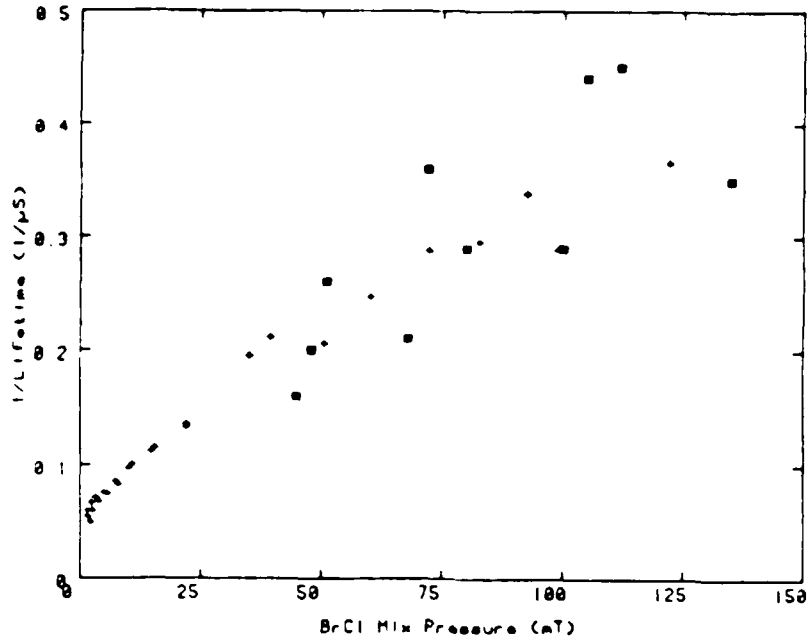

Figure 34. Stern-Volmer plot for total quenching of $Y(B^2\Sigma^+; v'=6)$. (X) Data from current studies, (□) Clyne and McDermid[122] data. Total fluorescence is monitored with C31034 and 600 nm filter.

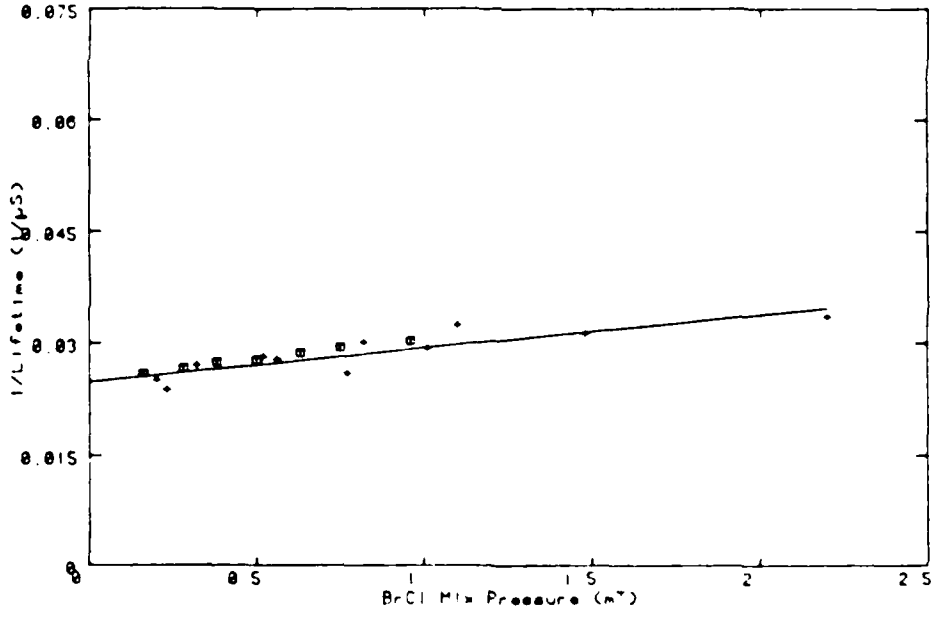

Figure 35. Stern-Volmer plot for total quenching of $BrCl(B;v'=6)$ under low pressure conditions. (+) Data from current studies, (□) Clyne and McDermid data.[122] Total fluorescence is monitored with C31034 and 600 nm filter.

Table IV
BrCl(B) Radiative Lifetimes

v′	Lifetime (10^{-6} sec)
0	40.9 +/- 2.0
1	38.8 +/- 2.6
2	38.0 +/- 1.5
3	**********
4	38.7 +/- 1.4
5	36.8 +/- 1.2
6	40.1 +/- 1.3
Average	38.7 +/- 1.7
Clyne's[121-123]	40.2 +/- 1.8

Table V
BrCl(B) Total Quenching Rate
(1 x 10^{-11} cm^3/molec-s)

v′	$k_Q^M(v')$	Clyne's[121-123] $k_Q^M(v')$
0	0.042 +/- 0.001	0.039 +/- 0.012
1	0.180 +/- 0.070	0.300 +/- 0.020
2	0.270 +/- 0.060	**********
3	0.96 +/- 0.53	0.40 +/- 0.03
4	4.7 +/- 1.4	6.2 +/- 2.3
5	6.2 +/- 1.7	9.6 +/- 2.8
6	14.0 +/- 3.0	21.0 +/- 4.0

These results and the earlier work by Clyne and coworkers[120-123] agree within experimental errors. Indeed, the complete work on BrCl(B) energy transfer by Clyne et al is consistent with the observations of this thesis presented to this point. However, a complete interpretation of these observations awaits the detailed analysis of the spectrally-resolved, temporally-resolved data which follows in section IVD of this thesis.

5. Scaling of Total Removal Rates

The scaling of total quenching rates with vibrational quantum number is exponential as shown in figure 36. The total quenching rates for $v'<3$ were measured for pressures greater than 10-20 mtorr. Data at lower pressures were not obtainable due to low signal intensities. These pressures are in the multiple-collision regime. It has been shown in section IIC4 and Appendix E that observed quenching rates may scale exponentially under multiple collision conditions even for a system where actual quenching rates are independent of v'. This occurs when the vibrational manifold is strongly coupled and a large variation in quenching rates exists. Strong vibrational coupling ($\Delta\varepsilon/k_BT = 1$) and a large variation in quenching rates (10^{-13} to 10^{-10} cm^3/molec-s) has been demonstrated for the case of BrCl(B). Therefore, the experimentally observed scaling for $v'<3$ may not indicate an exponential scaling of quenching rates.

Total quenching rates and their dependence on vibrational state has been measured with helium as the buffer gas under multiple collision conditions. The scaling of these observed rates for He is shown in figure 37 and listed in table VI. Quoted errors are the standard deviation in three measurements. The scaling is identical to the self transfer case. The slope of both plots is $\Delta\varepsilon/kT = 0.4$. Interestingly, this value for the slope is equal to the detailed balance

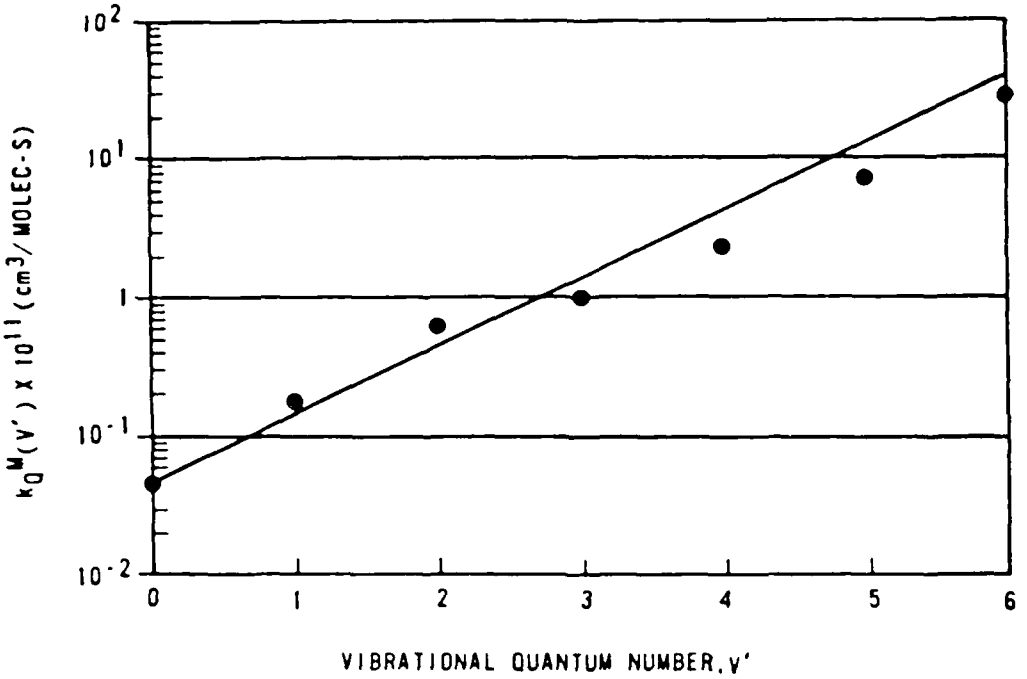

Figure 36. Vibrational scaling of total quenching rate for BrCl(B,v') by the mix.

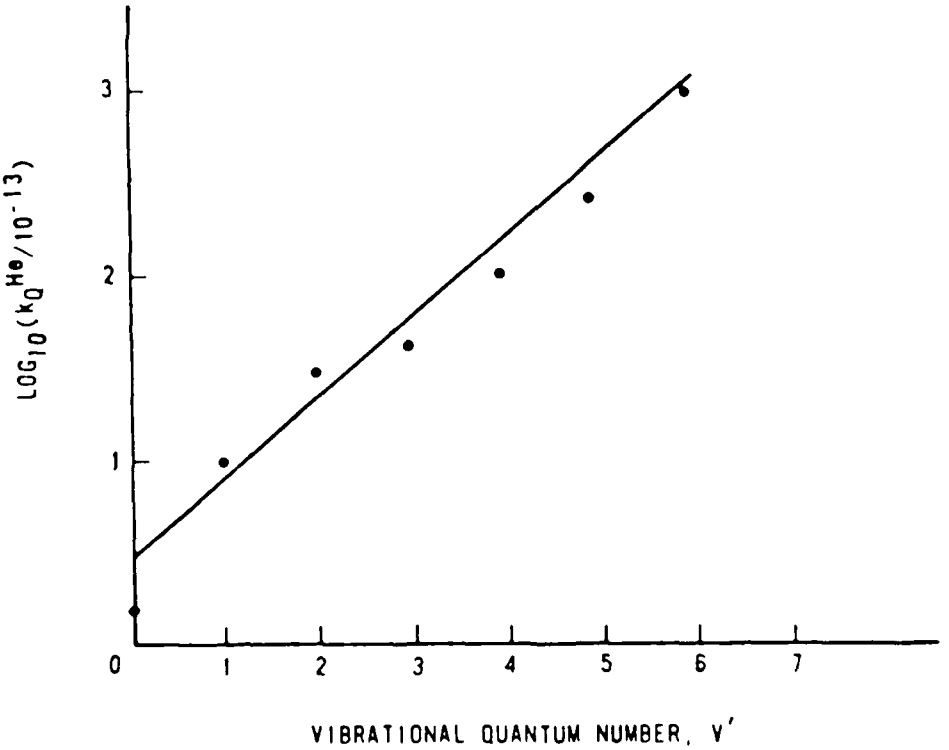

Figure 37. Vibrational scaling of the total quenching rate for BrCl(B;v') with helium as the buffer gas.

ratio, $k(v,v+1)/k(v+1,v)=\exp(-\Delta\varepsilon/k_BT)$, and may simply indicate a strongly coupled vibrational manifold.

Table VI
Helium Quenching Rates, $k_Q(v)$

v'	$k_Q(v')$ (10^{-11} cm^3/molec-s)
0	0.015 +/- 0.003
1	0.10 +/- 0.02
2	0.30 +/- 0.04
3	0.42 +/- 0.05
4	1.03 +/- 0.06
5	2.65 +/- 1.0
6	10.4 +/- 3.8

6. Summary of Pulsed Lifetime Studies

The electronic quenching of a thermalized BrCl(B) distribution by the BrCl mix is inefficient with a rate constant of k_{eq}^{M}= 4.3 +/- 0.7 x 10^{-13} cm^3/molec-s. Electronic quenching rates for buffer gases He, Ne, Ar, Kr, N_2, and O_2 have been obtained and all are inefficient ($k_{eq}^{Y} < 2 \times 10^{-13}$ cm^3/molec-s) except for oxygen with a rate constant of 6.5 x 10^{-12} cm^3/molec-s. The enhanced oxygen quenching may be due to a resonant electronic exchange reaction forming O_2 ($^1\Delta_g$).

The pressure dependence of the quenching rate has been confirmed and explained by vibrational dependent quenching rates. As the population distribution among vibrational states changes, we also observe variations in the average quenching rate. The state dependent quenching rates have been measured and range from 1.4 x 10^{-10} cm^3/molec-s for v'=6 to

4.3×10^{-13} cm^3/molec-s for $v'=0$. The mechanism for this removal process has not yet been completely defined. The spectrally-resolved, temporally-resolved data of the next section is required to determine the removal mechanism.

The BrCl(B) radiative lifetime is 38.7 +/- 1.7 μs independent of vibrational state for $v' < 7$.

The data presented in this section completely reproduces and is consistent with the BrCl(B) energy transfer studies by MA Clyne and coworkers.[120-123] The interpretation of this data, however, awaits the more detailed data from the spectrally-resolved, temporally-resolved experiments presented in the following section.

D. Temporally-Resolved, Spectrally-Resolved Studies

1. Time Evolution of BrCl(B;v′)

By including both temporal and spectral resolution in LIF energy transfer experiments, a great deal of information is obtained that details the full time history of the vibrational population distributions. Figure 38 illustrates typical data from such experiments. The initially populated state is $v_o'=6$ and the total mix pressure is 0.25 torr. A rapid exponential decay from the parent state is observed. The population rapidly cascades through intermediate vibrational states to $v'=1$ and $v'=0$. Figure 38 provides the first direct evidence for a rapid thermalization process. Note that $v'=0-4$ all decay with similar rates at long times. This indicates the strong coupling of the vibrational manifold and the rapid approach to equilibrium.

Due to the strong vibrational coupling, the rise and fall of the spectra of figure 38 cannot be simply attributed to the rate of transfer into and out-of the given state. That is, the radioactive series decay analogy is inapropriate. The extraction of state-to-state vibrational transfer rate constants from spectra like that in figure 38 is a difficult task requiring several approaches and is the topic of this section.

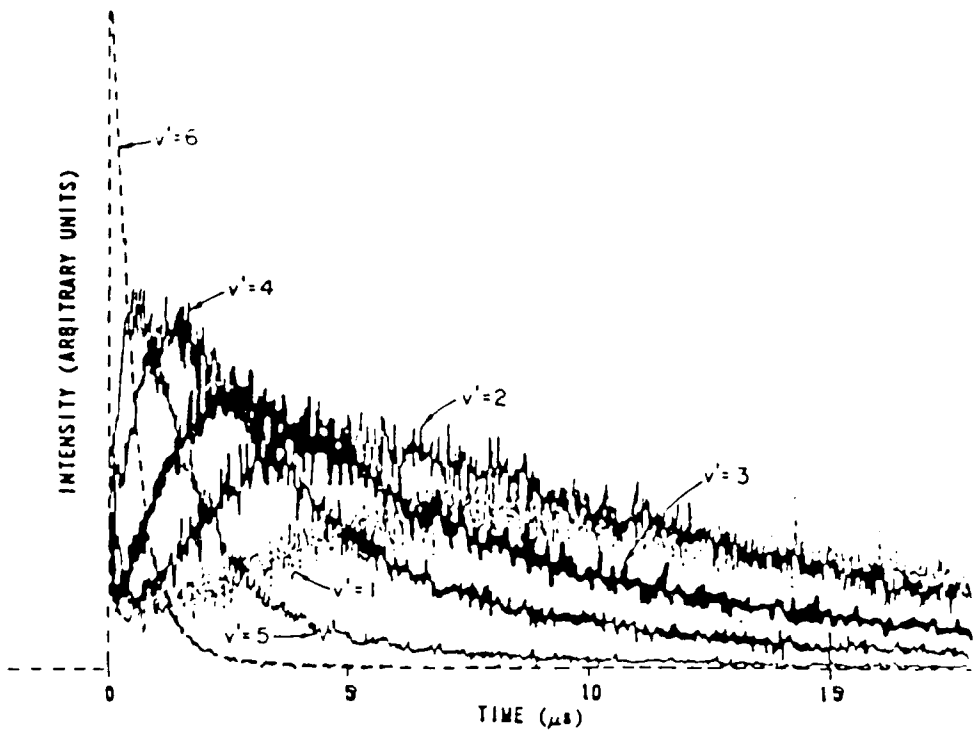

Figure 38. Typical temporally-resolved, spectrally-resolved LIF spectra.

2. Pressure Scaling

The pressure scaling of spectrally-resolved, temporally-resolved LIF data was discussed in section IIC4d. If the collisionless decay rate, Γ_o, is independent of quantum state, then the time history of population distributions, z_p, depends only on the product

$$t' = k_o M t \tag{83}$$

A plot of the distribution $z_p(t)$ for initially populating $v_o' = 5$ and observing the state $v' = 2$ as a function of the product variable, t', is given in figure 39. Two different pressure conditions are shown, one for 103 mtorr mix pressure and a second for 780 mtorr. The two spectra are not identical

and thus, the pressure scaling of equation (83) is inapropriate. The assumption that the collisionless decay rate, Γ_o, is independent of quantum state is therefore incorrect.

This conclusion was anticipated from the observation of collisional stabilization of predissociated distributions as presented in sections IVB3 and IVC1. In order to accurately describe the energy transfer processes of BrCl(B;v′), the predissociated states v′>6 must be considered to have finite decay rates and V,R-T transfer from these states to stable vibrational levels must be included in any model. This conclusion is an important aspect to describing why

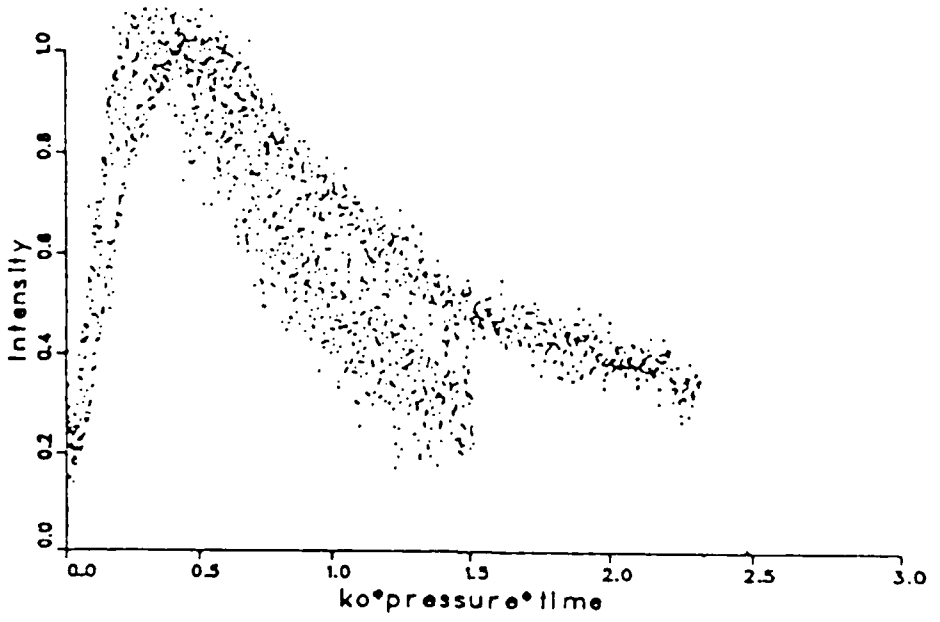

Figure 39. Comparison of two spectrally-resolved distributions for v_o'=5, v′=2 at a mix pressure of 103 mtorr and 780 mtorr.

previous transfer models have failed to accurately decribe BrCl(B) energy transfer processes.

3. The Montroll Shuler Solution

The Montroll-Shuler model[140] was described in section IIC3f and the analytic solution of equation (86) may be used to extract state-to-state vibrational transfer rates from the temporally-resolved, spectrally-resolved emission from a single observed v′ state′s spectrum. A nonlinear least square fit of equation (86) to the observed data provides the single parameter, $k_v^M(1\text{-}0)$. The curve fitting method has been described in detail elsewhere.[67]

Many of the assumptions of the Montroll-Shuler model do not apply to the full BrCl(B;v′) manifold. The small vibrational spacing and anharmonicity of the BrCl(B) state are not consistent with the prescription of $|\Delta v|=1$ only and the $k_v^M(v \rightarrow v-1) = v\, k_v^M(1\text{-}0)$ assumption of the Landau Teller theory used in the Montroll-Shuler Model. In addition, the collisionless decay rates and quenching rates are not state independent. These problems are much less severe for the lowest vibrational levels within BrCl(B). For these states, the system is far from predissocation and near the bottom of the potential energy well where the harmonic oscillator approximation is best. The effects of multiquantum transfer are minimized at low v′. The electronic quenching rates and

radiative lifetimes are state independent below $v'=3$ and the Montroll-Shuler model should be applicable to such states.

An example of a fit to the data using the Montroll-Shuler model is given in figure 40. The initially-populated state is $v_o'=1$ and observed state is $v'=0$. The total mix pressure is 4 torr. The fit for this data and similar data at other pressures is quite good. The parameter of the fit k_v^M (1-0), can be converted to a lifetime by

$$1/\tau = k_V^M(1\text{-}0)\ M \tag{93}$$

Plotting these lifetimes as a Stern-Volmer plot is a convenient way of presenting the data for various pressures. The intercept of such a plot should be zero and the slope provides the average rate constant $k_V^M(1\text{-}0)$. This type of plot for intially populating $v_o'=2$ and observing $v'=0$ is shown in figure 41. The resulting rate constant is $k_V^M(1\text{-}0) = 1.5 \times 10^{-11}$ cm^3/molec-s. The same procedure applied to the $v_o'=1$, $v'=0$ data yields the rate constant $k_V^M(1\text{-}0) = 1.2 \times 10^{-11}$ cm^3/molec-s. Therefore, the average fundamental rate is $k_V^M(1\text{-}0) = 1.3 \times 10^{-11}$ cm^3/molec-s. The magnitude of this rate is consistent with the rapid thermalization previously observed.

The Montroll-Shuler model applied to higher lying vibrational states fails completely to describe the transfer processes affecting these states. An example of a fit to the

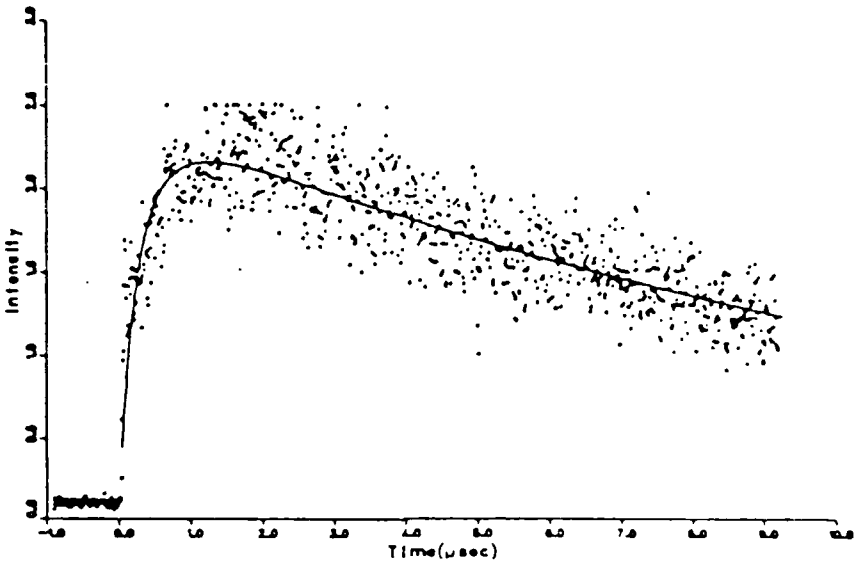

Figure 40. Example fit of Montroll-Shuler model to spectrally-resolved distribution.

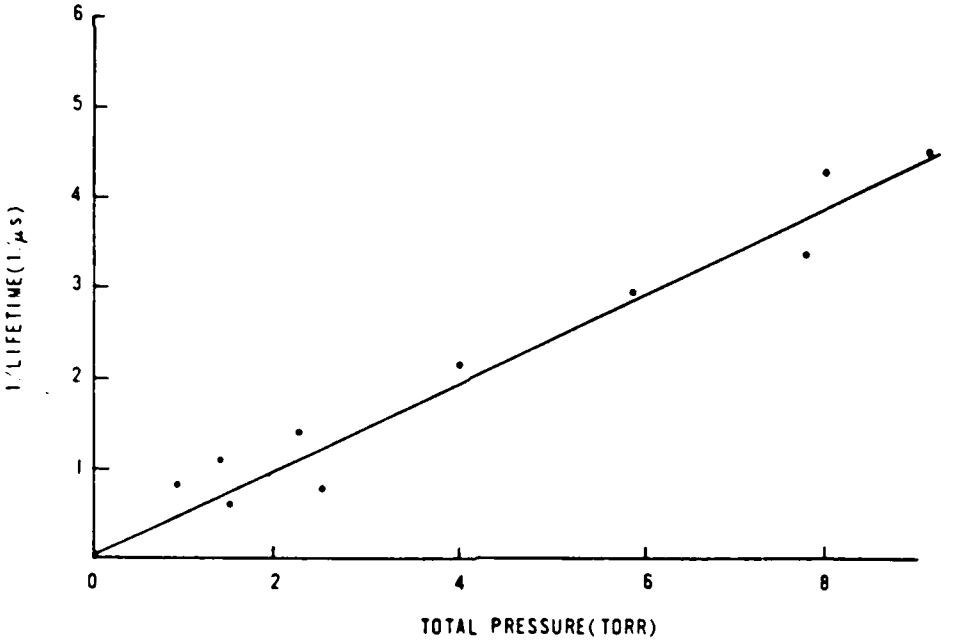

Figure 41. Stern-Volmer plot for Montroll-Shuler fit lifetimes.

data for $v_o' = 5$ and observing $v' = 0$ at 217 mtorr is given in figure 41. The fit is extremely poor and yields the unrealistic rate constant of $k_v^M(6-5) > 10^{-9}$ cm^3/molec-s. It is not surprising that the Montroll-Suler model fails at high v', since many of the assumptions required to derive equation (86) are not fulfilled. The strong variation of k_Q with vibrational state for $v'>2$ is probably the most important factor contributing to the poor fit of figure 42. The effects of predissociation are also important and are described in the following paragraphs.

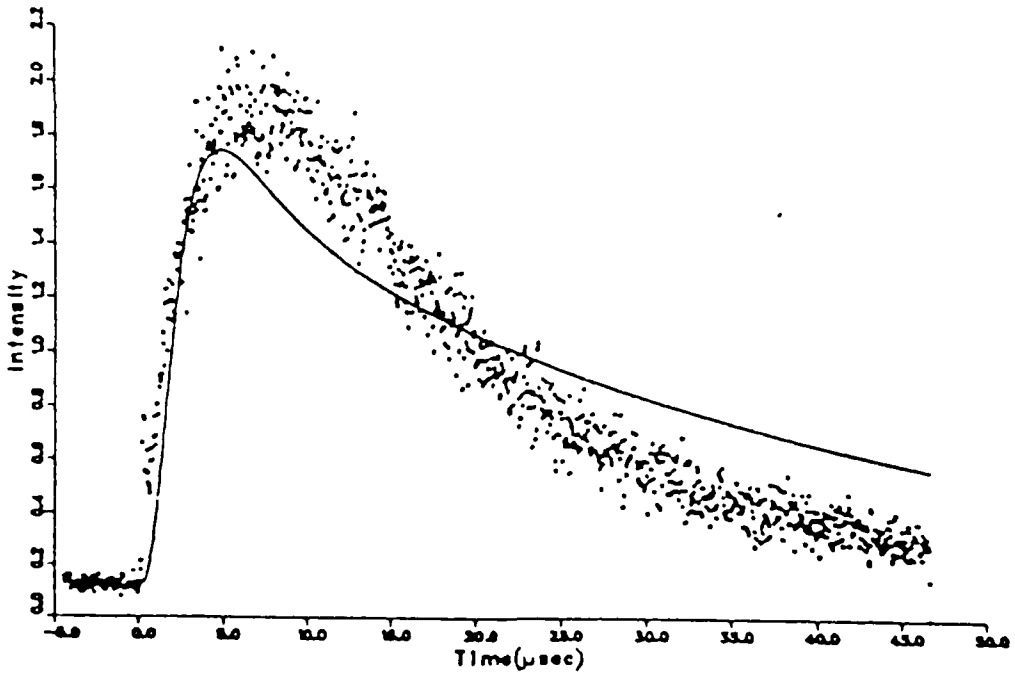

Figure 42. Failure of the Montroll-Shuler model to fit the observed data for high v' states. The initially populated state is $v_o' = 5$ and the observed state is $v' = 0$.

To illustrate the importance of the predissociated states to the overall energy transfer processes affecting BrCl(B), a Montroll-Shuler fit has been applied to a simulated spectrum for the BrCl(B) vibrational manifold. A rate matrix, R_{pq}, is established by appling the Montroll-Shuler model to a vibrational manifold with vibrational spacing $\Delta\varepsilon = 199\ cm^{-1}$ and a fundamental rate constant of $k_v^M(1\text{-}0)=2 \times 10^{-11} cm^3/molec\text{-}s$. An electronic quenching rate of $4.3 \times 10^{-13}\ cm^3/molec\text{-}s$ and radiative lifetime of 38.7 μs are used. Two different assumptions regarding the predissociated states v′=7-8 are used: (1) the predissociated states are not kinetically connected to the stable states and (2) the predissociated states have a finite decay rate, $\tau_o(v') = 0.1$ μs.

Using this rate matrix, the spectrum for initially-populating $v_o' = 5$ and observing the emission from v′=1 at a total mix pressure of 100 mtorr was simulated using equation (80). The Montroll-Shuler fitting routine was then applied to the simulated spectrum. The simulated spectrum and resultant Montroll-Shuler fits for the two assumptions regarding the predissociated states are shown in figures 43(a)-(b). The agreement using the uncoupled v′=7-8 states is excellent. This agreement is expected since the Montroll-Shuler fit applies to a vibrational manifold described exactly by a Montroll-Shuler model. The model using finite decay rates for the predissociated states v′=7-8 is not so well fit by the Montroll-Shuler routine. Several

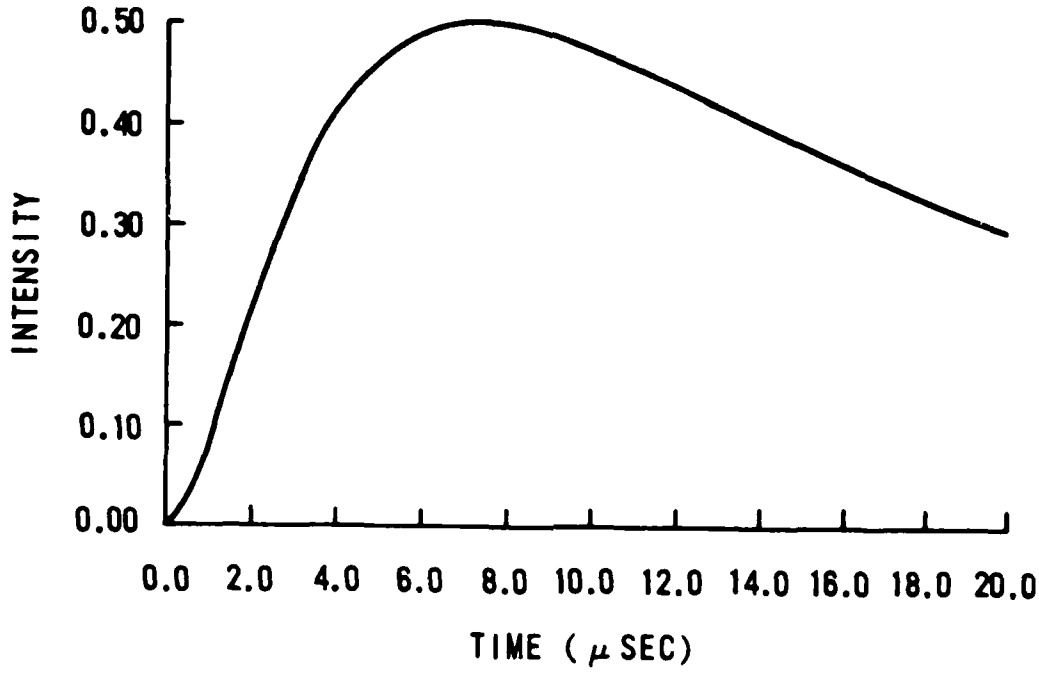

Figure 43a. Montroll-Shuler model fit to a simulated spectra for a harmonic oscillator vibrational manifold.

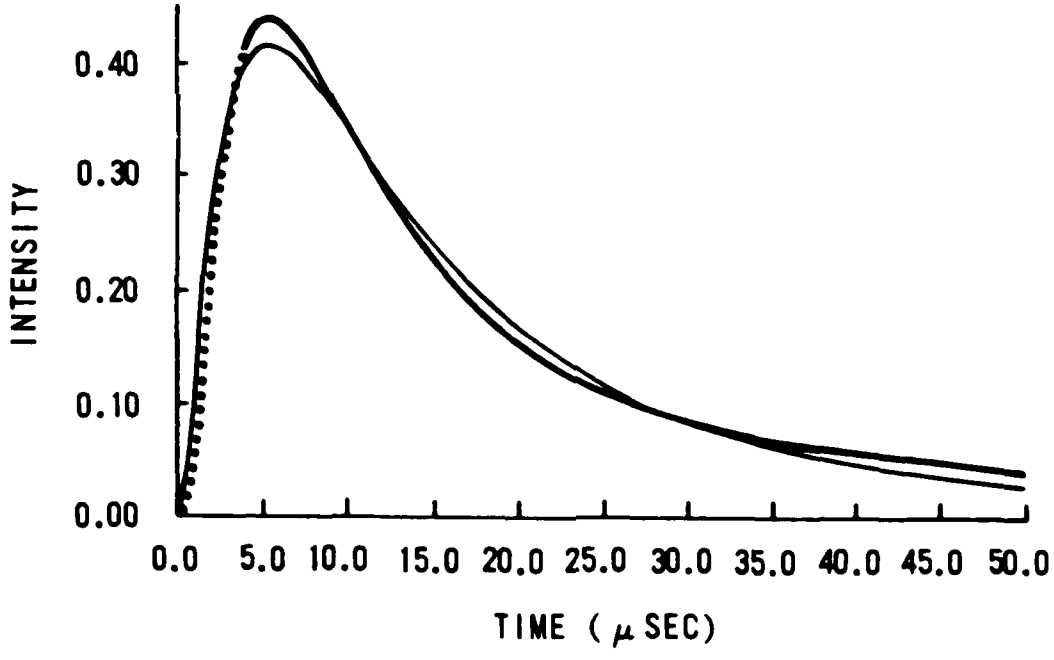

Figure 43b. Montroll-Shuler model fit to a simulated spectra of a harmonic oscillator with predissociation.

conclusions can be drawn from these observations: (1) the Montroll-Shuler fitting routine performs quite well when applied to an appropriate manifold, (2) the predissociated states v′=7-8 greatly affect the spectra of low lying v′ states when the vibrational population initially lies in high v′ states, and (3) the predissociated states must be considered to have finite decay rates in any BrCl(B) energy transfer model. These observations again illustrate the importance of including stablization of predissociated populations in the BrCl(B) vibrational energy transfer mechanism.

Despite the failure of the Montrol-Shuler model to accurately describe the full BrCl(B) energy transfer processes, the extraction of the fundamental rate constant for vibrational transfer from v′=1 to v′=0 is very important. This rate constant is generally the basis for vibrational scaling models. The rate also provides an anchor for the numerical methods to be described in section IVC5.

4. The Interpretations of Clyne and McDermid

Clyne and McDermid have studied energy transfer in BrCl(B) with $Cl_2(X)$ collisions in a series of papers using pulsed, spectrally unresolved LIF experiments.[120-123] No spectral resolution of vibrational states was achieved. The radiative lifetime of 40.2 +/- 1.8 μs and electronic quenching rate of 3.9×10^{-13} cm^3/molec-s were determined. In addition,

the scaling of total quenching rates with vibrational state was observed as presented in table V. Several models were then applied to these rates in an attempt to explain the removal mechanism by vibrational ladder climbing to predissociated states. Three specific models were suggested based on increasing amounts of and accuracy in total fluorescence data. All three of these models fail to adequately explain the spectrally-resolved, temporally-resolved data obtained in the current experiments. These three models will be described in order to demonstrate the difficulties of extracting state-to-state vibrational transfer rates from temporally-resolved spectrally-resolved data.

The first model[121] was very simple and based on an exponential energy gap scaling. The rate constant for $\Delta v = -1$ is assumed independent of v' and equal to $k_V^M(v \rightarrow v-1) = 2 \times 10^{-10}$ cm^3/molec-s. The rate constant for vibrational ladder climbing was assumed to scale exponentially with the energy required to reach predissociation:

$$k_V^M(v \rightarrow v+\Delta v) = 2 \times 10^{-11} \exp(-\Delta\varepsilon_{v,v+\Delta v}/k_B T) \quad \Delta v = 1,2.. \quad (94)$$

This model adquately reproduces the total quenching results of table V, but is inadequate in reproducing data like that shown in figure 38.

The second model[122] was an extension of the exponential energy gap scaling of the first model. The rate for

$k_V^M(v \rightarrow v+\Delta v)$ was assumed independent of v. The observed quenching rates are then attributed to vibrational ladder climbing to predissociated states:

$$\begin{aligned} k_Q^M(6) &= k_V^M(v \rightarrow v+1) + k_V^M(v \rightarrow v+2) + k_V^M(v \rightarrow v+3) + \ldots. \\ k_Q^M(5) &= + k_V^M(v \rightarrow v+2) + k_V^M(v \rightarrow v+3) + \ldots. \\ k_Q^M(4) &= + k_V^M(v \rightarrow v+3) + \ldots. \\ k_Q^M(3) &= + \ldots. \end{aligned} \quad (95)$$

The vibrational transfer rates are then obtained from the differences in quenching rates:

$$\begin{aligned} k_V^M(v \rightarrow v+1) &= k_Q^M(6) - k_Q^M(5) \\ k_V^M(v \rightarrow v+2) &= k_Q^M(5) - k_Q^M(4) \\ k_V^M(v \rightarrow v+3) &= k_Q^M(4) - k_Q^M(3) \end{aligned} \quad (96)$$

These equations assume that states $v'>6$ are completely unstable and a population transferred to these states immediately predissociates. In addition, no loss due to rotational transfer within $v'=6$ is considered. The resulting rates for vibrational transfer are given in table VII.

Table VII
Clyne's Second Model Rate Constants

v	$k_V^M(v \rightarrow v+\Delta v)$ (cm^3/molec-s)
+1	$1.1 \pm 0.4 \times 10^{-10}$
+2	$3.2 \pm 2.0 \times 10^{-11}$
+3	$5.8 \pm 2.3 \times 10^{-11}$

This model is inadequate in predicting the temporally-resolved, spectrally-resolved data of the present work. If

detailed balance is assumed in order to obtain the $\Delta v'<0$ rates, the thermalization process is much too fast (the fundamental rate constant would be $k_V^M(1-0) = 2 \times 10^{-10}$ cm^3/molec-s) and the total removal from BrCl(B) on the way to a thermalized $v'=0$ state is too slow.

The third model[123] attempts to overcome these problems by disregarding detailed balance and allowing some scaling of vibrational rate with quantum number, v'. Specifically, only $|\Delta v'|=1$ collisions were allowed, the vibrational scaling was based on the Troe[141-142] model (see Appendix D) and again, states $v'>6$ were assumed completely unstable. No loss due to rotational transfer within $v'=6$ is considered. By fitting the rates in such a model to the observed total fluorescence decay curves, the rates of table VIII were obtained. Note that at $v'=5$ the ratio of rate constants, $k_V^M(5-6)/k_V^M(6-5) = 9.4$ whereas the detailed balance ratio is 0.45.

Table VIII
Clyne's Third Model Rate Constants
(10^{-11} cm^3/molec-s)

v'	$k_V^M(v \rightarrow v-1)$	$k_V^M(v \rightarrow v+1)$
0	0	0.05
1	0.40	0.15
2	0.60	0.20
3	0.70	0.25
4	0.80	4.5
5	0.80	8.5
6	0.90	19.5

The large violation of detailed balance allows for a slower thermalization process and a larger removal rate than provided by the second model. No justification for the detailed balance violation is provided, however. The model again fails to accurately reproduce the temporal spectra of the present study. The thermalization process is too slow and the quenching too fast.

Several shortcomings of these models may be identified from comments previously made in this chapter and chapter II. First, the predissociated states are not completely unstable and collisional transfer from these states is important. Rotational transfer to predissociated states $v'=6$ $J' \geq 42$ is also neglected. Secondly, the restriction of $|\Delta v|=1$ only is improbable since $\Delta\varepsilon/kT=1$ and mutiquantum transfer is likely. Thirdly, in this thesis, the fundametal rate constant $k_V^M(1-0)$ has been established as 1.3×10^{-11} cm^3/molec-s from the Montroll-Shuler fits and the Clyne and McDermid models do not predict a fundametal rate constant of this order of magnitude. None of these models provide a rate matrix R_{pq} whose eigenvalue solutions predict the spectra similar to those presented in figure 39. Finally, the great violation of detailed balance suggested by the third model is a serious difficulty.

The Clyne et al models[120-123] assume the quenching process is completely described by vibrational ladder climbing

to predissociated states. Such models predict temporal spectra inconsistent with the data of this thesis. Thus, resonant electronic exchange reactions or other removal mechanisms are suggested.

The apparent inadequacy of these models illustrates the difficulty in extracting state-to-state vibrational transfer rates from total fluorescence lifetime measurements. The general problem, as described in section IIC4e, requires detailed temporally-resolved, spectrally-resolved data in order to determine the rate matrix R_{pq}. The data of this thesis provides this necessary information and the extraction of rate constants from this data will now be described.

5. Numerical Method and Vibrational Transfer Rates

As previously described, the radiative lifetime (38.7 μ s) and self electronic quenching rate (4.3×10^{-13} cm^3/molec-s) are now known. While the Montroll-Shuler (MS) model was sucessful in extracting the very important fundamental vibrational rate constant $k_V^M(1\text{-}0) = 1.3 \times 10^{-11}$ cm^3/molec-s, the scaling of this rate to higher vibrational levels could not be obtained directly from the MS model. In addition, the mechanism that leads to the total removal rates given in table V has yet to be established. The resolution of these issues requires the numerical methods suggested in section IIC4g.

For a given rate matrix, R_{pq}, the pulsed master rate equation (66) may be solved directly for the vibrational distribution, $x_p(t)$, using the eigenvalue solution of equation (80). Several features of the R_{pq} matrix are unknown, however. The following procedure is used to establish the unkown R_{pq} elements. The scaling of vibrational transfer rate constants $k_V^M(v \rightarrow v-1)$ is assumed to obey a power law,

$$k_V^M(v \rightarrow v-1) = v^n \, k_V^M(1-0) \tag{97}$$

For $n=1$, this law corresponds to the Landau-Teller scaling theory.[153] Several other energy transfer studies have indicated power law scaling with $n \neq 1$.[176-177] The variable n will be used as a parameter for the numerical solutions.

The principle of detailed balance will be used to calculate the rate constants for $\Delta v>0$:

$$\begin{aligned} k_V^M(v \rightarrow v+1) &= k_V^M(v+1 \rightarrow v) \exp(\Delta\varepsilon_{v,v+1}/k_B T) \\ k_V^M(v \rightarrow v+2) &= k_V^M(v+2 \rightarrow v) \exp(\Delta\varepsilon_{v,v+2}/k_B T) \end{aligned} \tag{98}$$

where

$\Delta\varepsilon_{v,w}$=energy difference between states v and w

The amount of multiquantum transfer is uncertain and difficult to separate from the single quantum transfer. Transfer will be limited to $|\Delta v| \leq 2$. The $\Delta v=-2$ rate will be

assumed to be a fixed percentage of the $\Delta v=-1$ rate:

$$k_v^M(v \rightarrow v-2) = f\ k_v^M(v \rightarrow v-1) \tag{99}$$

The variable f will be considered a parameter of the numerical solution. The value f=0.4 will be chosen initially since the exponential energy gap is

$$\exp\ (\Delta\varepsilon / k_B T) \sim 0.4 \tag{100}$$

The only remaining information needed to construct R_{pq} is the mechanism and rates for removal that lead to the values of table V. The detailed balance rates from equation (98) will yield some removal from the B state due to vibrational transfer to predissociated states. The magnitude of these rates will not, in general, account for the removal observed in the total fluorescence experiments. In fact, the modeling of Clyne et al[120-123] coupled with the data presented in this work indicates that quenching cannot be solely attributed to vibrational ladder climbing to predissociated states. An additional removal process is thus postulated to account for the required extra removal. Such a process could be resonant electronic exchange or any other process that removes population from the B-state with state selective rates. For the purpose of discussion, this additional removal process will be termed "extra removal".

The rate matrix R_{pq} can now be constructed and will depend on the scaling parameter, n, the multi-quantum

fraction, f, and the extra removal rates as just described. The values of these parameters can be varied and the population distributions $x_p(t)$ for all states p, after initially populating each v_o' can be obtained from equation (80). By comparing these solutions with the temporally-resolved, spectrally-resolved data, the best estimate for the values of the vibrational scaling and removal rates may be obtained.

There are two difficulties in comparing predicted spectra and observed spectra. First, the temporally-resolved spectra only provide relative intensities whereas the predictions, x_p, are based on the initial condition $x_p(0) = \delta_{ppo}$. The required normalization depends on many factors including pump intensity, pump wavelength, detection efficiencies, Franck-Condon factors, pump beam spot size, number of laser shots in signal averaging, and pump laser beam attenuation (mix pressure). The normalization varies from spectra to spectra and cannot be accurately predicted. In order to compare predicted and observed spectra, the maximum observed intensity and calculated number density are both normalized to 1.0.

The second difficulty in comparing predicted and observed spectra arises from incomplete resolution of individual vibrational levels in the observed emission spectra. The 2.5 nm emission resolution used in the pulsed experiments is insufficient to limit fluorescence intensity to a single

vibrational state. Pump transitions, observed emission wavelengths, and the estimated degree of spectral overlap for adjacent vibrational states are listed in appendix B. From 6 to 26 percent of the observed emission may be due to other vibrational states. In order to compare the predicted and observed spectra, the predicted densities of several states are convolved according to spectral overlap and detection efficiency as described in appendix B.

There is no guarantee of solution uniqueness with the numerical approach just described. Indeed, an entire set of solutions have been identified and will be discussed in the following section. The lack of uniqueness arises mainly from the lack of information on the relative normalization. The pulsed lifetime studies and the CW experiments do provide information regarding this normalization and are required to determine the correct rate matrix, R_{pq}. The data needed to obtain such a solution will be presented in section IVd7.

6. Non-Uniqueness of the Numerical Method

Based on the numerical approach just described, two substantially different rate matrices, R_{pq}, have been identified as solutions to the BrCl(B) + Cl_2(X) vibrational energy transfer problem. From these two solutions, an entire family of solutions may be inferred. By increasing the rates for extra removal and decreasing the vibrational transfer rates, very similar predicted temporal spectra are obtained.

Without information regarding the relative normalization of the temporal spectra, these various rate matrices predict the experimental data within the observed scatter equally well. This section will describe these solutions for the rate matrix and illustrate the agreement between predicted and observed spectra.

The first solution is based on the Landau Teller theory for scaling of V-T transfer rates, that is η=1. No extra removal is allowed, except from the state v′=6 where R-T transfer to predissociated states must be considered. The amount of extra removal from v′=6 and the fundamental rate constant $k_V^M(1\text{-}0)$ are taken as parameters of the solution. Table IX lists the values used to construct the rate matrix R_{pq} for this first pulsed solution.

Table IX
Numerical Solution Number One

η	= 1
$k_V^M(1\text{-}0)$	= 2.0×10^{-11} cm^3/molec-s
f^V	= 0.4
$k_q(v'=0\text{-}5)$	= 4.3×10^{-13} cm^3/molec-s
$k_q^q(v'=6)$	= 1.0×10^{-10} cm^3/molec-s

The second solution is based on the fundamental V-T rate constant $k_V^M(1\text{-}0) = 1.3 \times 10^{-11}$ cm^3/molec-s obtained from the Montroll-Shuler model as described earlier. The vibrational scaling, η, is taken as the parameter for the solution and the amount of extra removal is constrained to agree with the quenching rates obtained from the pulsed lifetime studies.

Table X lists the values used to construct the rate matrix R_{pq} for this second pulsed solution.

Table X
Numerical Solution Number Two

$\eta = 0.625$
$k_V^M(1\text{-}0) = 1.3 \times 10^{-11}$ cm^3/molec-s
$f = 0.4$
$k_q(v'=0\text{-}2) = 4.3 \times 10^{-13}$ cm^3/molec-s
$k_q^q(v'=3) = 4.4 \times 10^{-12}$ cm^3/molec-s
$k_q^q(v'=4) = 5.5 \times 10^{-11}$ cm^3/molec-s
$k_q^q(v'=5) = 7.5 \times 10^{-11}$ cm^3/molec-s
$k_q^q(v'=6) = 1.5 \times 10^{-10}$ cm^3/molec-s

Examples of observed spectra and numerical predictions based on the second solution (table X) are given in figures 44-46. The agreement is quite good for a wide range of conditions including initially-populated states $v_o'=6,3$, and 1, observed states $v'=6\text{-}0$, and mix pressures from 50 mT to 10 Torr. Recall that the calculated distributions are not fits to the data, but rather, are based on a single rate matrix R_{pq}. In addition, states $v'=0,2$, and 4 are particularly affected by emission from adjacent vibrational bands. Note, in figure 45(a), the peak in intensity for the observed $v'=0$ state at approximately 1 μs is due to emission from $v'=4$. The predicted and observed spectra agree quite well.

The observed and predicted spectra using the solution number one also produce reasonable agreement. No significant differences between the two solutions is discernable within the noise limits of the observed spectra.

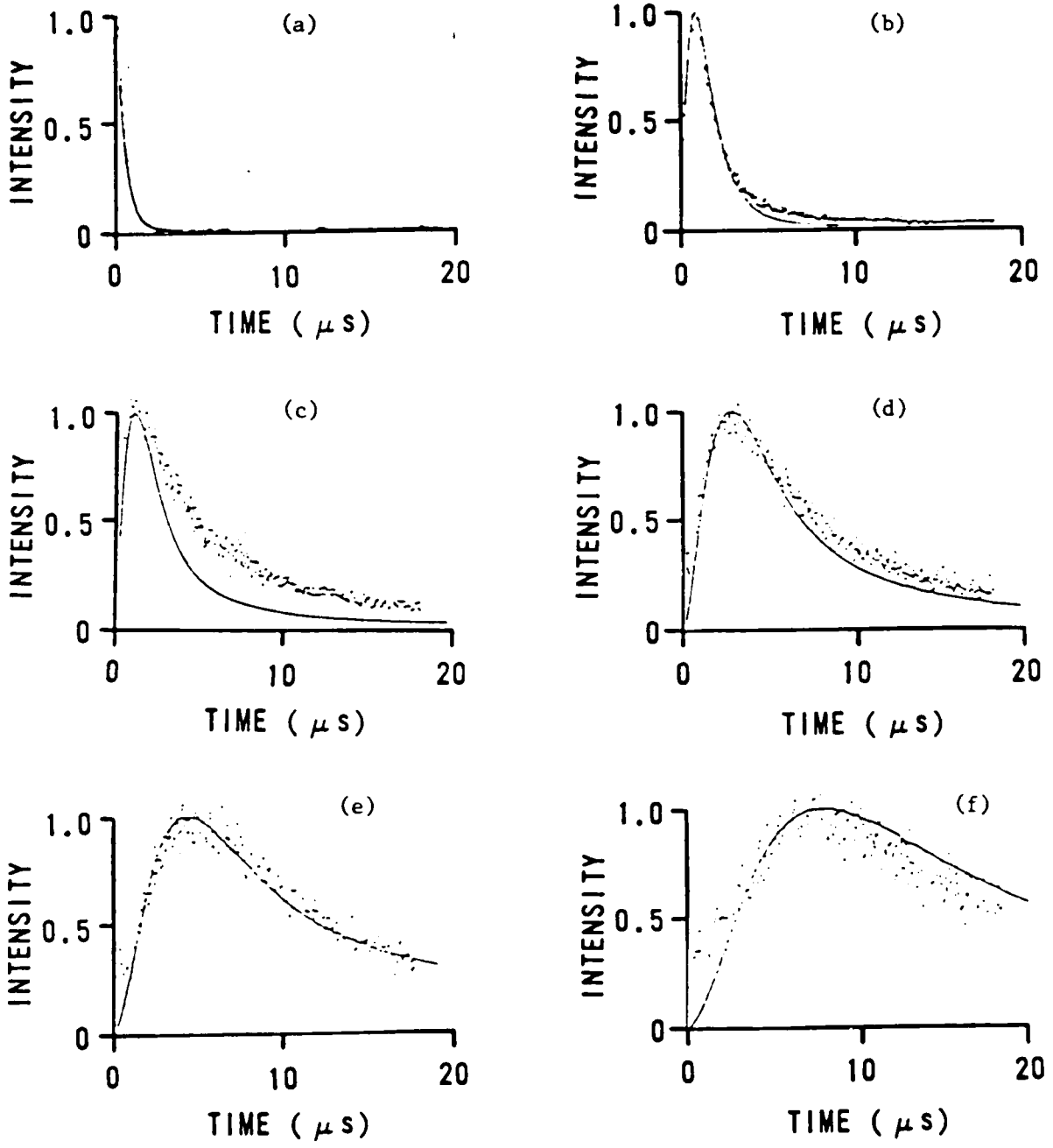

Figure 44. Examples of observed spectra and numerical predictions based on the second solution of table X. Total mix pressure is 244 mT, initially populated state is $v_o'=6$, and observed states are: (a) $v'=6$, (b) $v'=5$, (c) $v'=4$, (d) $v'=3$, (e) $v'=2$, (f) $v'=1$.

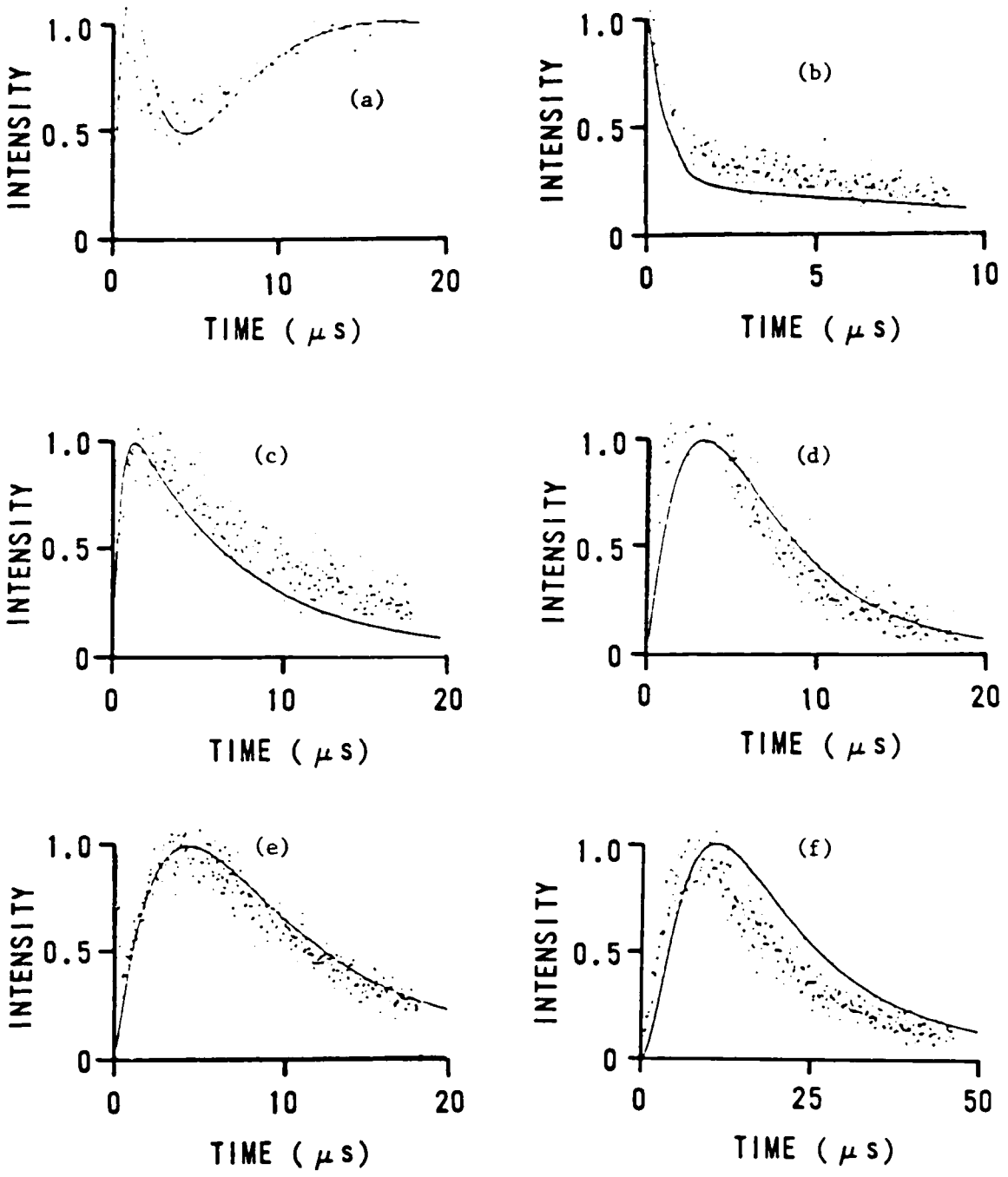

Figure 45. Examples of observed spectra and numerical predictions based on the second solution of table X. Total mix pressures, initially populated states, and observed states are: (a) p=244 mT, v_o'=6, v'=0, (b) p= 4 T, v_o'=1, v'=1, (c) p=4 T, v_o'=1, v'=0, (d) p=50 mT, v_o'=6, v'=5, (e) p=50 mT, v_o'=6, v'=4, (f) p=50 mT, v_o'=6, v'=3.

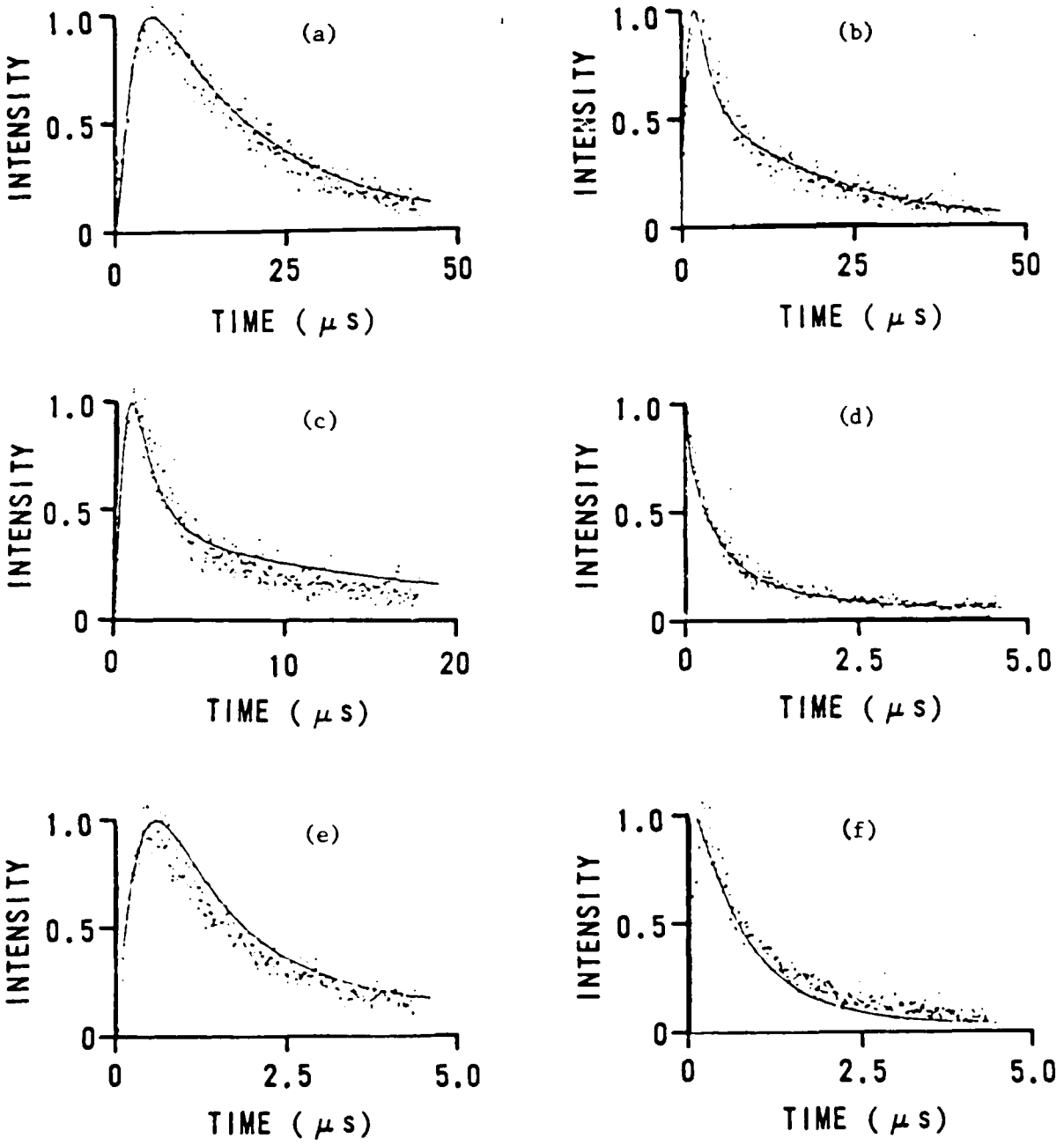

Figure 46. Examples of observed spectra and numerical predictions based on the second solution of table X. Total mix pressure is 1 torr, initially populated state is $v'=3$, and observed states are: (a) $v'=0$, (b) $v'=1$, (c) $v'=2$, (d) $v'=3$, (e) $v'=4$, (f) $v'=5$.

Additional solutions can be infered with parameters intermediate between solution #1 and solution #2. The first solution reflects the least amount of extra removal consistent with the observed temporal spectra whereas solution #2 reflects a large amount of extra removal and is consistent with both the fundamental rate constant obtained from the Montroll-Shuler model and with the quenching rates from the pulsed lifetime studies. By increasing the amount of extra removal (k_q) and decreasing the rate for V-T transfer (η), an entire family of rate matrices can be obtained that adequately predict the pulsed spectra within experimental scatter. All of these rate matrices represent physically reasonable rate processes and additional information is required to constrain the parameter space. The pulsed lifetime studies of section IVC and quenching rate constants reported in table V, as well as the high pressure relative CW number densities of the steady-state experiments provide this necessary information. It is the incoporation of this data that allows the establishment of a best estimate for the rate constants.

7. Selection of Rate Matrix from Lifetime and CW Data

The non-uniqueness of the unconstrained numerical method is largely a result of lacking information on the relative intensity from one pulsed spectra to another. The different pulsed solutions arise from varying degrees of quenching, $k_Q^M(v)$. Temporal spectra with similar profiles but greatly

different amplitudes are obtained with these varying pulsed solutions. The temporally-resolved, spectrally-resolved data provide information on the relative number density profiles and not the magnitude of the density distributions. Since the quenching rates control the relative number densities, they may be used to reduce the possible pulsed solutions to one best estimate. In addition, the steady-state experiments provide direct evidence for the relative number densities and may assist in the selection of the best rate matrix. A flow chart of the logic used to obtain the best estimate for a full kinetic description of $BrCl(B;v') + Cl_2$ energy transfer is given in figure 47.

The total quenching rate constants for each v′ state as experimentally observed from the pulsed lifetime Stern-Volmer plots of section IVC and as predicted from the pulsed solutions are shown in table XI. The minimal quenching of solution #1 is inconsistent with the observed quenching rates. The quenching of solution #2 agrees quite favorably with the observed rates, however. Indeed, the second pulsed solution is the only solution investigated that adequately predicts all of the observed temporal spectra and is consistent with the quenching rates.

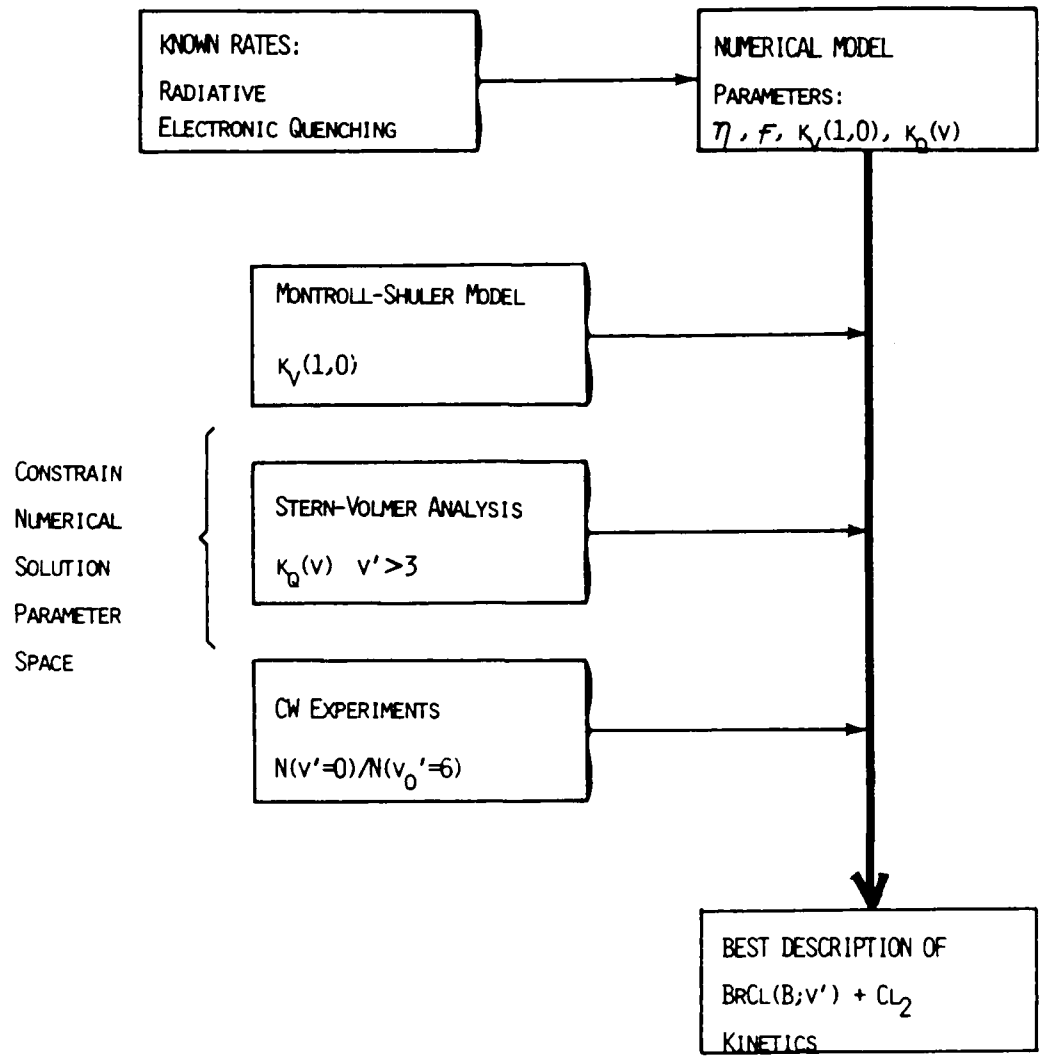

Figure 47. Numerical solution logical flow chart.

Table XI
Comparison of Predicted and Observed Quenching Rates
(1 x 10^{-11} cm^3/molec-s)

State	Observed $k_q(v)$	Solution #1	Solution #2
0	0.043	0.043	0.043
1	*****	0.043	0.043
2	*****	0.043	0.043
3	*****	0.043	0.40
4	4.7 +/- 1.4	0.043	5.5
5	6.2 +/- 1.7	0.94	7.9
6	14.0 +/- 3.0	16.7	17.6

The pulsed solutions of tables IX and X are also quite different when viewed from the perspective of the steady-state experiment. The extra removal and the slower V-T transfer rates of the second solution yield a much higher effective quenching of BrCl(B). Quenching during the cascade of the population to low vibrational states reduces the percentage of the population that eventually reaches $v'=0$. The ratio of the steady-state population in $v'=0$ to that of the initially-populated state $v_o'=6$, N(0)/N(6), would thus be considerably smaller for the second pulsed solution. This observation provides an additional basis for differentiating between pulsed solutions #1 and #2.

Figure 48 illustrates the relative steady-state number density in $v'=0$ after initially populating $v_o'=6$ for mix pressures in the range 0.25 - 5.0 torr. Also displayed are the predicted number densities based on the two pulsed solutions of tables IX and X. These steady-state density predictions are obtained by time averaging the time dependant distributions of equation (80) according to the procedure

described in section IIC4e. Clearly, pulsed solution #2 provides a much closer fit to the CW data. That is, the population reaching $v'=0$ is greatly reduced due to rapid quenching of $BrCl(B;v'>2)$.

The prediction of the second pulsed solution does not quite match the observed populations. The error bars indicated in figure 48 are for the error in relative areas of the vibrational emission bands, but do not reflect systematic errors arising from incorrect spectral response and Franck-Condon factors. The $v'=0$ to $v''=12$ emission is monitored at 855 nm and the spectral response of the C31034 PMT is dropping rapidly in this region (see appendix C). Because the spectral response curve is steep, a considerable error in the response $D(\nu)$ may exist. In addition, Franck-Condon factors for emission bands with wavelengths greater than 700 nm are not available in the literature. The Franck-Condon factors above 700 nm have been calculated from a simple extrapolation to higher v" states (see appendix B) and may be in considerable error. As a result, the absolute magnitude of the ordinate axis in figure 48a may be in error by at least a factor of two. This would allow for agreement between the predicted and observed number densities. The low pressure CW data to be presented in section IVE do not suffer from these problems, since strong emission bands for $v'>2$ are observed below 700 nm.

Figure 48b also shows the population in $v'=0$ for mix pressures of 0 - 35 torr. The data was obtained by observing the intensity of the $v'=0$ emission at 855 nm for a continuously increasing mix pressure. Also shown in figure 48b is the predicted population of $v'=0$ based on the second pulsed solution. The agreement is within the estimated error bounds.

The second solution adequately predicts the quenching rates as shown in table XI. In addition, the relative population reaching $v'=0$ (figure 48) is satisfactorily predicted by the second solution. The rate matrix for the second solution provides a solution that will reproduce all the steady-state and pulsed spectra. The full rate matrix for this solution is given in table XII. This rate matrix provides the best estimate for the complete description of the energy transfer processes affecting BrCl(B) with Cl_2 as the collision partner and is the final solution for the inverse problem of the pulsed experiments. The mechanism leading to the extra quenching rates has not been established, however.

Table XII
Final Pulsed Solution, R'_{pq} (10^{-11} cm^3/molec-s)

	q= 0	1	2	3	4	5	6	7	8
p= 0	0.0	1.3	0.8	0.0	0.0	0.0	0.0	0.0	0.0
p= 1	0.46	0.0	2.0	1.0	0.0	0.0	0.0	0.0	0.0
p= 2	0.11	0.75	0.0	2.6	1.2	0.0	0.0	0.0	0.0
p= 3	0.0	0.15	1.0	-0.4	3.1	1.4	0.0	0.0	0.0
p= 4	0.0	0.0	0.19	1.3	-5.5	3.6	1.6	0.0	0.0
p= 5	0.0	0.0	0.0	0.25	1.5	-7.5	4.0	1.8	0.0
p= 6	0.0	0.0	0.0	0.0	0.16	0.90	-15.0	2.2	.95
p= 7	0.0	0.0	0.0	0.0	0.0	0.38	2.1	-11.0	4.8
p= 8	0.0	0.0	0.0	0.0	0.0	0.0	0.49	2.5	-13.

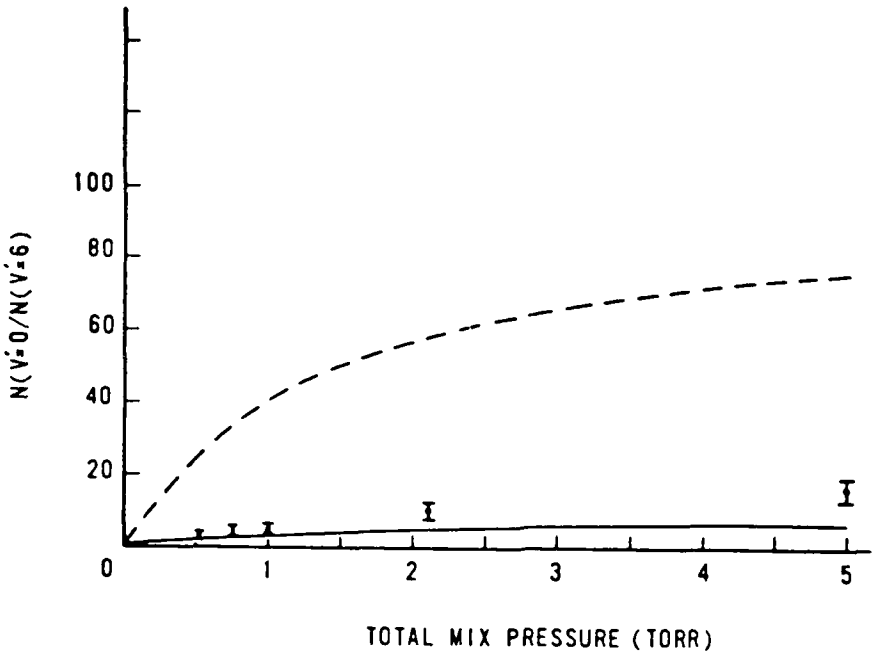

Figure 48a. Relative steady-state number density in $v'=0$ after initially populating $v_o'=6$.

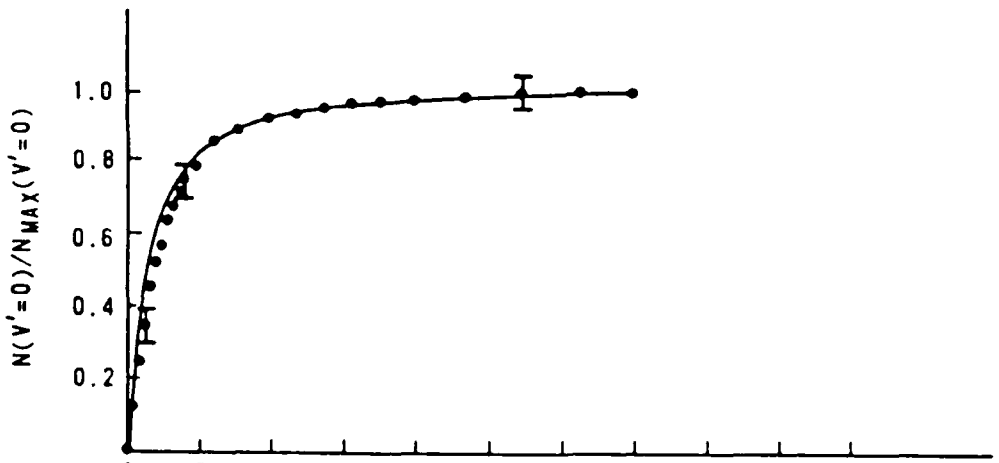

Figure 48b. Relative steady-state population of $v'=0$ after initially populating $v_o'=6$.

8. The BrCl(B) Quenching Mechanism

Two processes have already been identified for the quenching of BrCl(B): (1) electronic quenching with a rate constant of $k_{eq}^{M} = 4.3 \times 10^{-13}$ cm^3/molec-s and (2) ro-vibrational ladder climbing to predissociated states, $\sum_{wpd} k_V^M(v-w_{pd})$. The magnitude of the predissociative plus electronic quenching losses as predicted from the final pulsed solution and total quenching used in this model are given in table XIII. The difference between these rates must be due to an additional removal mechanism, or possibly a significant violation of the detailed balance property.

Table XIII
Comparison of Quenching Rates
(10^{-11} cm^3/molec-s)

v´	$k_{eq} + \sum_{w_{pd}} k_V^M(v-w_{pd})$	k_Q
0	0.043	0.043
1	0.043	0.043
2	0.043	0.043
3	0.043	0.40
4	0.043	5.5
5	0.40	7.9
6	2.6	17.6

The possibility of removal of BrCl(B) by resonant electronic exchange with $Cl_2(X)$ exists. The potential energy curves for some low lying electronic states of Cl_2 are given in figure 49. The Cl_2 B state lies slightly too high in energy (T_e = 17809 cm^{-1}) to be the recipient of the BrCl(B) energy for states BrCl(B;v´<5). The $A\,^3\Pi_u$ state of Cl_2 has

an energy approximately resonant with the energy of BrCl(B;v>2), however. Figure 51 shows the total energy above BrCl(X;v"=0) for BrCl(B), Cl_2(A), and Cl_2(B). The first vibrational state of BrCl(B) having sufficient energy to access Cl_2(A;v'=0) is v'=3. Interestingly, the BrCl(B;v'=3) state is also the first vibrational state to exhibit extra removal, see table XI. Thus, BrCl(B) resonant energy exchange with Cl_2(X) is possible and consistent with the rate matrix of table XII. While this explanation of the observed extra removal rates for BrCl(B) is plausible, it has not been proven. Several tests of this theory can be made, however.

If the extra removal process is due to the excited A and B states of Cl_2, then BrCl(B) energy transfer with other buffer gases should not exhibit the additional quenching. The case of BrCl(B) and rare gas collisions has been studied in detail in this thesis and the results are presented in the following sections.

9. Energy Transfer with Rare Gases

The study of BrCl(B;v') vibrational energy transfer with rare gas collision partners (He,Ne,Ar,Kr,Xe) is important for several reasons. Since the collision partners are atomic species, the effects of vibrational-vibrational transfer are eliminated. Only a few, isolated excited electronic states exist and resonant electronic exchange reactions are

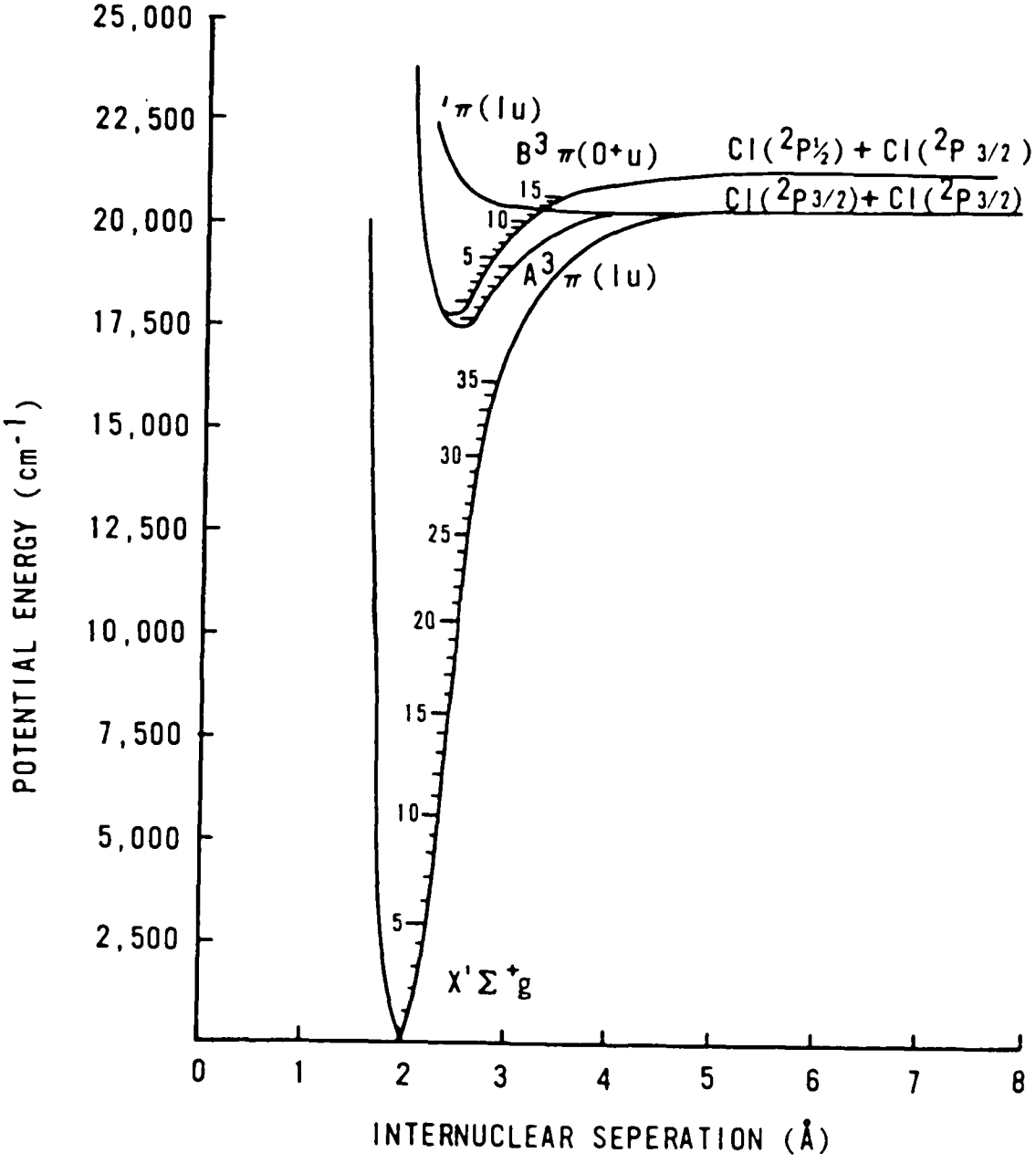

Figure 49. Chlorine potential energy curves.[188]

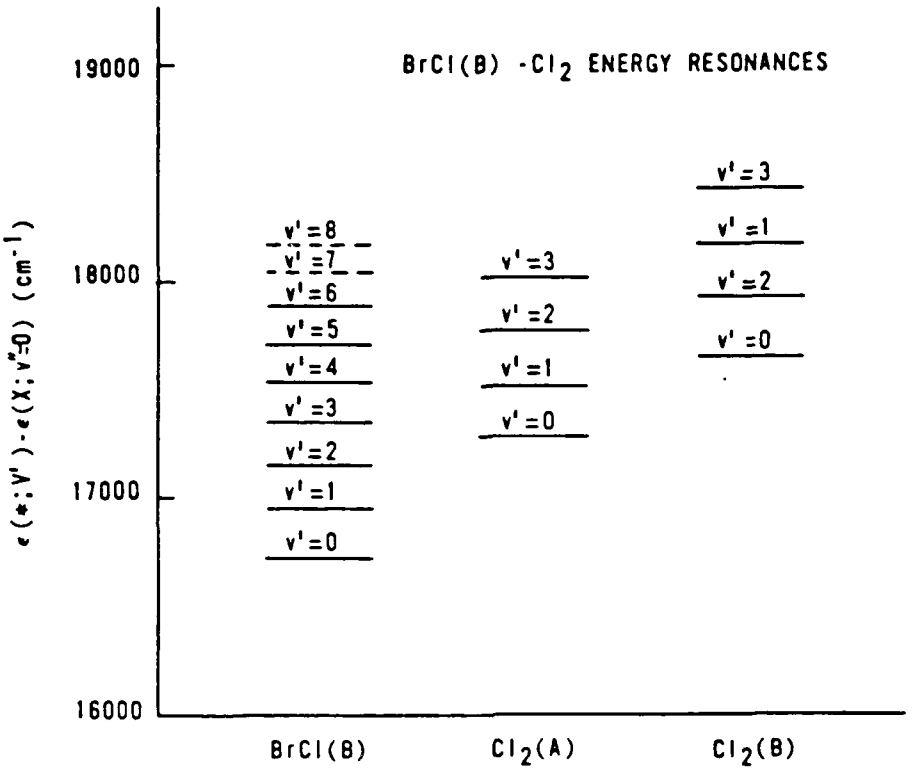

Figure 50. BrCl(B;v´) - Cl_2 energy resonances.

energetically impossible. The major difference between the rare gas collision partners is the nuclear mass. Temporally-resolved, spectrally-resolved data for rare gas collisions has been recorded in the pulsed experiments and the results of these experiments will be described in this section.

The numerical solution described in sections IVC6-8 has been applied to the rare gas transfer spectra in order to extract the fundamental vibrational rate constant, $k_v^Y(1\text{-}0)$. The results of table XII are used to describe the transfer due to BrCl(B) + Cl_2(X) collisions arising from the base mix

pressures used in these studies. The electronic quenching rates as reported in table III are used for each buffer specie. The fundamental rate constant $k_v^Y(1-0)$ is used as a parameter of the numerical solution and scaling to higher vibrational states is based on the Landau-Teller theory. Multi-quantum transfer is based on the fraction, f, as described in section IVC6. Detailed balance is applied to establish the $\Delta v>0$ rates. A vibrationally-dependent quenching is allowed and the rate constants for this quenching are used as a second set of parameters.

The case of BrCl(B) + He collisions has been modeled extensively using this numerical solution. Again the solution is not unique. A solution with a fundamental rate constant of $k_v^{He}(1-0) = 4 \times 10^{-12}$ cm^3/molec-s and no vibrationally-dependent quenching is described in table XIV. Note that an extra removal from $v'=6$ is included to account for rotational transfer to predissociated J states within $v'=6$. With this solution, the observed temporal spectra are predicted quite well. Several typical examples of observed and predicted He transfer spectra are shown in figure 51.

Table XIV
Pulsed Helium Solution Number One

η_M	= 1.0
$k_v^M(1-0)$	= 4.0×10^{-12} cm^3/molec-s
f^v	= 0.4
$k_q(v'=0-5)$	= 1.5×10^{-13} cm^3/molec-s
$k_q^q(v'=6)$	= 5.2×10^{-11} cm^3/molec-s

A second solution that includes some vibrationally-dependent quenching has also been identified and the results are shown in table XV. The agreement between observed and predicted spectra is similar to that given in figure 51.

Table XV
Pulsed Helium Solution Number Two

η_M	= 1.0
$k_v(1-0)$	= 3.0×10^{-12} cm^3/molec-s
f^v	= 0.4
$k_q(v'=0-2)$	= 1.5×10^{-13} cm^3/molec-s
$k_q(v'=3)$	= 6.9×10^{-13} cm^3/molec-s
$k_q(v'=4)$	= 7.0×10^{-12} cm^3/molec-s
$k_q(v'=5)$	= 9.4×10^{-12} cm^3/molec-s
$k_q(v'=6)$	= 1.9×10^{-11} cm^3/molec-s

As with the BrCl + Cl_2 collisions, the steady-state spectra of the CW experiments are required to select the correct numerical solution. The relative number density in $v'=0$ after initially populating $v_o'=6$ for a BrCl-Cl_2 mix pressure of 0.77 torr and a helium pressure of 0 to 2 torr is illustrated in figure 52. Also given are the predicted number densities based on the numerical solution of tables XIV and XV. The numerical solution with no vibrationally-dependent quenching (table XIV) agrees well with the observed data, whereas the solution of table XV does not. The transfer processes due to He collisions are well described without the extra quenching mechanism. We therefore conclude that the anomolous quenching observed in the BrCl(B) + Cl_2 collisions

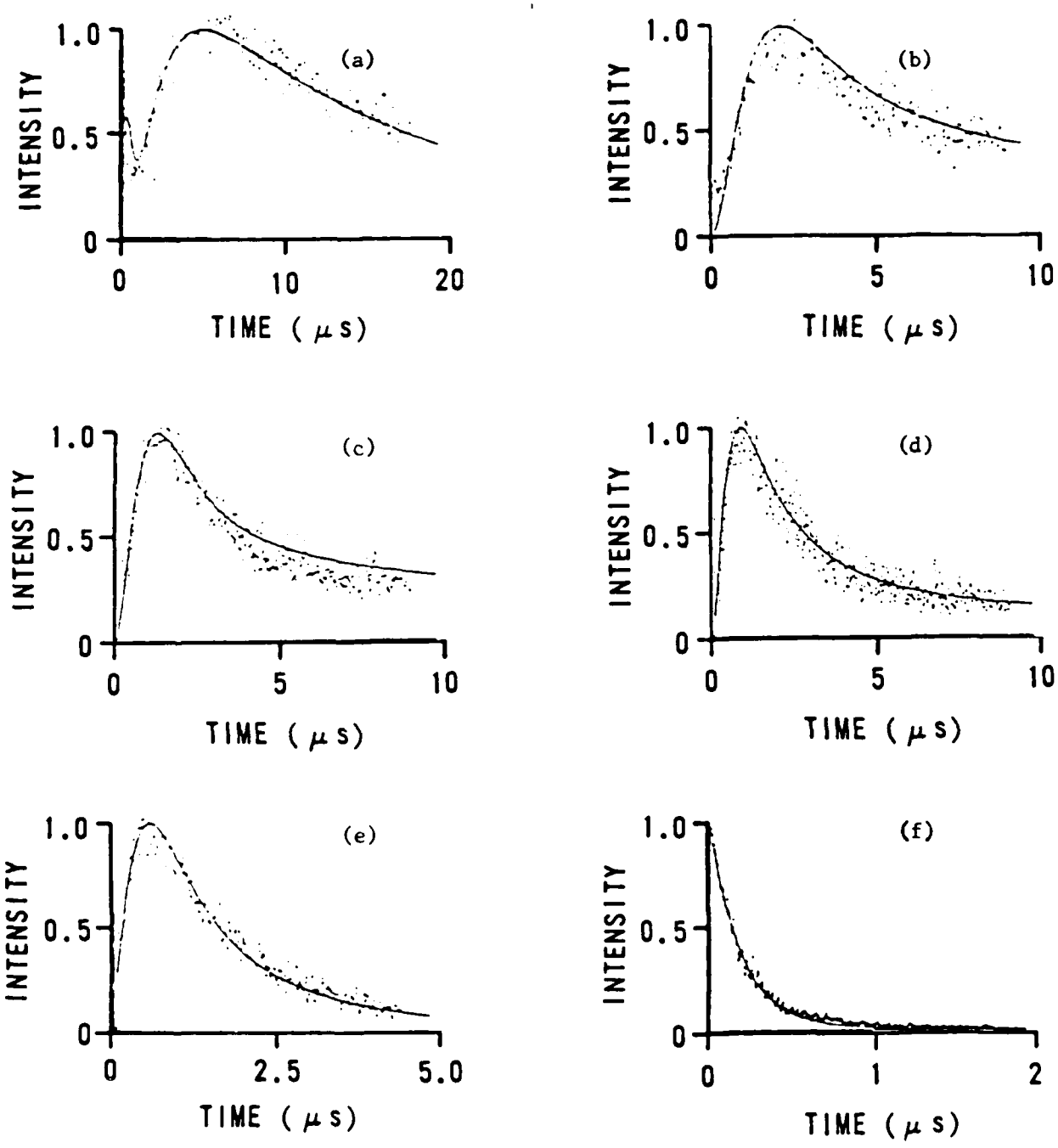

Figure 51. Examples of observed spectra and numerical predictions for BrCl(B) + He, based on the solution of table XIV. The intially populated state is $v'=6$, the mix pressure, helium pressure and observed states are: (a) M=0.711 T, He=1.3 T, $v'=0$, (b) M=0.524 T, He=1.5 T, $v'=1$, (c) M=0.397 T, He=1.6 T, $v'=2$, (d) M=0.203 T, He=1.8 T, $v'=3$, (e) M=0.210 T, He=1.8 T, $v'=4$, (f) M=0.048 T, He=1.5 T, $v'=6$.

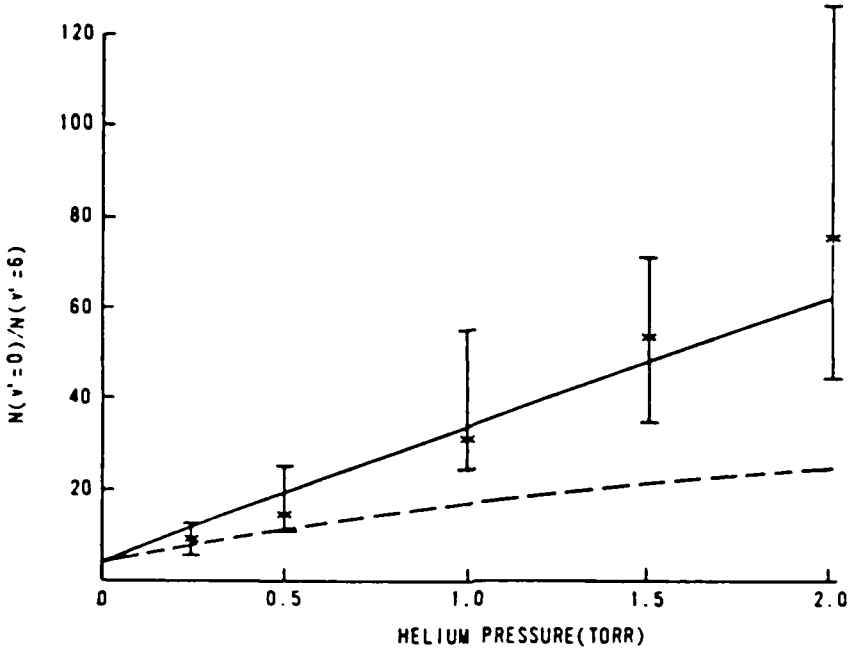

Figure 52. Steady-state relative number densities for $v'=0$ with helium as the buffer gas. The predicted distributions are based on the rate matrix of table XIV (——) and table (XV) (---).

is due to the chlorine collision partner rather than the BrCl(B) manifold. Thus, the helium data is consistent with the proposed resonant electronic exchange reaction involving $Cl_2(A)$ and $Cl_2(B)$.

The fundametal rate constants for the remaining rare gases were obtained by assuming no vibrationally-dependent quenching reactions. The single parameter for the numerical solutions was the rate constant $k_v^B(1-0)$. The resulting rate constants are reported in table XVI. The observed and predicted spectra were compared for pressures in the range

50 mtorr to 8 torr, for initially populated state, $v_o'=5$ and observed states $v'=0-6$. The agreements between predicted and observed spectra are similar to that shown in figure 51.

Table XVI
Rare Gas Fundamental Vibrational Rate Constants

Gas	$k_V^B(1-0)$ $(10^{-12}$ cm^3/molec-s)
He	4.0
Ne	4.0
Ar	4.0
Kr	2.0
Xe	3.0

In general, vibrational transfer is most efficient when the interaction time or mean time between collisions is similar to the vibrational period. The interaction time depends on the mean realtive velocity, $v=(8k_BT/\pi\mu)^{1/2}$, and thus on the reduced mass, μ, of the collision pair. Lower mass collision partners imply higher relative translational velocities and generally greater probability for vibrational transfer. The SSH theory[178] described in Appendix D addresses this reduced mass dependence and may be applied to the data of table XVI. The theory predicts

$$\ln(\sigma_{v,v-1}/\sigma_g) = A - B(\mu)^{1/3} \qquad (101)$$

where

$\sigma_{v,v-1}$ = collisional cross-section for V-T transfer from state v to state v-1

σ_g = gas kinetic collisional ss-section

A,B = constants, independant of reduced mass

Figure 53 illustrates the dependence of the vibrational transfer probability for $v'=1$ to $v'=0$ transfer as a function of the reduced mass as given by equation (101). Also shown in figure 53 are the trends for the halogen I_2 and interhalogen IF.

The reduced mass dependence of IF(B) V-T transfer agrees well with the SSH theory whereas the rates for I_2(B) and BrCl(B) deviate significantly from a $\mu^{1/3}$ dependence. The SSH theory uses time-dependent perturbation theory to describe vibrational transfer in a harmonic oscillator where interactions are relatively weak and restricted to $|\Delta v|=1$ transitions. The vibrational energy spacing in IF(B) is approximately 400 cm^{-1} and the restriction to single-quantum vibrational transfer is reasonable. The vibrational energy spacing in I_2(B) is $\sim$128 cm^{-1} and in BrCl(B) is $\sim$200 cm^{-1}. The interactions are strong and the probablility for multiquantum transfer is significant when the vibrational spacing is this small, $\Delta\varepsilon/k_BT = 1$. Therefore, it is not surprising that V-T transfer in I_2 and BrCl differ from the predictions of the SSH theory.

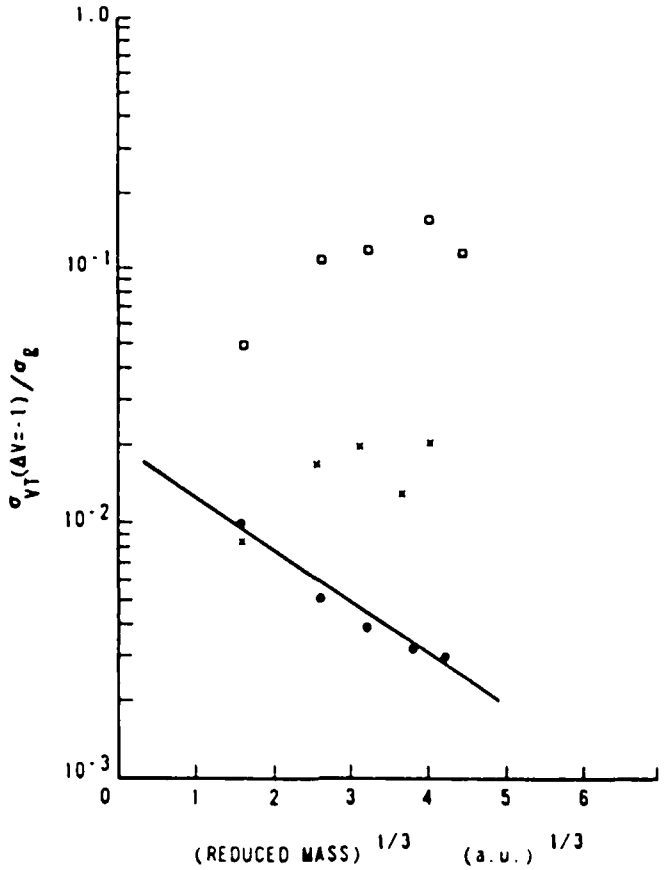

Figure 53. Scaling of vibrational transfer with reduced mass for (●) IF(B), (×) BrCl(B), and (□) I_2(B).

10. Summary of the Temporally-Resolved Studies

The fundamental vibrational transfer rate constant for BrCl(B) collisions with the mix has been obtained from the Montroll-Shuler model and is $k_V^M(1\text{-}0) = 1.3\times10^{-11}$ cm^3/molec-s. The Montroll-Shuler model adequately describes vibrational transfer in BrCl(B) only for the lowest vibrational states, v′=0-2. The higher vibrational states are greatly affected by increased quenching due to vibrational ladder climbing to predissociated states and another removal process, probably resonant electronic exchange with Cl_2. For these higher lying

states, no simple pressure scaling can be applied to the temporal spectra.

The interpretations of Clyne and McDermid[120-123] regarding vibrational transfer in BrCl(B) do not adequately describe the complete set of spectrally-resolved, temporally-resolved spectra obtained in this study. This descrepancy indicates the observed quenching cannot be adequately described only by vibrational ladder climbing to predissociated states. Indeed, resonant energy transfer from BrCl(B) to excited electronic states of Cl_2 is indicated.

A numerical solution to the vibrational energy transfer problem provides a set of possible solutions. The pulsed lifetime data for quenching rates and the high pressure CW LIF data provide the required information for the selection of a most favorable solution. This method has been applied to V-T transfer in BrCl(B) to obtain the scaling of the fundamental vibrational transfer rate constant to higher vibrational states. The scaling obeys a power law. For the mix collisions the result is $k_V^M(v \rightarrow v-1) = v^{0.62}\ k_V^M(1-0)$. With this solution, the entire set of temporally-resolved data for $v_o'=1-6$, $v'=0-6$ and for pressures 50 mtorr to 10 torr are reproduced.

Fundamental vibrational transfer rate constants for rare gas collision partners have been obtained and range from 2×10^{-12} cm^3/molec-s for Kr to 4.0×10^{-12} cm^3/molec-s for

He. The probability for vibrational transfer is relatively independent of reduced mass of the collision pair. Since the vibrational energy spacing is nearly resonant with the mean kinetic energy, all collision partners are efficient at inducing vibrational transfer. These rate constants have been obtained from the numerical solution, assuming the scaling of V-T transfer rates based on the Landau-Teller theory. The complete set of observed temporal spectra for rare gas collision partners is consistent with the Landau-Teller theory.

E. Steady-State Spectrally-Resolved Studies

1. Introduction

In Section IVB the general features of the steady-state spectrally-resolved data were discussed. The extraction of state-to-state vibrational transfer rates and total rotational removal rates was not possible since the quenching mechanism had not yet been identified. In section IVC the lifetimes needed for equations 45-47 were measured and in section IVD the quenching mechanisms were identified. Furthermore, the lifetimes needed to reduce the CW spectrally-resolved data may be predicted from the pulsed rate matrix, R_{pq}, given in table XII.

An independent measure of the vibrational transfer rates from the pulsed and CW experiments is not posssible. Data from both experiments are required in order to obtain a complete and accurate descripton of the BrCl(B) energy transfer processes. A complete description was established in section IVD. It is important to check the consistency of the pulsed R_{pq} matrix with the CW data, however. Several important observations regarding detailed balance and the scaling of vibrational transfer rates with vibrational quantum number will be obtained from the CW spectrally-resolved data. Also, the CW experiments provide the only information regarding total rotational removal rates.

2. Self Vibrational Transfer

CW spectrally-resolved data similar to that shown in figures 21-22 may be used to extract state-to-state vibrational transfer rates. The area under the spectra of each vibrational band is proportional to the population of that state as given by equation (6). The method used to obtain these areas and populations is described in appendix I.

Figure 54 illustrates typical data for the relative populations of spectrally-resolved vibrational bands as a function of total $BrCl-Cl_2$ mix pressure in the range 5-100 mtorr. States $v_o'=6,5,4$ were initially-populated and states $\Delta v = +1,-1$, and -2 were observed as satellite bands. For the pressures of the CW experiments, the vibrational transfer exists under roughly single collision conditions, but quenching is due to multiple collisions.

Equations 45-47 predict a linear dependence for relative population with the product $\tau_{v'} M$. The quenching rates are very large and thus the pressure dependence of the lifetime factor is very strong. In fact, as mix pressure approaches infinity, the product $\tau_{v'} M$ approaches $1/K_R^M(v')$ or $(\tau_{v'}/\tau_o) M = 3.1$ mtorr for $v'=6$. Thus, even large variations in total pressure imply only small changes in the product $\tau_{v'} M$ and the data all have similar values for the dependent variable. Therefore, a linear fit to plots of relative

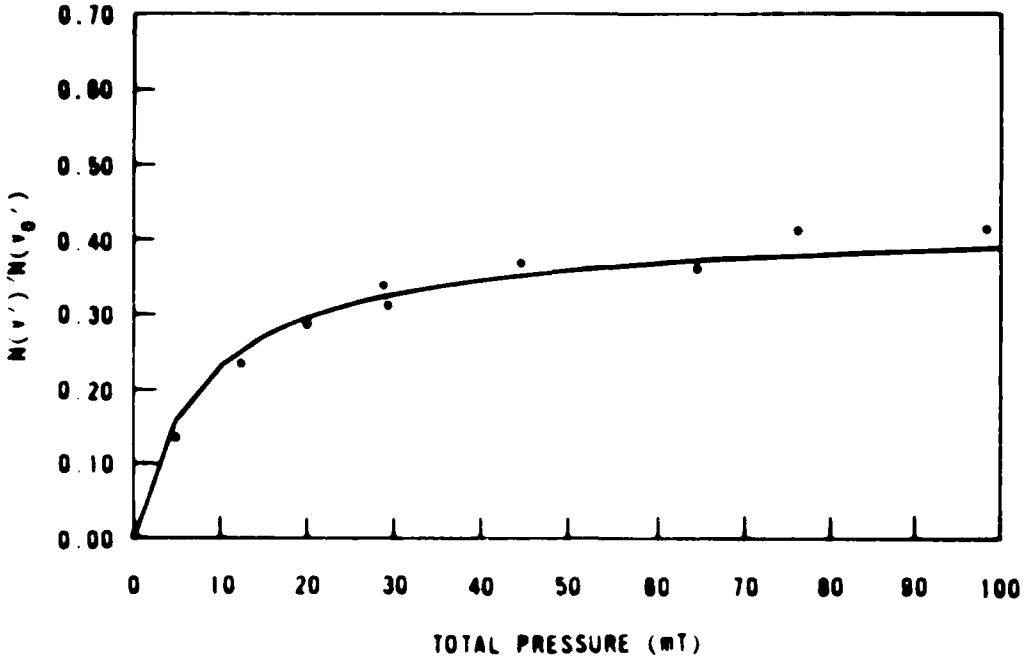

Figure 54a. Relative CW populations for initially populated state $v_0'=6$ and observed state $v'=5$.

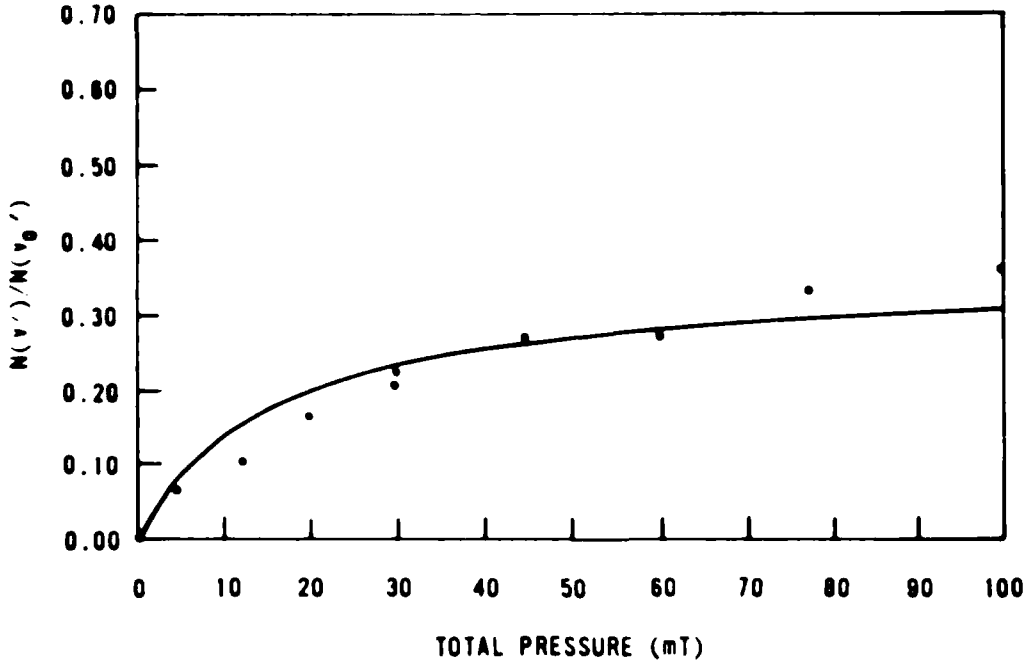

Figure 54b. Relative CW populations for initially populated state $v_0'=6$ and observed state $v'=4$.

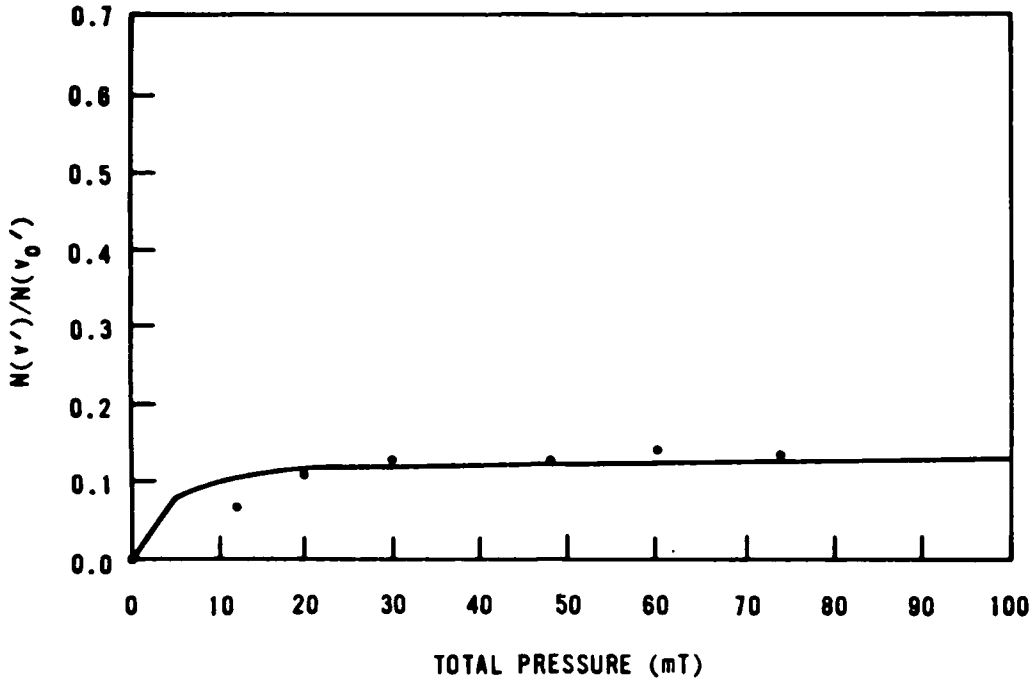

Figure 54c. Relative CW populations for initially populated state $v_0'=5$, observed state $v'=6$.

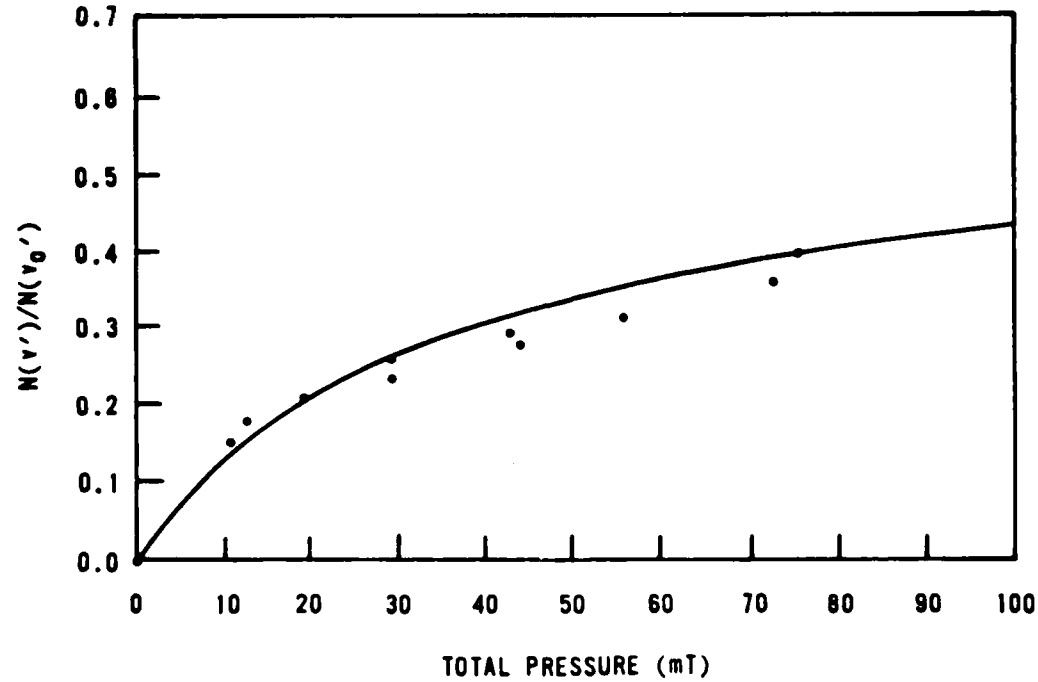

Figure 54d. Relative CW populations for initially populated state $v_0'=4$, and observed state $v'=3$.

population versus $\tau_{v'-M}$ provide rate constants with large error bounds.

The best consistency check for the rate matrix R_{pq} and the CW data is accomplished by solving the steady-state master equation (30) using the pulsed rate matrix and comparing these predictions with the observed CW spectra. This can be accomplished in two ways; (1) the system of linear equations given by equation (30) can be inverted directly to obtain the steady-state populations, or (2) the pulsed master equation (66) can be integrated over all time, yielding the time-averaged populations. The two methods are equivalent and both have been used, depending on the convenience of the particular case.

Two problems arise when the modeled results and the observed CW data are compared. First, the state-to-state vibrational transfer rates for $\Delta v'<0$ are slightly too large for the $v'=4$ and 5 states. Secondly, the $\Delta v'=+1$ bands have predicted number densities several times too low to match the observed CW spectra. These differences have been corrected for by decreasing the $\Delta v'=-1,-2$ rates for $v'=4$ and 5, increasing the $\Delta v'=+1$ rates for $v'=4$ and 5, and allowing for small variations in the resonant electronic exchange rates. This modified CW rate matrix is reported in table XVII and the predicted populations are presented as the solid curves in

figure 54. The agreement of the observed data and predicted populations is very good for a wide range of vibrational states and pressures. Note that these predicted populations do not represent independent fits to the data, but rather are based on a single rate matrix.

Table XVII
Self Transfer CW Rate Matrix, R_{pq}
(10^{-11} cm^3/molec-s)

q=	0	1	2	3	4	5	6	7	8
p=0	0.0	1.3	.52	0.0	0.0	0.0	0.0	0.0	0.0
p=1	.46	0.0	1.3	.52	0.0	0.0	0.0	0.0	0.0
p=2	.07	.49	-.28	1.3	.52	0.0	0.0	0.0	0.0
p=3	0.0	.08	.51	-.56	1.3	.75	0.0	0.0	0.0
p=4	0.0	0.0	.08	.53	-3.4	2.5	1.6	0.0	0.0
p=5	0.0	0.0	0.0	.09	2.6	-5.6	4.3	1.8	0.0
p=6	0.0	0.0	0.0	0.0	.16	3.2	-15.	2.2	.95
p=7	0.0	0.0	0.0	0.0	0.0	.38	2.1	-11.	4.8
p=8	0.0	0.0	0.0	0.0	0.0	0.0	.49	2.5	-13.

The differences in the CW and pulsed rate matrices can be observed by comparing tables XII and XVII. There are two primary differences; (1) the scaling of V-T rates with vibrational quantum number, and (2) the applicability of detailed balance to obtain the $\Delta v'>0$ rate constants.

The scaling of vibrational rate constants with vibrational quantum number for the pulsed and CW solutions are compared in figure 55. Also included is the scaling predicted by the Landau-Teller theory. Error bars are indicated and were estimated by noting the sensitivity of the modeled populations and spectra to the elements of R_{pq} and the scatter

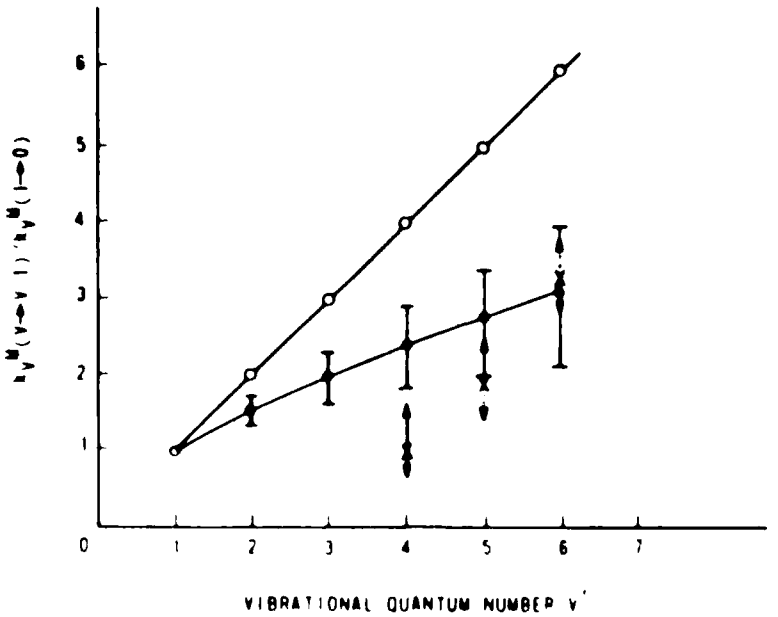

Figure 55. Scaling of self vibrational transfer rates with vibrational quantum number for (●) the pulsed data, (+) the cw data, and (O) as predicted by the Landau-Teller model.

in the experimental data. Appendix H describes this error analysis in detail. The error in the two experiments do not quite overlap for v'=4 and there appears to be a small difference in the two results. The error in the data is also not large enough to allow for agreement with the Landau-Teller scaling theory.

A comparison of the $\Delta v = +1$ rate constants for the pulsed and CW solutions is shown in figure 56. The pulsed solutions reflect the detailed balancing used to construct the pulsed R_{pq} rate matrix. The CW result clearly violates detailed balance. The CW populations in the $\Delta v = +1$ bands are simply too large to be accounted for by detailed balance. The CW results are not contradictory to the pulsed solution, however. If the

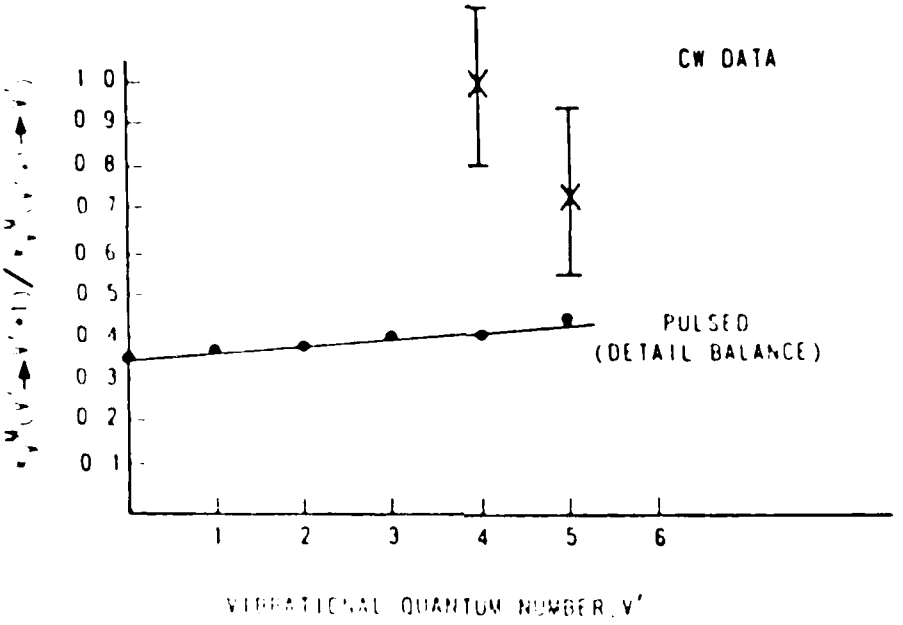

Figure 56. Comparison of pulsed and CW detailed balance rates for the mix vibrational transfer.

$\Delta v>0$ rates of the CW solution matrix are included in the pulsed model, the predicted spectra are not significantly altered. This is because the $\Delta v>0$ rates are small with respect to the total quenching.

The detailed balance violation of the third Clyne[123] model is much greater than the violation represented by the current results. In fact, the $\Delta v>0$ rates in the Clyne model are much too large for the CW populations observed in this thesis.

There are a number of factors that may contribute to the differences in the pulsed and CW results. The errors

discussed so far include only the scatter in the observed data and no account of systematic errors has been made. There may also be some transfer processes unaccounted for in the pulsed and CW models. Four specific issues will be addressed in the following paragraphs: (1) inaccurate accounting of mutiquantum transfer, (2) errors in the quenching rates, (3) accuracy of the Franck-Condon factors used in the CW experiment, and (4) the effects of Cl_2 energy resonances.

Multiquantum transfer was accounted for in both the CW and pulsed models by allowing only $|\Delta v| \leq 2$ transitions and assuming the $\Delta v=-2$ rates were a fixed 40 percent of the $\Delta v=-1$ rates, see equation (99). Variation of the mutiquantum transfer fraction, f, in predicting the CW populations will not account for the differences in the vibrational scaling or detailed balance ratio. Changing the multiquantum transfer fraction appreciably affects only the $\Delta v=-2$ populations. With $f=0.4$, the $\Delta v=-2$ populations are predicted quite well (see figure 54).

As noted earlier, the relative CW state-to-state vibrational populations are insensitive to total mix pressures above approximately 10 mtorr due to the large quenching removal from these states. The differences in vibrational scaling between the pulsed and CW data might therefore be due to errors in the quenching rate measurements. Indeed, at infinite pressure without return transfer to the satellite

states from other satellite states, the relative CW populations reach a limiting value equal to the ratio of V-T and total removal rate constants:

$$\lim_{M\to\infty}[N(v)/N(v_o)]=\lim_{M\to\infty}\{k_V^M(v_o-v)M/[\Gamma_o+K_R^M(v)M]\}$$
$$=k_V^M(v_o-v)/K_R^M(v) \qquad (102)$$

Since the CW data represents multiple collision conditions for quenching transfer, the CW modeling is largely dependent only on the rate constant ratio, $k_V^M(v_o-v)/K_R^M(v)$. Thus, the higher pressure CW data could be reproduced with the pulsed V-T transfer rates by increasing the total removal rates within the error of the measurement. Such CW models do not adequately predict the initial rise in population at mix pressures below approximately 20 mtorr, however. While the trade-off between quenching rates and vibrational transfer rates may explain some of the differences in the pulsed and CW results, it cannot completely explain the discrepancy.

The error in CW LIF energy transfer experiments is typically greater than in pulsed experiments due to systematic errors introduced from Franck-Condon factors (FCF's), spectral response of the detection system and other factors required to obtain relative steady-state populations. FCF's for the BrCl B-X system were discussed in section II and appendix B. These FCF's are not well established or experimentally verified. In the CW experiments, the data was recorded using transitions

where the FCF's are the largest and best established. Even so, the error in these numbers may be significant. The systematic errors introduced from the FCF's, spectral response calibration, and radiative lifetimes would need to be at least 20% to account for the differences in the CW and pulsed results. Appendix H establishes the uncertainty in these variables as at least 30 %.

It seems unlikely that errors in FCF's can account for the detailed balance violation observed in the CW data, however. The FCF's would need to be uniformly too small to account for the large populations in all the $\Delta v=+1$ states. In addition, the same high satellite populations are observed from transitions differing only in the terminal v" state.

The proposed mechanism for BrCl(B) electronic transfer to excited electronic states of Cl_2 did not include the posibility of return transfer from these excited chlorine states to the BrCl(B) manifold. Such return transfer events could modify the BrCl(B) vibrational distribution and partially account for the enhanced populations in $\Delta v=+1$ bands. Note that the BrCl(B) concentrations are small and thus the Cl_2(A) concentrations are small. Therefore, the return transfer to BrCl(B) must be a small effect.

While the pulsed and CW experimental results do not completely agree, the differences may be explained by the arguments just presented. No other rate matrices for the

pulsed and CW experiments have been identified that allow for a better agreement. There may be some minor energy transfer events such as transfer from excited chlorine states to BrCl(B,v') that have been excluded from the transfer rate matrix and would account for the seeming detailed balance violation and differences in vibrational transfer scaling.

3. Vibrational Transfer with Helium

The extraction of state-to-state vibrational transfer rate constants from CW spectrally-resolved data with helium as the collision partner is based on linear fits to the data from equation (51). Two factors make this feasible: (1) the magnitude of quenching and vibrational transfer rates is significantly less for the rare gases than for chlorine, and (2) there is no electronic exchange quenching for helium and the vibrational transfer rates are a sizeable fraction of the total vibrational removal rates.

Typical CW He data is shown in figure 57. To use equation (51) and make linear fits to the data of figure 57, the buffer gas pressure dependence to the vibrational state's lifetime is neglected. The slope of the linear fits, shown as a solid line in figure 57, provides the quantity

$$\tau_v \, k_v^Y(v_o-v) \, Y \, \{1-[N(v)/N(v_o)]_{Y=0} \, K_R^Y(v)/k_v^Y(v_o-v)\} \quad (103)$$

The lifetimes are calculated from the self transfer CW rate matrix of table XXII. The quantity in brackets is evaluted

from experimentally observed population ratios at zero helium pressure and a calculated rate constant ratio, $K_R^Y(v')/k_V^Y(v_o'-v')$. This rate constant ratio is calculated using detailed balance, Landau-Teller vibrational scaling and multiquantum transfer with f=0.4. The calculated ratios are discussed and listed in appendix J.

The resulting rate constants are listed in table XVIII. Several approximations have been made to obtain these rate constants. Rather than justifying the approximations, the exact solution based on the derived constants is obtained from the CW master equation (30). The predicted populations are also shown in figure 57. The agreements are good and well within the experimental scatter. Agreement is best for $\Delta v=-1$.

Table XVIII
CW Helium V-T Rate Constants
(10^{-11} cm^3/molec-s)

v'	$k_V^{He}(v \cdot v-1)$	$k_V^{He}(v \cdot v-2)$	$k_V^{He}(v \cdot v+1)$
4	0.61	0.2	0.80
5	1.6	0.4	1.5
6	2.3	0.7	1.1

Note that the helium vibrational transfer obeys detailed balance. The detailed balance rates and expected ratios are shown in table XIX.

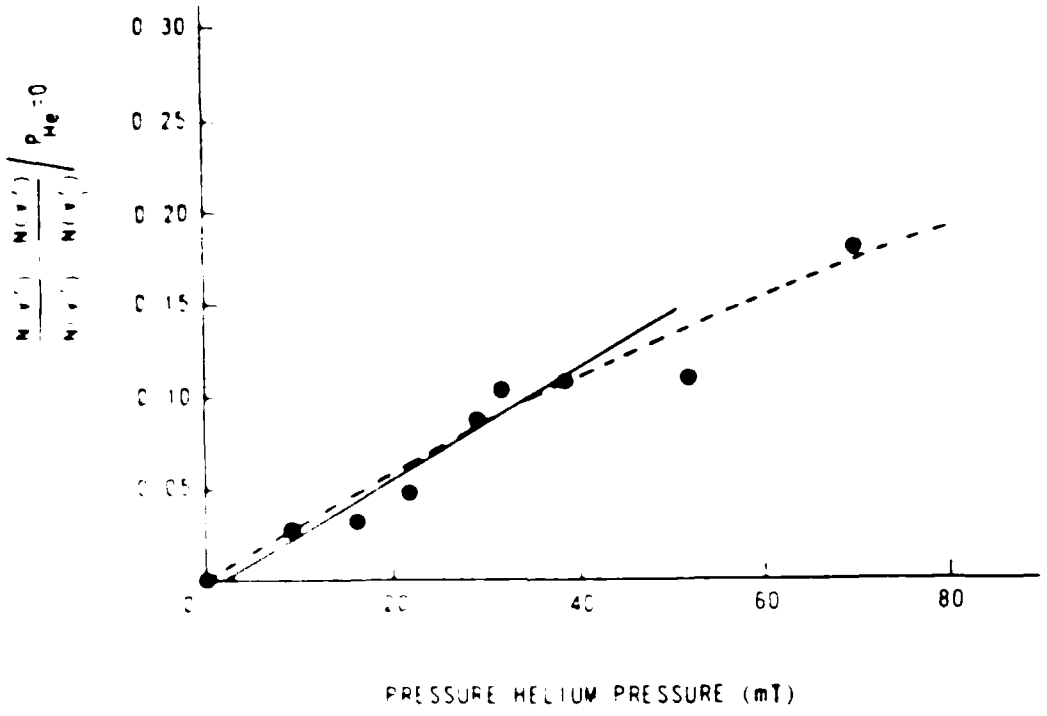

Figure 57a. Relative CW vibrational populations for Br[Cl(B,v′)] + He collisions. The initially populated state is v_o'=5 and the observed state is v′=5.

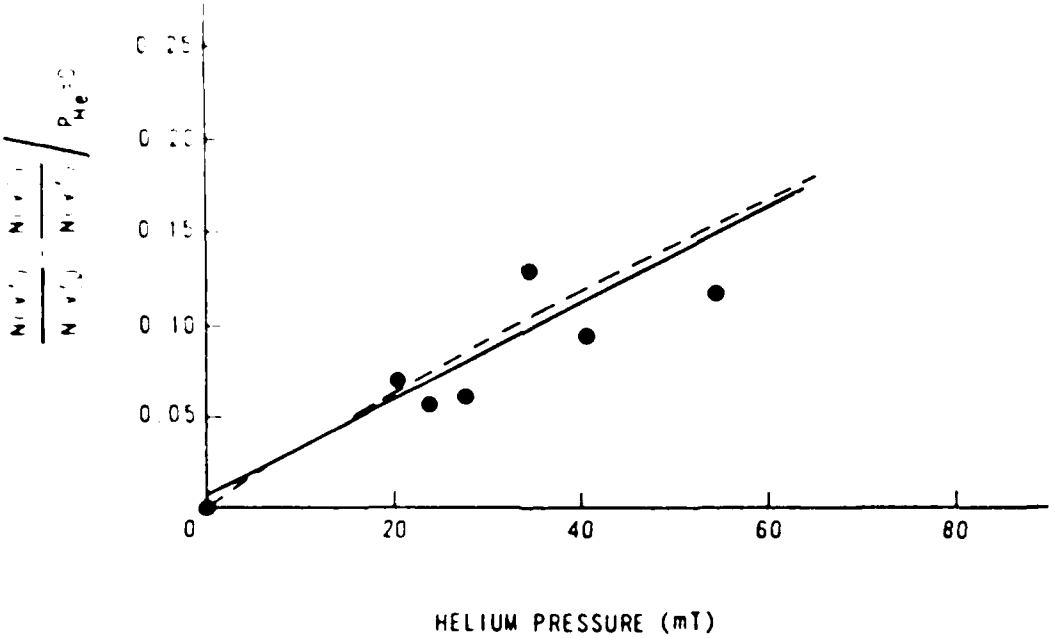

Figure 57b. Relative CW vibrational populations for BrCl(B;v′) + He collisions. The initially populated state is v_o'=5 and the observed state is v′=4.

AD-A179 575 COLLISIONAL DYNAMICS OF THE B 3PI(O+) STATE OF BROMINE MONOCHLORIDE(U) AIR FORCE INST OF TECH WRIGHT-PATTERSON AFB OH SCHOOL OF ENGINEERING G P PERRAM AUG 86 3/4

UNCLASSIFIED AFIT/DS/PH/86-1 F/G 7/2 NL

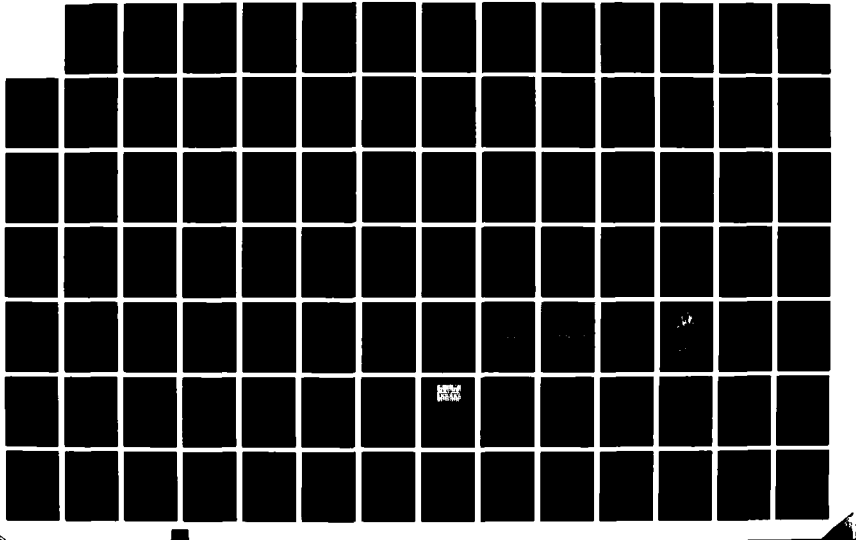

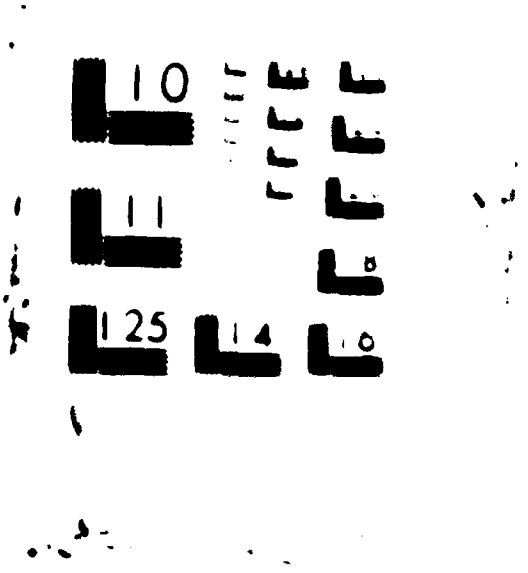
10
11
1.25
1.4
1.6

Table [illegible]

[illegible] transfer [illegible] Balance Ratio[illegible]

[illegible]

[illegible] are [illegible] again, the area under [illegible] and the [illegible] under the [illegible] area and thus the relative [illegible] detail in appendix [illegible]. The total [illegible] rate constants, k^{M} [illegible], are obtained from equation [illegible] for the self transfer case and from equation [illegible] for the buffer transfer case. The lifetimes [illegible] equation [illegible] and (64) are evaluated from [illegible] matrix k_{ij}. The [illegible] and [illegible] correction factors, as defined in equations [illegible] and (53), are obtained from the [illegible] rate matrix and the solutions for the steady-state matrix as a function of pressure. Some representative plots for rotational transfer are given in figure 58 for the self transfer case and figure 59 for the buffer transfer case. The dependent axis variable $R(v_0', J_0')$ is defined as the right hand side of equation (61) for the self transfer and of equation (64) for the buffer transfer. A list of the resulting rate constants is provided in table XX.

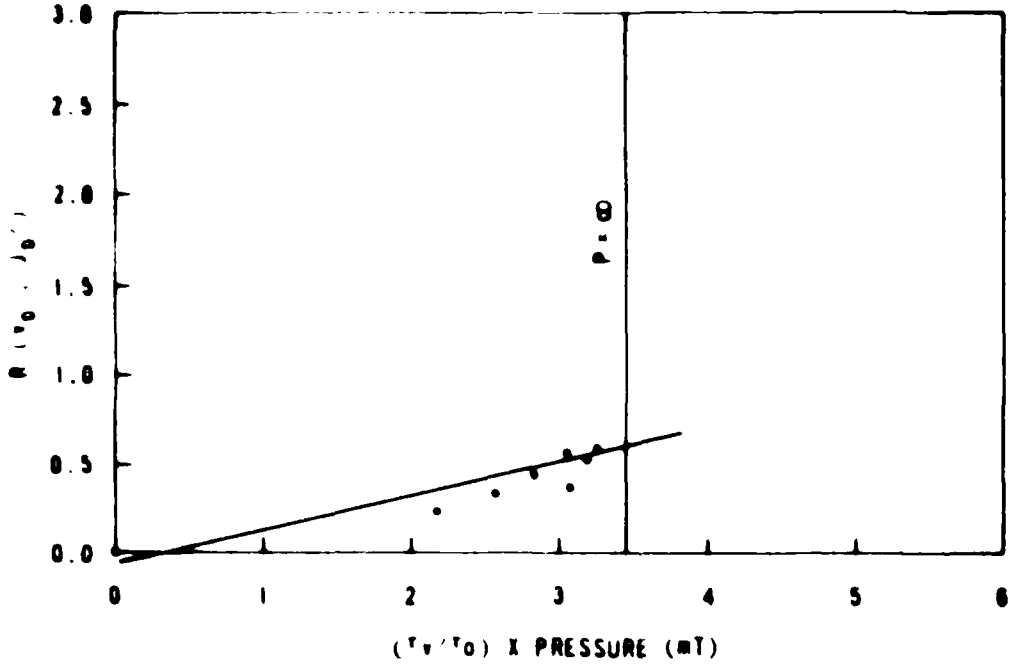

Figure 58a. Relative CW rotational populations for BrCl(B) collisions with the mix. The initially populated state is $v_o'=0$, $J_o'=37$.

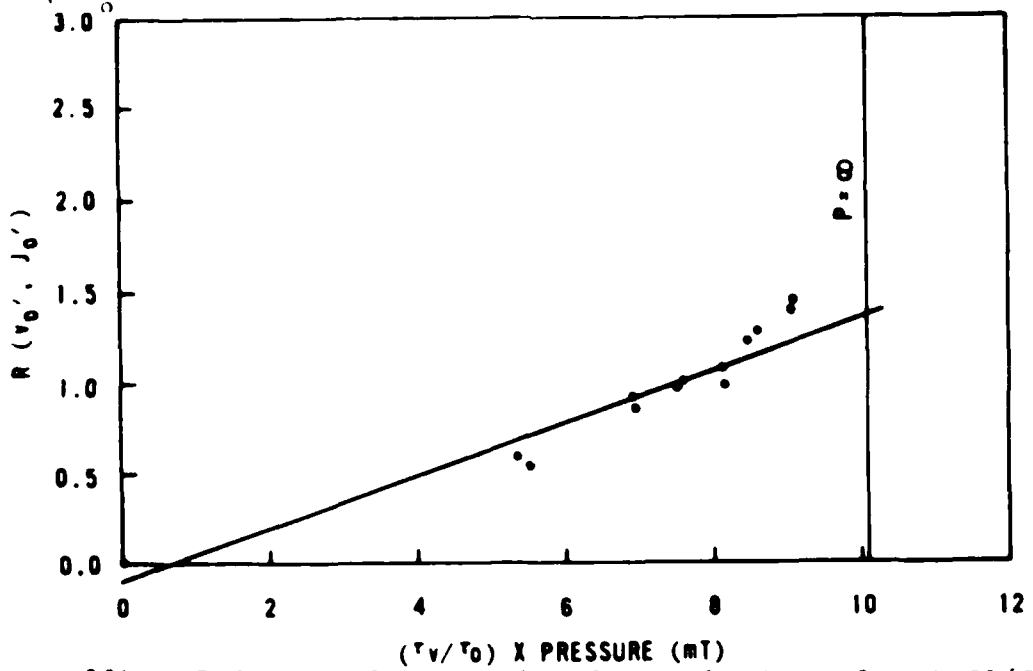

Figure 58b. Relative CW rotational populations for BrCl(B) collisions with the mix. The initially populated state is $v_o'=4$, $J_o'=27$.

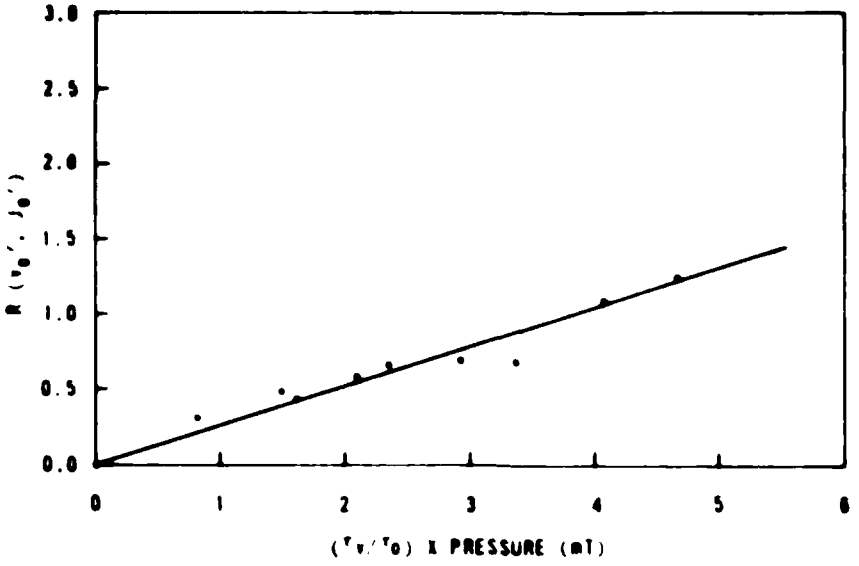

Figure 59a. Relative CW rotational populations for BrCl(B) collisions with helium. The initially populated state is $v_o'=6$, $J_o'=37$.

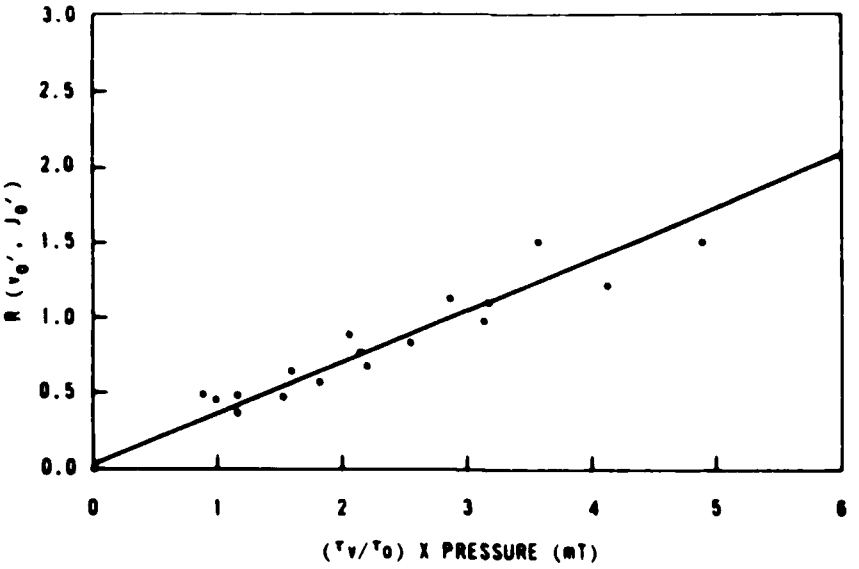

Figure 59b. Relative CW rotational populations for BrCl(B) collisions with argon. The initially populated state is $v_o'=6$, $J_o'=37$.

The relative rotational populations in figure 59 increase linearly with pressure, even at large buffer gas pressures. Typically, such rotational distributions do not continue to increase at high pressures, since rotational thermal equilibrium is eventually attained. Such an effect is not observed in BrCl(B), since quenching competes favorably with rotational transfer.

Table XX
Total Rotational Removal Rates
K_J (10^{-10} cm^3/molec-s)

Buffer Gas:	Cl_2	He	Ar	Xe
$v'=4$ $J'=27$	1.20	0.70	1.24	0.89
$v^o{}'=5$ $J^o{}'=39$	1.53	1.43	1.48	1.19
$v^o_o{}'=6$ $J^o_o{}'=37$	1.60	1.93	2.43	2.17

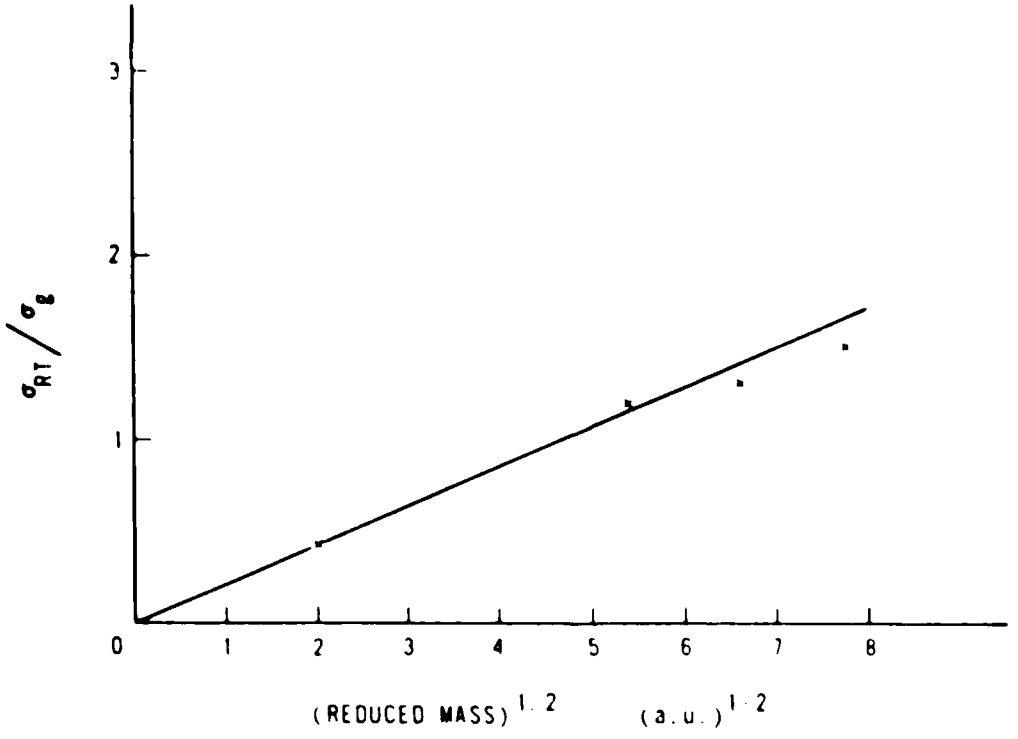

Figure 60. Scaling of rotational removal rates with reduced mass of the collision partner.

The scaling of the total rotational removal rates with the reduced mass of the collision partner is shown in figure 60. Collision partners with higher masses also have larger angular momentum to impart to the rotating BrCl(B) molecule. Simple classical arguments suggest the R-T rates should scale linearly with the square root of the reduced mass of the collision pair. Appendix D describes this classical model in more detail. The data of figure 56 do indeed scale linearly with $\mu^{1/2}$. Note also the cross-sections for rotational transfer are approximately gas kinetic. The rotational spacing in the interhalogens is quite small and one would expect near unit probability for rotational energy transfer.

Rotational transfer in several parent vibrational states (v_o'=6,5,and 4) was studied. Rotational transfer was noted to be more rapid in the higher vibrational states. A plot of the relative cross-sections versus vibrational quantum number for several collision partners is shown in figure 61. No obvious interpretation of this scaling is provided.

5. Summary of the Steady-State Studies

The steady-state experiments provide critical information regarding the relative population distributions and are required to obtain a unique solution to the temporally-resolved energy transfer problem. A solution for the rate

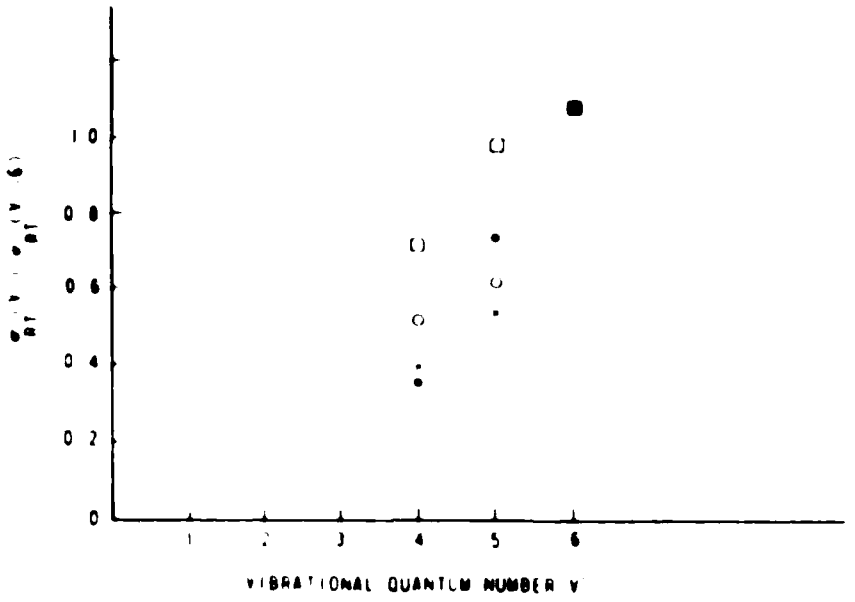

Figure 61. Cross-sections for total rotational removal for various vibrational levels of BrCl(B). Buffer gases are: (●) helium, (○) argon, (×) xenon, (□) chlorine.

matrix R_{pq} has been obtained from the CW spectrally-resolved data. This solution is consistent with the pulsed solution described in section IVD. The steady-state spectra of $\Delta v=+1$ states for self transfer indicate rates slightly larger than provided by detailed balance, whereas the same spectra for helium agree with detailed balance. State-resolved V-T transfer rates for the self transfer case are difficult to obtain since quenching is efficient. The CW vibrational populations reach a maximum value determined by the ratio of vibrational transfer rate to the quenching rate. The CW studies provide the only information regarding rotational transfer. The total rotational transfer rates are nearly gas kinetic and scale with the mass of the collision partner in accordance with classical angular momentum considerations.

V. CONCLUSIONS

The radiative and collisional dynamics within the excited $B\,^3\Pi_0^+$ electronic state of the interhalogen bromine monochloride have been studied using temporally-resolved and steady-state, spectrally-resolved laser induced fluorescence techniques. The processes of spontaneous emission, electronic quenching, predissociation, resonant electronic energy exchange, state-to-state vibrational transfer, and total rotational removal have been described in detail for BrCl(B) collisions with Cl_2, He, Ne, Ar, Kr, Xe, N_2, and O_2. The general problem of extracting quantum resolved transfer probabilities for a strongly coupled ro-vibrational manifold from observed population distributions has been studied. This research was conducted to evaluate the potential of BrCl(B) as the excited laser level for a visible chemical laser.

A. Summary of BrCl(B) Energy Transfer

The radiative lifetime of BrCl(B;v′) is 38.7 +/- 1.7 μs, independent of vibrational state for v′<7. The relatively long radiative lifetime is due to the difference in spin multiplicity and the large difference in equilibrium internuclear separation of the excited $B\,^3\Pi$ state and the ground $X\,^1\Sigma$ state. States with energy above that of the v′=6, J′=42 state are predissociated due to an intersystem crossing with a repulsive $^3\Pi 0^+$ state correlating to

$Br(^2P_{3/2}) + Cl(^2P_{3/2})$ seperated atomic states. The predissociated states have collisionless lifetimes of 8 - 0.1 μs.[121]

The vibrational energy spacing in BrCl(B) is small and deviates significantly from that of a harmonic oscillator. The energy spacing $\Delta\varepsilon = \varepsilon_v - \varepsilon_{v-1}$ ranges from 213 to 151 cm^{-1}, or $\Delta\varepsilon / k_B T = 0.36$ to 0.48, for v'=0-6. The entire ro-vibrational manifold is strongly coupled and multiquantum V-T transfer is probable.

The electronic quenching of a thermalized BrCl(B;v',J') distribution is inefficient with rate constants ranging from 7.8 +/- 1.9 x 10^{-14} cm^3/molec-s for Ne collisions to 4.3 +/- 0.7 x 10^{-13} cm^3/molec-s for Cl_2 collisions. Electronic quenching by ground state O_2 is anomolously fast with a rate constant of 6.5 +/- 0.6 x 10^{-12} cm^3/molec-s. The quenching of nonthermal BrCl(B;v') distributions is more complicated and depends strongly on the total pressure. The removal of states v'>2 is considerably faster than the electronic quenching and strongly depends on vibrational state. Overall quenching of nonthermalized BrCl(B) distributions are interpreted as population distribution weighted convolutions of the vibrationally dependent quenching rates. Two processes contribute to the increased quenching of high v' states: (1) ro-vibrational ladder climbing to predissociated states, and (2) resonant electronic exchange

reactions possibly involving Cl_2 A, B, and X states. The quenching rate constants for BrCl(B;v′) with Cl_2(X) collisons range from 4.3 +/- 0.7 x 10^{-13} cm^3/molec-s for v′=0 to 1.4 +/- 0.3 x 10^{-10} cm^3/molec-s for v′=6. No resonant electronic exchange reactions were observed for the rare gases.

The thermalization of the BrCl(B) manifold is rapid. Vibrational transfer rate constants for transfer from v′=1 to v′=0 vary from 1.3 x 10^{-11} cm^3/molec-s for Cl_2 collisions to 2.0 x 10^{-12} cm^3/molec-s for Kr collisions. There is little or no scaling of V-T transfer probabilities with the reduced mass of the collision partner for the rare gases. The scaling of V-T rates with vibrational quantum number obeys a power law, $k_v^Y(v\ v-1) = v^n\ k_v^Y(1-0)$. The power law yields n= 0.62 for Cl_2 collisions and n=1 for the rare gases. The rare gas vibrational transfer scales according to the Landau-Teller theory. Multiquantum vibrational transfer, $\Delta v'=-2$, is estimated as 40 percent of the single quantum, $\Delta v'=-1$, rate.

Rotational transfer is very efficient with nearly gas kinetic cross-sections. The rate constants for total rotational removal from $J_o'=37$ in v′=6 range from 1.60 x 10^{-10} cm^3/molec-s for Cl_2 to 2.43 x 10^{-10} cm^3/molec-s for Ar. Rotational transfer is slightly slower in lower v′ states. Change of rotational state in V,R-T collisions is likely and little memory of the initially-populated rotational

state is observed in satellite vibrational bands. Total rotational removal rates increase linearly with the square root of the reduced mass of the collision partner for the rare gases, as predicted from classical angular momentum considerations. Thermal ro-vibrational distributions are attained at Cl_2-BrCl mix pressures as low as several torr.

A summary of rate constants for quenching, V-T transfer and total rotational removal is given in table XXI.

B. Implications for LIF and Energy Transfer Studies

Since the 1930's, the field of chemical physics has been particularly interested in the problem of inelastic energy transfer among molecules in the gas phase.[135-136] There has been considerable progress in the theoretical development of quantum resolved energy transfer processes, and laser induced fluorescence techniques have been sucessfully applied to obtain experimental measurements of state resolved cross-sections for energy transfer events. Several general conclusions regarding these LIF energy transfer studies may be drawn from the results of the current studies. Specifically, spectral response, synergy between the pulsed and cw experiments, quenching versus vibrational transfer efficiency, and vibrational energy spacing will be addressed.

The importance of spectral response in both cw and pulsed LIF experiments has been considered in previous studies. The

Table XXI
Summary of BrCl(B) + Y Rate Constants

Y	k_{eq}^{Y} (10^{-13} cm^3/molec-s)	$k_V^Y(1,0)^a$ (10^{-12} cm^3/molec-s)	K_J^Y (10^{-10} cm^3/molec-s)
Cl_2	4.3 +/- 0.7	13.	1.60 +/- .28
He^2	1.5 +/- 0.2	4.0	1.93 +/- .34
Ne	0.78 +/- 0.19	4.0	**********
Ar	0.81 +/- 0.30	4.0	2.43 +/- .44
Kr	0.98 +/- 0.14	2.0	**********
Xe	**********	3.0	2.17 +/- .31
N_2	1.6 +/- 0.3	****	**********
O_2	65. +/- 5.7	****	**********

τ_r = 38.7 +/- .s

v'	$k_Q^M(v')^b$ (10^{-11} cm^3/molec-s)	$k_Q^{He}(v')^b$ (10^{-11} cm^3/molec-s)
0	0.043 +/- 0.007	0.015 +/- 0.002
1	0.043 +/- 0.007	0.015 +/- 0.002
2	0.043 +/- 0.007	0.015 +/- 0.002
3	0.40 +/- 0.2	0.015 +/- 0.002
4	5.5 +/- 1.8	0.015 +/- 0.002
5	7.9 +/- 2.2	0.015 +/- 0.002
6	17.0 +/- 3.6	6.8 +/- 2.6

a) Rate constants obtained from pulsed numerical solution. Error may be as large as 100%. See appendix H for error analysis.

b) Rate constants obtained from pulsed numerical solution. Error bounds are estimated from Stern-Volmer analysis.

current BrCl(B) pulsed lifetime studies provide an extreme example of these spectral response effects. Observed BrCl(B) lifetimes vary by as much as an order of magnitude with the various spectral responses used in the current pulsed experiments. Several factors contribute to the importance of spectral response in these experiments: (1) a large wavelength dispersion between the emission from different excited vibrational states, (2) a large variation in quenching rates with v′ state, (3) severe predissociation, and (4) rapid ro-vibrational thermalization processes.

The emission wavelengths from various v′ states within BrCl(B) are widely dispersed over the detected wavelength region 600 - 900 nm. The lowest v′ states (v′=0-3) emit strongly only at long wavelengths (750 - 900 nm) whereas the highest v′ states (v′=3-6) emit strongly only at short wavelengths (600 - 750 nm). As result, changes in spectral response can dramatically change the vibrational states being observed. Quenching rates and the effects of predissociation vary strongly with vibrational state and the observed lifetimes thus depend strongly on the spectral response of the detection system. The rapid ro-vibrational thermalization of BrCl(B) indicates that a rapid population of many (v′,J′) states occurs even at low buffer pressures. In addition, small changes in buffer pressure indicate large changes in the ro-vibrational distribution.

Theoretically, the pulsed and cw experiments provide the same information regarding state-to-state transition probabilities. The steady-state experiments are described by a temporal average of the pulsed experimental data. Practically, the pulsed and cw experiments provide quite different views of the energy transfer processes. In the present studies, both experiments where necessary to obtain a complete description of energy transfer in BrCl(B). The pulsed experiments provide a great deal of information detailing the full time history of the vibrational population distributions. Lifetimes are directly measured and the effects of systematic errors are reduced. The pulsed experiments do not provide accurate information regarding relative vibrational number densities, however. The cw experiments directly provide these relative populations. In addition, the higher average signal intensities of the cw experiments allow for greater spectral resolution and provide the only information regarding rotational transfer.

The conventional single-collision, steady-state kinetic analysis used to extract state-to-state vibrational transfer rate constants, as presented in section IIc2, is usually applied to systems where total quenching is inefficient with respect to vibrational transfer. In such cases, the lifetimes depend only slowly on buffer pressure and accurate vibrational rate constants are obtained. For BrCl(B), total quenching of high v′ states is very efficient. To obtain a significant

population in satellite vibrational bands, the collision conditions are single collision for V-T transfer but multicollision for quenching events. Therefore, lifetimes vary strongly with pressure and a significant variation in the dependent variable, τ_v M, is not obtainable and an accurate determination of state-to-state vibrational transfer rate constants is more difficult. The strong variation of quenching rates with total pressure also makes the cw data reduction more complicated.

The vibrational energy spacing is an important parameter in describing any vibrational transfer process. Large vibrational energy spacing effectively decouples the vibrational manifold. Theoretical descriptions of vibrational energy transfer in decoupled and weakly coupled vibrational manifolds are readily available and are easily applied to extract vibrational rate constants from observed population distributions. When the vibrational energy spacing approaches the average translational energy, $\langle \epsilon_g \rangle$, the vibrational states are strongly coupled and vibrational transfer is efficient. Low rotational level pumping for these strongly coupled systems [illegible] In addition, the experimental requirements for spectral and temporal resolution are more rigorous. Numerical models such as presented in this thesis are required to extract state-to-state vibrational transfer rates from strongly coupled vibrational manifolds.

Vibrational energy spacing also has important implications for the dynamical properties of the vibrational energy transfer process. Scaling of transfer probabilities with parameters such as reduced mass depend on the vibrational energy spacing. Further study, both theoretical and experimental, of vibrational transfer within strongly coupled vibrational manifolds is clearly needed.

C. Proposed Future Investigations

The radiative lifetimes, quenching rates, and vibrational transfer rates obtained for the B state of BrCl in this thesis provide detailed information for evaluating the potential of BrCl(B) as the excited electronic state for a chemical laser. Threshold chemical pumping requirements, expected gain, and optimal pressure operating conditions can be established based on the furnished rate constants. In addition, guidance for the selection of a chemical pumping mechanism can be provided.

Experiments to identify potential chemical-pumping mechanisms for BrCl(B) are needed to further evaluate the possibility of demonstrating a BrCl B-X chemical laser. A direct reaction of bromine with chlorine dioxide is known to produce a chemiluminescent BrCl(B) flame.[80] The photon yield of this reaction is 3%.[80] Two metastable transfer partners may provide alternate pumping mechanisms. Energy transfer with the metastables NF(b) or $O_2(^1\Sigma_g^+)$ may provide an efficient means of chemically populating the lower BrCl(B) vibrational

states. Flow tube studies should be conducted to determine the BrCl(B) yields of these and other chemical excitation mechanisms.

The results of this thesis have indicated that resonant electronic energy exchange between BrCl(B) and Cl_2(A,B) is an efficient process. No monitor of electronically-excited chlorine state populations was conducted in the present work. The detection of these excited chlorine states would be an important confirmation of the proposed quenching mechanism. Fluorescence from Cl_2(A,B) would be very weak, due to the unfavorable dipole moment with the ground electronic state. Optical excitation of Cl_2(A) to higher-lying electronic states of chlorine such as Cl_2(D) and the detection of the subsequent UV fluorescence may be the best way to detect the excited chlorine populations.

The spectroscopy of the BrCl(B-X) system is not completely characterized. Spectroscopic determination of transition frequencies involving high-lying vibrational states in the ground electronic state would be very valuable and lead to an important calculation of Franck-Condon factors for these states.

Several further studies based on the optically-pumped Br_2 B-X laser described in appendix A are provided at the end of appendix A. The study of state-to-state rotational transfer in Br_2(B) is strongly indicated.

Bibliography

1. J.V.V. Kasper and G.C. Pimentel, Appl Phys Lett, 5, 231, Dec 1,1964.

2. J.V.V. Kasper and G.C. Pimentel, Phys Rev Lett, 14, 352, Mar 8,1965.

3. J.H. Parker and G.C. Pimentel, J Chem Phys, 48, 5273, 1968.

4. M.A. Pollack, Appl Phys Lett, 9, 237, 1966.

5. D.J. Spencer, T.A. Jacobs, H. Mirels, and R.W.F. Gross, Int J Chem Kinetics, 1(5), 493, 1969.

6. J.C. Polanyi, J Chem Phys, 34(1), 347, 1961.

7. T.A. Cool, Int J Chem Kinetics, 1, 495, 1969.

8. A.N. Chester, Proc IEEE, 61(4), 414, 1973.

9. K.L. Kompa and G.C. Pimentel, J Chem Phys, 47, 857, 1967.

10. H. Pummer, W. Breitfeld, H. Wedler, G. Klement, and K.L. Kompa, Appl Phys Lett, 22(7), 319, 1 Apr 1973.

11. T.F. Deutsch, Appl Phys Lett, 10, 234, Apr 1967.

12. O.M. Batowskii, G.K. Vasilev, E.F. Makarov, and V.L. Talroze, JETP Lett, 9, 200, 1969.

13. D.J. Spencer, H. Mirels, and T.A. Jacobs,Appl Phys Lett, 16(10), 384, 1970.

14. T.J. Falk, Air Force Weapons Lab, Kirtland AFB, NM, AFWL-TR-71-96, June 1972.

15. S.N. Suchard, A. Ching, and J.S. Whittier, Appl Phys Lett, 21, 274, 15 Sep 1972.

16. T.A. Cool, T.J. Faulk, and R. Stephens, Appl Phys Lett, 15, 318, 1969.

17. R.W.F. Gross, J Chem Phys, 50, 1889, 1969.

18. H.S. Piloff, S.K. Searles, N. Djeu, Appl Phys Lett, 19, 1 July 1971.

19. S.K. Searles and N. Djeu, Chem Phys Lett, 12, 53, 1971.

20. W.Q. Jeffers, McDonnell Douglas Research, Lab Report No MDC Q0495, May 1973.

21. S.J. Davis, To be Published in Proceedings of Southwest Conference on Optics, 1985.

22. R.L. Byer, R.L. Herbst, H. Kildal, and M.D. Levenson, Appl Phys Lett, 20(1), 463, 1 June 1972.

23. B. Wellegehausen, K.H. Stephan, D. Friede, H. Welling, Optics Comm, 23(2), 157, Nov 1977.

24. J.B. Koffend and R.W. Field, J Appl Phys, 48(11), 4468, Nov 1977.

25. M.A. Henesian, R.L. Herbst, and R.L. Byer, J Appl Phys, 47(4), 1515, Apr 1976.

26. B. Wellegehausen, S. Shahdin, D. Friede, and H. Welling, Appl Phys, 13, 97, 1977.

27. H. Itoh, H. Uchiki, and M. Matsuka, Opt Comm, 18, 271, Aug 1976.

28. S.R. Leone and K.G. Kosnik, App Phys Lett, 30(7), 346, 1 Apr 1977.

29. B. Wellegehausen, IEEE J QE, QE-15(10), Oct 1979.

30. J.B. Koffend, R.W. Field, D.R. Guyer, S.R. Leone, Laser Spectroscopy III, Eds. J.L. Hall and J.L. Carlster.

31. F.J. Wodarczyk and H.R. Schlossberg, J Chem Phys, 67(10), 4476, Nov 1977.

32. S.J. Davis, L.Hanko, App Phys Lett, 37(8), 692, Oct 1980.

33. S.J. Davis, L. Hanko, R.F. Shea, J Chem Phys, 78(1), 172, 1983.

34. B. Wellegehausen, D. Friede, G. Steger, Opt Comm, 26, 391, Sep 1978.

35. R.F. Shea, International Chemical Congress of the Pacific Basin Societies, 1985.

36. M.D. Burrows, S.L. Baughcum, R.C. Oldenborg, Appl Phys Lett, 46(1), 1 Jan 1985.

37. R. Jones, AFWL Symposium on Chemical Lasers, July 1985.

38. R. Shea, Air Force Weapons Laboratory Memorandum, Chemical Laser Candidates.

39. R.B. Kurzel, J.I. Steinfeld, D.A. Hatzenguhler, G.E. Leroi, J Chem Phys, 55(10), 4822, 15 Nov 1971.

40. R.B. Kurzel amd J.I. Steinfeld, J Chem Phys, 53(8), 3293, 15 Oct 1970.

41. J.I. Steinfeld and W Klemperer, J Chem Phys, 42(10), 3465, 15 May 1965.

42. J.I. Steinfeld, J Chem Phys, 44(7), 2740, Apr 1966.

43. J.I. Steinfeld and A.N. Schweid, J Chem Phys, 53, 3304, 15 Oct 1970.

44. R.L. Brown and W. Klemperer, J Chem Phys, 41(10), 3072, 15 Nov 1964.

45. J. Tellinghuisen, J Chem Phys, 57(6), 2397, 15 Sep 1972.

46. M. Broyer, J. Vigue and J.C. Lehmann, J Chem Phys, 63(12), 5428, 15 Dec 1975.

47. G.A. Capelle and H.P. Broida, J Chem Phys, 58(10), 4212, 15 May 1973.

48. T.A. Brunner, R.D. Driver, N. Smith, and D.E. Pritchard, J Chem Phys, 70(9), 4155, 1 May 1979.

49. T.A. Brunner, N. Smith, A. Karp, D.E. Pritchard, J Chem Phys, 74(6), 3324, 15 Mar 1981.

50. K. Bergmann and W. Demtorder, J Phys B, 5, 1380, 1972.

51. K. Bergmann and W. Demtroder, J Phys B, 5, 2098, 1972.

52. K. Bergmann, W. Demtroder, M. Stuck, and G Vogl, J Phys B, 7(15), 2037, 1974.

53. M.P. Sinha, A. Schulz and R.N. Zare, J Chem Phys, 58(2), 549, 15 Jan 1973.

54. C. Ottinger and D. Poppe, Chem Phys Lett, 8(6), 513, 15 Mar 1971.

55. G. Ennen and C Ottinger, Chem Phys, 3, 404, 1974.

56. C. Ottinger and M Schroder, J Phys B, 13, 7163, 1980.

57. T.A. Caughey and D.R. Crosley, J Chem Phys, 71(2), 736, 15 Jul 1979.

58. T.A. Caughey and D.R. Crosley, J Chem Phys, 69(7), 3379, 1 Oct 1978.

59. L.A. Melton and W. Klemperer, J Chem Phys, 59(3), 1099, 1 Aug 1973.

60. H.P. Broida and T Carrington, J Chem Phys, 38(1), 136, 1 Jan 1963.

61. G.M. Jursich and F.F. Crim, J Chem Phys, 74(8), 4455, 15 Apr 1981.

62. J.J. Hinchen, J Chem Phys, 59(1), 233, 1 July 1973.

63. J.K. Hancock and W.H. Green, J Chem Phys, 57(11), 4515, 1 Dec 1972.

64. R.R. Stephens and T.A. Cool, J Chem Phys, 56(12), 5863, 15 June 1972.

65. K.R. German, J Chem Phys, 64(10), 4065, 15 May 1976.

66. J.G. Pruett and R. N. Zare, J Chem Phys, 62(6), 2050, 15 Mar 1975.

67. P.J. Wolf, J.H. Glover, L. Hanko, R.F. Shea, and S.J. Davis, J Chem Phys, 82(5), 2321, 1 Mar 1985.

68. P.J. Wolf and S.J. Davis, J Chem Phys, 83(1), 91, 1 July 1985.

69. P.J. Wolf, Collisional Dynamics In the B $^3\Pi(0^+)$ State of Iodine Monofluoride, Air Force Institute of Technology PhD Dissertation.

70. M.A.A. Clyne and I.S. McDermid, J Chem Soc Faraday Trans, 74, 1644, 1978.

71. M.A.A. Clyne and I.S. McDermid, J Chem Soc Faraday TransII, 73, 1094, 1977.

72. F. Zaraga, N.S. Nogar and C.B. Moore, J Mole Spec, 63, 564, 1976.

73. K.B. McAfee and R.S. Hozack, J Chem Phys, 34(6), 2041, 15 Mar 1961.

74. G. Capelle, Katsumi Sakurai, H.P. Broida, J Chem Phys, 54(4), 1728, 15 Feb 1971.

75. M.A.A. Clyne and M.C. Heaven, JCS Faraday Trans II, 74, 1992, 1978.

76. M.A.A Clyne, M.C. Heaven, and S.J. Davis, JCS Faraday Trans II, 76, 961, 1980.

77. M.A.A. Clyne, M.C. Heaven, and E. Martinez, JCS Faraday Trans II, 76, 405, 1980.

78. M.A.A. Clyne, M.C. Heaven, and E. Martinez, JCS Faraday Trans II, 76, 177, 1980.

79. M.A.A. Clyne, J.A. Coxon, and L.W. Townsend, JCS Faraday Trans II, 68, 2134, 1972.

80. M.A.A. Clyne and S. Toby, J Photochem, 11, 87, 1979.

81. R.D. Coombe and R.K. Horne, J Phys Chem, 83(19), 2435, 1979.

82. J.W. Birks, S.D. Gabelnick, H.S. Johnston, J Mole Spec, 57, 23, 1975.

83. R.A. Durie, Proc Royal Soc A, 207, 388.

84. M.A.A. Clyne and R. T. Watson, JCS Faraday Trans II, 72, 1169, 1976.

85. P.D. Whitefield, R.F. Shea and S.J. Davis, J Chem Phys, 78(11), 6793, 1 June 1983.

86. P.D. Whitefilled and S.J. Davis, Chem Phys Lett, 83(1), 44, 1 Oct 81.

87. J.A. Coxon and M.A. Wickramaaratchi, J Mole Spec, 87, 85, 1981.

88. R.A. Durie, Can J Phys, 44, 337, 1966.

89. R.F. Barrow, T.C. Clark, J.A. Coxon, and K.K. Yee, J Mole Spec, 51, 428, 1974.

90. J.A. Coxon, J Mole Spec, 37, 39, 1971.

91. J.A. Coxon, J Quant Spect Rad Trans, 12, 639, 1972.

92. A.P. Acton, R.G. Aickin and N.S.B. Bayliss, J Chem Phys, 4, 474, Aug 1936.

93. W.G. Brown, Phys Rev, 38, 1179, 15 Sep 1931.

94. A.A. Passchler, J..D. Christian, and N.W. Gregory, J Phys Chem, 73(4), 937, Mar 1967.

95. W.G. Brown, Phys Rev, 42,355, 1 Nov 1932.

96. Lars-Erik Selin, Arkiv Fysik, 21(27), 479.

97. Lars-Erik Selin and Berndt Soderburg, Arkiv Fysik, 21(28), 515.

98. Lars-Erik Selin, Arkiv Fysik, 21(29), 529.

99. J.A. Coxon and A.H. Curran, J Mole Spec, 75, 270, 1979.

100. J.A. Coxon, J Mole Spec, 50, 142, 1974.

101. S.G. Hadley and M.J. Bina, J Phys Chem, 78(8), 1833, 1974.

102. R.A. Harris and J.A. Montgomery, AFWL-TR-73-273, Air Force Weapons Laboratory, 1973.

103. A.N. Schweid and J.I. Steinfeld, J Chem Phys, 58(3), 844, 1 Feb 1973.

104. M.A.A. Clyne and M.C. Heaven, JCS Faraday Trans II, 76, 49, 1980.

105. M.A.A. Clyne and I.S. McDermid, JCS Faraday Trans II, 74, 1935, 1978.

106. M.A.A. Clyne and I.S. McDermid, JCS Faraday Trans II, 75, 280, 1979.

107. M.A.A. Clyne and I.S. McDermid, JCS Faraday Trans II, 75, 1313, 1979.

108. M.A.A. Clyne and I.S. McDermid, JCS Faraday Trans II, 75, 1677, 1979.

109. M.A.A. Clyne and E. Martinez, JCS Faraday Trans II, 76, 1275, 1980.

110. M.A.A. Clyne and E. Martinez, JCS Faraday Trans II, 76, 1561, 1980.

111. M.A.A. Clyne, A.H. Curran, and J.A. Coxon, J Mole Spec, 63, 43, 1976.

112. M.A.A. Clyne and I.S. McDermid, JCS Faraday Trans II, 74, 644, 1978.

113. M.A.A. Clyne and I.S. McDermid, JCS Faraday Trans II, 74, 664, 1978.

114. M.A.A. Clyne and I.S. McDermid, JCS Faraday Trans II, 74, 1376, 1978.

115. M.A.A. Clyne and J.P. Liddy, JCS Faraday Trans II, 76, 1569, 1980.

116. M.A.A. Clyne and I.S. McDermid, JCS Faraday Trans II, 72, 2252, 1976.

117. P.D. Whitefield, R.F. Shea, and S.J. Davis, AFWL-TR-81-136, Air Force Weapons Laboratory, 1981.

118. L.J. Van de Burgt and M.C. Heaven, to be published.

119. J.J. Wright, W.S. Spates, and S.J. Davis, J Chem Phys, 66(4), 1566, 15 Feb 1977.

120. M.A.A. Clyne and I.S. McDermid, JCS Faraday Trans II, 74, 798, 1978.

121. M.A.A. Clyne and I.S. McDermid, JCS Faraday Trans II, 74, 807, 1978.

122. M.A.A. Clyne and I.S. McDermid, JCS Faraday Disc, 67, 316, 1979.

123. M.A.A. Clyne and Lu Cheng Zai, JCS Faraday Trans II, 78, 1221, 1982.

124. J.W. Farthing, I.W. Fletcher, J.C. Whitehead, Molecular Physics, 48(5), 1067, 1983.

125. J.B. Koffend, F.J. Wodarczyk, R. Bacis and R.W. Field, J Chem Phys, 72(1), 478, 1 Jan 80.

126. J.B. Koffend, R. Bacis and R.W. Field, J Chem Phys, 70(5), 2366, 1 Mar 1979.

127. L. Hanko, D.J. Benard and S.J. Davis, Optics Comm, 30(1), 63, July 1979.

128. N.G. Basov, V.S. Zuev, L.D. Mikheev, and V.I. Valovoi, Sov J Quantum Electronics, 12, 674, May 1982.

129. J.B. Koffend, R. Bacis, and R.W. Field, J Mole Spec, 77, 202, 1979.

130. J.K. Rice, A Kagttays and J.R. Woodworth, App Phys Lett, 31(1), 31, 1 July 1977.

131. A.K. Hays, Optics Comm, 28(2), 209, Feb 1979.

132. M. Giegelmann, H.P. Grieneisen, K. Hola, Yue-Jing Hu, J Krasinski and K.L. Kompa, App Phys, 23, 283, 1980.

133. M. Diegelmann, K. Hola, and K.L. Kompa, Optics Comm, 29(3), 334, June 1979.

134. S.J. Davis, AFWL-TR-79-104, Air Force Weapons Laboratory, 167, 1979.

135. S.W. Benson, G.C. Berend and J.C. Wu, J Chem Phys, 38(1), 25, 1 Jan 1963.

136. R.J. Rubin and K.E. Shuler, J Chem Phys, 25(1), 59, July 1956.

137. O. Stern and M Volmer, Phsyik, Z80, 183, 1919.

138. D.J. Wilson, B.Noble and B. Lee, J Chem Phys, 34(4), 1392, Apr 1961.

139. T. Carrington, J Chem Phys, 35(3), 807, Sep 1961.

140. Montroll and Shuler, J Chem Phys, 26, 454, Mar 1957.

141. Troe, J Chem Phys, 66, 4745, June 1977.

142. Troe, J Chem Phys, 66, 4658, June 1977.

143. Rubin and Shuler, J Chem Phys, 25, 68, July 1956.

144. Rubin and Shuler, J Chem Phys, 26, 137, Jan 1957.

145. Herman and Shuler, J Chem Phys, 29, 366, Aug 1958.

146. Shuler, J Phys Fluids, 2, 442, 1959.

147. Shuler, J Chem Phys, 32, 1692, June 1960.

148. Shuler and Zwanzig, J Chem Phys, 33, 1778, Dec 1960.

149. Schwartz, Slawsky, and Hertzfeld, J Chem Phys, 20, 1591, Oct 1952.

150. Schwartz and Hertzfeld, J Chem Phys, 22, 767, May 1954.

151. Zelechow, Rapp, and Shap, J Chem Phys, 49, 286,July 1968.

152. Chan, Light, and Lin, J Chem Phys, 49, 86, July 1968.

153. V.L. Landau and E. Teller, Phys Z Sowj Un, 10,35, 1936.

154. J.F. Clarke and M. McChesney, The Dynamics of Real Gases, Butterworth, Washington, 1964.

155. B. Hartmann, B. Kleman and O. Steinvall, Optics Comm, 21, 33, 1977.

156. B. Wellegenhausen, K.H. Stephan, D. Friede and H. Welling, Optics Comm, 157, 1977.

157. J.A. Coxon, Molecular Spectroscopy, Chem Soc London, Billing ans Sons, Guildford, 1973.

158. R.F. Barrow and K.K. Yee, J Molec Spec, 69, 684, 1972.

159. F. Zaraga, N.S. Noger and C.B. Moore, J Mole Spec, 63, 564, 1976.

160. S.J. Davis, L. Hanko, and P.J. Wolf, to be published.

161. M.C. Heaven (private Communication).

162. C.W. McCurdy and W.H. Miller, J Chem Phys, 67, 463, July 1977.

163. G. Herzburg, Molecular Spectra and Molecular Structure, Van Nostrand Reinhold, New York, 1950.

164. M.A.A. Clyne and J.A. Coxon, Proc Roy Soc A, 298, 424.

165. W. Demtroder, Laser Spectroscopy, Springer Verlag, Berlin, 1982.

166. M.A.A. Clyne and I.S. McDermid, Dynamics of the Excited State, Ed. K.P. Lawley, Wiley and Sons, 1982.

167. R.D. Evans, The Atomic Nucleus, McGraw Hill, New York, 1955.

168. G.M. Jurisch and F.F. Crim, J Chem Phys, 74, 4455, 1981.

169. F.G. Tricomi, Integral Equations, Interscience, New York, 1957.

171. T Carrington, J Chem Phys, 35(3), 807, Sep 1961.

172. E.W. Montroll and K.E. Shuler, J Chem Phys, 26(3), 454, Mar 1957.

173. A. Shultz, H.W. Cruse and R.N. Zare, J Chem Phys, 57(3), 1354, 1 Aug 1972.

174. R.W. Wood, Phil Mag, 24, 673.

175. M.C. Heaven, Final report of AFOSR grant 83-0173, 1984.

176. "Demonstration of a Chemically-Pumped Laser in the Visible: NF Transfer to BiF", Aerospace Corporation,1985.

177. R.W.F. Gross and J.F. Bott, Handbook of Chemical Lasers, Wiley and Sons, New York, 1976.

178. J.D. Lambert, Vibrational and Rotational Relation in Gases, Clarendon Press, Oxford, 1977.

179. J.W. Glessner, to be published.

180. A. Yariv, Introduction to Optical Electronics, Holt, Reinhart and Winston, New York, 1976.

181. J.T. Yardley, Introduction to Molecular Energy Transfer, Academic Press, New York, 1980.

182. R.F. Weston and H.A. Schwartz, Chemical Kinetics, Prentice Hall, New Jersey, 1972.

183. W.G. Vincenti and C.H. Kruger, Introduction to Physical Gas Dynamics, Krieger Publishing, New York, 1965.

184. J.O. Herschfelder, C.F. Curtiss, and R.B. Bird, Molecular Theory of Gases and Liquids, Wiley and Sons, New York, 1954.

185. I.S. Sokolnikoff and R.M. Redheffer, Mathematics of Physics and Modern Engineering, McGraw-Hill, New York, 1966.

186. R. Courant and D. Hilbert, Methods of Mathematical Physics, Vol I, Interscience, New York, 1931.

187. P.R. Bevington, Data Reduction and Error Analysis for the Physical Sciences, McGraw Hill, New York,.

188. M.C. Heaven and M.A.A. Clyne, J Chem Soc, Faraday Trans II, 78, 1339, 1982.

Organization of Appendices

Appendices A-J are presented on pages 197-285.

Appendix A describes the characterization of an optically-pumped Br_2(B-X) laser. This discussion is not related to the BrCl(B) collisional dynamics presented in the main text, but rather, describes a second experiment conducted as part of this reserch effort.

Appendices B-J supplement the BrCl(B-X) collisional dynamics studies presented in the main text. Appendix B provides a description of BrCl(B-X) spectroscopy. Appendix describes calibration procedures and results for the laser induced fluorescence experiments. Appendices D-G outline theoretical and computational models pertaining to quenching, V-T, and R-T energy transfer. A detailed error analysis is presented in appednix H. Finally, appendices I-J describe the methods used to reduce the spectrally-resolved, steady-state data.

Appendix A

laser level. Modeling of the Br_2 lasing process can be used to test known kinetic rates under lasing conditions. The Br_2 B-X laser is a high gain system and parameters such as gain, saturation, and threshold can be directly observed from laser studies. Finally, the Br_2 laser is of interest for comparison with the other halogens and interhalogens.

The potential curves of the homonuclear diatomic halogens differ from those of the interhalogens in that interactions from electronic states of different symmetries are important. Predissociation of Herzberg type III (rotational predissociation) is observed in $v' > 3$ for Br_2 $B^3\Pi(O_u^+)$ due to the curve crossing of the repulsive $^1\Pi(1_u)$ state as shown in figure A1. As a result, the collisionless decay rate of the

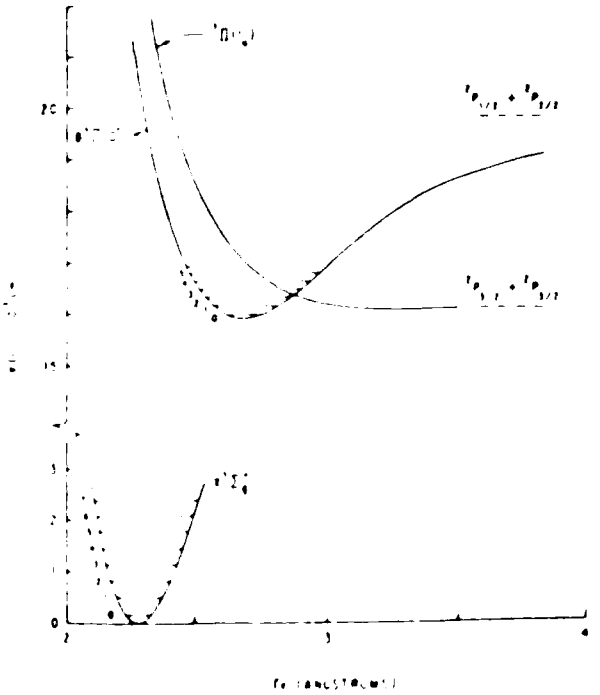

Figure A1. Br_2 potential energy curves.

$Br_2(B)$ state, τ_o, is given by the radiative rate, τ_r, and the natural predissociative rate described by the Kronig function

$$\tau_o = \tau_r + k_{pd}(v')J'(J'+1) \qquad (A1)$$

where $k_{pd}(v')$ is a constant that depends on v'. In I_2, $k_{pd}(v')$ has a strong dependence on v' with secondary maxima at the approximate values $v'=6$ and 25.[46] In Br_2 however, $k_{pd}(v')$ varies only slowly for $10 < v' < 25$.[75] In addition, $k_{pd}(v')$ are typically at least an order of magnitude larger in Br_2 than in I_2. Thus, natural predissociation in Br_2 is much stronger than in I_2 and its effects are much more uniform throughout the vibrational manifold. The radiative dynamics of Br_2 also differ markedly from IF(B). In IF(B) there are no natural predissociations and all $v'<9$ are stable. $Br_2(B)$ is intrinsically much less stable than the other two previously demonstrated halogen (B-X) lasers and these strong instabilities might be expected to prevent or severly limit laser action. Since the laser demonstrated by Wodarczyk and Schlossberg[31] operated over only a limited range of pumped (v',J') levels, we wished to significantly extend the range using a pulsed dye laser pump source.

In this appendix, a Br_2 laser pumped by a pulsed dye laser is discussed. A wide range of spectral excitation (555-575 nm) was used to excite several complete Br_2 bands. Pressure dependence of the laser output and saturation phenomenon are discussed. Evidence for isotopic selection in

the laser output is presented. A simple model is also presented that satisfactorily explains the processes which occur in th Br_2 laser.

II. Experiment

The experimental arrangement is shown in figure A2. The excitation source was a Quanta Ray PDL-1 dye laser pumped by a frequency doubled Quanta Ray DCR-1 pulsed Nd:YAG laser. The dye laser ouput consisted of 8 ns pulses (< 30 mJ/pulse) at a 10 Hz repetition rate. The bandwidth was approximately

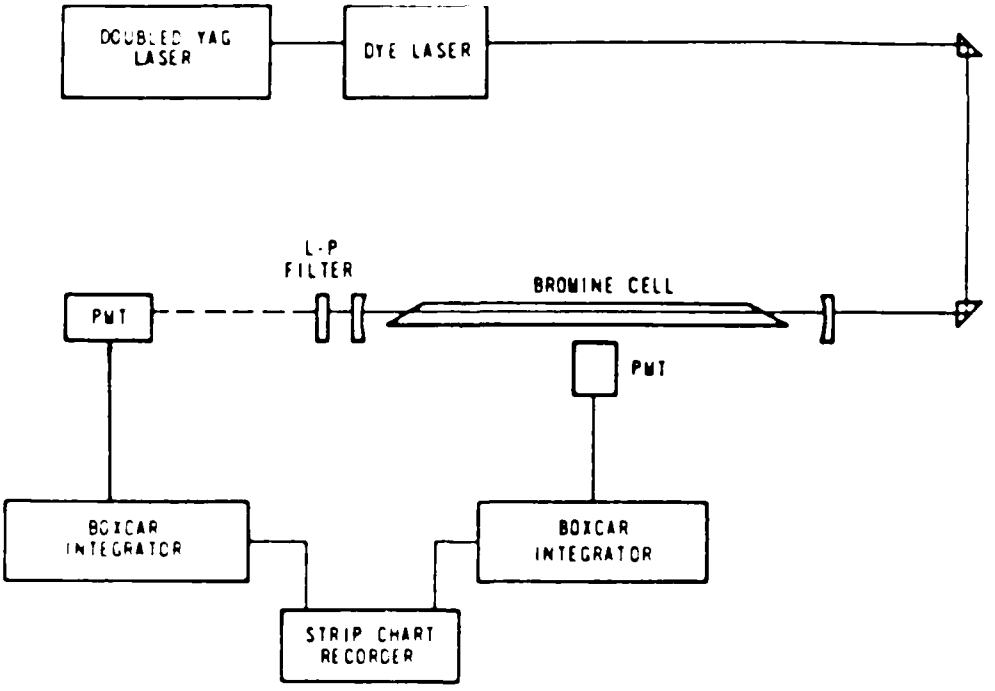

Figure A2. Br_2 optically-pumped laser experiment.

0.3 cm^{-1}, which is much wider than a single Br_2 rotational line Doppler width (~ 0.02 cm^{-1}). An intracavity etalon was also utilized for some experiments in order to narrow the dye laser bandwidth to ~0.03 cm-1 . Exciton Rhodamine 590 dye was used to cover the wavelength range 550 to 575 nm. This facilitated pumping of v'=12 through 17. No other dyes were used in the present work, but excitation resulting in lasing would be expected outside the range of the 590 dye. The output of the dye laser was focused to an approximately 2mm diameter inside the Br_2 cell. No careful attempts were made to mode match the dye laser beam to the Br_2 laser cavity.

The Br_2 laser cell was a pyrex tube 60 cm long with Brewster windows on each end and was connected to a gas handling vacuum system. The pressure in the Br_2 cell was measured with an MKS Baratron #220 capacitance manometer. In a typical run the cell was evacuated to 10^{-2} torr and then filled with Br_2 that had been previously purified by repeated freeze/thaw distillation cycles. The cell was then filled with a given Br_2 pressure and sealed off with a teflon valve.

The Br_2 laser cavity was constructed from two 3-meter radius of curvature dielectric mirrors. The mirrors passed greater than 80 percent of the dye laser pump beam and were 99 percent reflecting in the range 600-740 nm. A 630 nm long pass filter was used to block the dye beam from the detector. The broadband Br_2 output was detected on a Ge photodiode whose

output was fed to either an oscilliscope or a PARC Model 162 boxcar integrator. The boxcar was particularly useful in obtaining Br_2 excitation spectra. By monitoring spontaneous side fluorescence (perpendicular to the excitation beam) ordinary laser excitation spectra were obtained. For these laser excitation studies the etalon was removed to permit extensive (20nm) scanning of the dye laser. Because of the wide bandwidth (0.3 cm^{-1}) of the dye laser these excitation spectra were poorly resolved. The dye laser ouput wavelength was calibrated using a Hg pen lamp. The absolute wavelength of the dye laser was determined to better than 1 cm^{-1}. The differences between spectral features were determined to $< 0.2\ cm^{-1}$.

Using a second configuration in which the broadband Br_2 laser ouput was monitored as a function of dye laser wavelength, excellent resolution was obtained and many rotational lines were completely resolved. This resulted because stimulated emmission was utilized to detect Br_2 population distributions. Further discussion of this will be presented latter.

For some experiments the Br_2 laser output was spectrally resolved using a McPherson 218 monochromator. The monochromator output was detected with a PMT that was input into a picoammeter.

Several other experiments were performed on the Br_2 laser. The dependence of Br_2 laser power as a function of Br_2 pressure was studied. The output power was measured as a function of input power of the dye laser. Two methods were used to estimate optical gain. One involved measuring the time delay bewteen the establishment of a population inversion and the onset of lasing. We a'so directly measured the pump laser energy absorbed to determine the initial $Br_2(B)$ population

III. Results and Disscusion

A. Excitation Spectra

Molecular bromine consists of three isotopes: $^{79}Br^{79}Br$, $^{81}Br^{79}Br$, and $^{81}Br^{81}Br$ in the approximate relative abundances of 1:2:1. Consequently the Br_2 excitation spectra are very dense and the side fluorescence spectra using the 0.3 cm^{-1} bandwidth of the dye laser were of poor quality in that the overlap of rotational lines was severe. A typical spectrum is presented in figure A3a which shows the (14,0) band. The band head is at 562.0 nm, and the lack of resolution is obvious. The assignment of the pump transitions were made using the constants of Barrow et al.[89]

In contrast to the side fluorescence scans, the superior resolution of the stimulated emission scans is evident in figure 3b, which also shows the (14,0) band. Similar effects

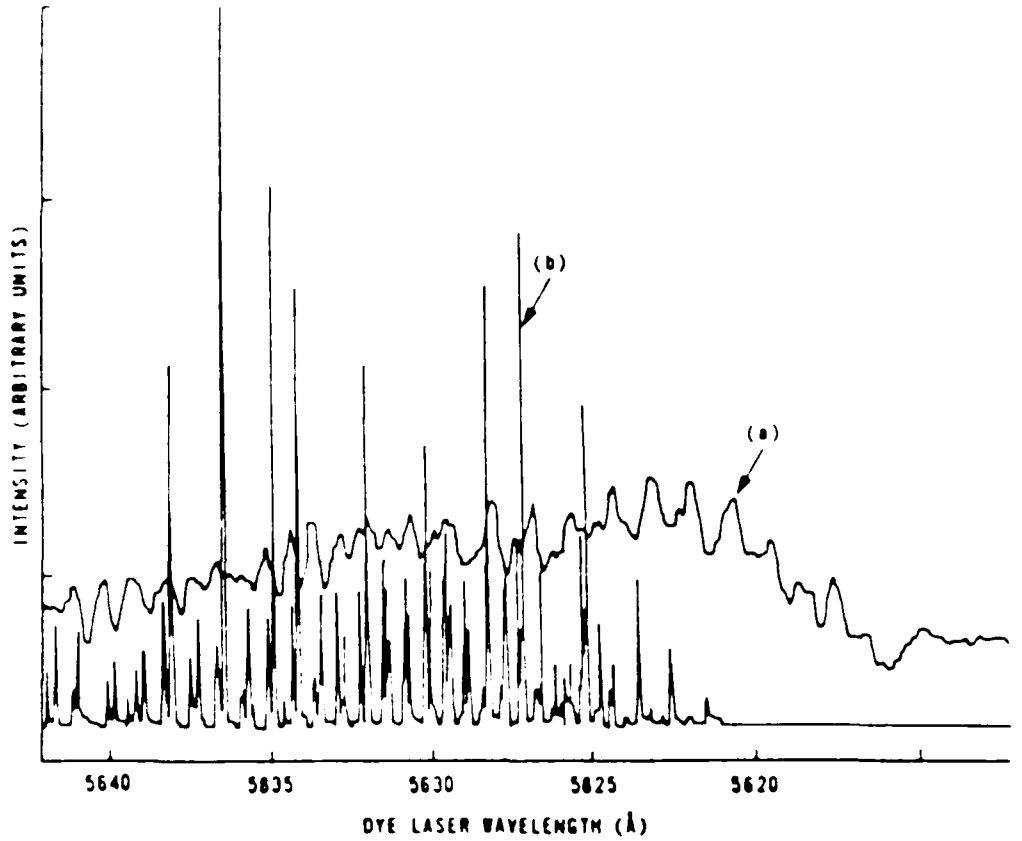

Figure A3. Comparison of excitation spectra using spontaneous side fluorescence as a signal monitor (a), and that obtained using stimulated emission as a signal monitor (b). These excitation spectra were obtained on the same scan of the (14,0) band with 10 torr of Br_2.

have also been observed in a CW IF(B-X) laser.[160] The Br_2 spectrum consists of a series of P-R doublets which are typical of the B-X transitions of the halogen molecules. The spectrum in figure A3b was assigned to the 79-81 isotope. The absence of the other two isotopes is an artifact resulting from using stimulated emission as the monitor of the Br_2 population. Since the Br_2 laser was run barely over threshold and lased only weakly, only the 79-81 isotope was excited sufficiently to lase. The thermal populations of the 79-81

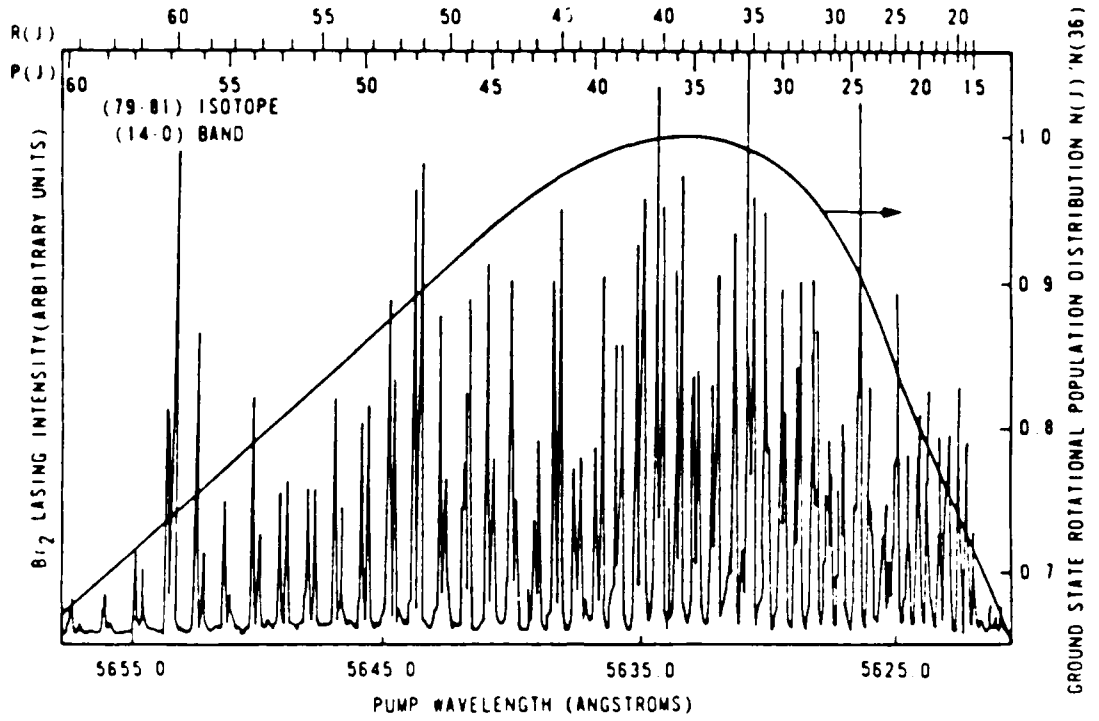

Figure A4. Excitation spectra of (14,0) band using stimulated emission as the signal monitor. Rotational assignments are indicated and show that the laser spectrum is predominately for the 81-79 isotope. Also shown (solid curve) is the calculated rotational population distribution in the v"=0 level of $Br_2(X)$. The Br_2 pressure is 8.8 torr.

and 81-81 isotopes were too small to be brought to threshold for the pump powers used. Further evidence for this is provided by examining the range of rotational lines that lased in a given band. In figure A4, also displaying the (14,0) band, note the solid line which represents the relative population of any J" level to that of J"=36 (the level of maximum population at T=300 K). The range of rotational levels in Br_2 X(v"=0) that were pumped to lasing oscillation was $10 \leqslant J" \leqslant 63$. The relative population of J"=10 and J"=63

are both approximately 65 percent of that of J"=36. Since the other two Br_2 isotopes are half as abundant, no lasing would be expected under the conditions depicted in figure A4.

By scanning the dye laser more slowly, the structure of the Br_2 spectrum could be studied in more detail. In figures A5 and A6 portions of the (14,0) and (16,0) bands are presented. Each spectral feature exhibits a great deal of noise. The three or four spikes observed in each transition is indicative of the intermittent nature of the Br_2 laser output. The noise patterns are not reproducible and thus are not considered to be hyperfine splitting. Note the lack of P-R doublet structure for the (16,0) band due to nearly complete overlap of the P(J) and R(J+3) lines.

The rotational assignments of the stimulated emission excitation spectra were made using combination differences between P and R lines. In figure A7 we show a comparison of the measured differences $\Delta_2 F''(J) = R(J-1) - P(J+1)$ for the (14,0) band to those calculated using Barrow's[89] constants. The agreement is excellent. Comparable agreements were observed for the other bands $12 \leq v' \leq 17$.

B. Br_2 Laser Spectra

Two examples of spectrally resolved Br_2 laser output are shown in figure A8. In both cases lasing originated from the

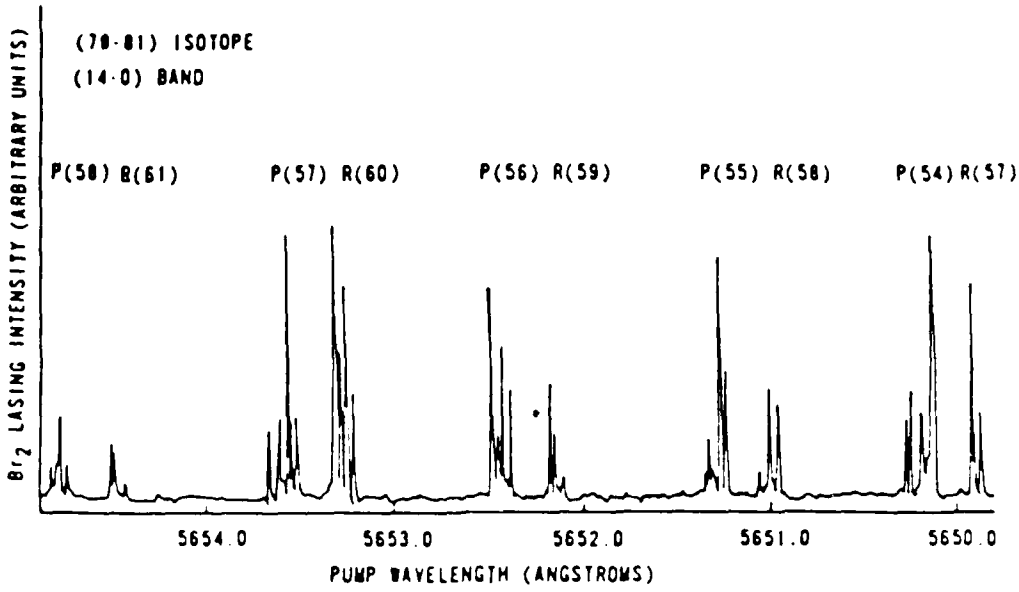

Figure A5. High resolution scan of the (14,0) band using stimulated emission as the signal monitor. The spectral width of the dye laser was approximately 0.01 nm. The Br_2 pressure is 6 torr.

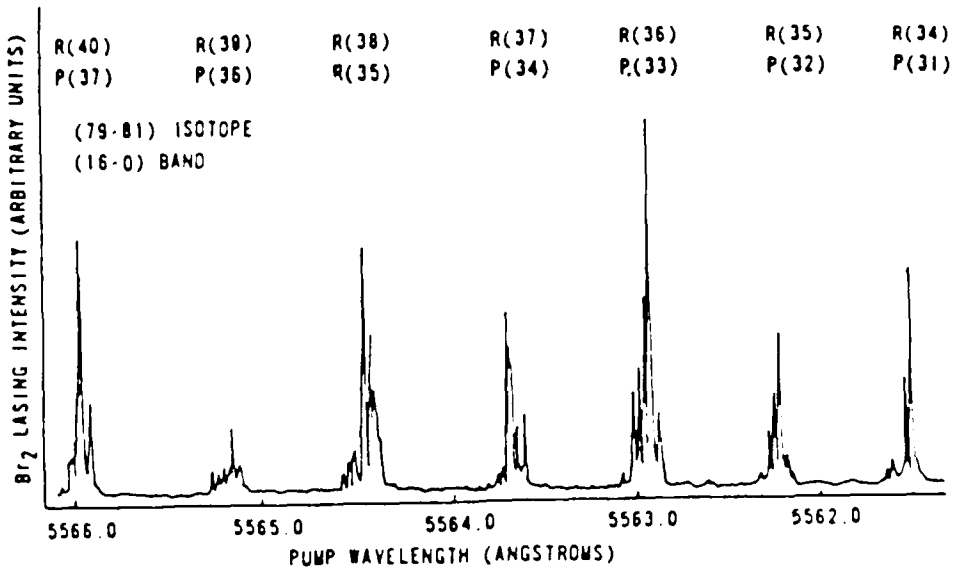

Figure A6. High resolution scan of a portion of the (16,0) band. The conditions are the same as for figure A5. Absence of apparent P-R doublet is due to severe blending of R(J+3) and P(J) lines.

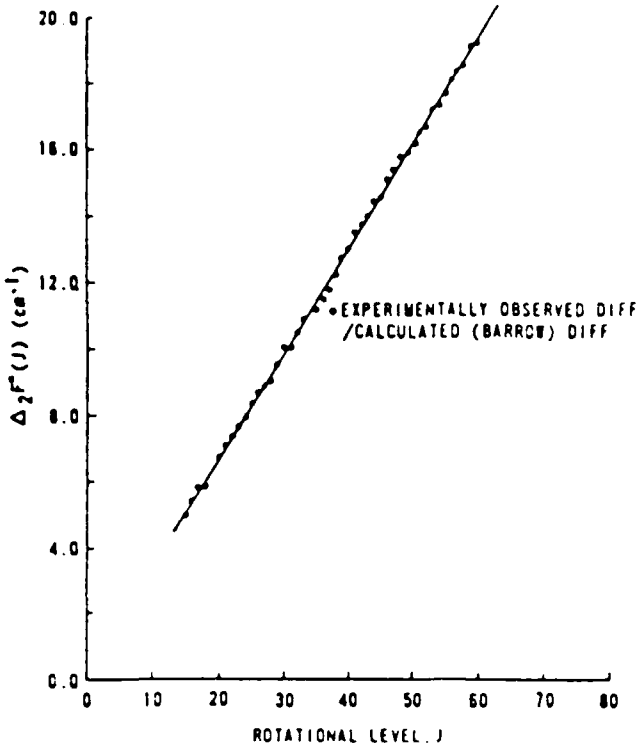

Figure A7. Comparison of measured and predicted second differences $\Delta_2F''(J) = R(J-1) - P(J+1)$. The predicted values were generated using the constants of Barrow et al.[89]

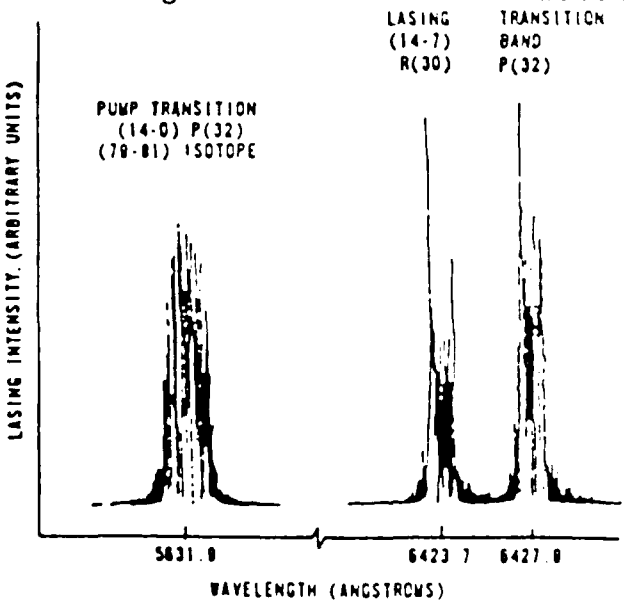

Figure A8. Spectrally-resolved Br_2 laser output. The pump transition at 563.19 nm is a monochromator scan of the pump dye laser emission. The lasing transitions at 643.27 and 642.79 nm originate from the single, initially populated rotational state $v'=14$, $J'=31$.

J´ level excited by the dye laser. Thus, even at the relatively high Br_2 pressures of 15 torr, no evidence of lasing from collisionally populated J´ levels is observed. This is similar to the behavior of the I_2(B-X) laser[156] but is in sharp contrast to IF where collisional energy transfer is so extensive that at pressure above 5 torr lasing is seen only from thermalized ro-vibrational levels.[33] However it should be noted that the observation of lasing exclusively from laser excited J´ levels in the present work is likely an artifact of the Br_2 laser running near threshold. The level, J_p, pumped by the dye laser will be depleted by R-T transfer collisions. A 35 percent reduction in the population of J_p is known to preclude lasing for our conditions (see Figure A4). It would be very unlikely that a collisionally populated J´ level could be brought to threshold. A better test of lasing from collisionally populated satellite levels would require higher pump laser intensities. Indeed, as shown in the following section, we could not saturate any Br_2 band.

C. Saturation Studies

Figure A9 shows a plot of the relative output power of the Br_2 laser as a function of the input power of the dye laser. The pump transition population difference decreases as the pump field intensity is increased. This phenomenon is

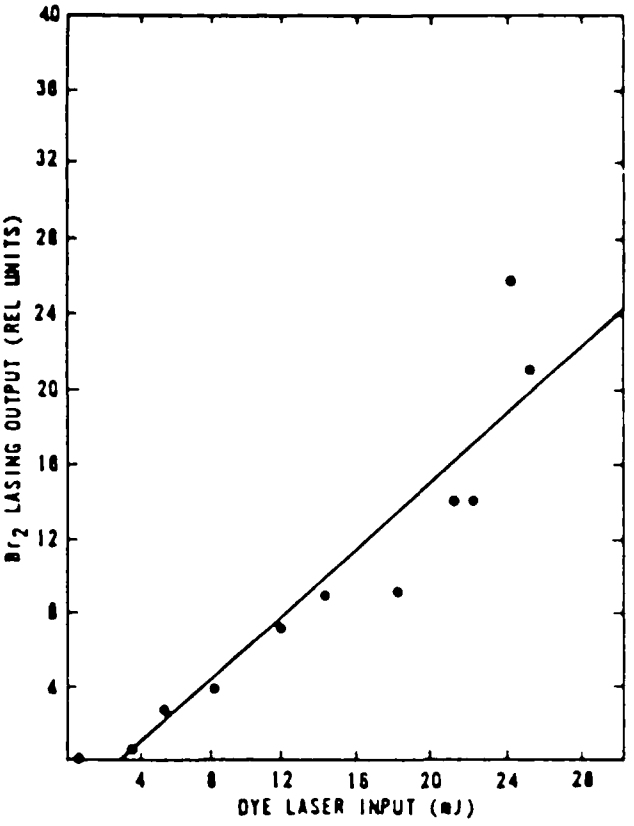

Figure A9. Plot of Br_2 laser output as a function of incident dye laser energy/pulse for the $v'=14$, $J'=45$ pumped state at a total Br_2 pressure of 10 torr. Note that the threshold pumping requirement is approximately 3 mJ/pulse.

termed saturation and becomes important when the pump transition population difference becomes small. For a saturated system, increasing pump intensity does not provide a proportional increase in the excited state density. The curve of figure A9 is linear and there is no evidence of saturation in our work over the dye laser energy range studied. No saturation studies using the intracavity etalon were performed in the present work. The ratio of incident photon quanta to target molecules in the present work is approximately one. This ratio must be greater than one to allow for saturation.

D. Laser Output Versus Br_2 Pressure

Although lasing was obtained over a wide range of Br_2 pressures (1.5 to 60 torr), the output was strongly peaked around the region of 10 to 15 torr. This result is similar to what was observed by Wodarczyk and Schlossberg.[31] The relative strength of Br_2 lasing was determined by scanning the dye laser wavelength over complete bands and averaging the five strongest Br_2 laser lines in each band. The scans were done at slow speeds so that each recorded spectral feature was the average of approximately 10 dye laser pulses, the averaging being done on the boxcar integrator. In spite of

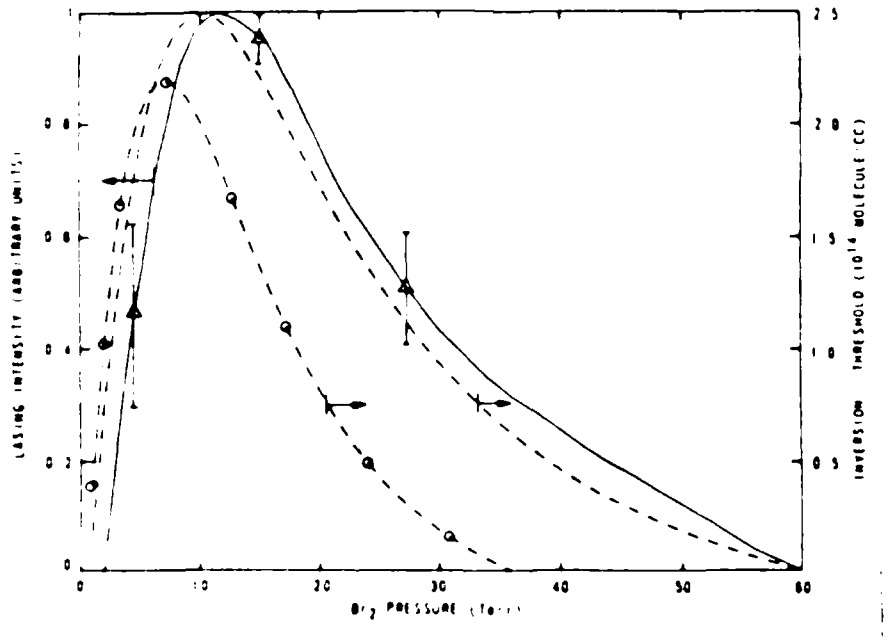

Figure A10. Comparison of measured and predicted Br_2 laser output as a function of Br_2 pressure. The measured values are labled by and the uncertainty in the amplitude is indicated. The two predicted curves show the Br_2 B-state population at the time of laser turn-on for two different Br_2 deactivation rates: --- $=2.5\times10^{-10}$ cm^3/molec-s and o $=5\times10^{-10}$ cm^3/molec-s.

these efforts, the reproducibility of the average Br_2 laser output was still fairly erratic. This is reflected in the Br_2 laser power as a function of Br_2 pressure data as seen in the solid line of figure A10. The other curves in figure A10 will be discussed later.

E. Modeling of the Br_2 Laser

In order to describe some of the properties of the Br_2 laser, the following simple model was utilized. Figure A11 illustrates the ground, upper laser and lower laser energy

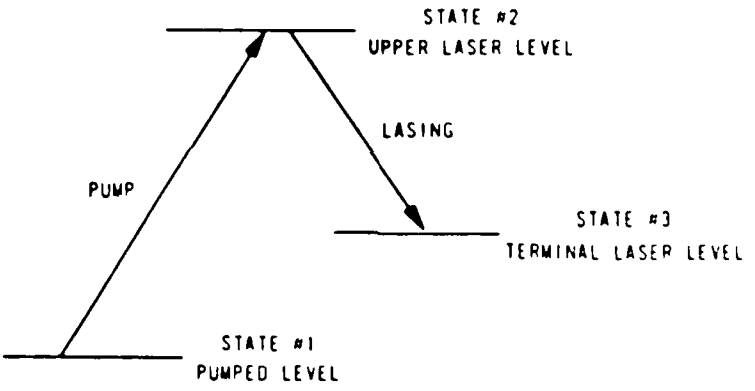

Figure A11. Energy levels of Br_2 laser model

levels used in this model. The time evolution of the upper laser level, N_2, is given by

$$dN_2/dt=(N_1B_{12}I_p/c-N_2B_{21}I_p/c)-(N_2B_{23}I_L/c-N_3B_{32}I_L/c)-N_2/\tau \quad (A4)$$

where

I_p, I_L are the pump and laser intensities, respectively

B_{ij} are the Einstein B coefficients connecting level i to level j

and

$$1/\tau = 1/\tau_r + k_Q[Br_2] + k_{pd}(v')J'(J'+1) \quad (A5)$$

τ_r is the radiative lifetime, k_Q is the collisional removal rate of Br_2 $B^3\Pi(0^+)$ from the originally excited v', J' level, and $k_{pd}(v')$ is the natural predissociative rate for level v'. The populations of the v", J" pumped (1), and the terminal laser level, (3) are described by:

$$dN_1/dt = N_2B_{21}I_p/c - N_1B_{12}I_p/c \quad (A6)$$

$$dN_3/dt = N_2B_{23}I_L/c - N_3B_{32}I_L/c + A_{23}N_2 \quad (A7)$$

Spontaneous emission and quenching were omitted in the rate equation for N_1, because the pump laser essentially dominated all kinetic processes while the dye laser was on and the Br_2 laser turned on only approximately 2 ns after the termination of the dye laser pulse. During this time the major kinetic process of importance was the depletion of the upper laser level 2 described by equation (A4). The major build-up of population in level 3 was via stimulated emission. The number of photons, n, in the cavity is described by the rate equation

$$dn/dt = B_{23}I_L/c - B_{32}I_L/c + A_{23}N_2(V/V_m)(g(\nu)/p(\nu)) - n/T_c \quad (A8)$$

where

T_c is the photon cavity lifetime determined by both scattering and mirror losses

$g(\nu)$ is the lasing transition lineshape function

$\rho(\nu) = 8\pi\nu^2/c^3$ is the mode desnity

V is the pump mode volume

V_m is the laser mode volume.

The pump and laser mode volumes are estimated as equal.

Using equations A4-A8 the population of a given v', J' level and the intracavity photon number at the termination of the dye laser pump were predicted as a function of time and Br_2 pressure.

Equations A4-A8 were solved numerically using the trapezoidal rule. The number density of any level (i) at time t_n is given by

$$N_i(t_n) = N_i(t=0) + \sum_n \left(f_i(t_{n-1}) + df_i/dt\ (t_{n-1})\ \Delta t/2 \right) \Delta t \quad (A9)$$

where Δt is the time increment, $\Delta t = t_n - t_{n-1}$, and the functions f_i are given by equations A4-A8. The computations were completed on a model 4051 Tektronix desktop calculator. A step size of Δt=0.8 ps provided convergence to within 0.4 percent.

The pump pulse is approximated by the triangle function

$$I(t) = I_o \begin{cases} 0 & t<0 \\ t/t_p & 0 \leq t \leq t_p/2 \\ 0.2[4-3(t/t_p)] & t_p/2 < t < t_p \\ 0 & t>t_p \end{cases} \qquad (A10)$$

where

t_p = 10 ns
I_o^p = incident pump intensity

The observed and approximated pump pulses are shown in figure A12.

A spatial dependence for the number density arises from a nonuniform spatial distribution of the pump intensity. As the pulse propogates through the gain medium, it is attenuated due to absorption. Rather than include this spatial variation, an average value for the pump intensity was used. The spatially-averaged intensity, using Beer's law for the attenuation[165], is

$$I_p = (1/L)\int_0^L I_p(0)\ \exp\{-\sigma(N_0-N_2)z\}dz \qquad (A11)$$

$$= I_p(0)\ [1-\exp\{-L\sigma(N_o-N_2)\}]/[L\sigma(N_o-N_2)]$$

where

L = length of the gain medium
z = axial distance through the gain medium
σ = optical cross section for single-line absorption

In equation (A11), it has been assumed that the number densities have already been averaged, or vary little spatially. For high pump intensities or low optical absorption, the approximation is satisfactory.

The radiative lifetime τ_r = 8.1 μs, predissociation rate constant $k_{pd}(v') = 6.7 \times 10^3\ s^{-1}$, and dipole moment $|R_e|^2 = .126\ D^2$ (Ref 75) were used in the numerical computations. Spectroscopic constants, wavelengths and Franck-Condon factors were obtained from references [91,157-158]. The optical losses due to scattering and output coupling were estimated at 0.06 over 100 cm.

In figure A10 the observed Br_2 pressure dependence of the bromine laser is shown. The peak output is seen to occur at approximately 10-12 torr, and lasing is observed all the way out to 60 torr. The error bars are typical of the erratic nature of the laser output. Also shown in figure A10 are two curves resulting from the previously described model. The ordinates for these curves are the predicted Br_2 B-X lasing inversions minus the threshold inversion at the time of the Br_2 laser turn on. Curve (a) was obtained using a collisional removal rate from (v',J') $k_Q = 2.5 \times 10^{-10}\ cm^3/molec\text{-}s$ and curve (b) used $k_Q = 5.0 \times 10^{-10}\ cm^3/molec\text{-}s$. Curve (a) was normalized to the observed Br_2 laser data for purposes of comparison. It is clear that the model using a quenching rate of $5 \times 10^{-10}\ cm^3/molec\text{-}s$ does not adequately predict the

observed pressure dependence. The best agreement using 2.5×10^{-10} cm^3/molec-s is much better. Even though the agreement is only qualitative, the model does indicate that a $Br_2(v',J')$ removal rate of 5×10^{-10} cm^3/molec-s is probably too fast to explain the observed trends.

In a laser fluorescence study Clyne, Heaven, and Davis[76] measured removal rates of $(v'J')$ levels in $Br_2(B)$. For $v'=14$ a collisional rate of 4.2×10^{-10} cm^3/molec-s was determined for J' levels within the range of those studied in the present work. This removal was attributed predominately to collisional predissociation. Our present results due not appear to agree with this fast rate. Our model, although somewhat simplified, should be a fairly accurate description of $Br_2(B)$ at least until the population in the upper laser level is nearly depleted. It is important to emphasize that the quenching rates obtained by Clyne et al.[76] were obtained under experimental conditions drastically different from the present work. Much of the Clyne et al.[76] data were obtained at bromine pressures of less than 20 mtorr, while in our studies Br_2 pressures several orders of magnitude higher were used. This apparently faster quenching rate measured by Clyne et al. may have contained R-T transfer contributions. Recent work by Heaven[161] at Br_2 pressures between 0.5 and 5.0 torr has produced a quenching rate of 4.0×10^{-10} cm^3/molec-s. The remaining discrepency in quenching rates should be investigated in the pressure region 5 to 60 torr. Measuring

the very short Br_2 lifetimes above 5 torr would require a less than 1 ns excitation source in order to preclude convolution effects. Heaven has also found that rotational energy transfer occurs with high efficiency.[161]

F. Gain of Br_2 Laser

There is an observed time delay between the termination of the dye laser pump pulse and the initiation of the Br_2 lasing pulse of approximately two ns which is due to the photon build-up time within the Br_2 laser cavity. The gain of the Br_2 laser can in principle be determined from a measurement of the photon build-up time as described by Byer et al.[22] in their I_2 laser. The Byer model asssumes the pump transition is rapidly saturated. In our device the pump transition is not saturated and the Byer model is not applicable. The model described earlier has been used to fit the predicted Br_2 laser pulse shapes to the observed shape at 20 torr Br_2. The optimal fit yielded a gain of 1.1×10^{-1} cm^{-1}. A plot showing the observed dye laser and Br_2 laser pulse and the predicted pulse shapes is shown in figure A12. It is important to note that the solution is not unique since other parameters such as quenching and optical thickness affect the pulse shape. The curve shown in figure A12 was derived using a self qunеching rate of $k_Q = 2.5 \times 10^{-10}$ cm^3/molec-s.

A more direct measurement of the gain was made by determining the intial $Br_2(B)$ population produced by the dye

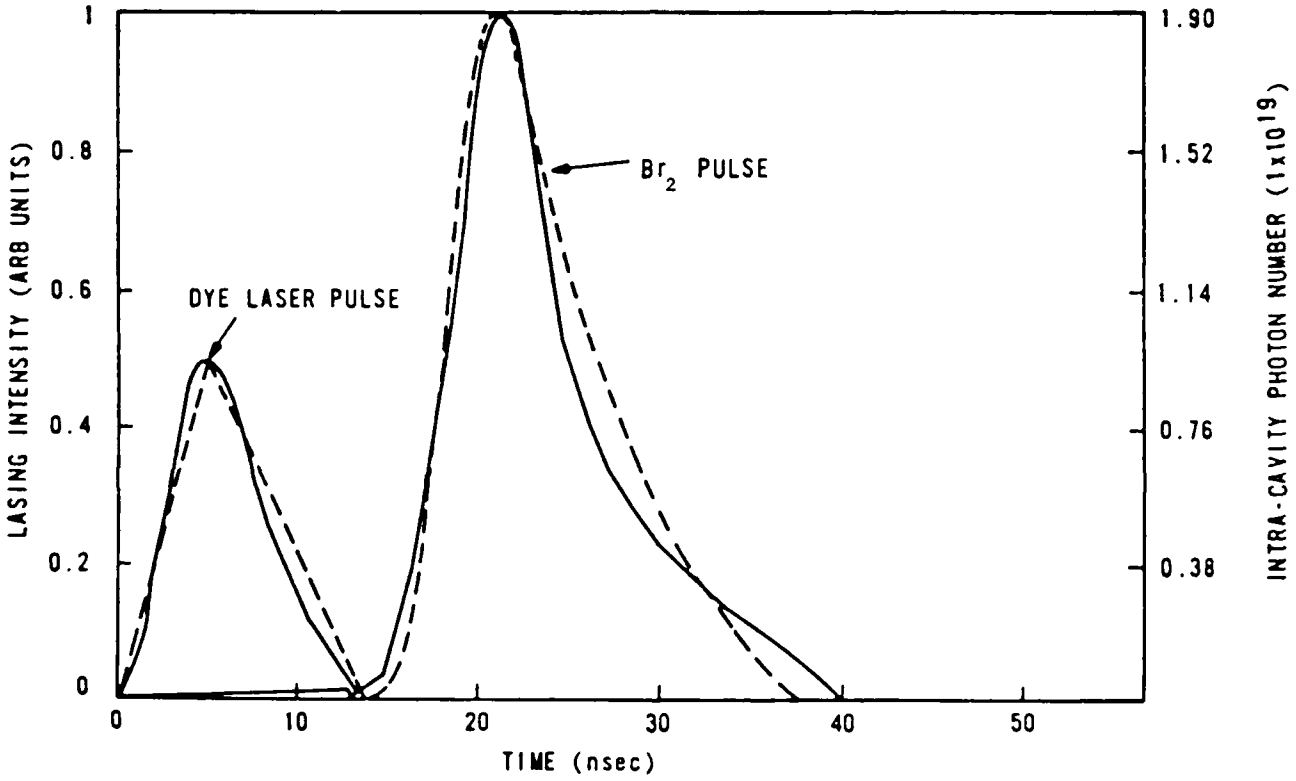

Figure A12. Comparison of predicted and observed Br_2 laser pulses. The dye laser intensity and photon number have been normalized to one-half of the Br_2 laser intensity. The actual dye laser intensity is approximately 5×10^4 times larger than shown.

laser. From this an upper limit of the gain at the turn on time can be determined. If we used the observed absorbed energy on a single $^{79}Br^{81}Br$ line at 10 torr (.34 mJ) on the (14,0) band, we calculate a population at the termination of the dye laser pulse of 4.8×10^{14} molec/cm^3. After 2 ns, the population is approximately 4.3×10^{14} molec/cm^3 assuming a quenching rate of 2.5×10^{-10} cm^3/molec-s. The most probable lasing transition in the range of our laser mirrors is the (14,7) band which has a stimulated emission cross section of 4.5×10^{-16} cm^2 for a single $J' \rightarrow J''$ line. The upper limit to the gain coefficient is thus $\gamma = 1.9 \times 10^{-1}$ cm^{-1}. This compares favorably with the previous estimate of 1.1×10^{-1} cm^{-1}. If we were to allow for rotational energy transfer in the excited state and allow for quenching during the laser pulse, then the gain would be reduced accordingly.

G. Amplified Spontaneous Emission

For one set of runs the intracavity etalon was installed in the dye laser and the etalon was tuned to excite the $v'=13$ P(46) line of $^{79}Br^{81}Br$. Using this configuration, amplified spontaneous emission (ASE) was observed when the cavity mirrors were removed. Similar behavior has been observed in I_2.[127] The observation of ASE in Br_2 demonstrates the high optical gains available even though collisional removal is rapid.

IV. Rotational Transfer Studies

Spectrally resolved continuous-wave (CW) laser induced fluorescence has been used to study rotational energy transfer in the B state of Br_2. An Ar^+ ion laser pumped ring dye laser using Rhodamine 590 dye was used to populate a pure ro-vibrational quantum state of a specific Br_2 isotope. See section III for a more complete description of the experimental apparatus. An emission spectra obtained from pumping $^{79}Br^{81}Br$ (B;v′=11,J′=35) at 26 mtorr Br_2 and with 376 mT of Ar buffer gas is shown in figure A13.

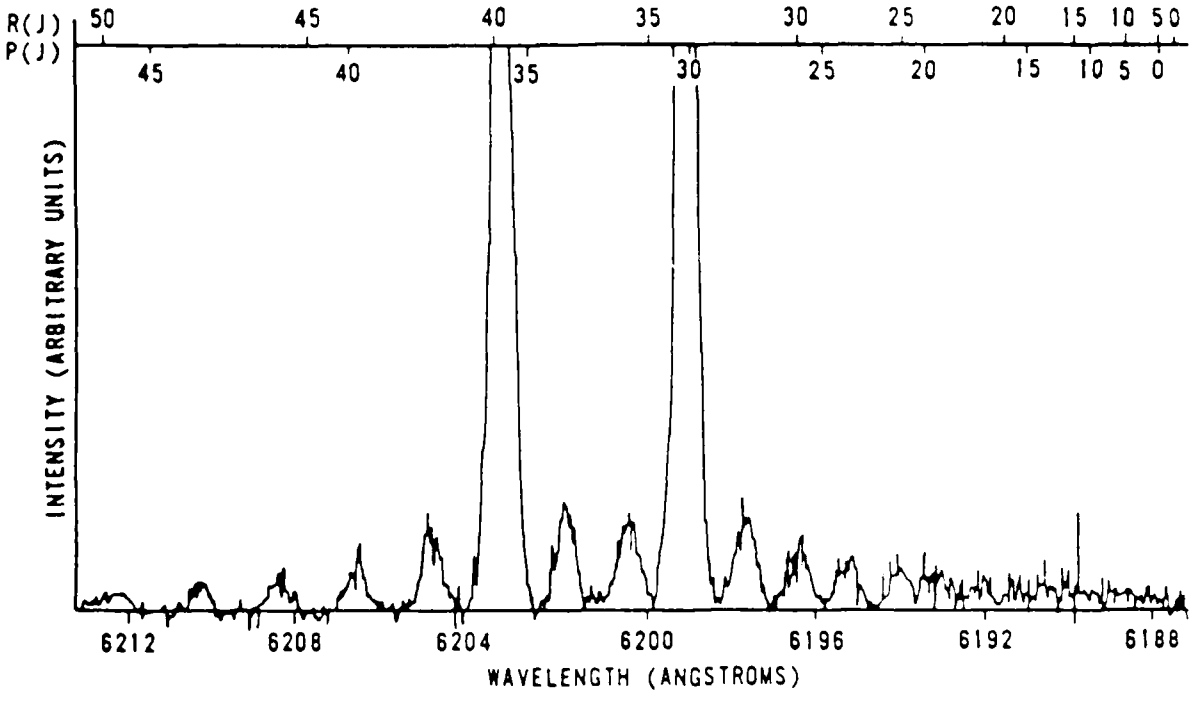

Figure A13. Rotationally-resolved Br_2 CW LIF spectrum.

A strong P-R emission doublet arising from the single, initially populated rotational state is evident. Weaker satellite transitions from collisionally populated rotational states (approximately 5% of the initially populated state) are also observed. The spectra indicates very little rotational transfer under the given conditions. This is consistent with the observation of Br_2 lasing only from the rotational level excited by the dye laser.

Emission is observed only from rotational states with the same parity as the initially populated state. That is, every other emission line in figure A13 is missing. A collisional selection rule of ΔJ = even is clearly indicated. This selection rule is predicted from quantum mechanics for homonuclear diatomic molecules. The $^{79}Br^{81}Br$ is not truly homonuclear since the symmetry is broken by the isotopic variation. McCordy and Miller[162] have shown that diatomic molecules with nearly identical nuclei may have a strong propensity for ΔJ = even collisions.

V. Proposed Future Studies

The dye laser pumped Br_2(B-X) laser is a high gain system that operates over a wide range of ro-vibrational states and pressures, despite severe natural predissociation and self-quenching. While the radiative and collisional dynamics of Br_2(B) are fairly well understood, the current Br_2 laser demonstration appears inconsistent with the established self

deactivation rates for $Br_2(B)$. The most recent $Br_2(B)$ lifetime studies[175] indicate a resonant V,R-T transfer process involving large changes in rotational state may be important in describing the self deactivation of $Br_2(B)$. Spectrally-resolved, CW laser induced fluorescence experiments similar to that described in this appendix, section IV, could be used to search for the predicted large change in rotational state during V,R-T collisions. Such an experiment would help resolve the current descrepency in measured quenching rates.

Currently, amplified spontaneous emission in $Br_2(B)$ is being studied in detail.[179] Specifically, ASE output power as a function of pressure has been investigated. The model presented in this appendix should be applied to this new data in order to extract another independent measurement of the self quenching rate.

Appendix B

Detailed spectroscopy of Br$_2$ $B\,^3\Pi_{0_u^+}$ and Br$_2$ $X\,^1\Sigma_g^+$

1. Rotational constants

The v and $v+1$ vibrational state rotational constants are empirically fit to $T_v = T_e + \omega_e(v+\tfrac{1}{2}) - \omega_e x_e(v+\tfrac{1}{2})^2 + \omega_e y_e(v+\tfrac{1}{2})^3 + \cdots$ as given in Table B.II. The experimental v-state B_v term values are given in Table B.III. The resulting rotational constants are given for the expression

$$T_{vJ} = T_{v0} + \gamma_v + B_v J(J+1) + \delta_v J^2(J+1)^2 + \eta_v J^3(J+1)^3 + \cdots$$

where

T_{vJ} = the v, J rovibronic energy,

T_{v0} = the vibronic energy,

γ_v = the spin-rotation constant,

B_v = [illegible],

[illegible]

[illegible]

[illegible]

[illegible]

[illegible]

[illegible]

Table B.II
BrCl(B) Rotational Term Values, $B_{v'}$ (cm^{-1})

v'	$^{79}Br^{35}Cl$	$^{81}Br^{35}Cl$
0	0.107015	0.106235
1	0.105627	0.104843
2	0.104165	0.103389
3	0.102571	0.101827
4	0.100846	0.100110
5	0.098871	0.098158
6	0.096476	0.095801
7	0.093430	0.092821
8	0.089171	0.088623

II. Extension of FCF's to v"$>$8

An RKR program first developed by H. Kildal and later modified by the Air Force Institute of Technology and a Franck-Condon Factor (FCF) program written by H. Michaels were used to calculate transition wavelengths and Franck-Condon Factors for 8$<$v"$<$14 and 0$<$v'$<$8. The potential curves were estimated using the X-state constants and B-state classical turning points reported by Coxon[100]. Lt. B McFeeters of the Air Force Weapons Laboratory provided the computer expertise required for the execution of these programs.

The results of these computations are given in tables B.III and B.IV. The FCF's in the region 0$<$v"$<$7 and 0$<$v'$<$8 agreed within Coxon's reported values to within 10%. Outside of this region the results are only extrapolations and no experimental data was used to make these estimates. The results do agree qualitatively with signal intensities

v''	v' = 0	v' = 1	v' = 2	v' = 3	v' = 4	v' = 5
0	0.595927e+03	0.588859e+03	0.581836e+03	0.575237e+03	0.569059e+03	0.563356e+03
1	0.611984e+03	0.604533e+03	0.597133e+03	0.590185e+03	0.583684e+03	0.577e84e+03
2	0.628799e+03	0.620936e+03	0.613131e+03	0.605808e+03	0.598960e+03	0.592644e+03
3	0.646408e+03	0.638101e+03	0.629861e+03	0.622136e+03	0.614916e+03	0.608261e+03
4	0.664866e+03	0.656081e+03	0.647374e+03	0.639216e+03	0.631597e+03	0.624578e+03
5	0.684252e+03	0.674950e+03	0.665739e+03	0.657114e+03	0.649065e+03	0.641655e+03
6	0.704620e+03	0.694761e+03	0.685004e+03	0.675877e+03	0.667365e+03	0.659533e+03
7	0.726049e+03	0.715585e+03	0.705239e+03	0.695568e+03	0.686556e+03	0.678271e+03
8	0.748638e+03	0.737518e+03	0.726533e+03	0.716273e+03	0.706720e+03	0.697944e+03
9	0.772465e+03	0.760632e+03	0.748953e+03	0.738055e+03	0.727916e+03	0.718609e+03
10	0.797632e+03	0.785022e+03	0.772588e+03	0.760997e+03	0.750223e+03	0.740340e+03
11	0.824269e+03	0.810809e+03	0.797552e+03	0.785205e+03	0.773740e+03	0.763233e+03
12	0.852495e+03	0.838106e+03	0.823949e+03	0.810778e+03	0.798560e+03	0.787373e+03
13	0.882466e+03	0.867056e+03	0.851913e+03	0.837641e+03	0.824800e+03	0.812871e+03
14	0.914338e+03	0.897805e+03	0.881579e+03	0.866518e+03	0.852577e+03	0.839837e+03
15	0.948298e+03	0.930527e+03	0.913108e+03	0.896960e+03	0.882030e+03	0.868402e+03
16	0.984548e+03	0.965406e+03	0.946670e+03	0.929325e+03	0.913308e+03	0.898704e+03
17	0.102334e+04	0.100267e+04	0.982479e+03	0.963809e+03	0.946593e+03	0.930914e+03
18	0.106493e+04	0.104257e+04	0.102076e+04	0.100062e+04	0.982074e+03	0.965209e+03
19	0.110966e+04	0.108540e+04	0.106178e+04	0.104001e+04	0.101999e+04	0.100181e+04
20	0.115787e+04	0.113149e+04	0.110584e+04	0.108224e+04	0.106058e+04	0.104094e+04
21	0.121001e+04	0.118123e+04	0.115330e+04	0.112766e+04	0.110416e+04	0.108289e+04
22	0.126656e+04	0.123505e+04	0.120455e+04	0.117661e+04	0.115105e+04	0.112795e+04
23	0.132809e+04	0.129350e+04	0.126008e+04	0.122954e+04	0.120166e+04	0.117650e+04
24	0.139528e+04	0.135714e+04	0.132041e+04	0.128691e+04	0.125639e+04	0.122892e+04
25	0.146896e+04	0.142676e+04	0.138621e+04	0.134933e+04	0.131583e+04	0.128573e+04
26	0.155011e+04	0.150319e+04	0.145825e+04	0.141749e+04	0.138056e+04	0.134747e+04
27	0.163991e+04	0.158748e+04	0.153745e+04	0.149222e+04	0.145135e+04	0.141481e+04
28	0.173978e+04	0.168089e+04	0.162489e+04	0.157445e+04	0.152902e+04	0.148853e+04
29	0.185148e+04	0.178493e+04	0.172192e+04	0.166538e+04	0.161464e+04	0.156955e+04
30	0.197707e+04	0.190137e+04	0.183003e+04	0.176630e+04	0.170933e+04	0.165888e+04

v''	v' = 6	v' = 7	v' = 8
0	0.558130e+03	0.553432e+03	0.549361e+03
1	0.572191e+03	0.567255e+03	0.562978e+03
2	0.586864e+03	0.581673e+03	0.577176e+03
3	0.602174e+03	0.596709e+03	0.591978e+03
4	0.618161e+03	0.612404e+03	0.607422e+03
5	0.634884e+03	0.628813e+03	0.623562e+03
6	0.652382e+03	0.645974e+03	0.640433e+03
7	0.670710e+03	0.663938e+03	0.658086e+03
8	0.689941e+03	0.682777e+03	0.676590e+03
9	0.710128e+03	0.702541e+03	0.695992e+03
10	0.731342e+03	0.723298e+03	0.716358e+03
11	0.753673e+03	0.745133e+03	0.737770e+03
12	0.777202e+03	0.768124e+03	0.760302e+03
13	0.802036e+03	0.792371e+03	0.784051e+03
14	0.828276e+03	0.817973e+03	0.809109e+03
15	0.856047e+03	0.845046e+03	0.835589e+03
16	0.885478e+03	0.873713e+03	0.863607e+03
17	0.916731e+03	0.904126e+03	0.893309e+03
18	0.949970e+03	0.936441e+03	0.924842e+03
19	0.985401e+03	0.970853e+03	0.958391e+03
20	0.102324e+04	0.100756e+04	0.994143e+03
21	0.106374e+04	0.104681e+04	0.103233e+04
22	0.110720e+04	0.108886e+04	0.107321e+04
23	0.115394e+04	0.113404e+04	0.111707e+04
24	0.120432e+04	0.118266e+04	0.116422e+04
25	0.125883e+04	0.123518e+04	0.121508e+04
26	0.131795e+04	0.129205e+04	0.127008e+04
27	0.138231e+04	0.135385e+04	0.132974e+04

Table B.III BrCl B-X transition wavelengths.

Franck-Condon factors .....

v- =	0	1	2	3	4	5
0	0.593657e-08	0.585714e-07	0.307953e-06	0.114950e-05	0.336214e-05	0.797670e-05
1	0.150325e-06	0.136904e-05	0.662988e-05	0.228504e-04	0.618850e-04	0.136476e-03
2	0.182718e-05	0.152071e-04	0.670725e-04	0.210924e-03	0.522371e-03	0.105716e-02
3	0.142301e-04	0.107024e-03	0.424376e-03	0.120050e-02	0.267720e-02	0.489104e-02
4	0.800154e-04	0.536936e-03	0.188512e-02	0.471448e-02	0.928242e-02	0.149755e-01
5	0.368255e-03	0.205457e-02	0.627036e-02	0.135616e-01	0.229591e-01	0.316936e-01
6	0.122119e-02	0.622579e-02	0.161464e-01	0.293379e-01	0.411232e-01	0.462206e-01
7	0.354958e-02	0.153151e-01	0.327767e-01	0.480223e-01	0.524846e-01	0.438022e-01
8	0.874165e-02	0.310912e-01	0.527298e-01	0.584137e-01	0.444424e-01	0.218731e-01
9	0.185141e-01	0.524542e-01	0.663863e-01	0.494746e-01	0.196173e-01	0.168238e-02
10	0.340810e-01	0.734112e-01	0.627617e-01	0.238905e-01	0.818892e-03	0.652207e-02
11	0.549785e-01	0.842078e-01	0.400109e-01	0.223716e-02	0.840014e-02	0.280761e-01
12	0.784813e-01	0.772007e-01	0.120394e-01	0.539078e-02	0.319955e-01	0.330654e-01
13	0.100039e+00	0.532559e-01	0.195753e-04	0.298127e-01	0.396277e-01	0.131591e-01
14	0.115026e+00	0.234571e-01	0.138411e-01	0.480149e-01	0.203485e-01	0.257086e-04
15	0.120258e+00	0.304508e-02	0.415893e-01	0.389844e-01	0.933060e-03	0.151093e-01
16	0.115205e+00	0.245113e-02	0.595122e-01	0.131457e-01	0.873615e-02	0.339870e-01
17	0.101629e+00	0.217196e-01	0.529715e-01	0.851164e-05	0.329552e-01	0.261298e-01
18	0.826496e-01	0.516015e-01	0.280084e-01	0.142545e-01	0.404018e-01	0.437517e-02
19	0.619726e-01	0.792139e-01	0.493537e-02	0.405759e-01	0.214331e-01	0.343256e-02
20	0.428766e-01	0.944968e-01	0.167802e-02	0.519675e-01	0.154265e-02	0.258893e-01
21	0.273252e-01	0.938390e-01	0.215560e-01	0.377408e-01	0.677841e-02	0.378504e-01
22	0.160474e-01	0.804055e-01	0.530049e-01	0.124311e-01	0.317994e-01	0.222112e-01
23	0.867367e-02	0.606707e-01	0.794492e-01	0.167429e-05	0.483686e-01	0.220397e-02
24	0.432615e-02	0.409252e-01	0.900593e-01	0.123441e-01	0.390075e-01	0.551101e-02
25	0.200278e-02	0.249360e-01	0.838997e-01	0.417748e-01	0.145783e-01	0.294134e-01
26	0.869145e-03	0.138687e-01	0.670552e-01	0.706248e-01	0.160833e-03	0.458041e-01
27	0.355671e-03	0.711520e-02	0.471928e-01	0.852859e-01	0.996251e-02	0.368773e-01
28	0.136896e-03	0.338931e-02	0.297697e-01	0.826488e-01	0.378066e-01	0.134808e-01
29	0.493031e-04	0.149972e-02	0.170751e-01	0.680358e-01	0.667111e-01	0.883186e-04
30	0.165446e-04	0.615912e-03	0.899611e-02	0.492572e-01	0.831383e-01	0.105234e-01

v- =	6	7	8
0	0.156155e-04	0.257968e-04	0.353662e-04
1	0.249431e-03	0.386805e-03	0.501415e-03
2	0.178053e-02	0.255894e-02	0.309891e-02
3	0.746173e-02	0.976495e-02	0.108595e-01
4	0.201976e-01	0.234476e-01	0.233124e-01
5	0.363993e-01	0.358835e-01	0.303781e-01
6	0.423045e-01	0.324118e-01	0.208059e-01
7	0.274703e-01	0.125027e-01	0.357158e-02
8	0.508164e-02	0.124117e-05	0.241951e-02
9	0.236365e-02	0.114522e-01	0.169350e-01
10	0.209807e-01	0.254555e-01	0.189561e-01
11	0.293988e-01	0.159853e-01	0.418535e-02
12	0.127044e-01	0.537732e-03	0.221609e-02
13	0.156489e-04	0.870958e-02	0.167504e-01
14	0.141509e-01	0.243260e-01	0.169588e-01
15	0.294871e-01	0.162570e-01	0.231654e-02
16	0.180006e-01	0.585131e-03	0.423036e-02
17	0.692344e-03	0.876654e-02	0.189195e-01
18	0.907039e-02	0.248571e-01	0.153280e-01
19	0.283532e-01	0.174361e-01	0.109761e-02
20	0.249014e-01	0.106523e-02	0.607726e-02
21	0.495332e-02	0.723247e-02	0.203563e-01
22	0.261391e-02	0.250489e-01	0.154158e-01
23	0.227652e-01	0.225757e-01	0.118666e-02
24	0.345316e-01	0.445008e-02	0.571505e-02
25	0.204827e-01	0.255294e-02	0.215281e-01
26	0.179798e-02	0.214014e-01	0.204010e-01
27	0.576746e-02	0.319958e-01	0.457213e-02
28	0.286204e-01	0.187157e-01	0.168159e-02
29	0.433600e-01	0.158319e-02	0.175813e-01
[illegible]	[illegible]	0.550429e-02	0.283310e-01

Table B.IV. BrCl B-X Franck-Condon factors.

observed in this work. In general, when FCF's were required in the data reduction, transitions were limited to the range $0 \leqslant v'' \leqslant 7$ and $2 \leqslant v' \leqslant 8$.

III. Vibrational Energy Spacing

The vibrational energies, energy spacings, and exponential energy gaps for $^{79}Br^{35}Cl(B;v')$ are given in table B.V.[100]

Table B.V
Vibrational Energy Spacing in $^{79}Br^{35}Cl(B)$, cm^{-1}

v'	G_v	$G_{v+1}-G_v$	$\exp[-(G_{v+1}-G_v)/k_BT]$
0	108.86	212.64	0.3595
1	321.50	205.33	0.3723
2	526.83	197.25	0.3871
3	724.08	188.27	0.4042
4	902.13	178.05	0.4246
5	1090.40	166.06	0.4498
6	1256.46	151.31	0.4829

IV. Absorption Bands and Intensity Factors

The absorption bands for BrCl(X) $v''=0-3$ to BrCl(B) $v'=0-6$ are listed in table B.VI. FCF's and intensity factors are also listed. Intensity factors, f_I, are defined as

$$f_I = q_{v',v''}\, N(v'')/N(v''=0) \qquad (B.2)$$

Note that the intensity factors drop off dramatically as v' is decreased. The $v'=0$ state is nearly unaccessible by optical excitation.

Table B.VI
$^{79}Br^{35}Cl$ Absorption Bands

Transition (v',v")	Band Head (cm^{-1})	FCF $q_{v',v"}$	Intensity Factor f_I
(6,0)	17883.71	1.8×10^{-5}	1.8×10^{-5}
(6,1)	17443.11	2.8×10^{-4}	3.4×10^{-5}
(6,2)	17006.05	1.9×10^{-3}	2.8×10^{-5}
(6,3)	16572.93	7.5×10^{-3}	1.3×10^{-6}
(5,0)	17717.68	9.1×10^{-6}	9.1×10^{-5}
(5,1)	17277.08	1.5×10^{-4}	1.8×10^{-5}
(5,2)	16840.13	1.1×10^{-3}	1.6×10^{-6}
(5,3)	16406.81	5.0×10^{-3}	9.1×10^{-6}
(4,0)	17539.66	3.8×10^{-6}	3.8×10^{-6}
(4,1)	17099.06	6.7×10^{-5}	8.0×10^{-6}
(4,2)	16662.11	5.5×10^{-4}	8.0×10^{-6}
(4,3)	16228.79	2.8×10^{-3}	5.0×10^{-6}
(3,0)	17351.42	1.3×10^{-6}	1.3×10^{-6}
(3,1)	16910.82	2.5×10^{-5}	3.0×10^{-6}
(3,2)	16473.87	2.2×10^{-4}	3.2×10^{-6}
(3,3)	16004.55	1.3×10^{-3}	2.3×10^{-7}
(2,0)	17154.18	3.3×10^{-7}	3.3×10^{-7}
(2,1)	16713.58	7.0×10^{-6}	8.4×10^{-7}
(2,2)	16276.63	6.9×10^{-5}	1.0×10^{-7}
(2,3)	15843.31	4.3×10^{-4}	7.7×10^{-8}
(1,0)	16941.87	5.9×10^{-8}	5.9×10^{-7}
(1,1)	16508.28	1.3×10^{-6}	1.6×10^{-7}
(1,2)	16071.33	1.5×10^{-5}	2.2×10^{-7}
(1,3)	15638.01	1.0×10^{-4}	1.8×10^{-9}
(0,0)	16736.25	5.4×10^{-9}	5.4×10^{-8}
(0,1)	16295.65	1.4×10^{-7}	1.4×10^{-8}
(0,2)	15858.70	1.6×10^{-6}	7.4×10^{-8}
(0,3)	15425.38	1.3×10^{-5}	7.3×10^{-8}

Based on the intensity factors reported in table B.VI, the $v_o"=1$ to $v_o'=4,5$, and 6 transitions were chosen to initially populate excited BrCl(B;v') states in the CW experiments.

V. Pulsed Emission Band Overlap

Due to the severe overlap of vibrational bands in B-X emission spectra and the maximum 2.5 nm resolution of the pulsed experiments, complete spectral isolation of individual v′ states was not possible. The "psuedo-CW" spectra described in the experimental chapter provides important information on the degree of vibrational overlap for various (v′,v") transitions. Sample "psuedo-CW" spectra are given in figures B1-B3. Also shown in figures B1-B3 are the emission bands from a pure Br_2 sample and the predicted BrCl(B;v′) transitions weighted by their Franck-Condon factors. The spectra were observed after initially populating v_o'=6. Solid vertical lines indicate the wavelengths used to observe emission from v′=0-6 in the *pulsed experiments*. Similar results were obtained for initially populated states v_o'=5-3. These observation wavelengths were chosen to minimize BrCl(B;v′) vibrational overlap as well as any Br_2 interferences. The observation wavelengths for each v′ state under conditions of various initially populated states, v_o', are listed in table B.VII. The pump transitions for the pulsed experiments are assigned from pulsed excitation spectra shown in figure 27 and figures B4-B6. Band heads are indicated in these figures.

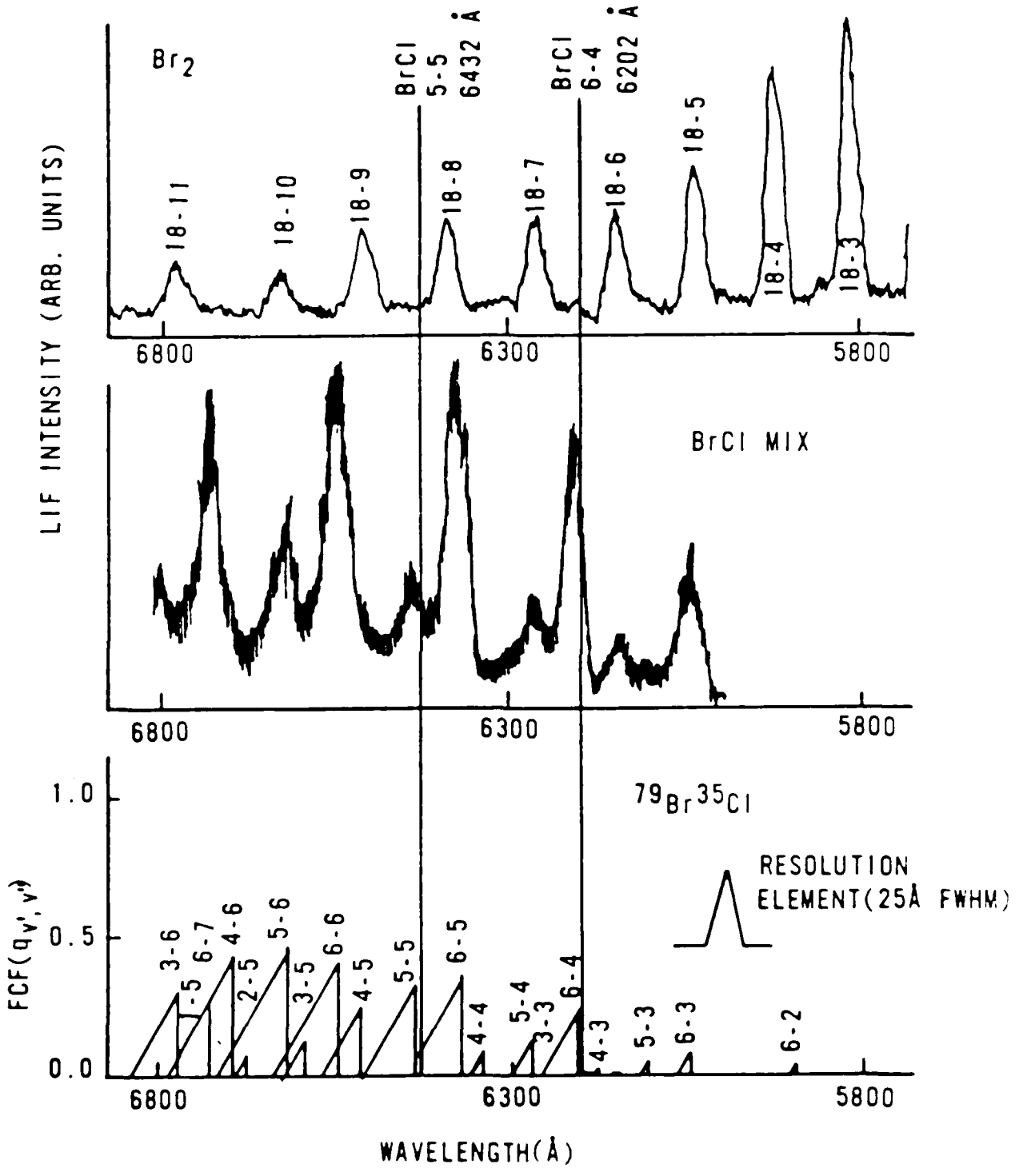

Figure B1. "Psuedo-CW" spectra. Time-averaged pulsed emission spectra for intially populating $v_o' = 6$.

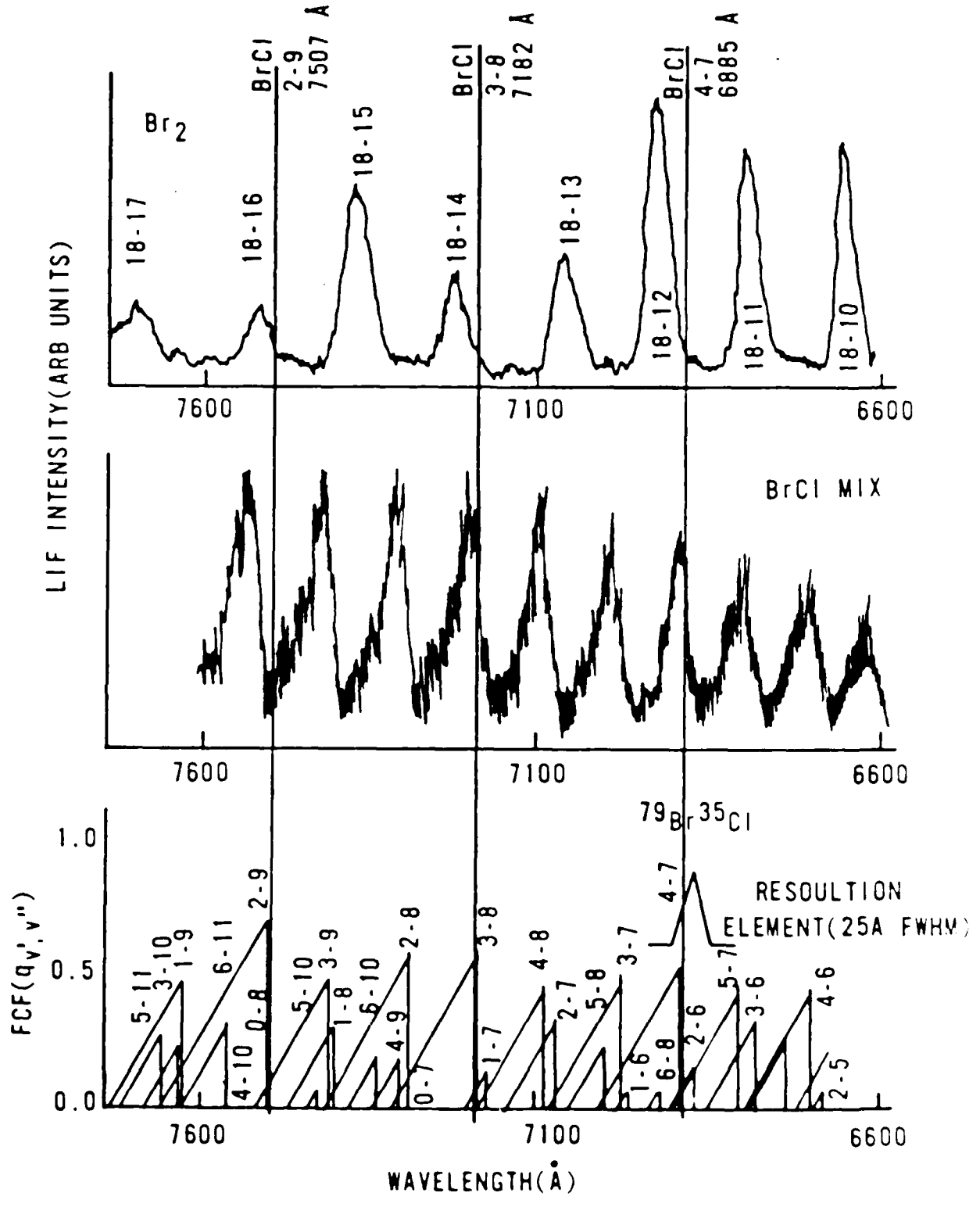

Figure B2. "Psuedo CW" spectra. Time averaged pulsed emission spectra for initially populating $v_o' = 6$.

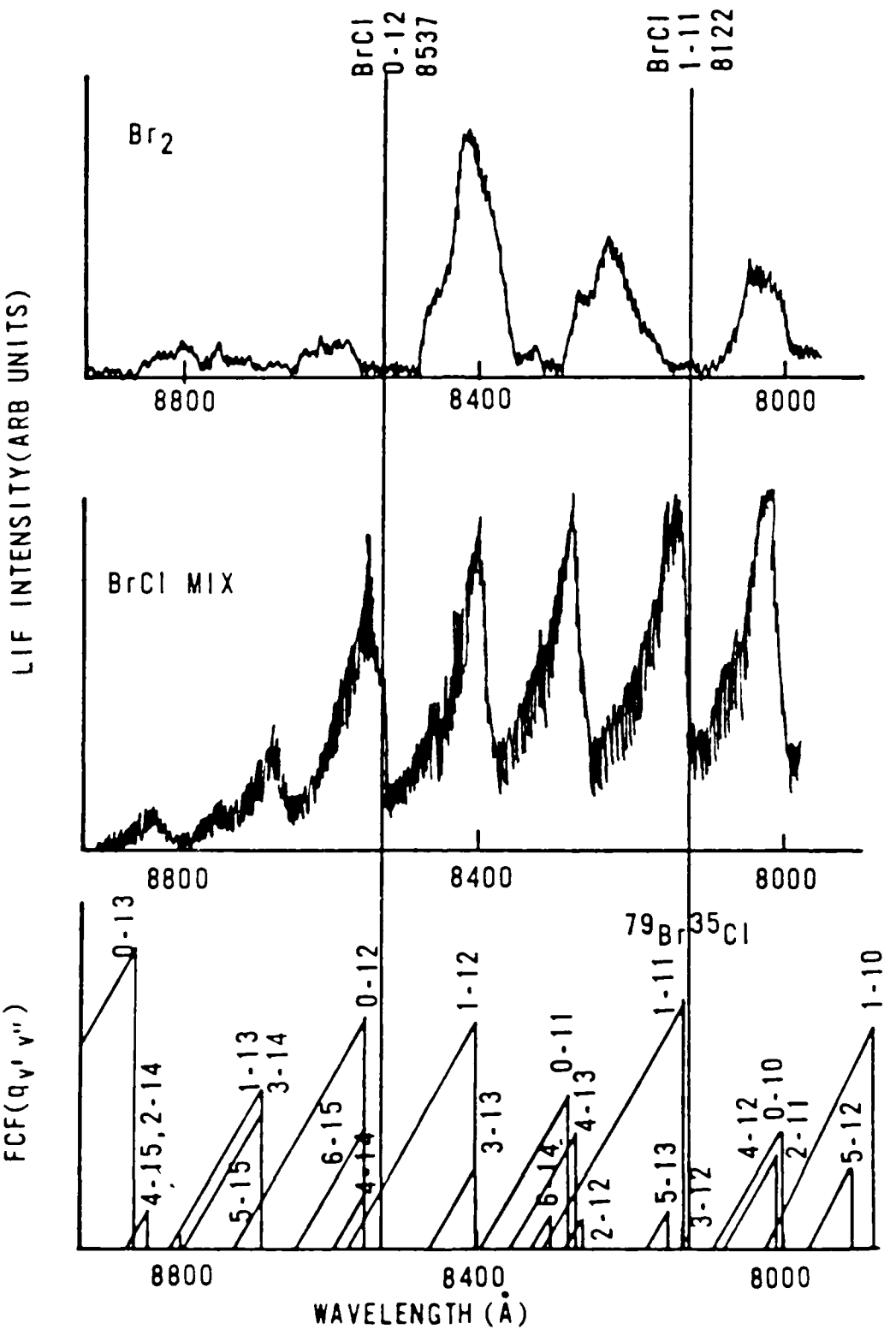

Figure B3. "Psuedo CW" spectra. Time-averaged pulsed emission spectra for initially populating $v_o' = 6$.

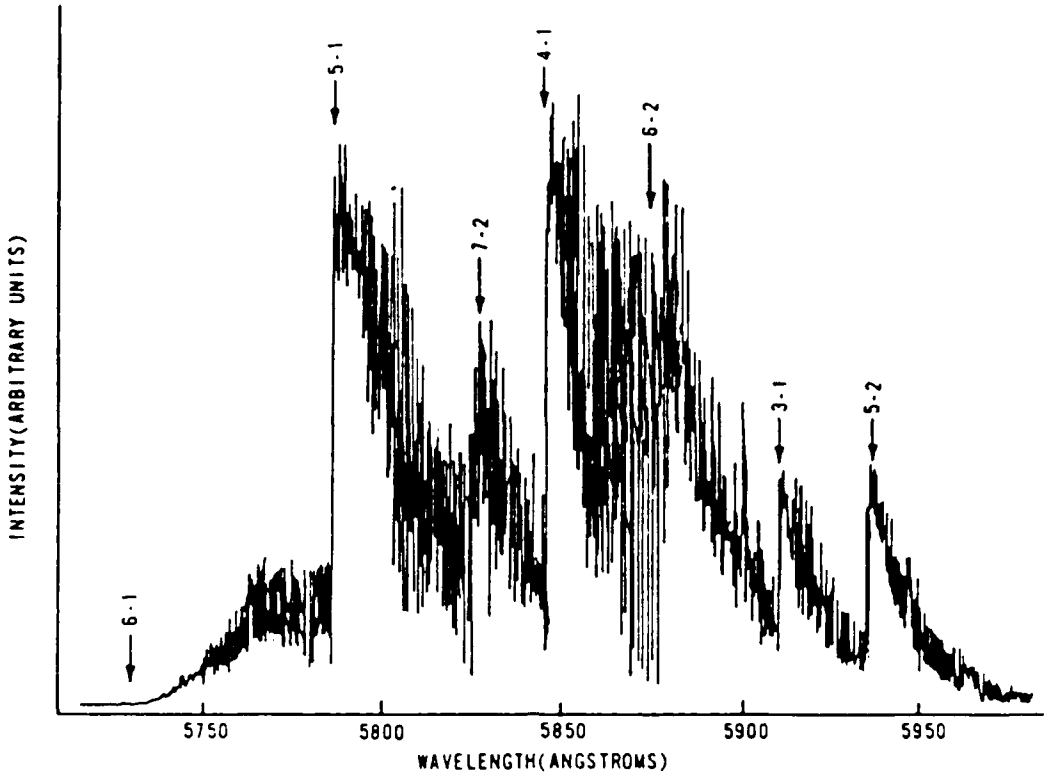

Figure B4. Pulsed excitation spectrum.

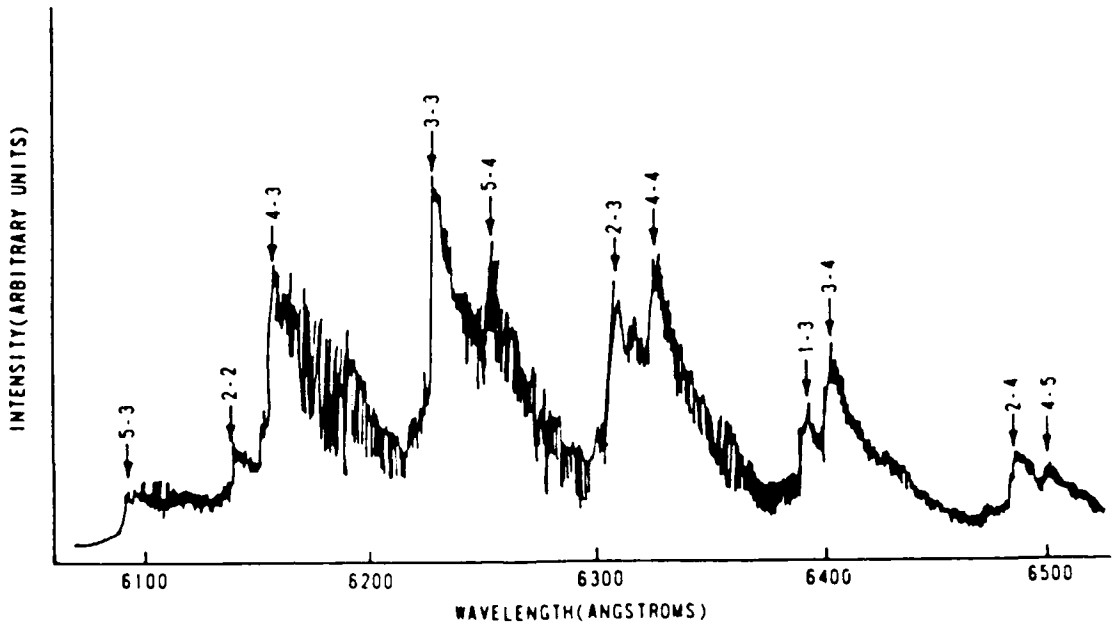

Figure B5. Pulsed excitation spectrum.

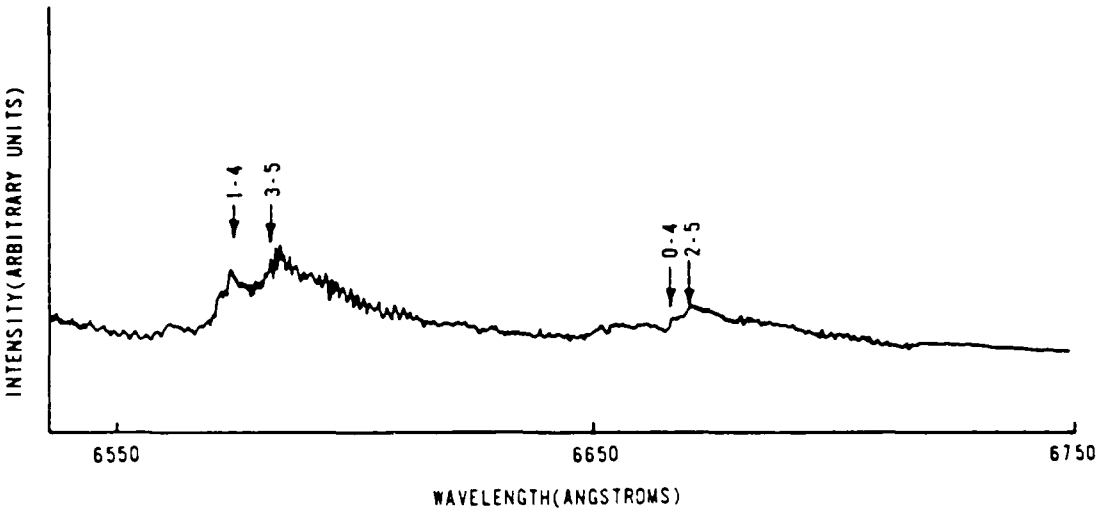

Figure B6. Pulsed excitation spectrum.

Table B.VII
Pulsed Emission Band Observation Wavelengths (nm)
for a given parent state and pump wavelength, λ_p

(v_o', v_o'')	λ_p	$v'=0$	1	2	3	4	5	6
(6,0)	560.0	853.7	811.2	750.7	718.2	688.5	643.2	620.2
(5,0)	565.0	853.7	840.5	752.0	718.2	689.0	662.6	637.2
(4,0)	570.5	853.7	812.2	775.0	718.2	688.5	643.2	620.2
(3,1)	592.0	853.7	812.2	750.7	718.2	688.5	662.5	637.2
(2,3)	631.1	856.5	814.0	776.0	719.0	688.5	*****	*****
(1,3)	639.3	856.5	814.0	750.7	719.0	688.5	*****	*****

In order to relate relative number densities to emission intensity, the amount of vibrational overlap at each observation wavelength must be quantified. Franck-Condon factors and relative band head locations have been used to calculate the percentage overlap of emission due to each v' state at the observation wavelengths of table B.VII. The

results are listed in table B.VIII. The intensity observed at a given observation wavelength, λ_{obs}, is described by the emission from all vibrational states {v'} that emit within the spectral region λ_{obs} +/- λ_{res}:

$$I_{obs} = C \sum_{v'v''} q_{v',v''} N_{v'} h(\lambda_{obs} - \lambda_{v',v''}) \qquad (B.3)$$

where

C = arbitrary constant

$q_{v',v''}$ = Franck-Condon factor for (v',v") transition

$\lambda_{v',v''}$ = band head for (v',v") transition

λ_{obs} = observation wavelength

λ_{res} = spectral resolution = 2.5 nm

$N_{v'}$ = number density of state v'

$h(\lambda_{obs} - \lambda_{v',v''})$ = function describing the relative observed intensity at λ_{obs} with respect to the observed intensity at the band head.

The function $h(\lambda_{obs} - \lambda_{v',v''})$ was estimated from the "psuedo-cw" spectra similar to that shown in figures B.1-B.3. By assuming a triangular vibrational band intensity distribution, the expression B.4 was obtained:

$$h(\lambda_{obs} - \lambda_{v',v''}) = \begin{cases} 1-(\lambda_{obs} - \lambda_{v',v''})/12.0 & 12.0 > \lambda_{obs} - \lambda_{v',v''} > 0 \\ 1-(\lambda_{v',v''} - \lambda_{obs})/3.5 & -3.5 < \lambda_{obs} - \lambda_{v',v''} < 0 \\ 0 & \text{elsewhere} \end{cases} \qquad (B.4)$$

Table B.VIII
Pulsed Emission Band Overlap Percentages

Observed v′	Percent of each v′ Observed								
	v′=0	1	2	3	4	5	6	7	8
0	.741	.000	.000	.000	.259	.000	.000	.000	.000
1	.000	.940	.000	.060	.000	.000	.000	.000	.000
2	.110	.000	.880	.000	.010	.000	.000	.000	.000
3	.000	.188	.000	.812	.000	.000	.000	.000	.000
4	.000	.000	.219	.000	.781	.000	.000	.000	.000
5	.000	.000	.000	.080	.000	.920	.000	.000	.000
6	.000	.000	.000	.000	.000	.000	1.00	.000	.000
7	.000	.000	.000	.000	.000	.000	.000	1.00	.000
8	.000	.000	.000	.000	.000	.000	.000	.000	1.00

function of emission wavelength is given in figure C2. Also shown in figure C2 is the theoretical Planck distribution for the blackbody emission (——) and the relative spectral response (---). The spectral response is calculated from equation (C.2):

$$D(\ ) = n_d(\ )/n_{bb}(\ ) \qquad (C.2)$$

where

$n_d(\ )$ = the number of photons/sec detected by the PMT

$n_{bb}(\ )$ = the number of photons/sec emitted by the blackbody

In figure C2, the relative spectral response is normalized to a maximum value of 1.0. Table C.1 provides a listing of the relative spectral responses for the emission transitions observed in the CW experiment. Note that the values have been normalized to the value of the (3,6) transition.

Table C.1
CW Relative Spectral Response

Transition v',v''	Band Head (cm^{-1})	Franck-London $q_{v',v''}$	Spectral Response $D(\ )$
[illegible]	[illegible]	[illegible]	[illegible]
[illegible]	[illegible]	[illegible]	[illegible]
[illegible]	[illegible]	[illegible]	[illegible]
[illegible]	[illegible]	[illegible]	[illegible]
[illegible]	[illegible]	[illegible]	[illegible]
[illegible]	[illegible]	[illegible]	[illegible]
[illegible]	[illegible]	[illegible]	[illegible]
[illegible]	[illegible]	[illegible]	[illegible]
[illegible]	[illegible]	[illegible]	[illegible]
[illegible]	[illegible]	[illegible]	[illegible]
[illegible]	[illegible]	[illegible]	[illegible]
[illegible]	[illegible]	[illegible]	[illegible]
[illegible]	[illegible]	[illegible]	[illegible]
[illegible]	[illegible]	[illegible]	[illegible]

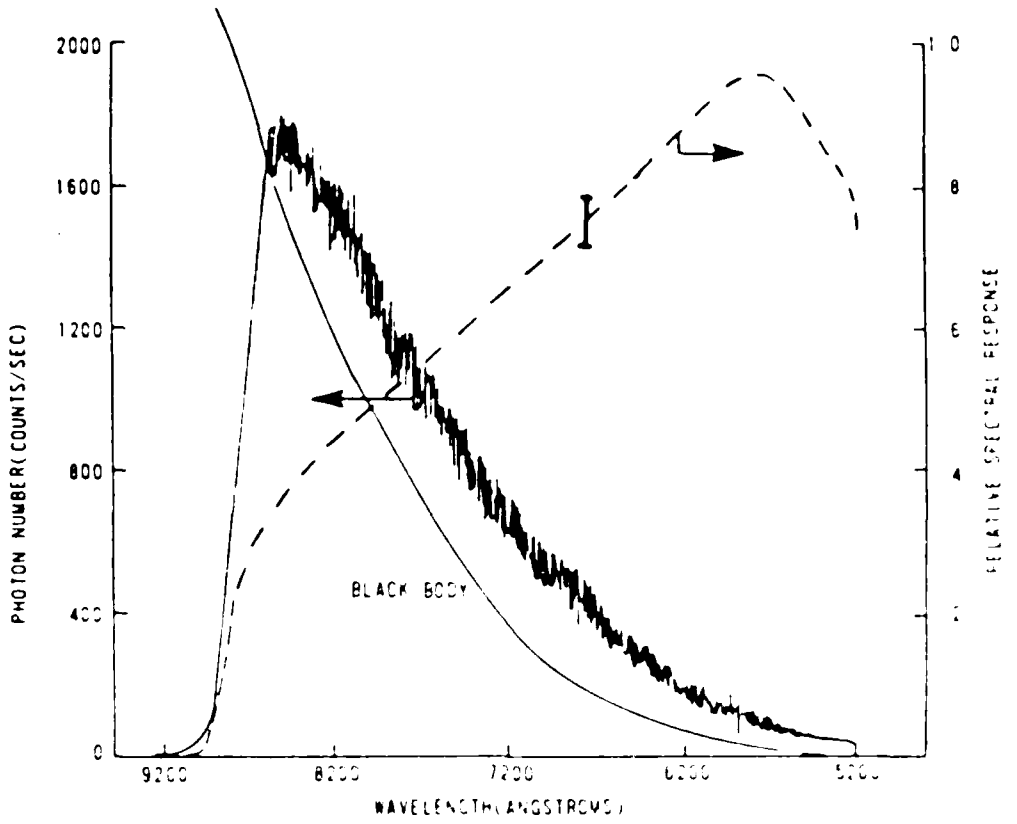

Figure C2. CW spectral response calibration curve.

C. Monochromator Calibration

The resolution of the 0.3 meter monochromator as a function of slit width is given in figure C3. The resolution was measured as the FWHM of the spectral features recorded from a Ne lamp.

The BrCl X - state vibrational spacing is nearly double that of the BrCl B - state (w_e'=444.3 cm^{-1}, w_e''=222.7 cm^{-1}). As a result, the emission bands separated by "v= even are all highly overlapped. A 200 ,m slit width was chosen to resolve all the vibrational band heads and still yield sufficient signal strengths. The 200 ,m slits provide a 0.6 nm

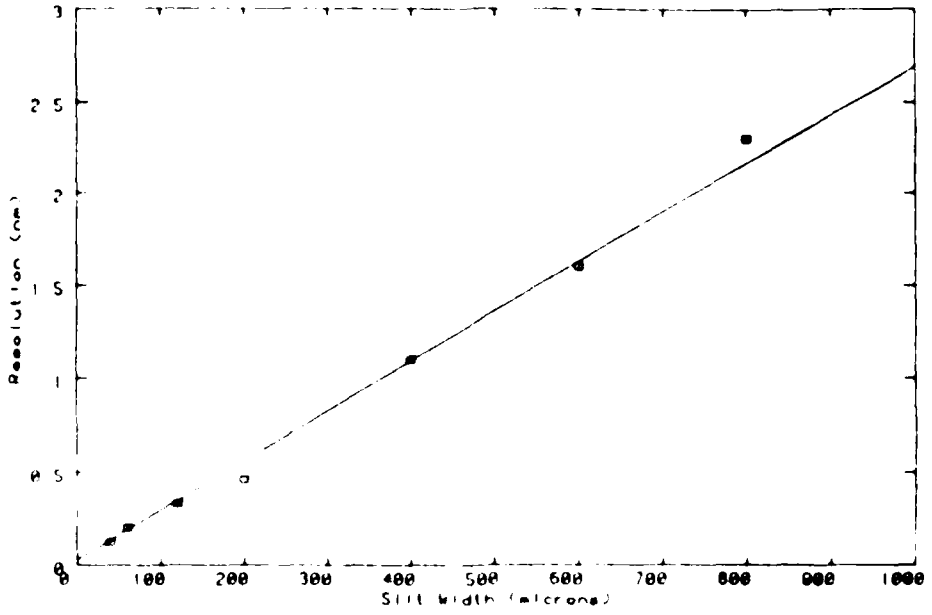

Figure C3. Monochromator resolution.

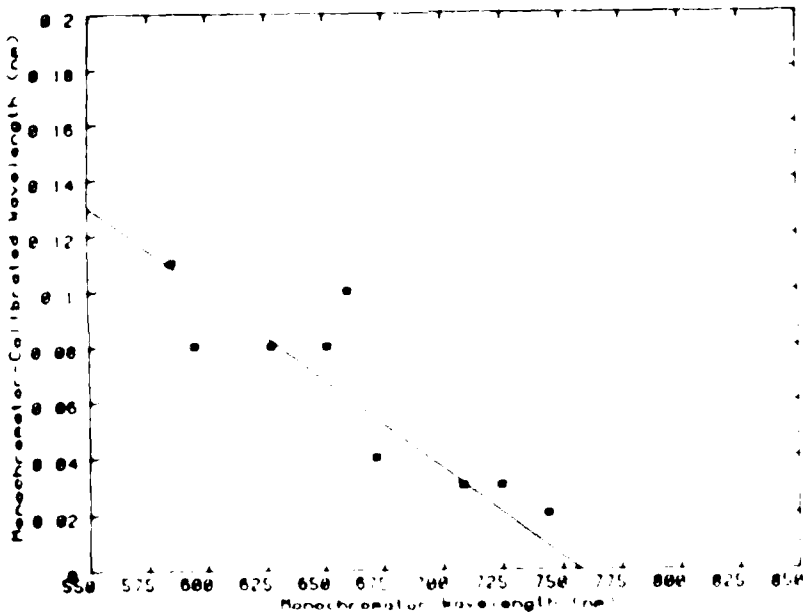

Figure C4. Monochromator wavelength calibration.

resolution. This resolution was also sufficient for resolving the P-R doublet emission from the parent rotational state for J>30.

The absolute wavelength of the monochromator was calibrated using a Ne lamp. The correction was less than 0.1 nm over the range 550 - 800 nm. The needed corrections are given in figure C4.

II. Pulsed Experiments

A. Time Base Calibration

The transient recorder time base used in the pulsed experiments has been calibrated by applying a sine wave of known frequency to the transient recorder and comparing the resulting digitized signal with the input function. Figure C5a shows an oscilliscope trace of the input sine function and figure C5b gives the resulting digitized waveform. Table C.II compares the input period as recorded on the oscilliscope with the period of the digitized signal for several recorder time bases. The measured period is about 2% shorter than the input period. This small difference in measured and observed periods is reproducible, but may be due to inaccurate time bases for either the oscilliscope or transient digitizer. Since the error is small, the transient recorder time scales are used without correction.

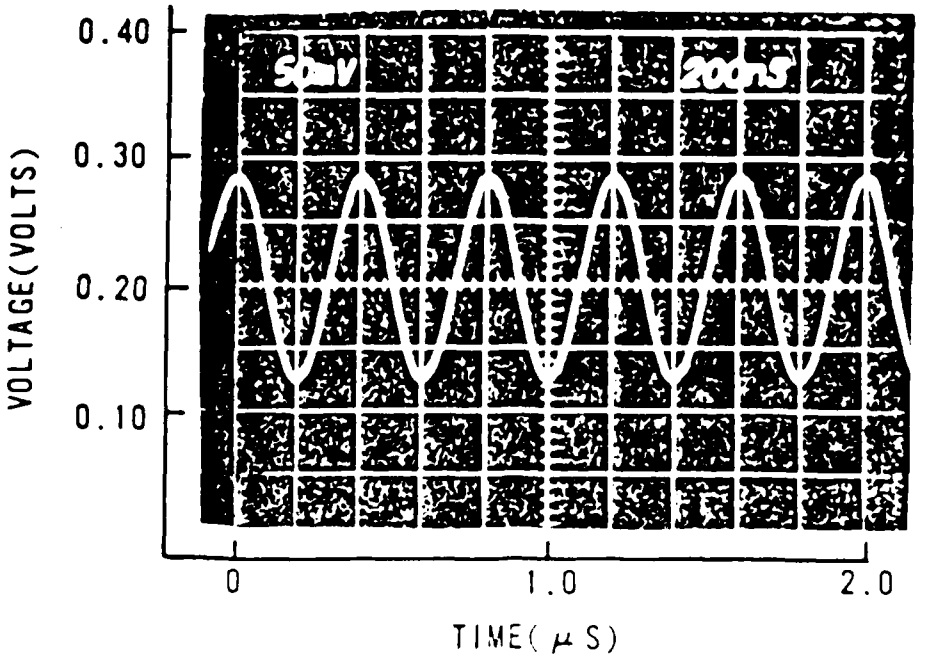

Figure C5a. Input sine wave to transient recorder for time base calibration.

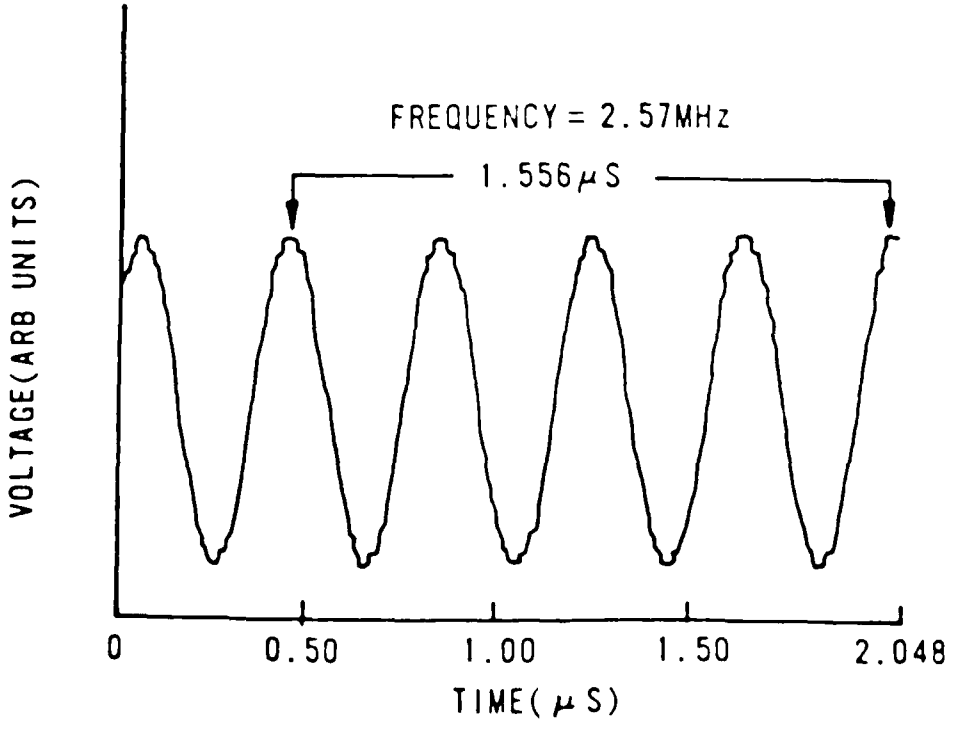

Figure C5b. Digitized sine waveform from transient recorder.

Table C.II
Transient Recorder Time-Base Calibration

Time/Channel (ns)	Input Period (10^{-6} s)	Measured Period (10^{-6} s)	% Deviation in Period
50	10.0	9.79 +/- 0.1	2.1 +/- 0.1
10	2.00	1.97 +/- 0.02	1.5 +/- 0.1
2	0.40	.389 +/- .004	2.7 +/- 0.1
		Average Deviation =	2.1 +/- 0.1

B. Spectral Response

The relative spectral response of the pulsed detection system was determined by resolving the emission from a blackbody source at 1010 C. Two detection systems were calibrated. The observed emission intensity for the C31034 PMT at 1400 V and room temperature is shown in figure C6a and the intensity for the S-20 PMT is shown in figure C6b. Also shown in the figures are the theoretical curve for blackbody emission (——) and the relative spectral response (---). The relative spectral response is obtained from equation (C.2).

Note that the C31034 PMT detects emission at high wavelengths much better than the S-20 PMT. As a result, the two detection systems observe various v′ states in total emission with varying efficiency. The detectable emission for each v′ state, $D_{v'}$, is calculated from equation C.3 and is reported in table C.III.

$$D_{v'} = \sum_{v''} q_{v',v''} \; D(\;_{v',v''}) \; / \;_{v',v''}{}^{4} \qquad (C.3)$$

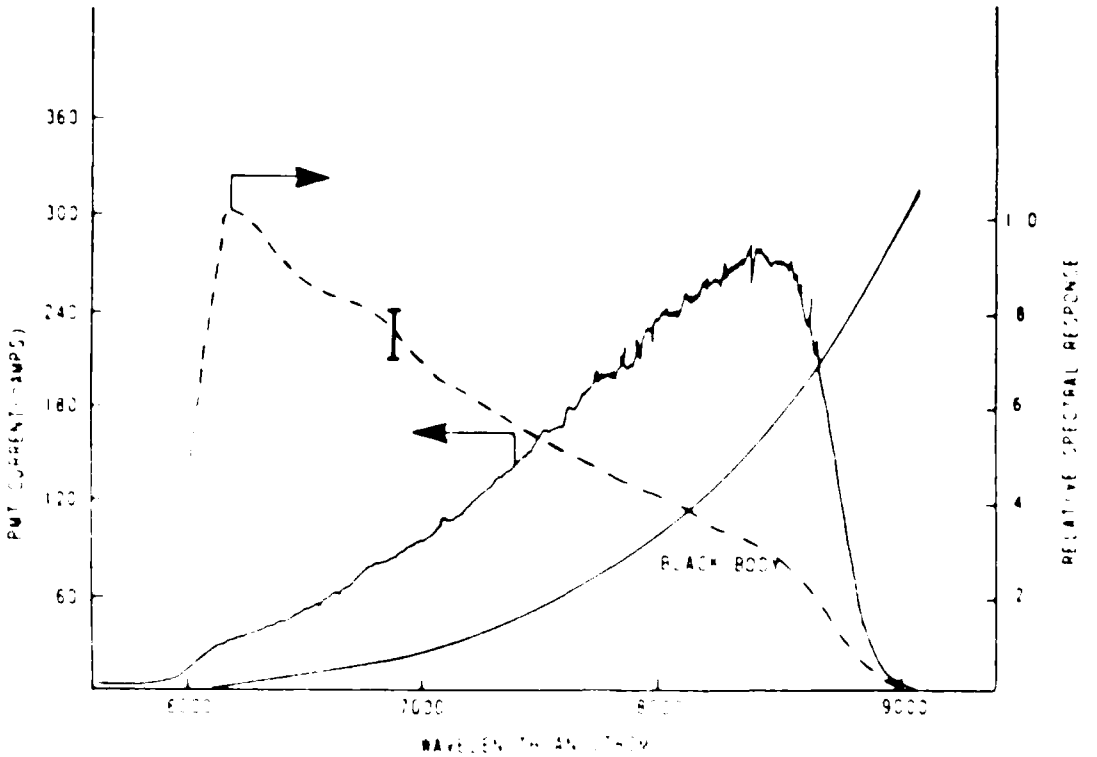

Figure C6a. Spectral response calibration for C31034 PMT.

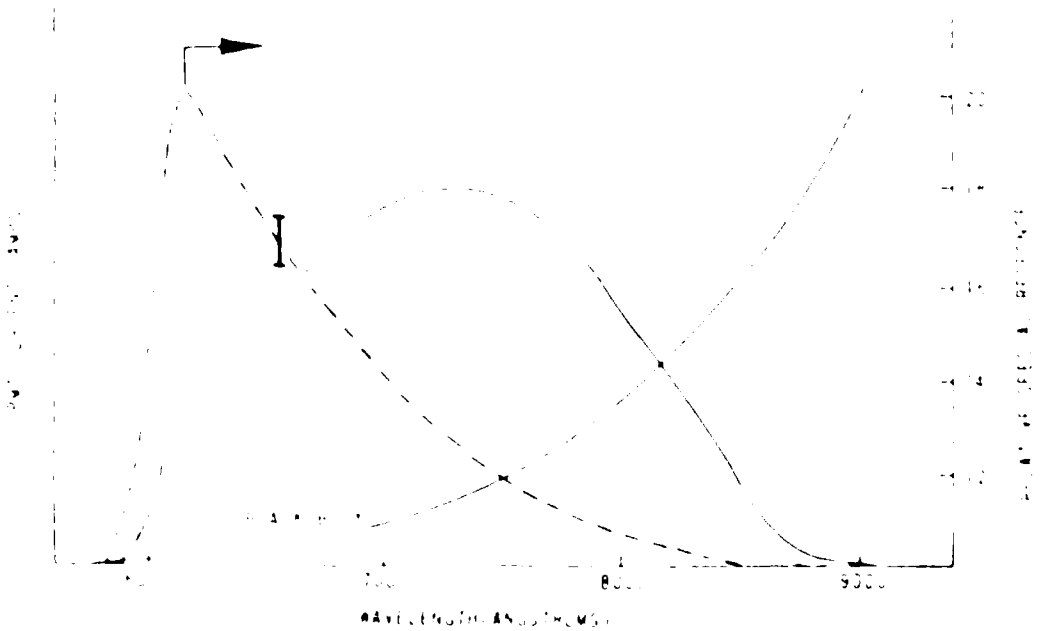

Figure C6b. Spectral response calibration for the S-20 PMT.

Table C.III
Detectable emission from BrCl(B;v′)

Vibrational State v′	Detectable Emission, $D_{v'}$ S-20 PMT (w/600 nm LP)	C31034 PMT (w/600 nm LP)	C31034 PMT (w/750 nm LP)
0	0.006	0.039	0.038
1	0.027	0.097	0.068
2	0.054	0.126	0.056
3	0.083	0.155	0.018
4	0.113	0.182	0.019
5	0.139	0.197	0.021
6	0.149	0.198	0.020

Appendix D

Basic Energy Transfer Theories

This appendix describes several basic energy transfer theories. The gas kinetic collision rate[182], Ehrenfest's adiabatic principle[181], the Landau-Teller theory[153,183], the Schwartz, Slawsky and Herzfeld theory[149,178], the Troe model[141-142], and the Montroll-Shuler model[140] are presented. In addition, basic angular momentum considerations in R-T transfer are discussed.

I. Gas Kinetic Collision Rates

For elastic collisions with particles considered to be hard spheres, the collision frequency for molecule A with buffer specie B is[182]

$$Z_A = N_B \sigma_{AB} v_{AB} \qquad (1.1)$$

where

Z_A = collision frequency

N_B = number density of specie B

σ_{AB} = velocity-averaged collision cross-section

$= \pi (r_A + r_B)^2$

r_A, r_B = radius of particle A,B

$v_{AB} = \langle v_{AB} \rangle = \left(\frac{8kT}{\pi \mu_{AB}} \right)^{1/2}$ = average relative velocity

μ_{AB} = reduced mass of the collision pair

The resulting rate constant for an elastic collision is

collisions is

$$k_g = \sigma_g v_{AB} \qquad (D.2)$$

This result is particularly valuable for comparing the relative efficiencies of various kinetic processes. The probability for any event may be defined as

$$P = \sigma / \sigma_g \qquad (D.3)$$

where

σ = cross-section for the kinetic process of interest

P = probability for event during a single collision

The gas kinetic cross-sections, reduced masses, relative speeds and rate constants for various collision partners with BrCl are given in table D.I.[184]

Table D.I
Gas Kinetic Collision Parameters
(For BrCl Collisions)

Collision Partner	Cross-section σ (Å^2)	Reduced Mass (a.u.)	Velocity (cm/sec)	Rate Constant (cm^3/molecule-sec)
H_2	[illegible]	[illegible]	[illegible]	[illegible]
N_2	[illegible]	[illegible]	[illegible]	[illegible]
Ar	[illegible]	[illegible]	[illegible]	[illegible]
Kr	[illegible]	[illegible]	[illegible]	[illegible]
Xe	[illegible]	[illegible]	[illegible]	[illegible]

II. Ehrenfest's Adiabatic Principle

An adiabatic vibrational collision occurs when no net exchange of energy occurs between the vibrating oscillator and the translating particle during the complete course of the collision. Such a collision will occur only if the vibrating molecule has sufficient time to adjust to the weak long range force of the collision partner. This will be true if the mean collision time is greater than the period of the oscillator,[15] that is

(D.4)

[illegible] interaction distance

[illegible] relative speed

[illegible] vibrational frequency

[illegible] collisions will be effective at V-T [illegible], vibrational transfer will be most [illegible] vibrational frequency, small mass [illegible], and strong long range interactions.

[illegible] first developed an elementary theory [illegible] based on Ehrenfest's adiabatic [illegible] range attractive portion of the [illegible] was neglected and the repulsive [illegible] the only potential with a large

enough gradient to affect vibrational transfer. A potential of the form $V(r)=V_o \exp(-\alpha r)$ with $\alpha=2\pi \nu_o/v$ was used.

The probability for vibrational transfer from $v'=1$ to $v'=0$, P_{10}, was calculated using time-dependent perturbation theory. The resulting probability is[181]

$$P_{10} = \exp\left[-3(2\pi^4 \mu \nu^2/\alpha^2 k_B T)^{1/3}\right] \qquad (D.5)$$

[illegible] that the logarithm of the probability is proportional to [illegible]. The matrix elements for collisional V-T transitions are [illegible]portional to the matrix elements for radiative transitions. [illegible] harmonic oscillator, the Hermite polynomials provide [illegible] transitions between adjacent states only, $|\Delta v| = 1$, and a [illegible] of transition probabilities as given in [illegible].

[illegible] $= v P_{10}$ (D.6)

[illegible]

[illegible], Slawsky, and Herzfeld (SSH) theory[149] is [illegible] for quantitative comparison of [illegible] V-T transfer rates. The attractive [illegible] molecular potential was neglected in the [illegible] theory includes the attractive [illegible]

[illegible] (D.7)

The attractive term, ε, increases the relative velocity or translational energy and thus, increases the V-T transfer probabilities.

The quantum mechanical SSH theory provides the probability for vibrational transfer from $v'=1$ to $v'=0$ as[181]

$$P_{10} \propto (\theta'/\theta)(\alpha'/T)^{1/6}\exp[-1.5(\theta'/T)^{1/3}+(\varepsilon/2T)+(\varepsilon/k_BT) \quad (D.8)$$

where

$\theta' = \mu 4\pi^2 L^2 \nu^2/k_B$

$\theta = h\nu/k_B$

$h\nu$ = vibrational energy

L = interaction length

If the vibrational spacing is relatively large, then the exponential factor will dominate the probability expression. In this case, the logarithm of the probability is proportional to $\mu^{1/3}$:

$$\ln P_{10} = A - B\,\mu^{1/3} \quad (D.9)$$

This is the same result as obtained from the Landau - Teller theory.

V. The Troe Model

The Troe model[141-142] treats thermal unimolecular reaction in gases at low pressures. A master rate equation similar to that of equation (30) is used to describe the

evolution of population in stable and unstable states. A theoretical expression for the rate constants is obtained under steady-state conditions, assuming an exponential scaling of collisional transition probabilities. The collisional transfer probability for a transition from a state with energy E′ to a state with energy E is assumed to be given by equation (D.10):

$$P(E' \; E) = 1/N \begin{cases} \exp[-(E-E')/C_1] & E'<E \\ \exp[-(E'-E)/C_2] & E'>E \end{cases} \qquad (D.10)$$

where C_1 and C_2 are constants related by detailed balance.

VII. The Montroll-Shuler Model

Montroll and Shuler[172] have obtained an analytic solution to the problem of vibrational relaxation for a system of harmonic oscillators. The oscillators are assumed to be in a chemically-inert, constant temperature heat bath. The excited state vibrational populations are considered small so that the only interactions are between the excited oscillators and the heat bath molecules. That is, the transfer processes are first order with respect to oscillator concentration. Both collisional and radiative transitions are considered. The master rate equation (30) describes such a system.

The Landau-Teller theory for V-T transfer probabilities is used for vibrational scaling:

$$k_V^M(v,v-1) = v\, k_V^M(1,0) \qquad |\Delta v| = 1 \text{ only} \qquad (D.11)$$

The principle of detailed balance is applied to obtain the $\Delta v=+1$ rates:

$$k_V^M(v-1,v) = k_V^M(v,v-1)\, \exp(-\Delta\varepsilon_{v,v-1}/k_B T) \qquad (D.12)$$

The radiative lifetimes and electronic quenching rates are assumed to be independent of vibrational state. In this way, all of the elements of the rate matrix R_{pq} are described by the radiative lifetime, electronic quenching rate, and fundamental vibrational transfer rate.

The radiative and electronic quenching effects are easily handled by transforming the population $x_n(t)$ by

$$z_n(t) = x_n(t)\, \exp(t/\tau) \qquad (D.13)$$

$$1/\tau = 1/\tau_r + k_{eq}^M\, M$$

With these assumptions and the transformation (D.13), the master rate equation (30) may be written as

$$dz_n/dt = k_V^M(1,0)\{ne^{-\theta} z_{n-1} - [n+(n+1)e^{-\theta}]z_n + (n+1)z_{n+1}\} \qquad (D.14)$$

where

$$\theta = h\nu/k_B T$$

If the equilibrium is disturbed by instantaneously populating a single vibrational state, m, then the Montroll-Shuler solution to equation (D.16) for the population in vibrational state n is[172]

$$z_n(t) = \left(\frac{(1-e^{-\theta})e^{m\theta}}{(e^{-t'}-e^{-\theta})}\right)\left(\frac{e^{-t'}-1}{e^{-t'}-e^{-\theta}}\right)^{m+n} F(-n,-m,1;U^2) \qquad (D.15)$$

where

$U = \sinh(\theta/2)/\sinh(t'/2)$

$t' = k_V^M(1,0)t(1-e^{-\theta})$

F= hypergeometric function

VI. Angular Momentum and R-T Transfer

Rotational transfer is strongly affected by angular momentum considerations. The total angular momentum in a collision must be conserved. There are two important modes of angular momentum; (1) the rotation of a diatomic molecule given by quantum number J, and (2) the angular momentum of the collision pair about the center of mass, L = r x p. In center of mass coordinates, the angular momentum of the collision pair may be written as

$$L = \mu b v \qquad (D.16)$$

where

L = angular momentum

b = impact parameter

v = average relative speed = $(8k_BT/\pi\mu)^{1/2}$

The probability for R-T transfer depends directly on the angular momentum available in the collision,

$$\sigma_R / \sigma_g \sim \mu^{1/2} \qquad \text{(D.17)}$$

Appendix E

Eigenvalue Solution to the Master Rate Equation

A system of homogeneous, linear, first-order differential equations with constant coefficients may be written[185]

$$dx_i/dt = a_{ij}\, x_j \qquad x_i(t=0) = x_i(0) \tag{E.1}$$

The master rate equation (30) is such a system of equations.

The transformation $x_i = u_i \exp(\ell t)$ yields a system of linear homogeneous algebraic equations:

$$(a_{ij} - \ell \delta_{ij})\, u_j = 0 \tag{E.2}$$

The equations (E.2) will have a nontrivial solution if, and only if, its determinent is zero:

$$\text{Det}\,(a_{ij} - \ell \delta_{ij}) = 0 \tag{E.3}$$

Equation (E.3) is termed the characteristic equation and the roots, ℓ, are termed the eigenvalues. Associated with each eigenvalue is a nonzero eigenvector, u_i, defined by equation (E.2).

The solution to the system of differential equations (E.1) is[185]

$$x_i = \sum_j C_j\, u_i^{\,j} \exp(\ell_j t) \tag{E.4}$$

where

u_i^j is the i^{th} element of the j^{th} eigenvector

ℓ_j is the j^{th} eigenvalue

and the initial condition constants, C_j, are defined by

$$x_i(0) = \sum_j C_j \, u_i^j \qquad (E.5)$$

The solution (E.4) applies to the case for distinct eigenvalues, $\ell_i \neq \ell_j$ for all i,j. The solution is complete and every solution can be represented by equation (E.4).

The problem just described can be easily transformed to a system of Volterra Integral Equations of the Second Kind.[169] By integrating equations (E.1) in time, equation (E.6) is obtained.

$$x_i(\tau) - \int_0^\tau a_{ij} \, x_j(t) \, dt = x_i(0) \qquad (E.6)$$

A system of Volterra Integral Equations of the Second Kind have unique solutions and the solution, $x_i(t)$, depends continuously on the data, a_{ij}.[169] That is, small changes in the data do not imply arbitrarily large changes in the response. Applying this result to the master rate equation (30) implies that the population distributions depend continuously on the rate constants.

The solution (E.4) is assymtotically stable if, and only if, all the eigenvalues have negative real parts.[185] The population distributions given by the master rate equations

must meet this requirement. Moreover, one would expect the population distributions not to oscillate in time. This would require real, non-negative eigenvalues. Hermitian matrices always have real eigenvalues.[186] However, the rate matrix, R_{pq}, is not symetric, and therefore not Hermitian. As will be shown in the following discussion, the detailed balance property inherent to the R_{pq} matrix does guarantee real, non-negative eigenvalues.

A similarity transformation preserves eigenvalues.[185] Thus, if a similarity transformation (equation E.7) can be found for the rate matrix R_{pq} that produces a symetric matrix b_{pq}, then the eigenvalues of R_{pq} are real.

$$b_{pq} = T_{ip} R_{ij} T_{jq} \tag{E.7}$$

If transformation matrix T_{ij} is chosen to be the diagonal matrix with elements equal to the square root of the elements of the equlibrium population distribution, x_i^e, then a symetric matrix b_{ij} is obtained from equation (E.7).[171] Thus, the eigenvalues for the master rate equation are real.

Under single collision conditions, the population in the initially-populated state must decay exponentially with a lifetime determined by the quenching rate for that state:

$$1/\tau = 1/\tau_r + k_Q^M(v)\, M \tag{E.8}$$

The eigenvalues of the rate matrix R_{pq} will not, in general, be equal to the quenching rates, however. It will be shown below that, at early times (or low pressures), the solution (E.4) does decay with a rate given by equation (E.8).

The solution (E.4), at early times, can be expanded in a Taylor Series to give

$$x_i(t) = \sum_j C_j \, u_i^{\,j} + \sum_j C_j u_i^{\,j} (\ell_j t) + \ldots . \qquad (E.9)$$

$$= \quad x_i(0) + \sum_j C_j u_i^{\,j} (\ell_j t) + \ldots .$$

In order for the fluorescence to decay with a rate constant $k_Q^{\,M}(v)$, the population distribution must be

$$x_i(t) = x_i(0) \exp(-R_{(i),(i)} \, t) \qquad (E.10)$$

$$= x_i(0) - R_{(i),(i)} t + \ldots .$$

and the t^1 - terms in equation (E.10) and equation (E.9) must be equal:

$$\sum_j C_j \, u_i^{\,j} \, \ell_j \quad = \quad -R_{(i),(i)} \qquad (E.11)$$

The eigenvalue problem, equation (E.2), can be written as

$$\sum_j R_{i,j} \, u_j^{\,k} = \ell_k \, u_i^{\,k} \qquad (E.12)$$

Multiplying equation (E.12) by C_k and summing over index k yields

$$\sum_k \sum_j C_k \, R_{ij} \, u_j^{\,k} = \sum_k C_k \, \ell_k \, u_i^{\,k} \qquad (E.13)$$

Substituting equation (E.5) in the left-hand-side of equation (E.13) provides

$$\sum_j R_{ij}\, x_j(0) = \sum_k C_{k'k}\, u_i^k \qquad (E.14)$$

Assuming a single quantum state is initially populated, $x_j(0)=\delta_{j,jo}$, and recognizing that $R_{(i),(i)} = k_Q^M M$, then

$$k_Q^M(i) = \sum_k C_{k'k}\, u_i^k \qquad (E.15)$$

Thus, the eigenvalue expansion does decay with the quenching rate at low pressures or at early times.

For a strongly coupled vibrational manifold, the eigenvalues of the rate matrix R_{pq} are obtained from a convolution of kinetic rates. Thus, under multiple collision conditions, the scaling of observed *quenching* rates (eigenvalues) is not equivalent to the scaling of individual quenching rates, $k_Q^M(v)$. Indeed, for the numerical pulsed solution #1 presented in table IX, the eigenvalues scale exponentially with vibrational state, as shown in figure E1. This is true even though the total quenching rate constants are independent of vibrational state for $v'<6$.

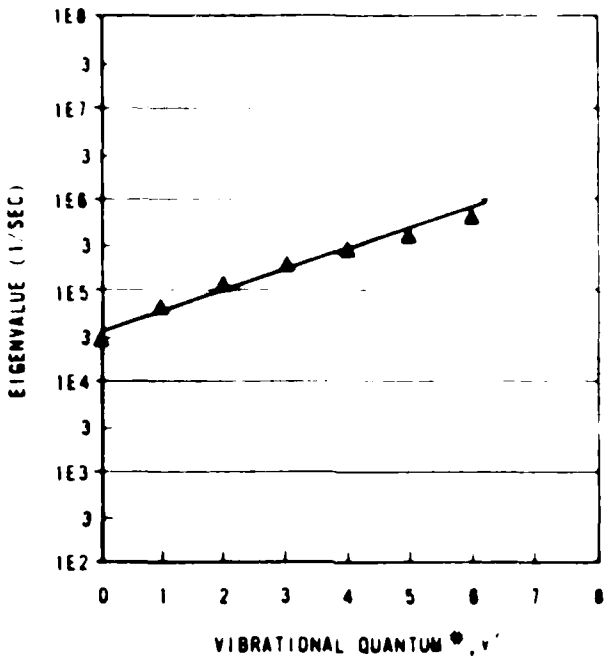

Figure E1. Vibrational scaling of rate matrix eigenvalues. Pumped state is $v_o'=6$ and total mix pressure is 50 mT.

The rovibrational distribution within $Br_2(B)$ may be split into two groups: (1) stable rotational states and (2) predissociated rotational states. The boundary between these two groups is clearly defined at $v'=0$, $J'=42$. Figure F1 illustrates these energy levels. The rate constants k_+ and k_- refer to the rate of rotational transfer across the barrier. R_p denotes the rate of pumping into the predissociated state.

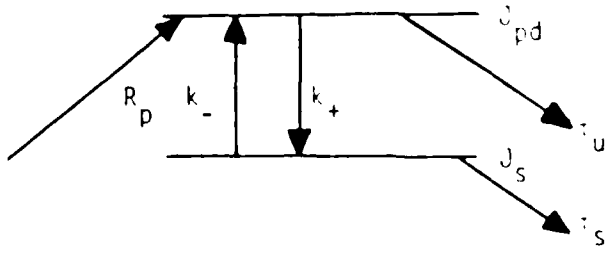

Figure F1. Energy states for rotational stablization model.

The rate equations for the populations in the stable and predissociated states are given by equations (F.1-F.2).

$$dN_s/dt = -N_s/\tau_s + k_+ N_u Y - k_- N_s Y \qquad (F.1)$$

$$dN_u/dt = R_p - N_u/\tau_u + k_- N_s Y - k_+ N_u Y \qquad (F.2)$$

where

N_s = number density in stable state, J_s

N_u = number density in predissociated state, J_{pd}

τ_s = lifetime of stable state

τ_u = lifetime of unstable state

The steady-state solutions of equations (F.1-F.2) are:

$$N_s/N_u = k_+ Y/(1/\tau_s + k_- Y) \qquad (F.3)$$

$$N_u = (R_p + k_- N_s Y)/(1/\tau_u + k_+ Y) \qquad (F.4)$$

The total excited state population, $N_s + N_u$, is therefore

$$N_s+N_u=R_p(k_+Y+k_-Y+1/\tau_s)/[(1/\tau_s)(1/\tau_u)+(k_-Y/\tau_u)+(k_+Y/\tau_s)] \qquad (F.5)$$

The total excited state density at zero buffer pressure ($Y=0$) is, from equation (F.5):

$$(N_s + N_u)_{Y=0} = R_p \tau_u$$

The total fluorescence intensity is proportional to the total excited state density, $I \propto N_s+N_u$. The relative intensity $I(Y=0)/I(Y)$ is obtained by dividing equation

AD-A179 575 COLLISIONAL DYNAMICS OF THE B 3PI(O+) STATE OF BROMINE 4/4
MONOCHLORIDE(U) AIR FORCE INST OF TECH WRIGHT-PATTERSON
AFB OH SCHOOL OF ENGINEERING G P PERRAM AUG 86
UNCLASSIFIED AFIT/DS/PH/86-1 F/G 7/2 NL

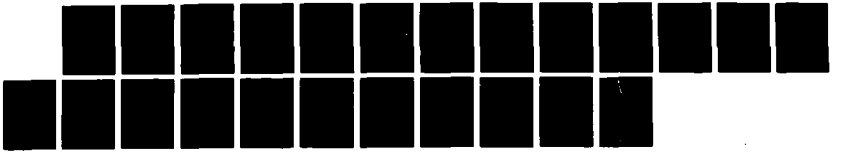

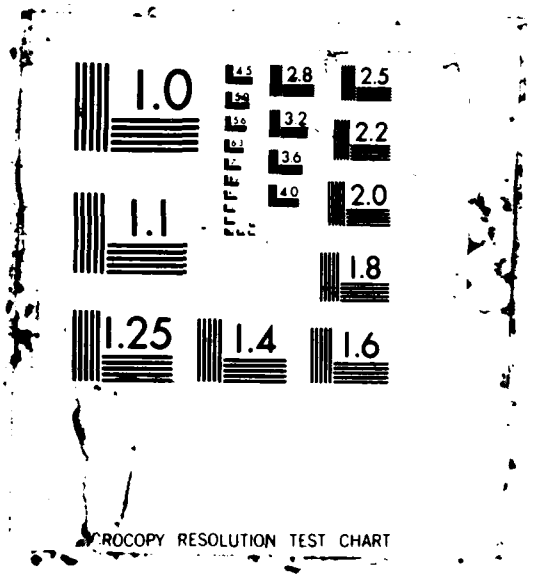
1.0
1.1
1.25
1.4
1.6
2.8
3.2
3.6
4.0
2.5
2.2
2.0
1.8
ROCOPY RESOLUTION TEST CHART

equation (F.5). The result is given by equation (F.7):

$$I(Y=0)/I(Y)=[(1/\tau_s)+(k_-Y)+(k_+Y\tau_u/\tau_s)]/(k_+Y+k_-Y+1/\tau_s) \quad (F.7)$$

The predicted relative intensity as a function of buffer gas pressure as given by equation (F.7) is shown with the observed fluorescence intensity in figure 26.

The lifetime of the stable states at zero buffer pressure, Y=0, is obtained from the pulsed lifetime studies of section IVC. For the mix pressure of 6.6 mTorr, the lifetime is 32.1 μs. The predissociated lifetimes of BrCl(B;v′=6,J′>42) range from 8.8 μs for J′= 42 to 1.0 μs for J′= 80.[122] An average predissociated lifetime of 2.5 μs is used in the modeling of equation (F.5). The stablization rate constants, k_- and k_+, are based on a simple fraction of the total rotational removal rate constants,

$$\begin{aligned} K_J^M(6) &= 1.60 \times 10^{-10}\ cm^3/molec\text{-}s \\ K_J^{He}(6) &= 1.93 \times 10^{-10}\ cm^3/molec\text{-}s \\ k_+ &= f_1\ K_J(6) \\ k_- &= f_2\ k_+ \end{aligned} \quad (F.8)$$

The modeled equation (F.5) is used to fit the observed data of figure 26 with the parameters f_1, f_2, and k_Q^{He}. The best agreement between the data and the model was obtained for the values f_1=0.6, f_2=0.7, and k_Q^{He}=5.0x10^{-12}cm^3/molec-s. Figure 26 illustrates the modeled quenching with these parameters. The agreement is quite good.

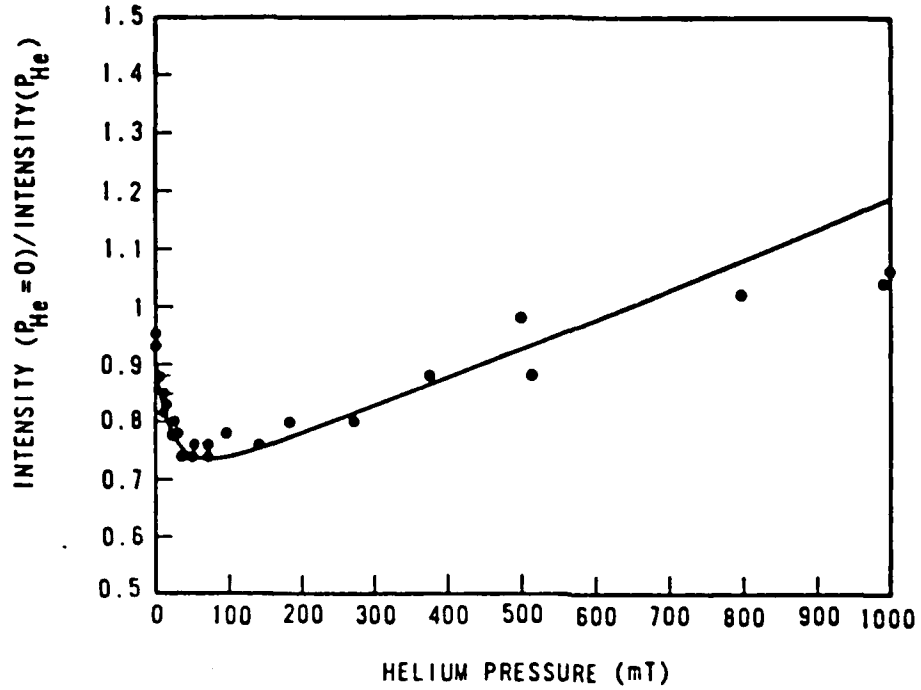

Figure 26. Quenching of BrCl(B) for initially-populating the predissociated state J´=44 in v´=6, indicating stabilization of the predissociated population. The mix pressure is 6.6 mT.

The parameters of the model are reasonable. The stabilization rate constant, k_+, should be slightly greater than one-half of the total rotational removal rate constant, since roughly half of the total rotational transfer would be for $\Delta J<0$. The transfer to predissociated states, k_-, is $k_-=(0.7)(0.6)K_R(6)=0.4\ K_R(6)$, which accounts for the remainder of the rotational removal. The helium quenching rate constant is intermediate between the quenching of v´=6 at very low pressures, $k_Q(6) = 5.2\times10^{-11}$ cm^3/molec-s and the electronic quenching rate, $k_{eq} = 1.3\times10^{-13}$ cm^3/molec-s. At helium pressures of 10 mTorr to 1 Torr the BrCl(B;v´) distribution will be nonthermal and a significant population will exist in all the stable vibrational states, v´<7. Thus, an intermediate quenching rate would be expected.

Appendix G

Synthetic CW LIF Emission Spectra

The spectral resolution in the CW experiment (see section IIIA) is insufficient to provide rotational state isolation. Some rotational state distribution information is available from rotationally-convolved spectra, however. This appendix describes a computer model that generates such convolved spectra. By comparing the computer generated spectra with the observed spectra, some conclusions regarding rotational transfer can be obtained (see Section IVB).

The fluorescence intensity from a single rotational state is given by equation (6). Converting intensity to photon counts, $I = n\,h\nu$, equation (G.1) is obtained.

$$n_{v',v''}(J',J'') = Cq_{v',v''}\nu^3 S(J',J'')N(v')f(J') \qquad (G.1)$$

where

$n_{v',v''}(J',J'')$ = intensity (in photons/s) of the (v',J') to (v'',J'') transition

C = arbitrary constant

ν = (v',J') to (v'',J'') transition frequency

$q_{v',v''}$ = Franck-Condon factor

$S(J',J'')$ = rotational linestrength factor

$$= \begin{cases} J/(2J+1) & \text{P-branch} \\ (J+1)/(2J+1) & \text{R-branch} \end{cases}$$

$N(v')$ = total population density in vibrational state v'

$f(J') = N(v',J')/N(v')$

Thus, for a given vibrational population distribution, $N(v')$, and a given rotational distribution, $f(J')$, the observed relative intensity of each ro-vibrational transition can be predicted. The "stick intensity" spectrum in figure G1 represents the intensity of each transition located at the transition emission wavelength. This "stick intensity" spectrum is indicative of the emission observed under infinite resolution.

The convolution of individual emission intensities under finite resolution can be computed by equation G.2.

$$n(\lambda_j) = \sum_{v,v'} \sum_{J,J'} n_{v',v''}(J',J'')\ R(\lambda_{v',v''}(J',J'') - \lambda_j) \qquad (G.2)$$

where

$$R(\lambda-\lambda_o) = [\sin d(\lambda-\lambda_o)/d(\lambda-\lambda_o)]^2 \qquad (G.3)$$

Figure G1 illustrates a resolution function, $R(\lambda-\lambda_o)$, with a 0.6 nm resolution centered at 664.0 nm as a dashed triangle. By calculating the convolved emission intensity from equation (G.2) as a function of emission wavelength, λ_j, the solid curve of figure G1 is obtained. This curve represents the predicted emission under the given resolution. Note that the intensity scales in figure G1 are arbitrary and different for the "stick intensity" and convolved spectra.

The predictions of equations (G.1) and (G.2) depend on the vibrational and rotational population distributions, $N(v')$ and $f(J')$. The vibrational distribution is input to the

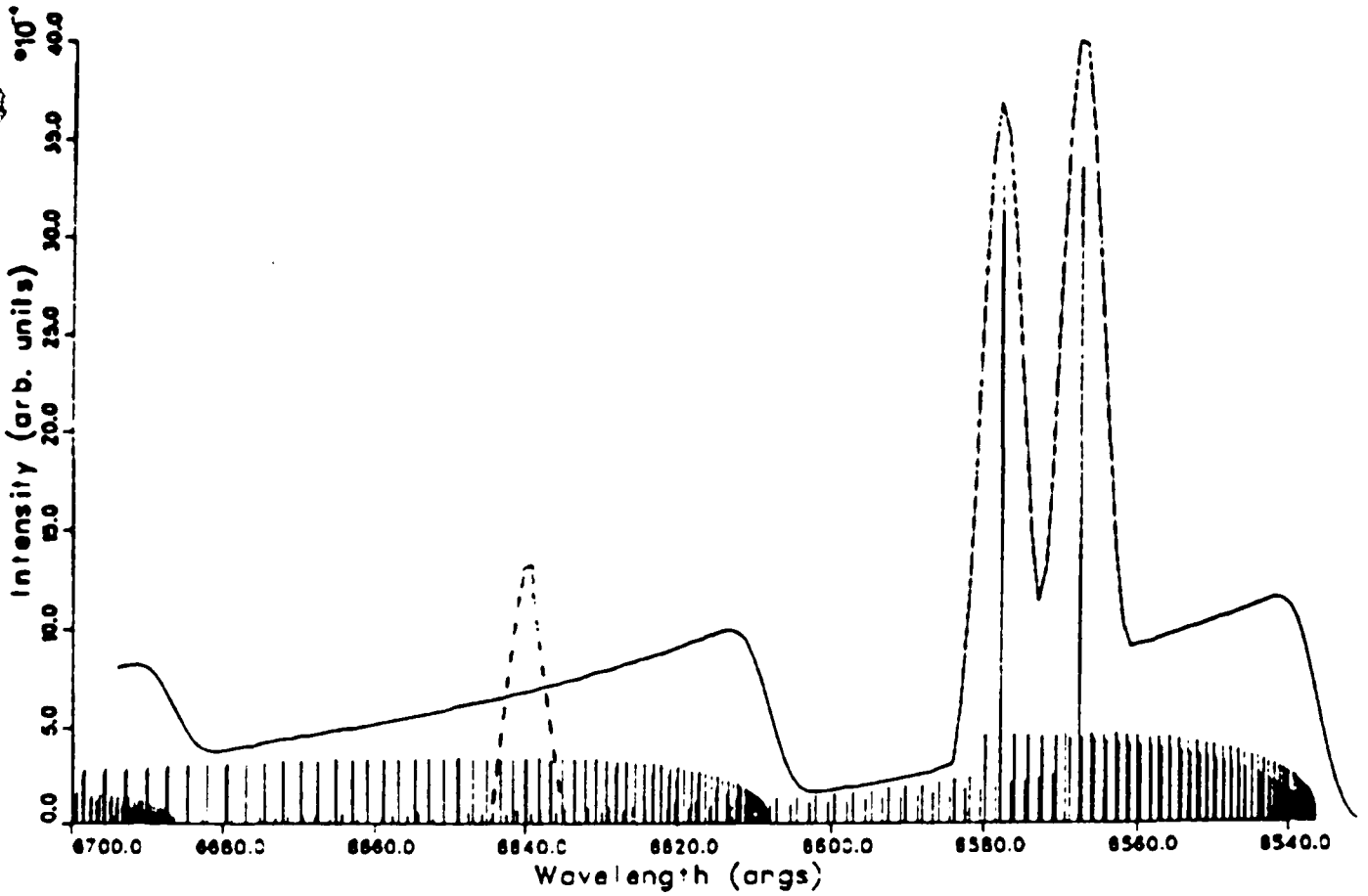

Figure G1. BrCl(B) synthetic LIF emission spectrum.

computer model from the relative populations observed in the CW spectra at the same conditions. A thermal distribution of rotational states, see equation (89), is used for the rotational distribution factor, f(J′). The rotational temperature is a parameter of the computer model. The population of the parent rotational state must be modified to reflect the pump source term. The additional population in the parent rotational state is also taken as a parameter of the computer model.

The rotational population distribution within $v'=6$ is modified due to rotational predissociation for $J' \geq 42$. The lifetimes of these states are drastically reduced. A second, non-radiative decay path is available for these states and the intensity observed in emission is correspondingly reduced. The steady state population in any rotational level is described by equation (52),

$$N_J = \sum_{J'} k_J^M (J'-J)\ N_{J'} M/[k_r + k_{pd} J(J+1) + K_R^M\ M] \qquad (G.4)$$

The number density in a predissociated state (and thus the fluorescencve intensity from that state) compared to the number density in a stable rotational state is therefore,

$$N_J/N_J^{PD} = 1 + k_{PD} J(J+1)/(k_r + K_R^M\ M) \qquad (G.5)$$

The predicted population in a predissociated state is then modeled by the equation (G.6):

$$N_J^{PD} = (N_J^{PD}/N_J)\ f(J')\ N(v') \qquad (G.6)$$

The abrupt reduction in intensity of the "stick" spectra at roughly 658.0 nm in figure G1 is due to this predissocation effect.

This computer model has been applied to the observed CW LIF spectrally resolved data as presented in section IVB. Conclusions regarding rotational temperaure at low mix pressures and rotational memory in V-T collisions are presented in section IVB.

Appendix H

Error Analysis

The error analysis for the pulsed lifetime studies and the steady-state experiments are described in this appendix.

I. Pulsed Lifetime Studies

The Stern-Volmer method described in chapter IIC requires the determination of excited state lifetimes at various kinetic conditions. Fluorescence decay curves such as shown in figure 28, provide the needed data for these lifetimes. Equation (72) is used to obtain the lifetimes from the logarithm of the fluorescence decay curves.

An actual temporal spectra will have some non-zero baseline intensity and equation (72) must be modified to include this baseline.

$$I(t) = I_o \exp(-t/\tau) + I_B \qquad (H.1)$$

$$\ln[I(t)-I_B] = \ln I_o - t/\tau \qquad (H.2)$$

where

I_B = baseline intensity

The Biomation transient recorder was operated in the pre-trigger mode and the first approximately 100 channels of the waveform were recorded before the initiation of the exciting

laser pulse. The average intensity of these channels was used as the baseline intensity.

A weighted linear regression fit to the observed fluorescence decay curve based on equation (H.2) was used to obtain the lifetime, τ. The uncertainty in the lifetime measurement, $\Delta\tau$, was also obtained from the linear regression.

The general, weighted linear regression is based on a least-squares analysis of the data.[187] Consider a set of N data points (x_i, y_i) with uncertainty in the dependent variable y_i of σ_i. The least-square analysis provides the following values for the intercept, a, slope, m, standard deviation, σ, uncertainty in the intercept, σ_a, uncertainty in the slope, σ_m, and correlation coefficient, r:

$$a=(1/\sigma^4\Delta)[\sum(x_i^2/w_i^2)\sum(y_i/w_i^2)-\sum(x_i/w_i^2)\sum(x_iy_i/w_i^2)]$$

$$m=(1/\sigma^4\Delta)[\sum(1/w_i^2)\sum(x_iy_i/w_i^2)-\sum(x_i/w_i^2)\sum(y_i/w_i^2)]$$

$$\sigma_a^2 = (1/\sigma^2\Delta)\sum(x_i^2/w_i^2) \qquad \text{(H.3)}$$

$$\sigma_m^2 = (1/\sigma^2\Delta)\sum(1/w_i^2)$$

$$\sigma^4\Delta = \sum(1/w_i^2)\sum(x_i^2/w_i^2)-[\sum(x_i/w_i^2)]^2$$

$$r=[\sigma^4\Delta m/(\sigma^4\Delta)^{1/2}]\{\sum(1/w_i^2)\sum(y_i^2/w_i^2)-[\sum(y_i/w_i^2)]^2\}^{1/2}$$

where

$w_i = \sigma_i/\sigma$, the weights

$$\sigma^2 = [1/(N-2)]\sum[(y_i-a-mx_i)^2/\sigma_i^2]$$

For the transient raw data counts, the uncertainty, σ_i, is statistical and thus[187],

$$\sigma_y^2 \sim y_i \tag{H.4}$$

The error in the logarithm of the dependent variable y_i is

$$d\ \ln(y) = dy/y \tag{H.5}$$

Thus, the uncertainty in the logarithm is

$$\sigma_{lny} = \sigma_i = \sigma_y/y_i = 1/(y_i)^{1/2} \tag{H.6}$$

This weighting has been used in the pulsed lifetime linear regression data fits.

Weighted linear regressions for the Stern-Volmer plots have been used to obtain the rate constants (see equation (71)). The uncertainty in the lifetimes (σ_m) obtained in the above procedure are used for the weights (σ_i) in the Stern-Volmer analysis. The uncertainty in the Stern-Volmer plot slopes, (σ_k), is therefore the final statistical uncertainty in the rate constant k. The weighted average and standard deviation in N measurements of the rate constant are given by equation (H.7).

$$\langle k \rangle = \sum (k_i/\sigma_k) \ / \sum (1/\sigma_k) \tag{H.7}$$

$$\sigma_k^2 = [1/(N-2)] \sum (k_i - \langle k \rangle)^2$$

Systematic errors in the pulsed lifetime experiments are relatively small. Sources of systematic errors include pressure changes during the acquisition of a single decay profile, inaccurate time-base calibrations, and inaccurate pressure transducer calibrations. The magnitude of these systematic errors is small with respect to the statistical error. For example, pressure changes were always less than 2% and typically less than 0.02%. Variation in laser power and small changes in laser frequency affect the absolute intensities of the decay curves by as much as 50%. However, such variations do not affect lifetime measurements. Statistical error alone is reported for the pulsed lifetime experiments.

Estimates for the uncertainty in rate constants obtained from the pulsed numerical solution of section IVD5 are difficult to obtain. The analysis of T. Carrington presented in section IIC4e implies the error in determined rate constants is approximately ten times greater than the scatter in observed temporal spectra. The standard deviation in observed temporal spectra was typically 10%. Thus, the error in the rate constants may be as large as 100%.

A rough estimate for error limits in the spectrally-resolved, temporally-resolved V-T transfer data may be established by varing the fundamental vibrational rate constant in the numerical solution and observing the effect on

predicted temporal spectra. By requiring the newly predicted spectra to match the observed spectra within experimental scatter, a limit to the uncertainty in rate constants was estimated to be 15-20%. This error estimate applies to a highly constrained system, however. Allowing simultaneous variation in other parameters such as total quenching rates, provides a significantly larger error bound, approximately 25-35%. Figure 52 indicates typical error estimates for $k_v^M(v,v-1)$ rate constants based on this numerical sensitivity analysis.

II. Steady-State Error Analysis

The CW LIF spectrally-resolved energy transfer experiment intrinsicly has more sources of systematic error and generally produces rate constants with larger uncertainty than does the pulsed experiment. The CW systematic errors arise from uncertainty in the variables used to relate intensity and number density (see equation (6)). These errors include, (1) uncertainty in Franck-Condon factors, (2) uncertainty in radiative lifetimes, (3) error in determining the relative spectral response, and (4) uncertainty and error in the calculation of spectral band areas.

The uncertainty in the Franck-Condon Factors is difficult to establish. For states v"<8, the Franck-Condon factors reported in the literature were used (see appendix B). No estimates for the uncertainty in these FCF's were reported.

The FCF's calculated in this thesis (see appendix B) reproduced the Coxon values[100] to within 10%. For vibrational states v">8, FCF's were calculated based on a simple extrapolation. No spectral data were used in this calculation. For these states the FCF's could have significant error. For this reason, emission to v">8 was avoided as much as possible. For v'=0, the only transitions with significant FCF's are to states v">9 and the extrapolated FCF's are necessary.

The radiative lifetimes determined in this thesis had an uncertainty of 4%. The radiative lifetimes were independent of vibrational state within the error bound, but variations within this bound would directly affect the number density calculations.

The relative spectral response was determined by observing the emission from a calibrated blackbody source (see appendix C). The error in the measured response is difficult to estimate, but the spectral response was reproducible to within 15-20%. The error in the spectral region near the PMT cutoff and long pass filter cut-off wavelengths is considerably larger.

The uncertainty in measuring spectral band areas is affected by the reproducibility of the Lasico planimeter (see appendix I). For areas greater than 1 cm^2, this uncertainty was approximately 10%. Additional error may be introduced

into the band areas by incomplete deconvolution of overlapping vibrational bands.

The propogation of these errors may lead to an uncertainty in the rate constants of greater than 30%. Such an error bound applies only to the CW data reduced by linear regression fit to equation (42).

Some of the CW data was used as a comparison to computer predicted populations. In this case, no fit to the data was accomplished and error estimates are more subjective. The only practical method of estimating errors was to determine the sensitivity of predicted populations to the input rate constants. By requiring the predicted populations to lie within the scatter of the observed data, limits on the range for rate constants were established. The rate constants are correlated and more than one rate constant affects each predicted population. Thus, the method is very subjective. Constraining the quenching rate constants to within the established error bounds of the rate constants determined in the pulsed lifetime studies, the uncertainty in the $\Delta v=-1$ vibrational transfer rates is established as 30-50 %. This error estimate in shown in figure 55.

Appendix I

Steady-State Number Densities and Spectral Band Areas

The relative areas under the spectral features of CW LIF spectrally resolved data like that presented in figures 21-22 are proportional to the relative steady-state populations of the excited states, see equation (6). The methods for determining the relative areas of the spectral features are described in this appendix.

I. Vibrational Transfer Data

The areas bounded by the photon count intensity and the baseline (dark current) in the spectrally-resolved CW LIF spectra like that shown in figure 21, were measured with a Lasico Model 9314 electronic planimeter. The linearity of the planimeter was better than 10 percent for areas greater than 1 cm^2. The absolute calibration of the planimeter was unimportant, since only relative areas were required.

The higher rotational levels of vibrational states v are overlapped with low rotational levels of vibrational states $v+\Delta v$, where Δv=even. For example, in figure 21, the "tail" of the $v'=3$ to $v''=5$ emission is overlapped with the band head of the $v'=5$ to $v''=6$ emission. Deconvolution of these spectral features is required to obtain accurate relative number densities.

It has been shown in section IVB that the satellite rotational states in all vibrational levels are approximately thermally populated, possibly with elevated rotational temperatures. The convolved rotational populations decrease approximately linearly at high rotational levels (see figure 25). This observation provides a simple method for deconvolution of the vibrational emission areas. The emission intensity of a given vibrational band may be linearly extrapolated to higher rotational levels from the trend at lower rotational levels. When this extrapolation reaches the baseline intensity, the rotational population is assumed to be zero. Figure 21 is reproduced in figure I1 with the extrapolated intensities shown as dashed lines. The areas bounded by the extrapolation and baseline are added to the area of the associated vibrational band and subtracted from the convolved vibrational band.

II. Rotational Transfer Data

Total rotational removal rates are obtained by applying equation (64) to the spectrally-resolved CW LIF data. The relative population of the parent rotational state is required for the data reduction. This population is proportional to the area under the sharp P-R doublet emission feature as observed in figures 21-22. At higher buffer pressures, the P-R doublet emission from the parent rotational state is

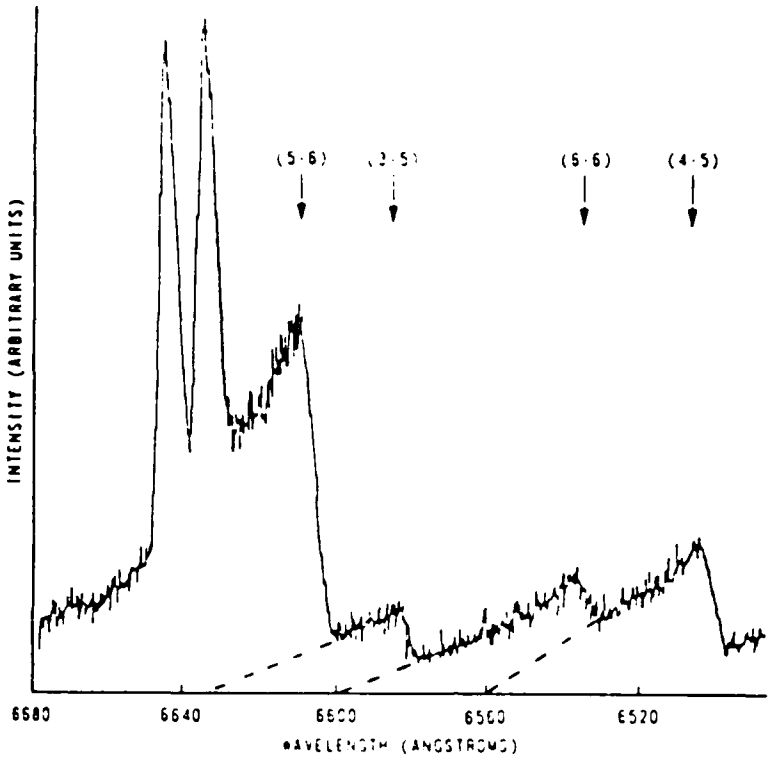

Figure II. Spectral band area deconvolution.

partially blended with the emission in the adjacent rotational states.

The resolution lineshape of a single spectral feature is given by

$$R(\lambda - \lambda_o) = [\ \sin d(\lambda - \lambda_o)/d(\lambda - \lambda_o)]^2 \qquad (I.1)$$

Such a function is well approximated by an isosceles triangle. The area of such a feature is therefore proportional to the FWHM times the peak height. The FWHM depends only on the resolution and not on the kinetic conditions. The peak heights can be slightly affected by rotational convolution and should not be used directly to obtain the relative areas. By

locating the intensity at the FWHM point of the doublet emission, the peak height can be more accurately determined. This calculated peak height and FWHM determine an isosceles triangle. The area of this triangle as measured by the planimeter was used to obtain the relative population in the parent rotational state. The areas under both pieces of the P-R doublet were added to obtain the total population in the parent rotational state. Note that for $J_o'=38$, the relative rotational line strength of the P- and R- branches is

$$S_P(38)/S_R(38) = 39/38 = 1.02 \qquad \text{(I.2)}$$

The areas obtained for the two spikes of the P-R doublet are indeed equal within the experimental scatter of approximately 10 percent.

Appendix J

Steady-State Removal Rates

The buffer gas, steady-state, spectrally-resolved LIF data reduction is based on equation (103). The ratio of the total removal rate constant, $K_R^Y(v)$, to the vibrational transfer rate constant, $k_V^Y(v,v_o)$, is needed to apply this equation to the observed data and to extract the vibrational rate constants. This ratio,

$$K_R^Y(v)/k_V^Y(v,v_o) \tag{J.1}$$

is easily calculated, assuming detailed balance, Landau-Teller scaling and a multiquantum fraction of f=0.4 applies. The electronic quenching is assumed negligible. The only important quenching is due to the rotational transfer in v'=6, $k_Q^{He}(6) = 5.2 \times 10^{-11}$ cm^3/molec-s. The total removal rate constant based on these assumptions is, from equation (25):

$$K_R^Y(v) = k_Q^Y(v) + \sum_{\Delta v} k_V^Y(v,v+\Delta v) \tag{J.2}$$

The vibrational transfer rate constants are related to the rate constant $k_V^B(v,v-1)$ by the relationships (J.3)

$$k_V^Y(v,v-2) = (0.4)\, k_V^Y(v,v-1) \tag{J.3}$$
$$k_V^Y(v,v+1) = \exp(-\Delta\varepsilon_{v,v+1}/k_BT)(v+1/v)k_V^Y(v,v-1)$$
$$k_V^Y(v,v+2) = \exp(-\Delta\varepsilon_{v,v+2}/k_BT)(0.4)(v+2/v)k_V^Y(v,v-1)$$

The total removal rate constant for $v'<6$ is therefore

$$K_R^Y(v)=[0.4 + 0.4(v+1)/v + .064(v+2)/v]k_V^Y(v,v-1) \quad (J.4)$$

Table J.I lists the ratio (J.1) for various v' states based on equation (J.5).

Table J.I
Rotational Removal Rate Constant Ratio

v'	v'	$K_R^Y(v)/k_V^Y(v,v+\Delta v)$
6	5	1.65
5	4	1.60
4	3	1.54
6	4	3.85
5	3	3.70
4	2	3.50
5	6	10.4
4	5	4.88

VITA

Glen Paul Perram was born on 6 May 1958 in Phoenix, Arizona. He graduated from Westland High School in Columbus, Ohio in 1976 and then attended the School of Engineering, Cornell University, from which he received the degree of Bachelor of Science, with distinction, in May 1980. Upon graduation, he received a commision as a Second Lieutenant in the United States Air Force as a distinguished graduate of the Air Force Reserve Officer Training Corps. He then entered the Air Force Institute of Technology, Wright-Patterson Air Force Base, Ohio from which he received a Master of Science degree in Engineering Physics in December 1981. He continued his education at AFIT and completed the course work and qualifying examinations for a Doctor of Philosophy degree in physics. He is currently assigned to the Advanced Radiation Technology Office of the Air Force Weapons Laboratory, Kirtland Air Force Base, New Mexico.

Address: 3398 51st Loop SE
Kirtland AFB, NM 87116

REPORT DOCUMENTATION PAGE

1a. REPORT SECURITY CLASSIFICATION: Unclassified	1b. RESTRICTIVE MARKINGS
2a. SECURITY CLASSIFICATION AUTHORITY	3. DISTRIBUTION/AVAILABILITY OF REPORT: Approved for public release; distribution unlimited.
2b. DECLASSIFICATION/DOWNGRADING SCHEDULE	
4. PERFORMING ORGANIZATION REPORT NUMBER(S): AFIT/DS/PH/86-1	5. MONITORING ORGANIZATION REPORT NUMBER(S)
6a. NAME OF PERFORMING ORGANIZATION: Air Force Institute of Technology; 6b. OFFICE SYMBOL (If applicable): AFIT/EN	7a. NAME OF MONITORING ORGANIZATION: Air Force Weapons Laboratory, Advanced Chemical Laser Branch
6c. ADDRESS (City, State and ZIP Code): Wright-Patterson AFB, OH 45433	7b. ADDRESS (City, State and ZIP Code): Kirtland AFB, NM 87117-6008
8a. NAME OF FUNDING/SPONSORING ORGANIZATION: Air Force Office of Scientific Research; 8b. OFFICE SYMBOL (If applicable): AFOSR/NC	9. PROCUREMENT INSTRUMENT IDENTIFICATION NUMBER: Approved for public release IAW AFR 190-1. LYNN E. WOLAVER, Dean for Research and Professional Development, Air Force Institute of Technology (ATC), Wright Patterson AFB OH
8c. ADDRESS (City, State and ZIP Code): Bolling AFB, Washington DC	10. SOURCE OF FUNDING NOS: PROGRAM ELEMENT NO: 61102F; PROJECT NO: ---; TASK NO: ---; WORK UNIT NO: 2303Y202
11. TITLE (Include Security Classification): Collisional Dynamics of $B^3\Pi(0^+)$ State of Bromine Monochloride (u)	
12. PERSONAL AUTHOR(S): PERRAM, GLEN PAUL	
13a. TYPE OF REPORT: PhD Dissertation; 13b. TIME COVERED: FROM ~~Jan 83~~ TO ~~Mar 86~~	14. DATE OF REPORT (Yr., Mo., Day): 1986 August; 15. PAGE COUNT: 307
16. SUPPLEMENTARY NOTATION	

17. COSATI CODES		
FIELD	GROUP	SUB GR
07	04	0
20	05	0

18. SUBJECT TERMS (Continue on reverse if necessary and identify by block number): Bromine monochloride, laser induced fluorescence, electronic quenching, vibrational transfer, rotational transfer, bromine, optical excitation, laser, chemical laser

19. ABSTRACT (Continue on reverse if necessary and identify by block number)

The radiative and collisional dynamics in the $B^3\Pi(0^+)$ state of bromine monochloride have been studied using time-resolved and steady-state, spectrally-resolved laser induced fluorescence techniques. Radiative lifetimes and rate constants for electronic quenching, state-to-state vibrational transfer, and total rotational removal were obtained from observed BrCl (B-X) emission in the presence of Cl_2, He, Ne, Ar, Kr, Xe, N_2, and O_2 buffer gases. Vibrational states $v' = 0$-7 were probed and emission observed from states $v'=0$-6.

The BrCl(B) radiative lifetime is 38.7 +/- 1.7 us, independent of vibrational state for $v'<6$. The electronic quenching of a thermalized BrCl(B;v') distribution is inefficient with rate constants/ranging from 7.8×10^{-14} cm^3/molec-s for Neon to 4.3×10^{-13} cm^3/molec-s for Cl_2. The quenching of nonthermal vibrational distributions is considerably more rapid and due to both ro-vibrational ladder climbing to predissociated states

(Continue on next page)

20. DISTRIBUTION/AVAILABILITY OF ABSTRACT: UNCLASSIFIED/UNLIMITED ☒ SAME AS RPT ☐ DTIC USERS ☐	21. ABSTRACT SECURITY CLASSIFICATION: Unclassified
22a. NAME OF RESPONSIBLE INDIVIDUAL: Glen P. Perram	22b. TELEPHONE NUMBER (Include Area Code): (505)-844-1871; 22c. OFFICE SYMBOL: AFWL/ARDA

DD FORM 1473, 83 APR — EDITION OF 1 JAN 73 IS OBSOLETE

and resonant electronic transfer to excited electronic states of Cl_2. The Cl_2 quenching rate constants vary from 4.3 x 10^{-13} cm^3/molec-s for $v'=0$ to 1.4 x 10^{-10} cm^3/molec-s for $v'=6$.

The fundamental rate constant for vibrational transfer from $v'=1$ to $v'=0$ with chlorine as the collision partner is 1.3 x 10^{-11} cm^3/molec-s. Scaling of the vibrational rate constant with vibrational quantum number obeys a power law with an exponent of 0.63. Vibrational transfer with the noble gases is less efficient with fundamental rate constants ranging from 4 x 10^{-12} cm^3/molec-s for helium to 2.0 x 10^{-12} cm^3/molec-s for krypton. Rotational transfer in BrCl(B) is very efficient with total removal rates ranging from 1.6 x 10^{-10} cm^3/molec-s for chlorine to 2.43 x 10^{-10} cm^3/molec-s for argon.

A dye laser pumped Br_2 $B^3\pi(0^+)$ - X $1\Sigma_g^+$ laser has been demonstrated. Spectroscopic assignments have shown that lasing occurs from $10 < J' < 63$ in $12 < v' < 17$ using Rhodamine 590 dye. By utilizing stimulated emission as a monitor for laser excitation spectra, dramatic increases in the resolution were obtained that exceed the normal resolution of the dye laser. The Br_2 laser operated at Br_2 pressures of up to 60 torr, despite severe natural predissociation and self quenching. A simple model to explain the characteristics of the Br_2 laser is described.

END

5-81

DTIC